AD-A031 621 PENNSYLVANIA STATE UNIV UNIVERSITY PARK PETROLEUM RE--ETC F/G 11/8
FLUIDS, LUBRICANTS, FUELS AND RELATED MATERIALS. PART II.(U)
OCT 75 E E KLAUS, E J TEWKSBURY, B Y SO F33615-73-C-5101
UNCLASSIFIED AFML-TR-74-201-PT-2 NL

1 OF 3
AD
A031621

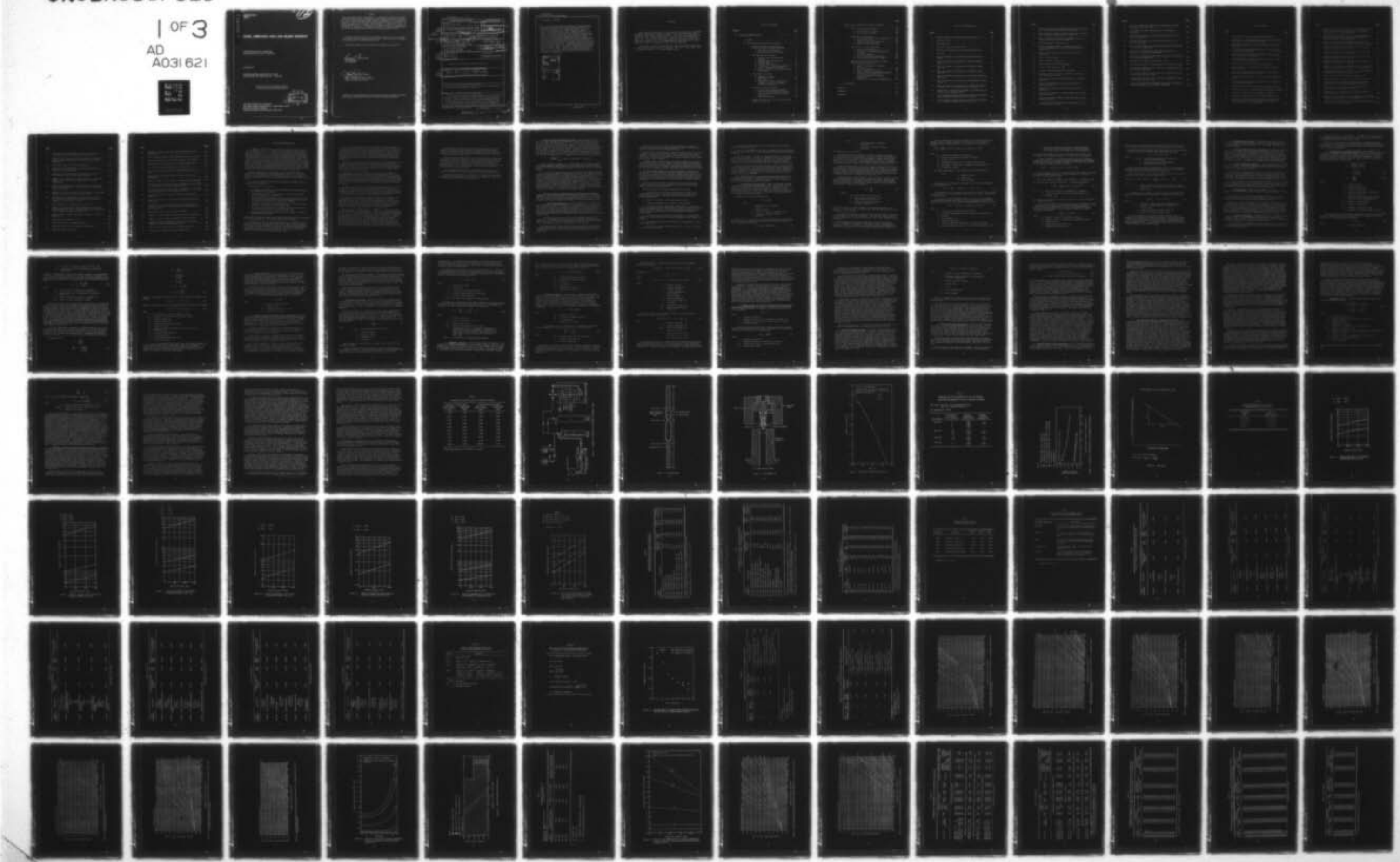

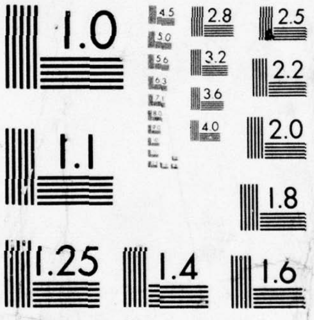

MICROCOPY RESOLUTION TEST CHART
NATIONAL BUREAU OF STANDARDS-1963-A

FG. 12

AFML-TR-74-201
PART II

FLUIDS, LUBRICANTS, FUELS AND RELATED MATERIALS

PETROLEUM REFINING LABORATORY
THE PENNSYLVANIA STATE UNIVERSITY

OCTOBER 1975

TECHNICAL REPORT AFML-TR-74-201, PART II
FINAL REPORT FOR PERIOD MAY 1974 - APRIL 1975

Approved for public release; distribution unlimited

AIR FORCE MATERIALS LABORATORY
AIR FORCE WRIGHT AERONAUTICAL LABORATORIES (AFSC)
AIR FORCE SYSTEMS COMMAND
WRIGHT-PATTERSON AIR FORCE BASE, OHIO 45433

This report has been reviewed by the Information Office (OI) and is releasable to the National Technical Information Service (NTIS). At NTIS, it will be available to the general public, including foreign nations.

This technical report has been reviewed and is approved for publication.

George J. Morris

GEORGE J. MORRIS
Project Engineer

Larry L. Fehrenbacher

LARRY L. FEHRENBACHER, Major, USAF
Chief, Lubricants and Tribology Branch
Nonmetallic Materials Division

UNCLASSIFIED

SECURITY CLASSIFICATION OF THIS PAGE (When Data Entered)

REPORT DOCUMENTATION PAGE	READ INSTRUCTIONS BEFORE COMPLETING FORM
1. REPORT NUMBER AFML-TR-74-201, Part II 2. GOVT ACCESSION NO.	3. RECIPIENT'S CATALOG NUMBER (9)
4. TITLE (and Subtitle) (6) FLUIDS, LUBRICANTS, FUELS AND RELATED MATERIALS, Part II.	5. ~~TYPE OF REPORT & PERIOD COVERED~~ Final Report, 1 May 74 ~~through~~ 30 April 75, 6. ~~PERFORMING ORG. REPORT NUMBER~~
7. AUTHOR(s) (10) E. Erwin Klaus, Elmer J. Tewksbury, ~~et al.~~ Bernard Y. C. So, Steven M. Hsu	8. ~~CONTRACT OR GRANT NUMBER(s)~~ (15) F33615-73-C-5101
9. PERFORMING ORGANIZATION NAME AND ADDRESS Petroleum Refining Lab., Chem. Engr. Dept. The Pennsylvania State University University Park, PENNSYLVANIA 16802	10. PROGRAM ELEMENT, PROJECT, TASK AREA & WORK UNIT NUMBERS 7343 - 734303
11. CONTROLLING OFFICE NAME AND ADDRESS Air Force Materials Laboratory Air Force Systems Command Wright-Patterson AFB, OHIO 45433	12. REPORT DATE (11) October 1975 (12) 247p. 13. ~~NUMBER OF PAGES~~
14. MONITORING AGENCY NAME & ADDRESS (if different from Controlling Office) (18) AFML	15. SECURITY CLASS. (of this report) Unclassified 15a. DECLASSIFICATION/DOWNGRADING SCHEDULE
16. DISTRIBUTION STATEMENT (of this Report) Approved for Public Release, Distribution Unlimited	
17. ~~DISTRIBUTION STATEMENT (of the abstract entered in Block 20, if different from Report)~~ (19) TR-74-201-Pt-2	
18. SUPPLEMENTARY NOTES	
19. KEY WORDS (Continue on reverse side if necessary and identify by block number) Fluids, Lubricants, Lubrication, Four-Ball Wear Tester, Atomic Absorption Spectrometer, Pressure-Viscosity Correlation	

20. ABSTRACT (Continue on reverse side if necessary and identify by block number)

A diffusion effect at the gas liquid interface during the determination of pressure viscosity values in a capillary instrument is shown to be a problem. A method to minimize the effects of gas diffusion is proposed. Pressure coefficients for fluids such as mineral oils, "dumbbell" blends of mineral oil fractions, and paraffinic resin-solvent blends are shown to be independent of pressure at pressures up to at least 3000 psig at a variety of temperatures. Several empirical correlations involving viscosity

over

DD FORM 1 JAN 73 1473 EDITION OF 1 NOV 65 IS OBSOLETE

UNCLASSIFIED

280450 lb PER SQUARE IN. GRAVITY

P

20. Abstract (concluded)

level, ASTM slope, and density are presented for viscosity-pressure data. These correlations are tested using data determined by a variety of investigators over a temperature range of 32° to 275°F. The correlations developed are shown to require less physical property data, apply to a wider range in fluidity, apply to a wide range of chemical type fluids, and to provide better accuracy when compared to a number leading correlations from the literature. Wear debris analysis can be used to measure the production of metal particles, metal oxides, and organometallic reaction products produced in the wear conjunction. The Shell four-ball wear tester and the atomic absorption spectrophotometer have been used for the production and analysis of the wear debris. Temperature conditions at the contact area are varied by using static, slow-sliding, and high speed sliding at the lubricated surfaces. The junction temperature rise has been determined using a chemical conversion correlation between static and dynamic runs. It is shown to be higher than generally used flash temperatures. Chemical reactions are shown to play an important role in boundary lubrication.

ACCESSION for
NTIS White Section ☑
DDC Buff Section ☐
UNANNOUNCED ☐
JUSTIFICATION ....
....
BY..
DISTRIBUTION/AVAILABILITY CODES

Dist.	AVAIL. and/or SPECIAL	
A		

FOREWORD

This report was prepared by the Petroleum Refining Laboratory, Department of Chemical Engineering, College of Engineering at The Pennsylvania State University under Contract F33615-73-C-5101. This project was initiated under Project No. 7343 "Aerospace Lubricants," Task No. 734303 "Fluid Lubricant Materials." This work was administered under the direction of the Air Force Materials Laboratory, Air Force Systems Command, Wright-Patterson Air Force Base, Ohio, with Mr. George Morris (MBT) as Project Engineer.

This report covers work conducted from 1 May 1974 through 30 April 1975; it was submitted by the authors 15 June 1975. They are E. Erwin Klaus, Elmer J. Tewksbury, Bernard Y. C. So, and Stephen M. Hsu.

TABLE OF CONTENTS

Section Page

LIST OF ILLUSTRATIONS

LIST OF TABLES

I. FLUID AND LUBRICANT STUDIES

A. SUMMARY. Studies have been continued to understand better the interaction of lubricants and working fluids and the environment in which these materials must function. Film thickness of the lubricant in the bearing has particular application to aircraft uses where minimum viscosity levels (high temperature operation) are used to achieve operability similar to that shown at lower temperatures. Earlier reports include the development of correlations enabling one to derive a value for the viscosity-pressure coefficient α. The pressure coefficient determinations carried out using the PRL pressure viscometer appear to be pertinent for use in elastohydrodynamic equations for the measurement of film thickness. Techniques have been developed which allow the accurate determination of wear debris developed using the four-ball wear tester. Organometallic materials both soluble and insoluble in the test oil can be determined. Iron and iron oxides can be determined in the presence of each other.

Current theory indicates that pressure viscosity may be an important parameter for hydrodynamic and elastohydrodynamic lubrication. Due to the difficulty and cost required to obtain experimental data, it is desirable to develop simple pressure viscosity correlations which cover a wide range of fluid types.

Gas solubility during the determination represents the largest error in these viscosity-pressure data.

The objectives of this study are:

1. To evaluate the quality of viscosity-pressure data obtained from the PRL high pressure viscometer;
2. To determine the effect of dissolved gas on the viscosity pressure properties measured in the PRL unit;
3. To obtain experimental pressure viscosity values on a series of "dumbbell" blends of low and high molecular weight components such as gas oil-bright stock and paraffinic resin-gas oil blends;
4. To derive correlations for viscosity-pressure as a function of fluid properties from the PRL pressure-viscosity data;
5. To test the correlations with the available viscosity-pressure data from other sources as well as the PRL unit data; and
6. To relate the correlating parameters, wherever possible, to physical significance and or theory.

Gas solubility studies have been used to determine the diffusion effect indicated by viscosity stability as a function of time at constant pressure.

The pressure viscosity of Pennsylvania mineral oils, "dumbbell" blends of mineral oil fractions, and paraffinic resin-solvent blends have been measured with the PRL pressure viscometer at pressures up to 3000 psig and temperatures of 32°, 100°, and 130°F. The results show that the pressure coefficients are independent of pressure for the fluids studied. This is in agreement with previous results with the PRL high pressure viscometer.

Data for pure hydrocarbons, mineral oils, nonhydrocarbons, and blends of mineral oils, polymers and resins at 100°F were used to establish the correlations. The final form of the correlations for viscosity-pressure data were obtained by regressional analysis. The resultant empirical relationships involve viscosity level, ASTM Slope and density. These parameters appear to be related to such physical characteristics as molecular interlocking, molecular packing, molecular rigidity, and size of the flow unit. In all cases the parameters used in the correlations are consistent with the void volume theory proposed by Cohen and Turnbull (1).

The resultant correlations were not only tested with viscosity-pressure data at 100°F from a variety of investigators but were also tested with data at temperatures ranging from 32° to 275°F. The current correlations when compared with the other leading correlations were shown to require less physical property data, apply to a wider range of chemical compositions, cover a wider range in fluidity and provide better accuracy.

The mechanism of boundary lubrication is important for the design of a lubricant-bearing system. Wear debris analysis has been used to measure the production of metal particles, metal oxides, and organometallic reaction products. The separation of metal particles and metal oxides can be done by preferentially dissolving the iron oxides using an acridine-inhibited hydrochloric acid solution. The iron can be preferentially dissolved from the iron oxides by the use of nitric acid. The iron-iron oxide separation can be measured both ways with relatively good results.

The qualitative results in the four-ball wear tester operated in the normal way (600 rpm, 40 kilograms, 167°F) with a hydrocarbon lubricant have been analyzed. The results show that in all cases there is some iron oxide and some organometallic formed in the wear conjunction. These reactions would be predicted for high temperatures of the order of those measured in elastohydrodynamic lubrication or the higher temperatures predicted in boundary lubrication.

A series of four-ball wear tests have been conducted at low speed to limit the heat generated at the bearing conjunction. In these tests, the bulk temperature has been used to control the bearing temperatures. These tests with hydrocarbon lubricants have shown low levels of chemical activity at low bulk temperatures. On the other hand, there is a sharp rise in chemical activity at higher bulk temperatures. The chemical activity to produce organometallic products is substantial at bulk temperatures of 500°F and higher.

There is clearly a temperature effect on chemical reactivity that follows the bulk temperature in a manner similar to the results of microcorrosion studies. The microcorrosion studies are conducted in a static system where bulk temperature is the only source of energy for the reaction. One of the problems in comparing the slow speed four-ball with the high speed four-ball is the area to consider. The high speed four-ball test at low bulk temperature focuses the chemical reaction on the wear scar areas. For the high bulk temperature, low speed four-ball tests the total ball area may be more important than the wear scars. In order to determine the relative importance of the total ball area and the wear scar, low speed four-ball tests have been run without contact between the balls. These data are compared with the high speed four-ball and the microcorrosion tests.

The information from microcorrosion studies indicates that the reaction between the oxidized hydrocarbon and the iron or iron oxide surface has an initial rate that shows a typical temperature dependence. In the case of the four-ball wear tester, the wear scars are continuously wiped by the wear action and provide a continuing active surface.

Reduced reaction with growing wear scar and decreasing load is demonstrated by sequential tests with the same set of balls. This result suggests that the temperature of the reacting environment is changing with time and actual unit load in the bearing area. Estimates of reaction kinetics are based on the assumptions of no change in the reactivity of the surface and an average wear scar area and temperature. It is apparent that the wear scar area and surface temperatures are changing continuously.

Data for estimating reaction rates and temperatures are obtained using standard and sequential four-ball wear tests with a super-refined mineral oil.

The junction temperature rise determined using a chemical conversion correlation between static and dynamic runs is shown to be substantially higher than the generally used Blok-Archard flash temperatures.

B. VISCOSITY-PRESSURE CORRELATION OF LIQUIDS. Bearing pressures of the order of 50,000 to 500,000 psig are encountered in elastohydrodynamic and other thin film, fluid lubricant applications. As a result, many of the viscosity-pressure studies with liquids have been conducted in this high pressure range. However, the recent studies by Bell (2) and Cheng (3) on the elastohydrodynamic theory, suggest that the inlet film thickness is largely governed by the pressure-viscosity effect in the low pressure region. Westlake (4) further pointed out that the best correlation on film thickness seems to be obtained with viscosity data obtained at 10,000 psig. It is the current theory that the most important viscosity-pressure characteristic of liquids is the pressure-viscosity coefficient

$$\left(\left.\frac{\partial(\log \mu)}{\partial p}\right|_{p=0}, \text{ where } \mu = \text{viscosity, } p = \text{pressure.}\right)$$

Advanced hydraulic systems typical of those used in aircraft and aerospace applications operate at bulk pressures of up to 10,000 psig. Precise viscosity properties in this pressure range are required to study the fluid flow in hydraulic systems.

Most of the high pressure-viscosity data were obtained with rugged equipment capable of achieving pressures of 100,000 psig or higher. The ruggedness of most of these viscometers resulted in low precision data at low pressures (0 to 10,000 psig). The development of a low pressure precision capillary-type pressure viscometer by this laboratory is discussed in previous reports. The use of this viscometer to measure the viscosity-pressure characteristics of a wide variety of fluid types is presented in Annual Report AFML-TR-67-101, Part I. The use of the same pressure viscometer to measure the effect of polymers and resin on the viscosity-pressure characteristics of the solvents is included in Annual Report AFML-TR-70-304, Part II. It is desirable to obtain a general pressure coefficient correlation to include both polymeric and nonpolymer fluids.

1. Review of Methods for Determining and Predicting Viscosity-Pressure Properties. Viscosity-pressure data for liquids are relatively limited in the literature because of the relatively complex apparatus required for measurement. Pertinent literature concerning the experimental determinations and the correlations of the viscosity-pressure characteristic of liquids are summarized below.

a. Experimental Determination. There are basically four types of low shear viscometers. Bridgman (5), Kuss (6), and the ASME Project (7) used the falling weight viscometer. A rolling ball viscometer was used by Webb and Dixon (8). These viscometers were designed to obtain data at very high pressures. Pressures up to 170,000 psig are readily obtainable with the apparatus and with modification pressures exceeding 400,000 psig may be reached. However, for pressures below 10,000 psig, this apparatus doesn't produce high accuracy pressure viscosity data.

By determining the change in the resonant frequency and electrical resistance of a longitudinally vibrating probe, a commercial instrument called Utraviscoson (9) can be used to determine viscosity-pressure effects at low shear rates. The maximum pressure for this apparatus is only 1000 psi.

Data obtained using a capillary type pressure viscometer are discussed in previous Annual Reports. The PRL pressure viscometer was specifically designed to obtain highly accurate data for pressures below 10,000 psig and under low shear rate.

There are also three major types of high shear pressure viscometers. The problems connected with the high shear viscometers are that it is difficult to separate the shear, pressure, and temperature effects.

Novak and Winer (10) constructed a two-way high pressure capillary viscometer. Although it covers a shear stress range of 300 to 1.1 x 10^6 dynes per square centimeter, the uncertainty of the pressure level increases with the decreasing shear stress. Therefore, data obtained by this apparatus under low shear stresses give the lowest level of accuracy.

Appeldoorn, Okrent, and Philippoff (11) modified the Mason (12) vibrating crystal viscometer for viscoelastic behavior studies of polymer blended solutions. Viscosity and elasticity are determined by the change in the resonant frequency and electrical resistance of the probe. Limited by the flatness of the resonance peak the highest atmospheric viscosity fluid tested was 69.28 centipoises at 100°F.

Optical elastohydrodynamic fluid testing was developed by Cameron (13,14) and co-workers. Optical interference was used to measure the film thickness between a glass or quartz plate and a specially finished rolling steel ball which is loaded against the plate. By calibrating the apparatus with fluids of known pressure-viscosity characteristics, the pressure-viscosity of unknown fluids can be measured. The operational range of the rate of shear is between 0.1 and 40 million sec^{-1}.

Other than the work discussed in AFML-TR-70-304, Part II using polymer solutions, all the low shear viscosity-pressure studies were with pure hydrocarbons, mineral oils and synthetic oils.

From these studies, the following generalizations can be made:

1. Plots of the log of viscosity versus pressure up to 10,000 psig at constant temperature result in a straight line for almost all fluids. Some notable exceptions include a slight upward curvature for phenylethers and chlorinated hydrocarbons;

2. Viscosity is a function of both temperature and volume;

3. In general, temperature effects are less at high pressure;

4. For the lower molecular weight range, chain length has a significant effect on the pressure-viscosity characteristics. However, the effect of molecular structure is very much greater. For the long chain molecule, viscosity level increases with chain length whereas the viscosity-pressure characteristics remains constant;

5. The increased internal mobility of the molecule (e.g., building ether linkage into a long chain molecule) decreases the dependency of the viscosity on pressure;

6. The viscosity-pressure effect increases with the introduction of rigid or bulky side groups;

7. Introduction of certain functional groups (e.g., Cl or OH) can increase the viscosity-pressure effect;

8. The largest pressure effects are for those substances with the most complicated molecular structure;

9. For a close approximation, the effect of nitrogen gas saturation on the pressure viscosity of fluids is to reduce the pressure viscosity to its atmospheric level; and

10. Reduced viscosity is the ratio of solution viscosity over the solvent viscosity at one atmosphere. The effect of polymers and resin on the viscosity-pressure characteristics of the solvent is the same, up to a reduced viscosity level of twelve. For a reduced viscosity level above twelve, the effect of polymers on the viscosity-pressure characteristics is a function of polymer type.

The only extensive work on the viscosity-pressure effect of binary mixtures has been done by Dow (15). For mixtures of molecules with linear structure, the viscosity-temperature and viscosity-pressure coefficients of the components are additive. However, for complex molecules, the viscosity isobars of the mixtures display variations with concentration. The deviation from the additive rule always increases with the pressure.

Griest, Webb and Schiessler (16) studied three hydrocarbon mixtures. The viscosity of these compounds is some additive function of their constituent groups whether these groups are combined in the same or different molecules, as long as the basic molecular symmetry is unchanged.

b. Available Prediction Techniques. Several attempts have been made to calculate the viscosity of a liquid under pressure in the absence of experimental data. All have met with very little success. Therefore, the major predictive effort has been directed toward empirical correlations. Since pressure-viscosity data are difficult to obtain, any correlations requiring such data have very limited use. This survey includes only those correlations which do not require pressure-viscosity data.

A definition of α is given in Equation [1].

$$\alpha = \frac{1}{p} \log \frac{\eta_p}{\eta_o} \qquad [1]$$

where:

α = viscosity-pressure coefficient, cm^2/kg,

p = pressure, kg/cm^2,

η_p = viscosity at pressure p, centipoise, and

η_o = viscosity at atmospheric pressure, centipoise.

By assuming that α is constant for a particular liquid and is not a function of pressure, Worster (17) proposed the following linear relationship between α and $\log \eta_o$ for naphthenic mineral oils.

$$\alpha = 0.006 + 0.00097 \log \eta_o \qquad [2]$$

where:

α = viscosity-pressure coefficient, cm^2/kg, and

η_o = viscosity at atmospheric pressure, centipoise.

The scatter for α is ± 20 percent.

Hartung (18) proposed a graphical correlation to predict the pressure viscosity isotherms of liquid lubricants at 100° and 210°F up to 100,000 psig. Data required to make the prediction are atmospheric pressure densities and viscosities at 100° and 210°F. This method has an accuracy of ± 20 percent. However, errors in this method are increased for oils which have less than four centistokes viscosity at 210°F or have viscosity indices of less than -100.

Clark (19) assumed that for all oils the pressure change required to duplicate the effect of any specified temperature change is the same. As a result, the ASTM Kinematic Viscosity-Temperature Chart D341 may be adapted for viscosity-pressure properties by replacing each temperature value on the scale with its equivalent pressure value. This method usually gives results reliable to only ± 50 percent even after classifying oils as paraffinic, etc.

Lockhart and Lenoir (20) presented a viscosity-pressure correlation for high molecular weight pure hydrocarbons, lubricating oils, neutral stocks, bright stocks, and distillates. This method requires a knowledge of the atmospheric pressure-viscosity at the temperature of interest and of the Watson characterization factor. This factor is defined as:

$$K_w = \frac{\sqrt{T_b}}{\rho_{60}} \qquad [3]$$

where:

K_w = Watson characterization factor,

T_b = mean average boiling point of the petroleum fraction in °R, and

ρ_{60} = density at 60°F and atmospheric pressure in $grams/cm^3$.

The accuracy of the correlation decreases as the pressure increases. At a pressure of 10,000 psig, and for viscosities of less than 1000 centipoises, the average error is ± 9 percent.

Chu and Cameron (21) gave a correlation which relates pressure coefficient, α, to atmospheric viscosity and temperature. The correlation predicts that at constant temperature, α decreases with viscosity level. This contradicts experimental data.

Dixon and Webb (22) presented a monograph for constant viscosity as a function of temperature and pressure. This method requires the knowledge of viscosity as a function of temperature to predict the pressure-viscosity. The average error is reported to be ± 20 percent at pressures up to 25,000 psig.

The first quantitative correlation between viscosity-temperature-pressure dependence and the chemical constitution of mineral oils was obtained by Roelands, Vlugter, and Waterman (23). The correlation can be expressed as follows:

$$\log \frac{\eta_p}{\eta_o} = \left(\frac{p}{500}\right)^y [(0.002\ C_A + 0.003\ C_N + 0.055) \log \eta + 0.228] \qquad [4]$$

where:

η_p = viscosity at pressure p, centipoise,
η_o = viscosity at atmospheric pressure, centipoise,
p = pressure, psig,
C_A = percentage of carbon atoms in aromatic ring structure,
C_N = percentage of carbon atoms in naphthenic ring structure, and
y = an empirical constant.

The carbon percentages, C_A, are determined by the n-d-M method (24).

where:

n = refractive index,
d = density, and
M = molecular weight.

The exponent y has been empirically related to the carbon percentages by the following equation:

$$\log (y - 0.890) = 0.00855\ (C_A + 1.5\ C_N) - 1.930 \qquad [5]$$

A maximum deviation of five percent is reported for values of log η_o ranging from about -0.1 to 1.5, for temperatures from 25° to 90°C, and for pressures up to 1000 atmospheres.

By combining the Slotte-Fahrenheit equation for the viscosity-temperature relationship and the Barus equation for the viscosity-pressure relationship, Appeldoorn (25) obtained a four-constant viscosity-temperature-pressure equation.

$$\log \eta = \log \eta_o + a \log \frac{t}{t_o} + b_p + C_p \log \frac{t}{t_o} \qquad [6]$$

where:

η = viscosity at any temperature and pressure,
η_o = viscosity at atmospheric pressure and reference temperature, t_o,
p = pressure,
t = any temperature, °F,
t_o = reference temperature, °F,
a = viscosity-temperature coefficient at atmospheric pressure,
b = pressure-viscosity coefficient at the reference temperature, and

c = constant which determines how much the viscosity-temperature coefficient increases with pressure or, conversely, how much the viscosity-pressure coefficient decreases with temperature.

This equation was claimed to be accurate (< 10% error) for 95 percent of the data tested over the temperature range of 70° to 250°F and up to 15,000 psi.

In order to eliminate the two pressure-viscosity data points required to evaluate the constants for the equation, Appeldoorn assumed that the relationship between constants c and b and between constants b and a are linear and obtained the following two-constant empirical correlation.

$$\log \frac{\eta}{\eta_o} = a \left(\log \frac{t}{t_o} - 0.0234\, p + 0.0302\, p \log \frac{t}{t_o}\right) \qquad [7]$$

The two constants, a and η_o, can be determined from two atmospheric viscosity data points at temperatures t_o and t. The two-constant equation is not as accurate as the four-constant equation.

Kouzel (26) assumed that $\left(\frac{1}{\eta}\frac{d\eta}{dp}\right)_{p=o}$ versus $\left(\frac{1}{\eta}\frac{d\eta}{dt}\right)_{p=o}$, $\log \left(\frac{1}{\eta}\frac{d\eta}{dt}\right)_{p=o}$ versus $\log \eta|p=o$, and $\log \eta$ versus p are all linear. The resulting equation is

$$\log \frac{\eta_p}{\eta_o} = \frac{p}{1000} (0.0239 + 0.01638\, \eta_o^{0.278} \qquad [8]$$

where:

η_p = viscosity at pressure p and temperature T, centipoise,

η_o = viscosity at atmospheric pressure and temperature T, and

p = pressure, psig.

The equation is correlated for the viscosity range of 0.5 to 200 centipoises and up to 5000 psig and 425°F.

Fresco, Klaus and Tewksbury (27) developed a graphical relationship involving the logarithm of viscosity, the pressure coefficient, and the viscosity-temperature properties (ASTM Slope) of the fluid. Second-degree polynomial equations were also developed to try to reproduce the graph. The pressure coefficient is defined as:

$$\log \frac{\mu_p}{\mu_o} = P\alpha^a (10^{-4}) \qquad [9]$$

where:

μ_p = kinematic viscosity in centistokes at pressure p,

μ_o = kinematic viscosity in centistokes at atmospheric pressure,

p = pressure, psig,

α = pressure coefficient, psig^{-1}, and

a = temperature correction, 560/°R

When the resultant general correlation was tested with data from mineral oils, pure hydrocarbons and nonhydrocarbons, the average deviation was ± 11 percent.

Roelands (28) made the assumption that sixty percent of the solvent viscosity-pressure index contributes toward the blend viscosity-pressure index.

$$Z_{Bl} = 0.6\ Z_{or} + 0.4\ Z_{Bl} \qquad [10]$$

where:

Z_{or}, Z_{Bl} = viscosity-pressure indexes of the base oil and blend respectively, and

Z_{Bl} = hypothetical viscosity-pressure index of the blend read from the chart.

The above equation requires the knowledge of a total of four atmospheric viscosities; two for the blend, and two for the base oil. For some base oils, density and refractive index at 104°C may also be required.

After calculating the viscosity-pressure index of the blend, the following equation is used to calculate the pressure-viscosity.

$$\log (\log \eta_p + 1.2000) = Z_{Bl} \log\ 1 + \frac{p}{28,400} + \log (\log \eta_o + 1.200) \qquad [11]$$

where:

η_p, η_o = dynamic viscosity at pressure p and atmospheric pressure respectively at the temperature of interest, centipoise, and

p = pressure, psig.

The pressure-viscosity studies discussed in Annual Report AFML-TR-70-304, Part II, separated the pressure coefficient of the polymer solution into two parts.

$$\log \frac{\mu_p}{\mu_o} = (\alpha + \beta)\ p\ (10^{-4}) \qquad [12]$$

where:

μ_p, μ_o = viscosity of polymer solution at pressure p, and at atmospheric pressure respectively, centistokes,

p = pressure, psig,

α = pressure coefficient of solvent, psig^{-1}, and

β = pressure coefficient of polymer, psig^{-1}.

This work correlated the pressure coefficients of polymer solutions graphically as a function of the relative viscosities. The relative viscosity is the ratio of the viscosity of the polymer solution to the viscosity of the solvent at atmospheric pressure. The graph can also be represented by second degree polynomial equations. The value of the solvent pressure coefficient can be predicted by one of the available methods.

2. Test Apparatus and Procedures. The design and operation of the PRL pressure viscometer have been described in detail in former Annual Reports and in a paper by Klaus, Johnson, and Fresco (29). The overall viscometer system is shown in Figure 1.

a. Pressure Supply and Measurement Equipment. The pressurized nitrogen gas bottle (A) is used to obtain pressures from 0 to 2000 psig. Additional pressures up to 10,000 psig are obtained with the hydraulic booster system (B,C,D). Two pressure gages (E, 5000 psig, and F, 10,000 psig) are connected in parallel to provide adequate sensitivity over the entire pressure range. The 5000 psig gage has a precision of ± 5 psig. Whereas, the 10,000 psig gage has a precision of ± 10 psig. Both gages are calibrated using a dead weight tester which has an accuracy of ± 1 psig. The calibration data are shown in Table 1.

b. Constant Temperature Apparatus. A Pyrex glass jar twelve inches in diameter and twenty inches deep is used as the constant-temperature water bath (I), shown in Figure 1, for determinations at 100° and 130°F. For 32°F determinations, an ice-water slurry is used.

For 100° and 130°F determinations the bath is controlled by a magnetic roto-set type low voltage thermoregulator in conjunction with a low voltage relay system which controls the power input to an electric immersion heater. Air is continuously bubbled through the water to insure even temperature distribution in the bath. The temperature of the bath can be controlled to within ± 0.05°F.

An air driven stirrer connected above the bath is used to stir the ice-water slurry. Screens are set up to prohibit the flow of ice past the sight glass of the Jerguson gage without prohibiting the flow of water. Bath temperature can be maintained to within 0.2°F from the desired 32°F temperature.

c. Pressure Vessel. The pressure viscometer (I in Figure 1) is a modified 21-T-50 Jerguson level gage. The gage has a pressure rating of 10,000 psig.

The capillary unit (Figure 2) used to measure the viscosity of fluids is attached to the top closure (K) by a Teflon compression cone (see Figure 3). The whole capillary unit is placed inside the pressure vessel (J).

The series of valves and passages on the viscometer are designed to permit the manipulation of the fluid from reservoir to the efflux bulb. By proper valve settings the fluid can then be allowed to flow from the efflux bulb under the head of test fluid represented by the difference in height between the liquid levels in the efflux bulb and the reservoir. The liquid levels in the capillary and the reservoir can be observed through the series of one-half inch diameter "bull's eye" windows on both sides of the gage as indicated in Figure 1.

d. Viscometer Capillaries. A detailed drawing of a viscometer capillary is shown in Figure 2. The upper etched line above the storage bulb (W) is designated as the fill line. The viscometer capillary is filled to this line for each viscosity determination to insure a constant drainage.

The bottom bulb (X) is denoted as the efflux bulb and the efflux time is the time required for the fluid to pass from the etched line on the top of bulb (X) to the one below the bulb (X).

The small bulb (W) is a storage bulb. Its purpose is to allow time for the manipulations required at the start of a test and also to insure steady-state conditions before the measured flow begins.

The bottom of the capillary is trumpet shaped to minimize the kinetic energy effects. A series of capillaries ranging in inside diameter from 0.9 to 5.0 millimeters are available to obtain efflux times for viscosities ranging from 0.4 to 10,000 centistokes.

e. Calibration of a Viscometer Capillary. The viscometers are calibrated at atmospheric pressure with fluids of known viscosity and are used subsequently as relative instruments to determine the viscosity of unknown liquids in the general fashion of modified Ostwald viscometers. The flow through the capillary viscometer can be adequately described by Poiseuille's law expressed in terms of efflux time.

$$t = \left[\frac{8LV}{\pi g r^4 h}\right] \left[\frac{\rho_1}{\rho_1 - \rho_g}\right]^{\mu}$$

$$= K \left[\frac{\rho_1}{\rho_1 - \rho_g}\right]^{\mu} \qquad [13]$$

$$K = \frac{8LV}{\pi g r^4 h} \qquad [14]$$

where:

t = efflux time, sec,

L = capillary length, cm,

V = volume of liquid, cm^3,

g = gravitational constant, 980.6 cm/sec,

r = capillary radius, cm,

h = height of liquid from reservoir level to the top of the efflux bulb, cm,

ρ_1 = density of liquid, gm/cm^3,

ρ_g = density of gas, gm/cm^3,

μ = kinematic viscosity, cm, and

K = function of viscometer geometry, cm^3/sec.

When the viscometer is calibrated at atmospheric pressure, the gas density, ρ_g, can be neglected since it is on the order of 0.1 percent of the liquid density, ρ_1. Then the Equation [14] becomes:

$$t = K \mu_a \qquad [15]$$

where:

t = efflux time, sec,

K = function of viscometer geometry, cm^2/sec, and

μ_a = apparent viscosity from atmospheric calibration, centistokes.

Therefore, at atmospheric pressure, the apparent viscosity is the atmospheric viscosity. In the case of pressure viscosities, however, the density of the gas, ρ_{gp} becomes a substantial factor. In order to use the atmospheric calibration in the pressure-viscosity determination, the following relationship is used.

$$\mu_p = \mu_a \frac{\rho_{1p} - \rho_{gp}}{\rho_{1p}} \qquad [16]$$

where:

μ_p = true viscosity at pressure, p, centistokes,

μ_a = apparent viscosity from atmospheric calibration, centistokes,

ρ_{1p} = density of liquid at pressure, p, gm/cm^3, and

ρ_{gp} = density of gas at pressure, p, gm/cm^3.

Values of the density-pressure-temperature relationship for nitrogen were obtained by Sage and Lacy (30). Wright (31) developed a series of charts to predict the density-pressure-temperature relationships for petroleum oils and pure hydrocarbons. The correlation covers a temperature range of 0° to 500°F and pressures up to 100,000 psig. An average error of less than one percent is obtained from this method The only required data are the density of the liquid at atmospheric pressure and the desired temperature. These data have also been curve fitted into equations which show an average error of about 1.7 percent. As the critical point is approached, the error may be as high as five percent (32). In viscosity-pressure studies of polymer solutions by this laboratory, these same relationships are used to predict the density-pressure-temperature properties for the polymer and high molecular weight petroleum resin solutions used (AFML-TR-70-304, Part II).

At constant temperature and pressure, calibration constant, K, is only a function of the height of the liquid from reservoir level to the top of the efflux bulb, h. Since the calibration constant, K, is a strong function of capillary radius, r, which is a weak function of temperature and pressure, calibration constant, K, is also a weak function of temperature and pressure.

From Equation [14]

$$K = \frac{8LV}{\pi g r^4 h}$$

$$\frac{dK}{dr} = -4 \left[\frac{8LV}{\pi g r^5 h}\right] \qquad [17]$$

$$\Delta K = \left[\frac{dK}{dr}\right] \Delta r$$

$$= -4 \left[\frac{8LV}{\pi g r^5 h}\right] \Delta r$$

$$= -4\ K_c \left[\frac{\Delta r}{r}\right] \qquad [18]$$

$$K - K_2 = -4\ K_c \left[\frac{\Delta r}{r}\right]$$

$$K = K_c \left(1 - 4 \left[\frac{\Delta r}{r}\right]\right) \qquad [19]$$

When $\Delta r/r$ is expressed as the glass expansion coefficient and is assumed to be constant,

$$K = K_c\left(1 - 7.47 \times 10^{-6}\ (T_c - T)\right) \qquad [20]$$

When $\Delta r/r$ is expressed as the glass compressibility and is assumed to be constant,

$$K = K_c[1 - 8.33 \times 10^{-7}\ (p - p_c)] \qquad [21]$$

where:

K = real function of viscometer geometry, cm^2/sec,
K_c = function of viscometer from calibration, cm^2/sec,
L = capillary length, cm,
V = volume of liquid, cm^3,
g = gravitation constant, 980.6 cm/sec^2,
r = capillary radius,
h = height of liquid from reservoir level to the top of the efflux bulb, cm,
T_c = calibration temperature, °F,
T = real temperature, °F,
p_c = calibration pressure, psig, and
p = real pressure, psig.

It is obvious from Equations [20] and [21] that the calibration constant, K, can be considered constant for a wide range of temperature and pressure. Figure 4 shows a typical calibration curve with data at 100° and 130°F. The calibration curve has a curvature rather than being straight, because the radius of the reservoir varies with liquid height.

f. Viscosity Measurement. The details of the viscosity measurement procedures have been described in previous Annual Reports. In brief, for each fluid, the pressure gage is disassembled, cleaned and reassembled. The test fluid is degassed before being put into the pressure gage. The pressure gage is kept in the constant-temperature bath for two hours to ensure thermal equilibrium. Then, the system is pressurized slowly. The test fluid is raised from the reservoir to the top etched line of the viscometer capillary slowly by proper manipulation of the valve settings.

The system is allowed to stand for another hour to ensure thermal equilibrium. Then, the fluid is allowed to run down the capillary under its own head. The efflux time is measured with a stop watch to ± 0.1 second. The height of liquid from reservoir level to the top of the efflux bulb is measured by cathetometer to ± 0.005 cm. The reproducibility of the pressure-viscosity measurements is shown in Table 2 in terms of the pressure coefficient which is defined as:

$$\alpha = \frac{1}{p} \ln \frac{\mu_p}{\mu_o} \qquad [22]$$

where:

α = pressure coefficient, $psig^{-1}$,

p = pressure, psig,

μ_p = viscosity at pressure p, cs., and

μ_o = atmospheric viscosity, cs.

g. Effect of Variables on Pressure Viscosity Determinations. Many of the variables affecting pressure viscosity determinations, such as misalignment, drainage, kinetic energy, surface tension, and heat of compression of the gas, have been studied and have been presented in detail in previous reports and by Klaus, et al. (29). By means of proper equipment design and calibration procedures, each of these items has been shown to have negligible effect under normal variation on the pressure-viscosity determination.

The effect of temperature and pressure on the calibration constant, K, can be corrected by using Equations [20] and [21]. The effect of dissolved gas in the fluid film on the wall of the viscometer capillary is eliminated by using a dry viscometer capillary for every run.

Since one hour in the constant temperature bath is required to eliminate the effect of heat of compression, a minimum gas-liquid contact time of one hour at the pressure of interest is required. Data on Figure 5 show the effect of gas-liquid contact time on the pressure coefficients.

For a close approximation, the effect of nitrogen gas saturation on the pressure-viscosity of fluids is to reduce the pressure viscosity to its atmospheric level. On this basis the average percent saturation of di-2-ethylhexyl sebacate after one hour at both 3000 and 5000 psig is about 0.94. This corresponds to 0.29 and 0.59 percent deviation in the pressure viscosity at 3000 and 6000 psig, respectively. For the polyolefin oil MLO 7754 after one hour gas-oil contact time at 3000 and 6000 psig, the percent saturations are on the order of 0.35 and 3.52, respectively. This corresponds to 0.15 and 2.95 percent deviation in the pressure viscosity at 3000 and 6000 psig, respectively.

The study showed that the gas solubility is the major contribution to experimental error for pressures as low as 3000 psig. The quantity of gas dissolved in the fluid increases with test time and the solubility increases with system pressure. Therefore, PRL Viscometer should be operated under low pressure and with minimum contact time to minimize the gas solubility problem. The limiting slope of the viscosity-pressure curve at 0 psig can then be used to predict the viscosities at higher pressures.

Shear stress has no effect on the viscosity level of a Newtonian fluid. For most non-Newtonian fluids the shear effect is avoided by operating the system at a shear stress below 100 dynes per square centimeter. It has been shown that for shear stresses of up to approximately 3 x 10^3 dynes per square centimeter, non-Newtonian properties of the types of polymer solutions used in the pressure viscosity study are not observed (33, 10).

3. Development of Variables. Based on the concept that the mobility of the molecules in a liquid is governed by their free volume, different models have been derived to describe the molecular transport phenomena such as viscous flow and diffusion. The basic concept underlying free-volume theories implies that each molecule in a liquid is confined to a "cage" bounded by its immediate neighbors.

Eyring and co-workers (34) interpreted the "cage" as an energy barrier. Viscous flow is defined in this system as the result of the movement of an activated molecule from one equilibrium position to another in the preferred direction of shear. This movement is treated as a jump over the energy barrier and is called activation energy for viscous flow. As the result of an elaborate theoretical treatment of this model, a rate equation of the following form is proposed.

$$\eta = \frac{E_{vis}}{RT} + D \qquad [23]$$

where:

E_{vis} = activation energy for viscous flow,

η = absolute viscosity,

R = molar gas constant,

T = temperature, and

D = a constant.

Both E_{vis} and D are characteristic of a given liquid. E_{vis} is also a function of pressure.

Cohen and Turnbull (1,35) introduced the concept that the statistical redistribution of the free volume occasionally opens up a void within the "cage" sufficiently large to permit considerable displacement of the molecule contained by it. For the molecular displacement to be diffusive, the void created should exceed a characteristic minimum volume which approaches the molecular volume, and should be just large enough to enable another molecule to jump in after this displacement.

By treating the free volume of the individual molecules of a liquid as a random variable, and by describing the distribution of the free volume among the numerous molecules by a simple exponential distribution function, Cohen and Turnbull obtained the following relationship.

$$\ln \eta = -\gamma \frac{v}{v_f} + \ln \eta_e \qquad [24]$$

where:

η = absolute viscosity,

η_e = a constant,

γ = overlap factor between 1/2 and 1,

v^* = minimum required specific free volume,

v_f = specific free volume, and

v^*/v_f = is a function of temperature and pressure.

Following this concept Roeland (28) used the Weibull distribution function instead of the simple exponential distribution function to approximate the distribution of free volume and developed a new correlation:

$$\ln \eta = \left| \frac{V_f^*}{V_f} \, r \left(1 + \frac{1}{n}\right) \right|^n + \ln \eta_e \qquad [25]$$

where:

η = absolute viscosity,

η_e = fictitious viscosity for $V_f = \infty$,

V_f = specific free volume,

V_f^* = minimum required specific free volume,

n = shape parameter which is essentially independent of temperature, and which predominately determines the overall form of the statistical distribution of the free volume of liquid concerned as a function of V_f^*/V_f, and

V_f^*/V_f = is a function of temperature and pressure.

a. Atmospheric Viscosity. From the concept that the mobility of the molecule in a liquid is governed by its free volume, kinematic viscosity can be considered as a function of three variables: (1) free volume which is defined as the volume per cage available for free redistribution, (2) flow unit which is considered to be the volume completely occupied by an individual molecule or an effective segment of a molecule, and (3) average formula weight per atom which is molecular weight divided by the total number of atoms in the molecule. Then, at atmospheric pressure and at the temperature of interest,

$$\mu_{o\,T} = f\,[W_A, (R, V_f)_{T,P_o}] \qquad [26]$$

where:

μ_o = atmospheric kinematic viscosity,
W_A = average formula weight per atom,
R = flow unit,
V_f = free volume,
P_o = atmospheric pressure, and
T = temperature of interest.

b. Atmospheric Density. The differences in density among isomers at constant temperature and pressure are due to the differences in packing. It is logical to assume that tighter packing corresponds to smaller free volume. For liquids with the same average formula weight per atom, the differences in density at constant temperature and pressure are due to the differences in packing. Density can be used to measure the difference of free volume on a relative basis. High density corresponds to small free volume. Low density corresponds to a large free volume. At atmospheric pressure and the temperature of interest:

$$\rho_{o\,T} = f\,[W_a, (V_f)_T] \qquad [27]$$

where:

ρ_o = atmospheric density,
W_A = average formula weight per atom,
V_f = free volume, and
T = temperature of interest.

c. ASTM Slope. In assessing the effect of temperature on the ratio V_f*/V_f in Equation [25], Roeland (19) assumed the following expression:

$$\frac{V_f*}{V_f} = \frac{k}{(T-T)^r} \qquad [28]$$

where:

V_f* = minimum required specific free volume,
V_f = specific free volume, and
T = absolute temperature.

The exponent r approximates unity and the parameter T_o denotes the absolute temperature where the specific free volume, V_f, of the liquid would become zero. Further, the constant k represents the value of the ratio V_f*/V_f that would be reached when the absolute temperature T is decreased to 1 °K above the limiting temperature T_o.

When Equation [28] is substituted in Equation [25], the rearranged Equation [29] results:

$$\ln \ln [\frac{\eta}{\eta_e}] = - rn \ln (T-T_o) + \ln [kr (1 + \frac{1}{n})]^{\eta} \qquad [29]$$

Assume $T_o = 0$

$$\frac{\eta}{\eta_e} = \eta + c$$

Then:

$$\ln \ln (\eta + c) = - rn \ln (T) + \ln [kr (1 + \frac{1}{n})]^{\eta} \qquad [30]$$

where:

η = absolute viscosity,

η_e = absolute viscosity for v_t equal infinite

r = constant approximately equal to unity,

n = shape parameter,

T = absolute temperature,

k = V_f*/V_f when T equal 1 °K,

c = a constant,

V_f = specific free volume, and

V_f* = minimum required specific free volume.

MacCoull - Walther (36) developed an emperical viscosity-temperature equation which has the following form:

$$\log \log (\mu_o + c) = - m_o \cdot \log T + N_o \qquad [31]$$

where:

μ_o = kinematic viscosity, cs,

T = absolute temperature, °R,

m_o, N_o = empirical constants, and

c = 0.6 for $\mu_o > 1.5$ cs.

0.65 for $1.0 < \mu_o < 1.5$ cs.

0.70 for $0.7 < \mu_o < 1.0$ cs.

0.75 for $0.4 < \mu_o < 0.7$ cs.

On the basis of the McCoull - Walther equation, standardized ASTM kinematic viscosity-temperature charts (37) in which the ordinate is a log log scale of viscosity (cs.) and the abscissa is a log temperature (°F) scale, were developed. ASTM slope of a liquid may be defined as the negative "measured" slope, or the measured linear distance on the ordinate of the ASTM charts C and D (D 341-39) between the viscosity values at 100° and 210°F and divided by the measured linear distance between 210° and 100°F on the abscissa. Any other two temperatures may be used with the designation of ASTM slope between two specified temperatures as shown in Figure 6. Therefore, the ASTM slope is directly proportional to the slope m_o in Equation [31]. For kinematic viscosities above 1.5 cs., slope m_o is equal to 4.5 times the ASTM slope. Proportionality constants for kinematic viscosities below 1.5 cs. are listed in Table 3. ASTM slope is also tabulated in table form (38).

A comparison of Equations [30] and [31] shows that since c can be assumed to be a constant for kinematic viscosities above 1.5 cs., M_o is directly proportional to rn. Since r is close to unity, M_o is approximately directly proportional to n. This means that ASTM slope is also approximately directly proportional to the shape parameter n in Weibull's function for describing the statistical distribution of free volume amongst the numerous molecules of a given liquid. Conversely, the ASTM slope may now be interpreted as the quantity which predominantly determinates the overall form of the statistical distribution of the free volume of the liquid concerned as a function of temperature. This in turn means that ASTM slope can be considered as a measurement of the flexibility of the molecule. A rigid molecule will have a large ASTM slope, while a flexible molecule will have a low ASTM slope.

d. Relating the Pressure Coefficient to Atmospheric Viscosity, Atmospheric Density and ASTM Slope. As long ago as 1893 Barus (39) established an empirical equation to describe the isothermal viscosity-pressure relationship for a given liquid.

$$\ln \frac{\eta}{\eta_o} = \alpha P$$

where:

η = viscosity at pressure p,

η_o = atmospheric viscosity at the temperature of interest, and

α = pressure coefficient which for a given liquid is a function of temperature only.

An equation of the same form was later obtained as a theoretical approximation by the Eyring theory of viscous flow. The isothermal viscosity-pressure relationship for a given liquid can be expressed as:

$$\ln \frac{\eta}{\eta_o} = \frac{V_{vis}}{RT} P \qquad [33]$$

where:

η = viscosity at pressure p,

η_o = atmospheric viscosity at temperature of interest T,

V_{vis} = characteristic constant for a given liquid, and

R = the molar gas constant.

According to the Eyring Model of Viscous Flow, the indicated jump of activated molecules over a potential energy barrier is only possible if a suitable "hole" has been created in the neighborhood. The size of such holes (per mole) is represented by the quantity V_{vis}.

V_{vis} should increase with flow unit size because a larger "hole" is required for a larger flow unit. A more rigid molecule would require a larger "hole" than a flexible one. By introducing the concept of molecular interlocking, the increase of V_{vis} with respect to ASTM slope can be further explained. An increase in ASTM slope corresponds to an increase in molecular rigidity. Molecular interlocking is more effective for more rigid molecules, which in turn increases the flow unit and the V_{vis}. The effect of free volume on molecular interlocking is more abstract. When the free volume is large, the amount of molecular interlocking introduced by applying external pressure is larger than when the free volume is small. In other words, when the free volume is small, the molecules are already tightly packed. Molecular interlocking already exists. Applying pressure just forces the already interlocked molecules to interlock tighter. Thus the effect on the flow unit and V_{vis} is much smaller than when the free volume is large and external pressure introduces interlocking of free molecules.

The same type of logic can also apply to the statistical distribution of the free volume concept introduced by Cohen and Turnbull (1, 35). From Equation [32] the pressure coefficient can be interpreted as the rate of log viscosity change with respect to pressure or simply the pressure effect on the opportunity to locate a proper size free volume. The pressure effect on the free volume decreases the opportunity for a large flow unit to find the right size free volume over that of a small flow unit. The reduction of free volume by external pressure is also more significant in decreasing the opportunity for a rigid molecule to locate a right size free volume than for a more flexible molecule. Again, interlocking is more effective for rigid molecules, which in turn increases the size of the flow unit and makes it more susceptible to pressure effects. Moreover, the amount of molecular interlocking introduced by external pressure is larger for large free volume than for smaller free volume fluids. As a result, the pressure effect on the opportunity to find a right size free volume is larger for a fluid which has large free volume than for a fluid which has small free volume.

From the above discussion, it is clear that the pressure coefficient, α, is a function of atmospheric viscosity, atmospheric density and ASTM slope.

4. Correlation Methods and Results. In order to study the pressure effect on the viscosities of Pennsylvania paraffinic mineral oils, mineral oil blends, and a resin blend, pressure-viscosities of a series of paraffinic mineral oils ranging from gas oils to bright stock, two mineral oil blends and a Pa. resin blend were evaluated at pressures up to 3000 psig at 100°F. For some of the fluids the pressure-viscosities were also measured at 32° and 130°F. As shown in Figures 7 through 13, plots of the log of kinematic viscosity versus pressure are straight lines for pressures up to 3000 psig. This is in agreement with the results obtained in previous studies (AFML-TR-67-107, Part I; AFML-TR-70-304, Part II). These data also showed that almost all fluids when plotted in terms of log kinematic viscosity versus pressure result in straight lines for pressures up to 10,000 psig. Thus, the pressure coefficient α, is independent of pressure when it is expressed as follows:

$$\log \frac{\mu}{\mu_o} = \alpha \, p \log (e) \text{ or } \ln \frac{\mu}{\mu_o} = \alpha \, p \qquad [34]$$

where:

μ = kinematic viscosity at pressure p, centistokes,

μ_o = atmospheric kinematic viscosity at the temperature of interest, centistokes,

α = pressure coefficient, 1/psig,

p = pressure, psig,

e = 2.718,

log = base 10 logarithm, and

ln = nature logarithm

Data for the mineral oils, mineral oil blends and Pa. resin blend at 100°F produced by this investigation were used as part of the data to establish the new correlations.

Data from previous studies at this laboratory and from an API Project 42 were also used to develop a correlation at 100°F. The data for this correlation was further restricted to an average formula weight in the neighborhood of 4.5, and a viscosity level above one centistoke. This eliminated some of the non-hydrocarbon data from AFML-TR-67-107, Part I, and a few fluids from the API Project 42 (8). All of the polymer blends and resin blends discussed in AFML-TR-70-304, Part II were included to develop these correlations. Data from the ASME Report (7) and Roelands (23) were not included because of the low level of precision in the low pressure region. Brief descriptions and physical properties of fluids used to develop the correlations are listed in Tables 4 through 9. These data cover a density range of from 0.75 to 0.96 gm/cc, and a range of ASTM slope of from 0.28 to 0.93, and a viscosity range of from 1.4 to 1984 centistokes.

a. Multiple Linear Regression Analysis. In section three, development of variables, it was shown that the pressure coefficient is probably a function of atmospheric density, atmospheric viscosity, and ASTM slope. However, the functional form of the relationship was not known. It was decided that multiple linear regression analysis would be used as a first step to search for the functional form. Multiple regression analysis is defined as linear when in searching for the best fit, only the constant and the coefficient of the variable are being changed. The best fit is obtained by the least squares method.

Among the many available multiple linear regression methods, the step-up multiple linear regression of the statistical package program from the Computation Center of The Pennsylvania State University was used. This method allows the user to examine the significance of each individual variable used in the correlation.

In step-up multiple linear regression, intermediate results are used to give statistical information at each step in the calculation. These intermediate answers are also used to control the method of calculation. A number of intermediate regression equations are obtained as well as the final multiple regression equation. These equations are obtained by adding or deleting one variable at a time as follows:

$$y = b(o) + b(1)\ x\ (1) \qquad [35]$$

$$y = b'(o) + b'(1)\ x\ (1) + b'(2)\ x\ (2) \qquad [36]$$

$$y = b''(o) + b'(1)\ x\ (1) + b''(2)\ x\ (2) + b''(3)\ x\ (3) \qquad [37]$$

The variable added is the one which makes the greatest improvement in "goodness of fit." The coefficients represent the best values when the equation is fitted using the specific variables included in the equation. An important feature of this procedure is that a variable may be indicated to be significant in an early stage and enters the equation, but after several variables are added to the equation, the initial variable may be indicated to be insignificant. The insignificant variable is then removed from the regression equation before another variable is added. Therefore, only significant variables are included in the final multiple regression Equation [44].

The three variables, atmospheric viscosity, atmospheric density and ASTM slope, were evaluated as independent variables and associated variables. A set of pseudo linear variables to a maximum of fourth order was created. The maximum of fourth order was used because it is desirable to give the regression the maximum freedom but also to minimize the possibility of obtaining a correlation with abrupt fluctuations which are very unlikely in the actual physical situation. The variable, atmospheric viscosity was expressed in terms of log atmospheric viscosity to reduce the range of its variation. The pseudo linear variables are shown in Table 10.

In curve fitting, as the number of variables increases, the average deviation (see Table 11) always decreases until it becomes zero. There is no unique statistical procedure to determine the best regression equation. One of the most common indicators is standard error of estimate (see Table 11). This indicator should always decrease with the addition of more variables. If the standard error of estimate increases with the additional variable, this indicates that the addition of the variable isn't statistically sound. However, the overriding factor is always whether the model described by the regression equation is physically reasonable. Moreover, in order for the regression equation to be useful, it has to be convenient and economical to use. Figure 14 shows the standard error of estimate versus number of variables from the multiple linear regression analysis. The regression equations with one to four variables are shown in Table 12. After a detailed examination of plots of the regression equations obtained, it was found that none of the regression equations was satisfactory. When the number of variables was kept low, the average of deviation (see Table 11) was deemed to be too large. When the number of variables was increased, the model obtained was considered to be physically unreasonable. It was then decided to use multiple nonlinear regression analysis.

b. Multiple Nonlinear Regression Analysis. When the regression analysis involves multiple variables with nonlinear parameters, it is called multiple nonlinear regression analysis. The type of nonlinear model being considered here is the polynominal type with variable powers. One of the advantages of multiple nonlinear regression analysis is that it provides maximum orderly flexibility with a minimum number of variables. However, multiple nonlinear regression analysis requires definite functional form and good initial values for the parameters. If the initial values for the parameters are too far off, the system will probably diverge.

Equations [39], [40], and [41] from the multiple linear regression analysis were picked as the functional form. The multiple nonlinear regressional analysis program, NLIN-2, from the Computation Center of The Pennsylvania State University, University Park, Pennsylvania, was used. The program is based on least squares estimation. Using parameter values from the multiple linear regression analysis as initial values, all three of the equations successfully converged. The regression equations are shown in Table 13 as Equations [42], [43], and [44] respectively. Results show that the ASTM slope term in the third variable of Equation [43] is insignificant. Therefore, a new function was created by omitting the ASTM slope term. The new regression equation is shown in Table 13 as Equation [45]. After examining Equations [42], [44], and [45] in detail both from the physical soundness and the statistical (standard error of estimate) point of view, Equation [45] is the best among all the regression equations tested.

Since only ASTM slope and atmospheric viscosity were used as independent variables in Equation [42], it was assumed that the differences in free volumes were being accounted for by the use of kinematic viscosity. Equation [42] can be used as a close approximation when atmospheric viscosity data are not available. As it will be shown, Equation [42] is the better equation when the average formula weights per atom of the fluids deviate significantly from the 4.5 average. In order to be sure that an additional term in Equation [42] would not improve the equation significantly, a new group of pseudo linear variables made up of the independent variables, *ASTM slope and atmospheric viscosity*, to the maximum of fourth order were constructed. The multiple linear regression analysis was again used to pick the third variable. The new functional form was used in the multiple nonlinear regression analysis to obtain Equation [46]. As shown in Table 13, Equation [46] has a larger standard error of estimate. In terms of physical reasonableness, Equation [46] is also inferior to Equation [42].

c. Discussion and Comparison of Equations [45] and [42]. Data calculated by the relationship expressed in Equation [45] are plotted on a semi-log scale of pressure coefficient versus log of the atmospheric viscosity with lines of constant ASTM slope. The fluids of constant density levels of 0.75, 0.85, 0.95 and 1.00 gm/cc are shown on Figures 15, 16, 17 and 18, respectively. The figures show that all constant ASTM slope lines converge to a single point at an atmospheric viscosity level of one centistoke. This is due to the constraint of Equation [45]. The significant message from Figures 15 through 18 is that the dependency of the pressure coefficient on ASTM slope decreases with decreasing atmospheric viscosity level. This result is shown more clearly in Figure 19. This trend can be explained in terms of molecular interlocking. For constant free volume, low viscosity level represents a comparatively small flow unit which has relatively little branching and coiling. The rigidity of the molecule, ASTM slope, has little effect on the amount of molecular interlocking introduced by the external pressure. Therefore, the effect of ASTM slope on the pressure coefficient is small. For low ASTM slopes, the molecules are relatively flexible, and the molecular interlocking introduced by the external pressure is not very effective. These effects explain the lower effects of fluids with low ASTM slope and/or low atmospheric viscosity on the pressure coefficient.

The increase of pressure coefficient with respect to atmospheric viscosity was explained in detail in Section 3 on the development of variables. Data from Figures 15 through 18 show a leveling off of the pressure coefficient at high atmospheric viscosity. This can be explained by segmental flow. Long chain molecules have a high degree of freedom. The flow unit is no longer a function of molecular chain length. The flow unit is only a segment of the long-chain molecule. The concept of segmental flow has been suggested by many authors (41). For some density levels the use of Equation [45] actually predicts a decrease in pressure coefficient with increasing atmospheric viscosity. This is considered to be physically unreasonable. As a result, horizontal dotted lines were drawn in the regions where Equation [45] predicts a decrease in pressure coefficient. This analysis is in compliance with the segmental flow concept. This functional form was chosen by the statistical analysis based on the data available where pressure coefficient appears to decrease with viscosity. This apparent decrease, upon analysis, appears to represent no change in viscosity-pressure coefficient with viscosity level within the limits of error of the measurement of the properties measured. Some of the errors in measurement come from the data obtained from different investigators.

Considering the nature of the data obtained from Equation [45], Figure 20 was constructed to show the operational regions of the equation. This region covered all of the data used for the correlation. The maximum deviation of 0.111×10^{-4} psig from the horizontal line is well within the experimental limits of different investigators. There are four data points inside this region. The differences between the predicted values from Equation [45] and from Figures 15 through 18 are shown in Table 14. The results show that the differences are insignificant.

The effect of atmospheric density at constant atmospheric viscosity and ASTM slope on the pressure coefficient based on Equation [45] is shown in Figure 21. The decrease in the pressure coefficient with increasing atmospheric density has been explained in detail in Section 3. This effect is due to the different effects on the size of the flow unit introduced by the newly formed interlocking molecules and the tightening of the already interlocked molecules. These molecular configurations in turn affect the pressure coefficient. The data on Figure 21 show that the effect of atmospheric density is much greater for high viscosities than for low viscosities. At high viscosity levels there is more branching and coiling on the molecules. The free volume has a strong effect on the molecular interlocking introduced by the application of external pressure.

Data derived from the relationship in Equation [42] are plotted on Figure 22 as pressure coefficient versus the log of the atmospheric viscosity with lines of constant ASTM slope. The general trend of these data is the same as those in Figures 15 through 18. The biggest difference between the two equations is that no segmental flow is indicated from the data on Figure 22. The density term in the kinematic viscosity has less effect than the differences in free volume. By not accounting for the differences of free volumes between fluids at high viscosity, the segmental flow effect is obscured.

In order to understand the significance of the deviations between the experimental values and the predicted values, the discrepency of the experimental data among different investigators must be considered. The experimental values of the pressure coefficients for the same fluids as obtained by different investigators are compared on Table 15. In order to show the effect of the variation of atmospheric viscosity and density, and ASTM slope on the prediction of the pressure coefficient, the deviations of the predicted values among different investigators based on Equation [45] are also shown in Table 15. From the data on Table 15, the maximum deviation among reported experimental values on pressure coefficient is 0.154×10^{-4} psig^{-1} and the maximum deviation among the predicted values based on Equation [45] is 0.098×10^{-4} psig^{-1}. Therefore, the combined maximum deviation can be as large as 0.252×10^{-4} psig.

The data on Figure 21 show that atmospheric density has little effect on the pressure coefficient at low viscosity. As the viscosity increases, the effect of atmospheric density on the pressure coefficient increases substantially. This indicates that the differences between Equation [45] and [42] should be small at low viscosities. The differences should increase with increasing atmospheric viscosity. The comparisons of Equations [45] and [42] in predicting pressure coefficients used to develop the equation at atmospheric viscosity range of 1 to 10 cs., 10 to 100 cs. and 100 to 2000 cs. are listed in Tables 16, 17, and 18. A summary of the comparisons is shown in Table 19. The summary indicates that the differences between Equations [45] and [42] are mainly in the atmospheric viscosity range of 100 to 2000 centistokes.

d. Temperature Effects. Combining Erying's theory on viscous flow (Equation [33]) and Equation [34]

$$\begin{aligned}\left(\ln\left(\frac{\eta}{\eta_o}\right)\right)\left(\frac{RT}{V_{vis}}\right) &= \left(\ln\left(\frac{\mu}{\mu_o}\right)\right)\frac{1}{\alpha} \\ &= \left(\ln\left(\frac{\eta}{\eta_o}\right) + \ln\left(\frac{\rho_o}{\rho}\right)\right)\frac{1}{\alpha}\end{aligned} \qquad [47]$$

where

η = absolute viscosity at p, cp,

η_o = atmospheric viscosity at temperature of interest, cp,

R = molar gas constant,

T = temperature of interest,

V_{vis} = characteristic constant for a given liquid, cm^3,

μ = kinematic viscosity at p, cs,

μ_o = atmospheric kinematic viscosity at temperature of interest, cs,

ρ = density at p, gm/cc,

ρ_o = atmospheric density at temperature of interest, gm/cc,

α = pressure coefficient, psig^{-1}, and

ln = natural logarithm.

Since $\ln(\rho_o/\rho)$ is on the order of 2.5 percent of $\ln(\mu/\mu_o)$, it can be assumed that

$$\frac{RT}{V_{vis}} = \frac{1}{\alpha} \qquad [48]$$

Since V_{vis} can be considered independent of temperature,

$$\alpha_T = \alpha_{100°F} \left(\frac{560}{T + 460}\right) \qquad [49]$$

where:

α_T = pressure coefficient at temperature T, $psig^{-1}$,
$\alpha_{100°F}$ = pressure coefficient at 100°F, $psig^{-1}$, and
T = temperature of interest, °F.

The pressure coefficient of a fluid at 100°F is controlled by atmospheric viscosity and density at 100°F along with the ASTM slope which can be considered to be independent of temperature. The pressure coefficient of a fluid at the temperature of interest should then be controlled by the atmospheric viscosity and density at the temperature of interest along with the ASTM slope. A comparison of equations [49], [45] and [42] at several temperatures is shown in Tables 20 through 23. A summary of the comparisons is shown in Table 24. Differences in the average absolute deviation is defined as the average absolute deviation at a given temperature minus the average absolute deviation at 100°F. The results show that Equation [47], which was developed from Erying's theory on viscous flow, can only be used as a rough estimation of the effects of temperature on the pressure coefficients. Equation [42] with ASTM slope, and atmospheric viscosity at the temperature of interest is a second choice if the information for atmospheric density at the temperature of interest is not available. In general, the average absolute deviations of the fluids at all the temperatures of interest other than 100°F are about the same as the average absolute deviations of the fluids at 100°F. The exception is in the fluids at 32°F. This is at least partially due to the fact that at such a low temperature, the ASTM slopes of some polymeric fluids and dense or congested center molecules do tend to change from their 100°-210°F ASTM slope values (42, 43).

5. Comparison of Equations [45] and [42] with other Methods of Prediction. According to the analysis of the Technical Data Book - Petroleum Refining (44) and previous studies at this laboratory, the correlations provided by Kouzel (26), Roelands et al. (23), and the data reported in previous Annual Reports are the best available to predict the effect of pressure on viscosity. The detailed discussions of the above correlations are in Section 1 of this study. A summary of the various correlations used for the comparison is shown in Table 25. Lists of physical properties required for each correlation are shown on Table 27. Pressure viscosity values at 5000 psig were used to calculate the pressure coefficient for the correlations requiring pressure. Since some of the correlations were based on absolute viscosity, the ratio of density at 5000 psig, ρ, and atmospheric density, ρ_0, was required. In general ρ/ρ_0 only varies from 0.9815 to 0.9840. The exact value can be estimated from available data and correlations (31).

Pressure coefficient data from four different sources were used for comparison. The comparison of various methods for predicting the pressure coefficient at 100°F using the data from the current investigation and that taken from Annual Report AFML-TR-67-107, Part I, shown in Table 28. The fluid types include mineral oils, mineral oil blends, resin blends and nonhydrocarbons. Brief descriptions of the fluids are shown on Tables 4 and 5. Polymer and resin blends at 100°F are compared in Table 29. The comparisons of the PRL pressure coefficient data at 32° and 130°F are shown on Table 30. The above comparisons are summarized in Table 31 in terms of average absolute deviation, bias and RMS. The definitions of these terms are given in Table 11. Data on Table 31 show that the predicted pressure coefficient from Fresco's correlation in general tends to be lower than the experimental values. Roelands' correlation for polymer blends showed a tendency to predict a higher pressure coefficient. The large average absolute deviation in Roeland's prediction for data from Fresco at 100°F is largely due to its inability to predict the pressure coefficient of hydrogenated polybutene. Kouzel's correlation predicts pressure coefficients consistently below the experimental values.

The comparison of various methods of predicting the pressure coefficient of hydrocarbons from the API Project 42 (8) is shown on Tables 32 and 33. The data is summarized in Table 34. The pressure coefficient data for pure hydrocarbons, mineral oils, and polymer blends from the ASME Report (7), and data on mineral oils from Roelands et al. (23) were used for comparisons in Tables 36 and 37, respectively. The summaries of the comparisons are shown in Tables 38 and 39. In comparing the bias between the different data sources, it is interesting to note that the data from Roelands et al. gives larger positive bias which indicates that the experimental data from Roelands et al. tends to have higher experimental pressure coefficients.

In order to understand the effectiveness of the various methods in predicting the pressure coefficients of different fluid types, the data were separated into a mineral oil group, a pure hydrocarbon group, a resin blend and polymer blends and a nonhydrocarbon group. The resin and polymer blends were considered as one group since the data reported in AFML-TR-70-304, Part II, showed that resin and polymer blends can be correlated on the same basis. The summary of the comparison is shown in Table 40.

In the course of examining the difference in the average absolute deviations based on different methods, it should be noted that the correlations do not cover the same range of fluids. The method of Fresco does not include polymer blends and resin blends. On the other hand, the data from AFML-TR-70-304; Part II are useful only for polymer and resin blends. Roelands, et al. proposed separate methods for polymeric fluids and for nonpolymeric fluids. However, their method does not include nonhydrocarbons. The method of Kouzel includes all fluids, but as shown in Table 40, its predictive effectiveness is the poorest of the five correlations evaluated. This is particularly true with polymer blends, resin blends and nonhydrocarbons.

Equations [45] and [42] from the current investigation are the only correlations that cover all four groups of fluids. For mineral oils, Equation [45] is as good as Roeland's method and Equation [42] has an edge over both. The other methods are less effective. It is important to point out that the method of Roelands requires four physical property values and four additional correlations. Equation [45] requires only three physical property values and one additional correlation as shown on Table 27. Only two physical property values and one additional correlation are required for Equation [42]. For pure hydrocarbons, Equation [45] has the lowest average absolute deviation. Equation [42] is a close second in predictive accuracy. The average absolute deviations of the other methods are at least 1.9 times higher than the average absolute deviation obtained with Equation [45].

For polymer and resin blends, the method reported in AFML-TR-304, Part II, has a slightly lower average absolute deviation than does Equation [45]. That method was used to predict only 17 out of 34 available polymer and resin blends. Moreover, that method requires viscosity information for both base oil and finished blends. Roeland's method ranked below those of AFML-TR-70-304, Part II, Equation [45], and Equation [42] in predictability. The method of Roelands was limited by the assumption that the viscosity-pressure index of the blend consists of a fixed 60 percent of solvent viscosity-pressure index and 40 percent of a hypothetical polymer viscosity-pressure index as shown on Table 25. The method of Roelands also requires viscosity information for both the solvent and the blend. Kouzel's correlation is very poor for polymer and resin blends. For nonhydrocarbons, Equation [45] again has the lowest average absolute deviation. Equation [42] and the method of Fresco can be considered about equal but less effective than Equation [45]. However, the number of nonhydrocarbons studied is too small to be significant relative to the differences in the effectiveness between Equation [45] and [42], and the method of Fresco.

For correlations which can be used for a wide variety of fluids, Equation [45] has the lowest average absolute deviation. Equation [42] represents a close second choice. Equation [45] is the best general relationship. If atmospheric density data are not available, Equation [42] is the one to use. For the mineral oils studied, Table 40 shows that Equation [42] is slightly better than Equation [45]. However, the weakness of Equation [42] shows up for polymer and resin blends.

Although in general, Equations [45] and [42] are better than any other methods in predicting the pressure coefficients of fluids, they also have limitations. First of all, the equations were developed for fluids which have an average formula weight per atom in the neighborhood of 4.5. The equations tend to predict too low a pressure coefficient for fluids with much higher average formula weights per atom. This is because the higher density values of these fluids are due partly to the higher average formula weight per atom and not due entirely to tighter molecular packing. Both highly aromatic fluids and fluids with heavy elements are in this category.

Secondly, the ASTM slope was assumed to be independent of temperature. However, Klaus, Hersh, Pohorilla and Fenske (42, 43) showed that the ASTM slope decreases at low temperature for dense center molecules in the synthetic fluids. They also pointed out that for waxy mineral oils, polymeric fluids, and polymer-thickened blends the ASTM slope increases at low temperature. Silicones and organic esters generally show a decrease in ASTM slope at high temperatures. The ASTM slope of a chlorinated aromatic hydrocarbon and tricresyl phosphate were shown to increase at high temperature. Therefore, for some of the fluids, the ASTM slope depends on the temperature range used to calculate the ASTM slope. This will have an effect on the predicted pressure coefficient value.

Thirdly, Equations [45] and [42] do not fully account for the differences in the smoothness of the molecules. Under constant temperature, pressure and average formula weight per atom one can increase the kinematic viscosity either by increasing chain length and branching or by introducing fused rings. If the molecular chain is stiff and its branches are rigid, a highly branched molecule may have the same ASTM slope and viscosity level as a molecule made up of smooth fused rings. The result is that molecular interlocking introduced by external pressure will be more pronounced for highly branched molecules. As a result the highly branched molecule will have a larger pressure coefficient than the fused ring molecule. These differences are not fully accounted for by the current models.

Since the above three limitations have different effects on the fluid, the net result may not be clear. Moreover, in examining the deviations of the individual fluids, one has to keep in mind that the discrepancy of the experimental values for pressure coefficient among different investigators can be as high as 0.25×10^{-4} psig (see Table 15). The deviations in the comparisons show that for Equation [45], in general the fluids with large negative deviations are of the dense center type molecules. The ASTM slope of the dense center molecule decreases with temperature. Therefore, the ASTM slope based on 100° and 210°F is larger than the ASTM slope based on a wider temperature range. When the ASTM slope is higher than anticipated for a molecular structure, Equation [45] predicts a pressure coefficient larger than the experimental one. This causes a negative deviation.

On the other hand, the fluids which have large positive deviations in the comparison are waxy mineral oils, polymeric fluids and polymer-thickened blends. The ASTM slopes of these type of fluids tend to increase at low temperature. Therefore, the ASTM slope based on 100° - 210°F is smaller than the ASTM slope based on a wider temperature range. Because the ASTM slope is smaller than it should be, predicted pressure coefficients are too small. This causes a positive deviation. The higher average formula weight per atom of some of the compounds also causes a positive deviation.

By examining the comparison of the various methods in predicting the pressure coefficients of nonhydrocarbons which lie beyond the limits designed for Equations [45] and [42] in Table 41, a better understanding of the limitations of the equations is found.

All the fluids in Table 41 have average formula weights per atom above 4.5. It is interesting to note that Equation [45] predicts some of the fluids quite accurately. These fluids are the ones with low enough atmospheric viscosities so that the difference in molecular packing doesn't have much effect on the pressure coefficient (see Figure 21). Once again the large positive deviations are due to higher average formula weight per atom and the low 100-210°F ASTM slope for polymeric fluid. The large negative deviation is due to higher 100°-210°F, ASTM slope for dense center material. The summary of the data on Table 41 is shown in Table 43.

The data on Table 43 show that Equation [42] has the lowest average deviation. For these fluids, Equation [45] is not effective for predictions. This is understandable because Equation [45] has a strong dependence on density. The high average formula weight per atom distorted the meaning of density as a comparative measurement of the differences in free volume. Therefore, for fluids with average formula weights per atom above 4.5, Equation [42] is the best relationship to use for an approximation of the pressure coefficients.

Table 1

CALIBRATION OF GAGES FOR THE PRL PRESSURE VISCOMETER

5,000 psig Capacity Gage		10,000 psig Capacity Gage	
Dead Weight Gage Pressure*, psig	Average Gage Reading, psig	Dead Weight Gage Pressure* psig	Average Gage Reading, psig
530	545	1,030	1,040
1,030	1,045	2,030	2,045
1,530	1,545	3,030	3,075
2,030	2,045	4,030	4,078
2,530	2,558	5,030	5,085
3,030	3,045	6,030	6,100
3,530	3,550	7,030	7,090
4,030	4,045	8,030	8,095
4,530	4,543	9,030	9,130
4,930	4,950	10,030	10,150

*Dead Weight Gage has an accuracy of ± 1 psig

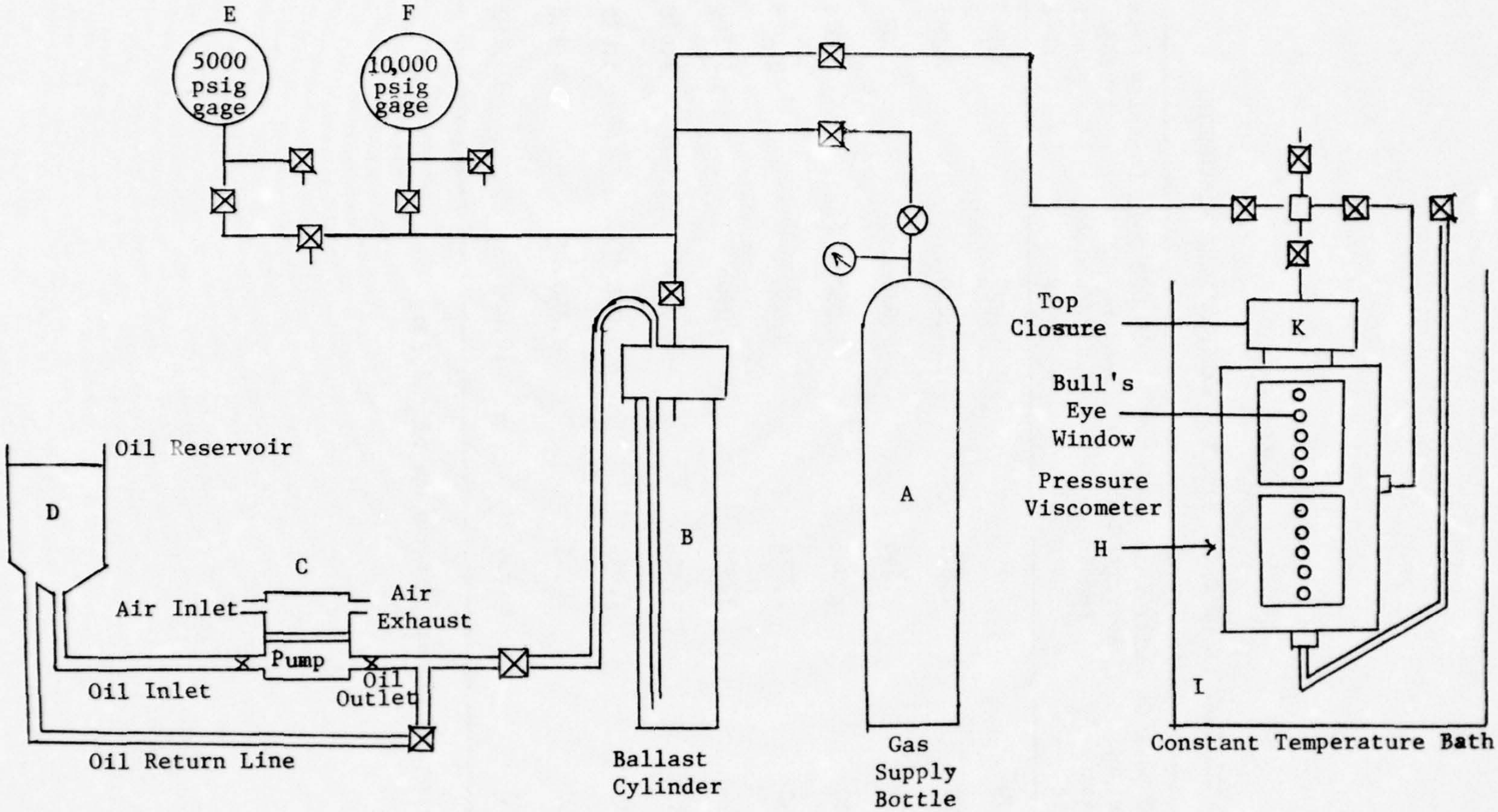

Figure 1. SCHEMATIC DIAGRAM OF PRL PRESSURE VISCOMETER SYSTEM

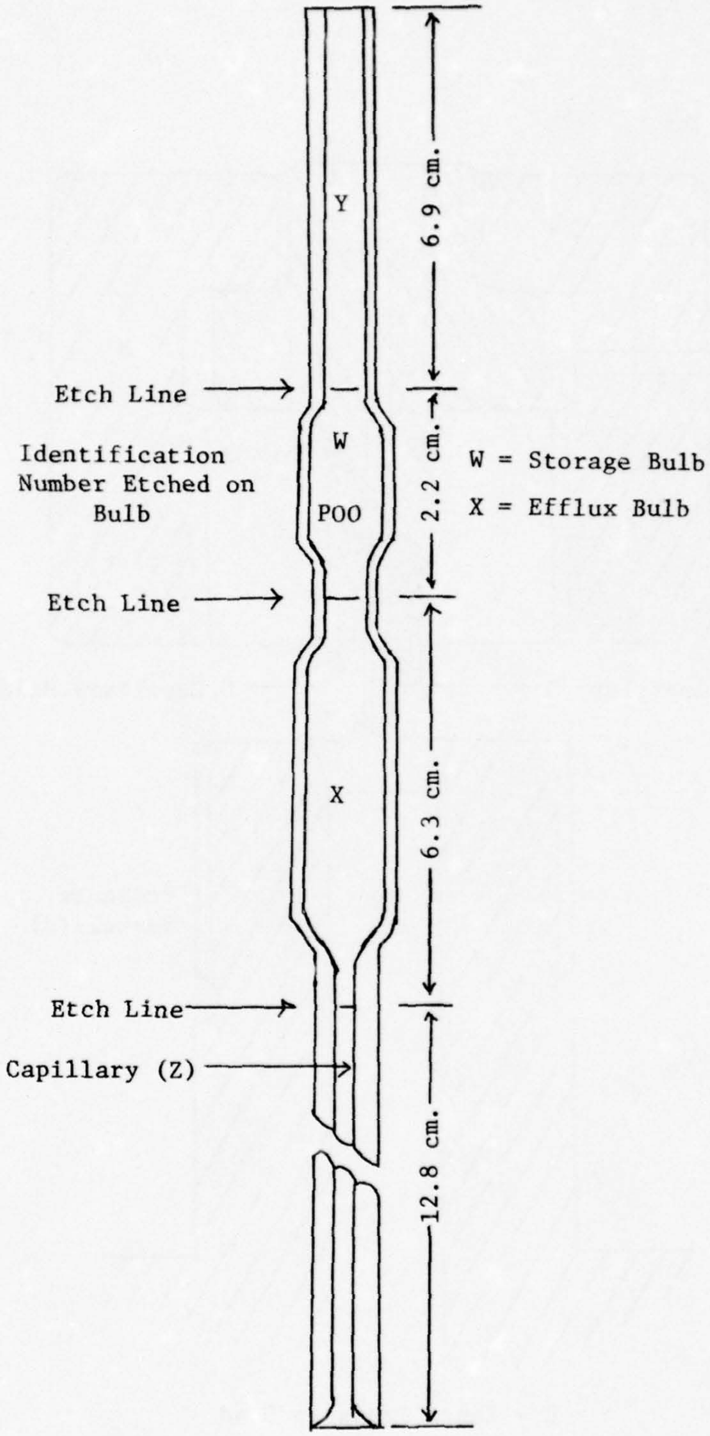

Figure 2. CAPILLARY UNIT

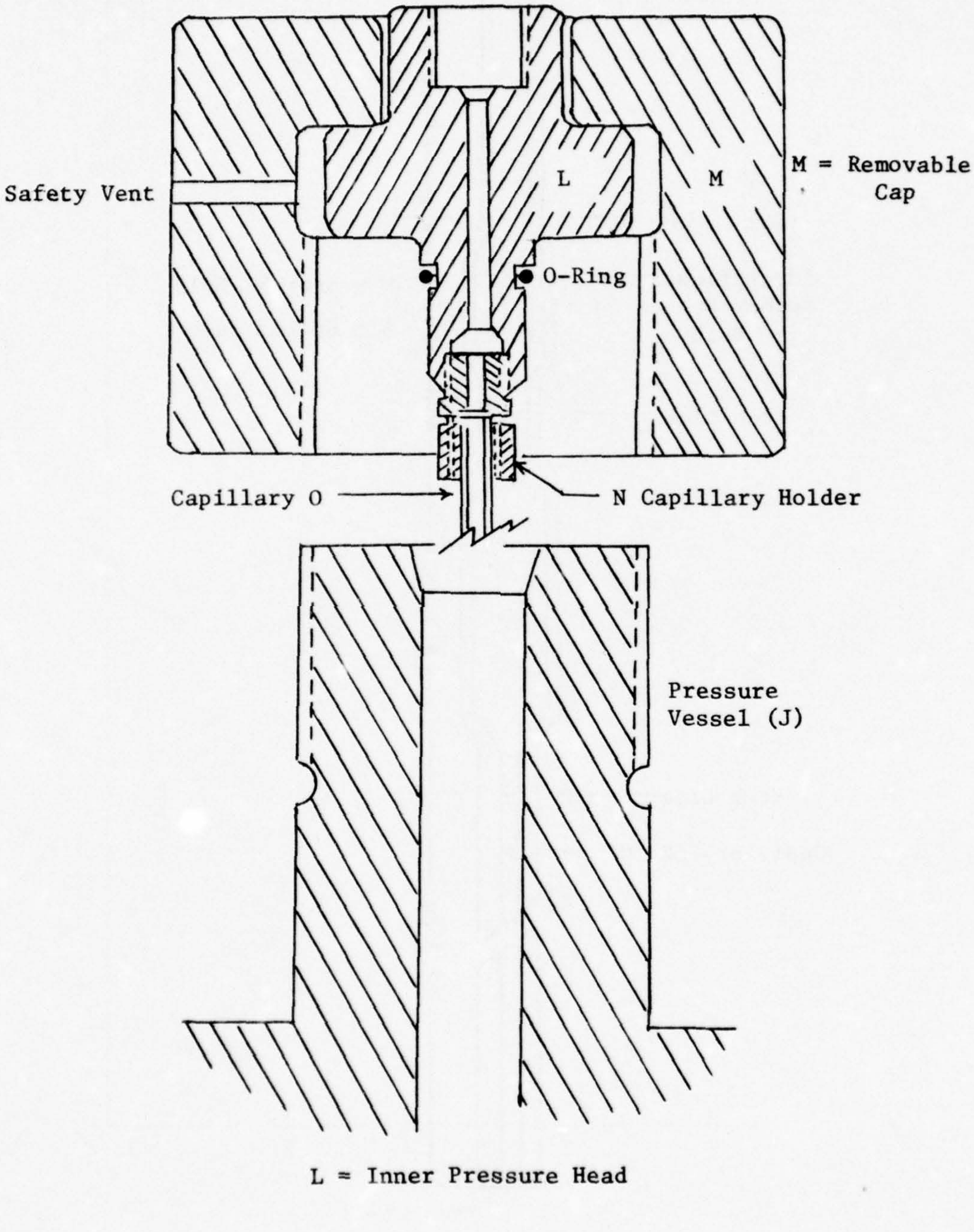

L = Inner Pressure Head

Figure 3. TOP CLOSURE (K)

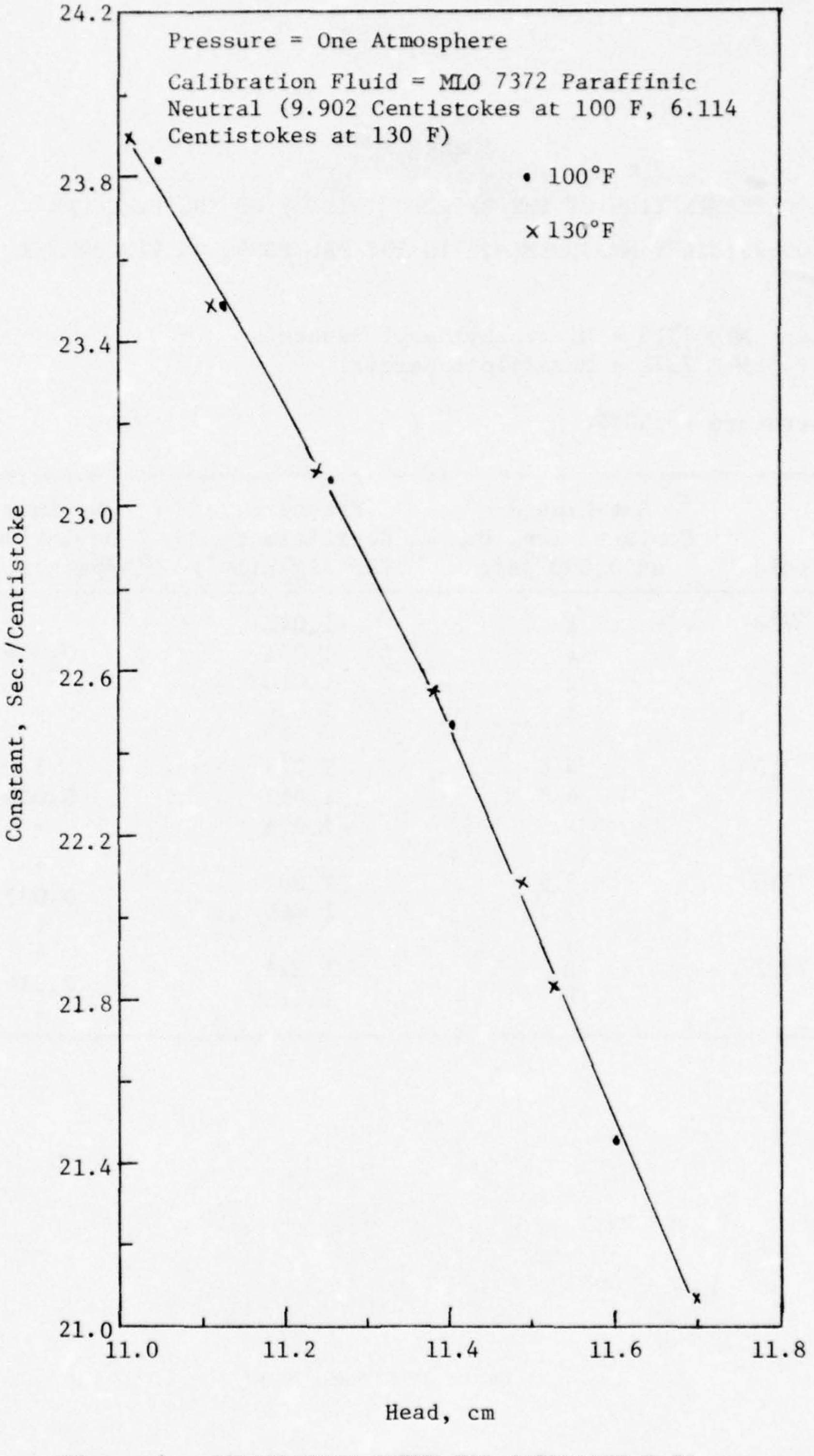

Figure 4. CALIBRATION CURVE FOR CAPILLARY P-81

Table 2

DETERMINATION OF THE REPRODUCIBILITY OF THE PRESSURE COEFFICIENT MEASUREMENTS IN THE PRL PRESSURE VISCOMETER

Test Fluid: MLO 7710 = Di-2-ethylhexyl Sebacate
MLO 7372 = Paraffinic Neutral

Test Temperature = 100°F.

Test Fluid	Gas-Liquid Contact Time, hr at 3,000 psig	Pressure Coefficient, (1/psig)x(10^4)	Maximum Deviation, (1/psig)x(10^4)
MLO 7710	1	1,048	↑ 0.008 ↓
	1	1.051	
	1	1.050	
	1	1.056	
MLO 7710	4.5	1.026	↑ 0.005 ↓
	4.5	1.021	
	4.5	1.024	
MLO 7710	7.5	1.002	↑ 0.003 ↓
	7.5	1.005	
MLO 7372	1	1.326	↑ 0.014 ↓
	1	1.312	

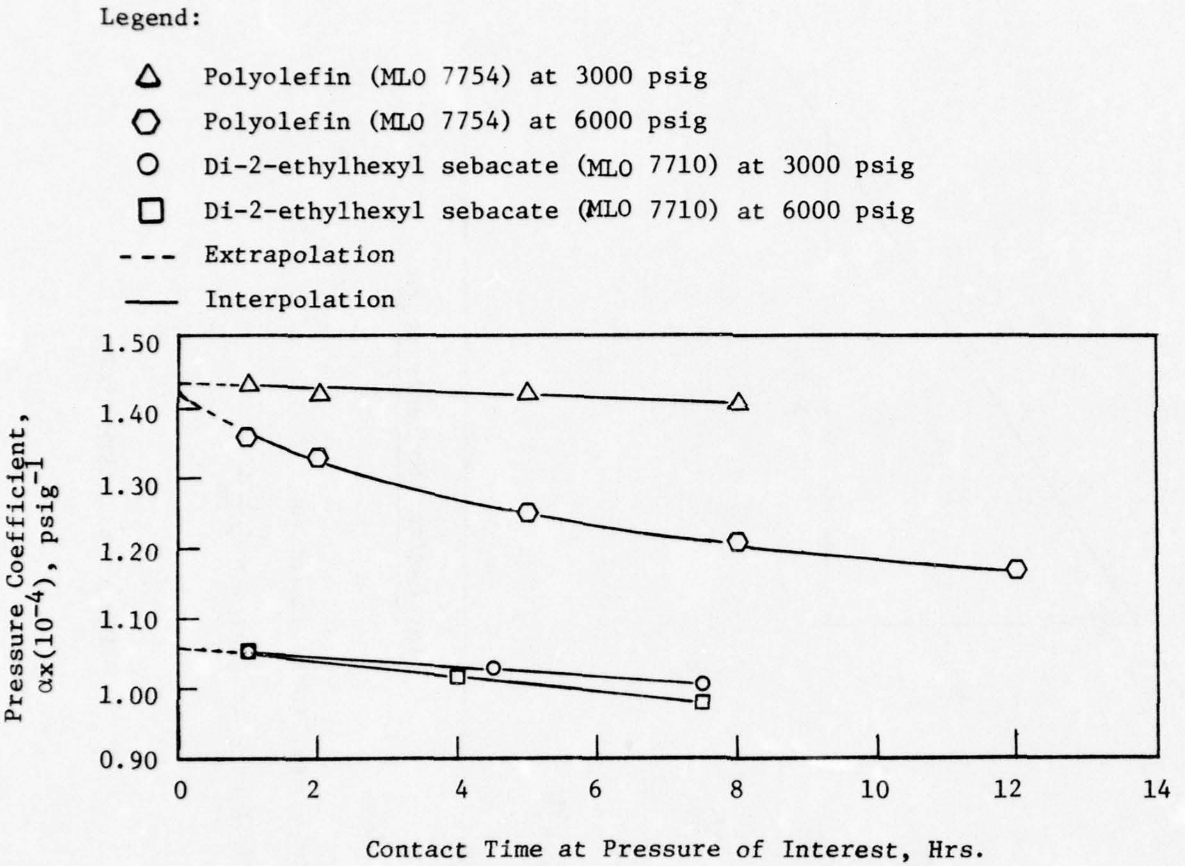

Figure 5. THE EFFECT OF DISSOLVED GAS ON THE PRESSURE COEFFICIENTS

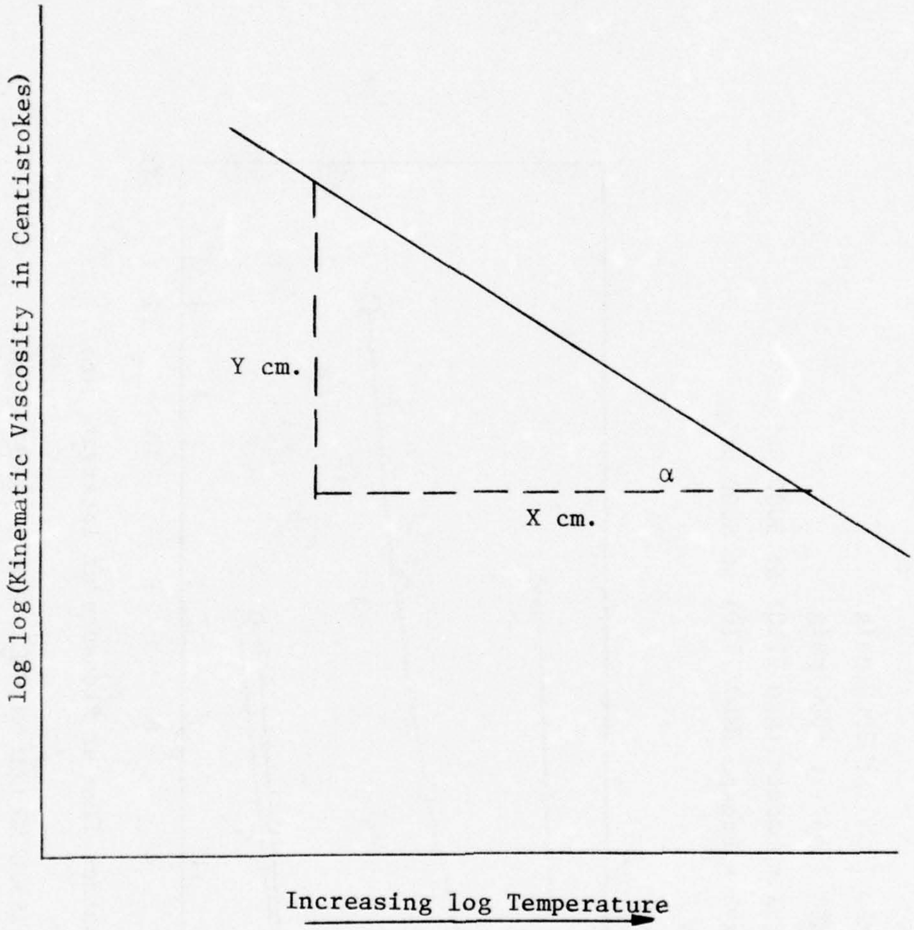

ASTM Kinematic Viscosity-Temperature Chart

Y and X are linear distances

$$\text{ASTM Slope} = \text{tangent } \alpha = \frac{Y \text{ cm.}}{X \text{ cm.}}$$

Figure 6. ASTM SLOPE

Table 3

RELATION BETWEEN SLOPE m OF MacCoull-WALTHER EQUATION AND ASTM SLOPE

Viscosity Range, cs.	Relation Between m and ASTM Slope (C)
0.4 to 0.7	m = 4.521 C
0.7 to 1.0	m = 4.447 C
1.0 to 1.5	m = 4.701 C
1.5 up	m = 5.056 C

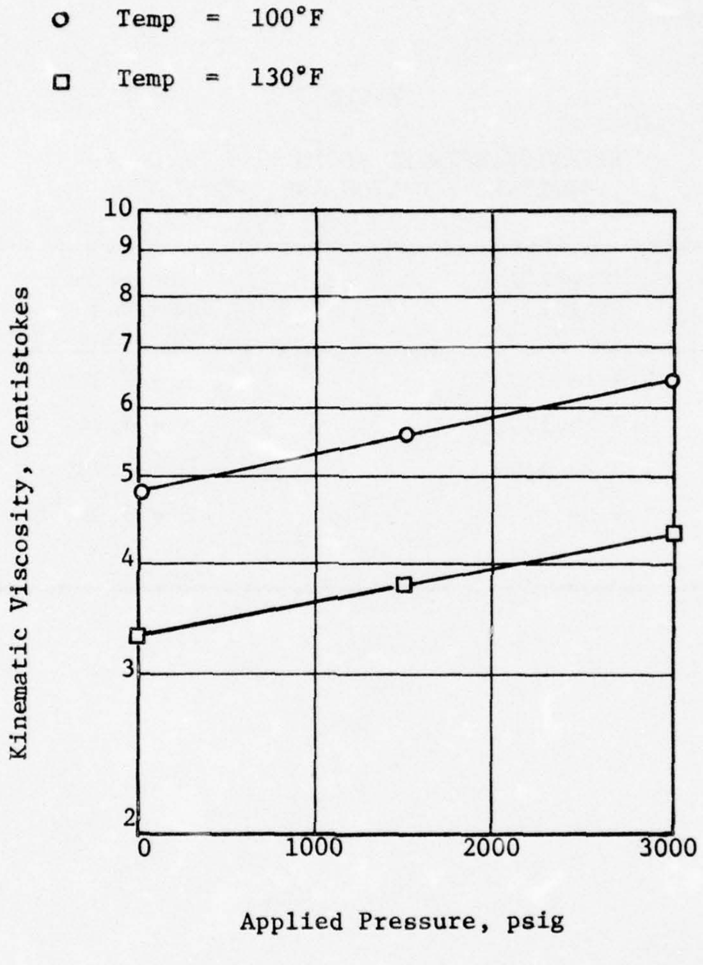

Figure 7. EFFECT OF PRESSURE ON THE VISCOSITY OF PARAFFINIC GAS OIL (O-266)

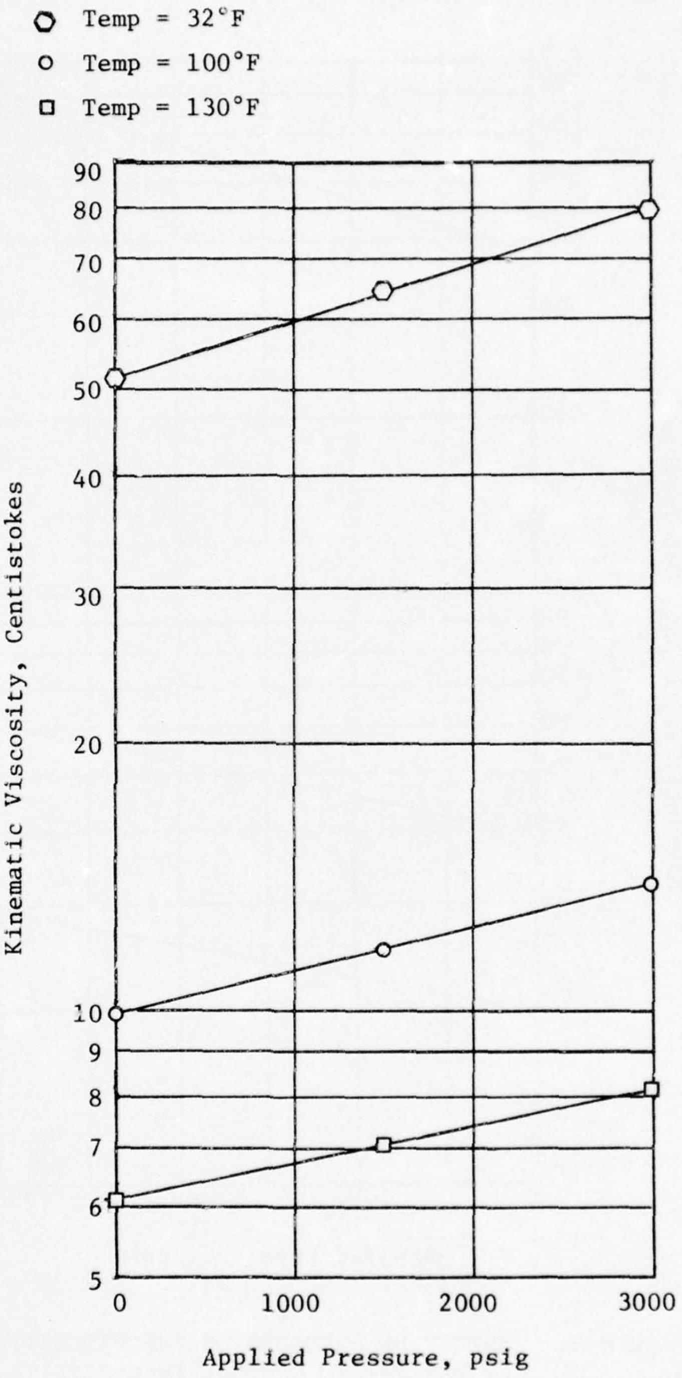

Figure 8. EFFECT OF PRESSURE ON THE VISCOSITY OF PARAFFINIC NEUTRAL (MLO 7372)

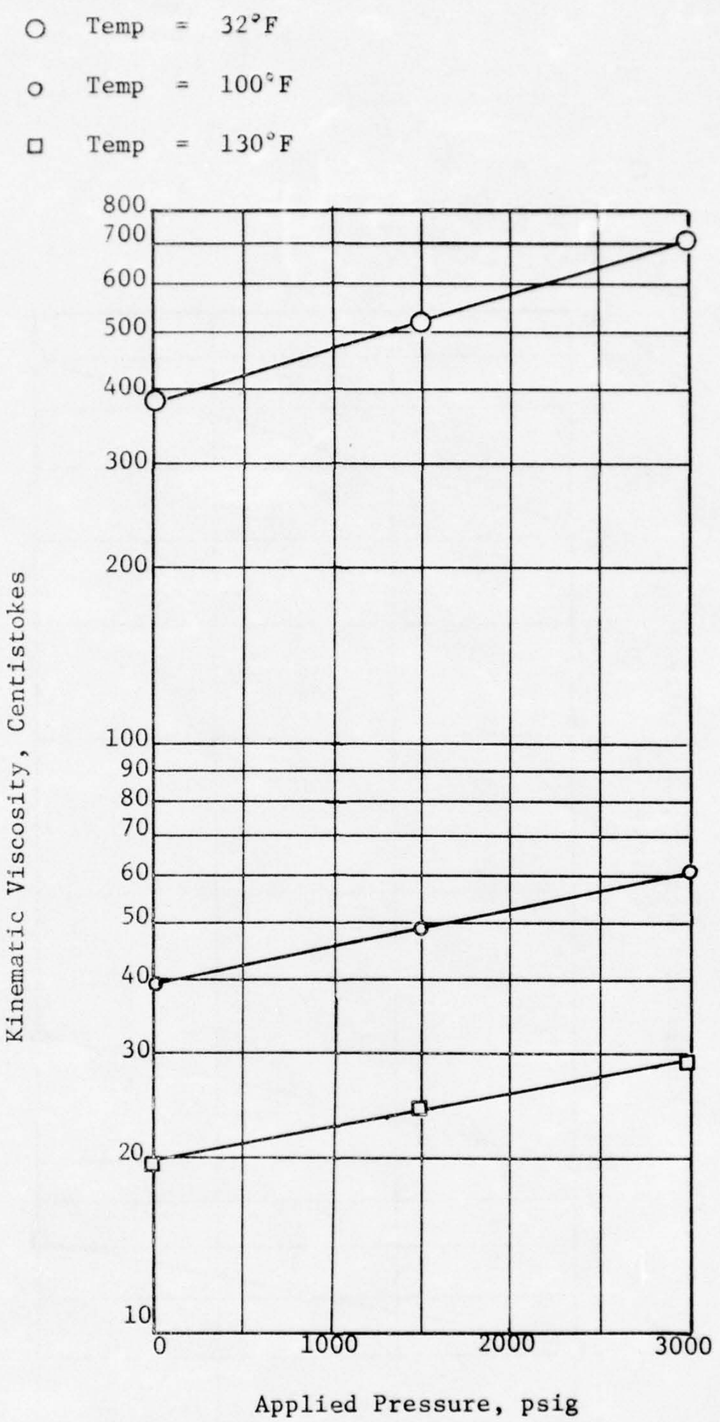

Figure 9. EFFECT OF PRESSURE ON THE VISCOSITY OF PARAFFINIC NEUTRAL (MLO 7375)

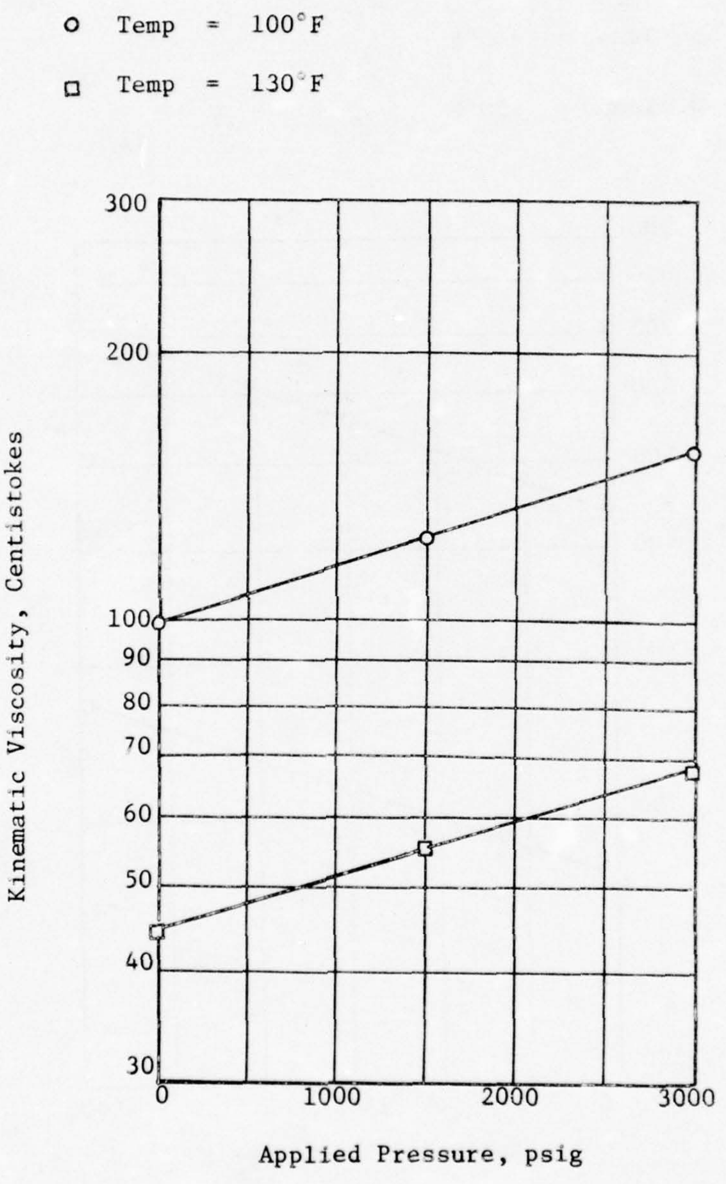

Figure 10. EFFECT OF PRESSURE ON THE VISCOSITY OF PARAFFINIC NEUTRAL (MLO 7120)

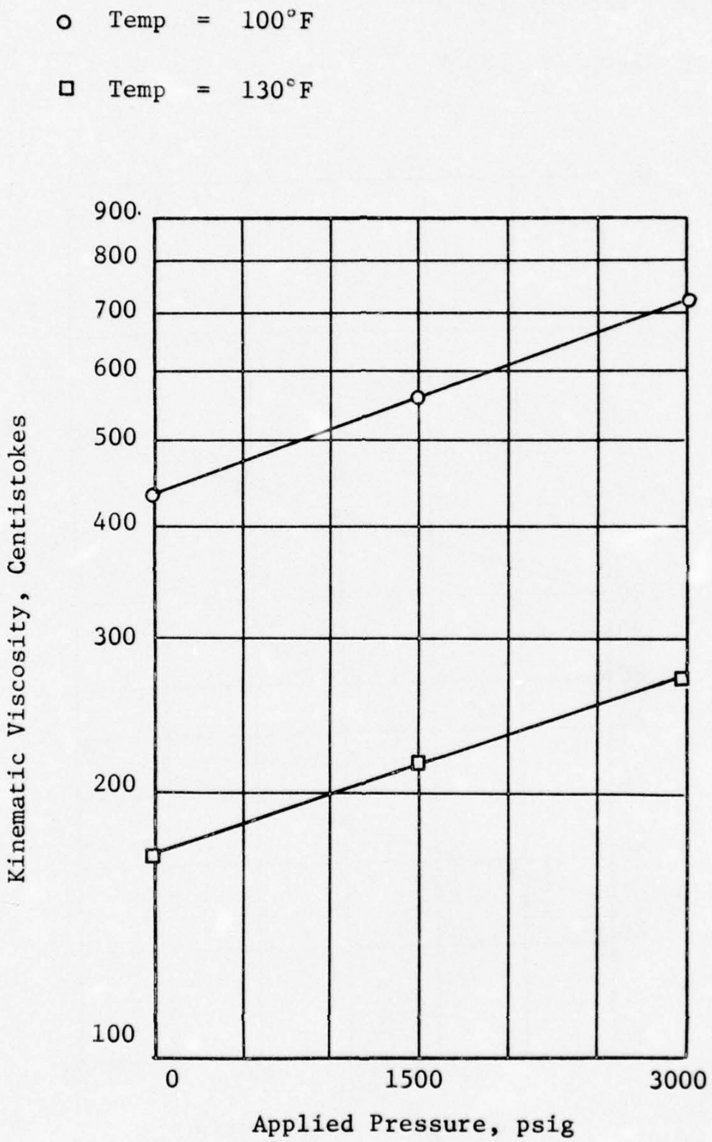

Figure 11. EFFECT OF PRESSURE ON THE VISCOSITY OF PARAFFINIC BRIGHT STOCK (MLO 7246)

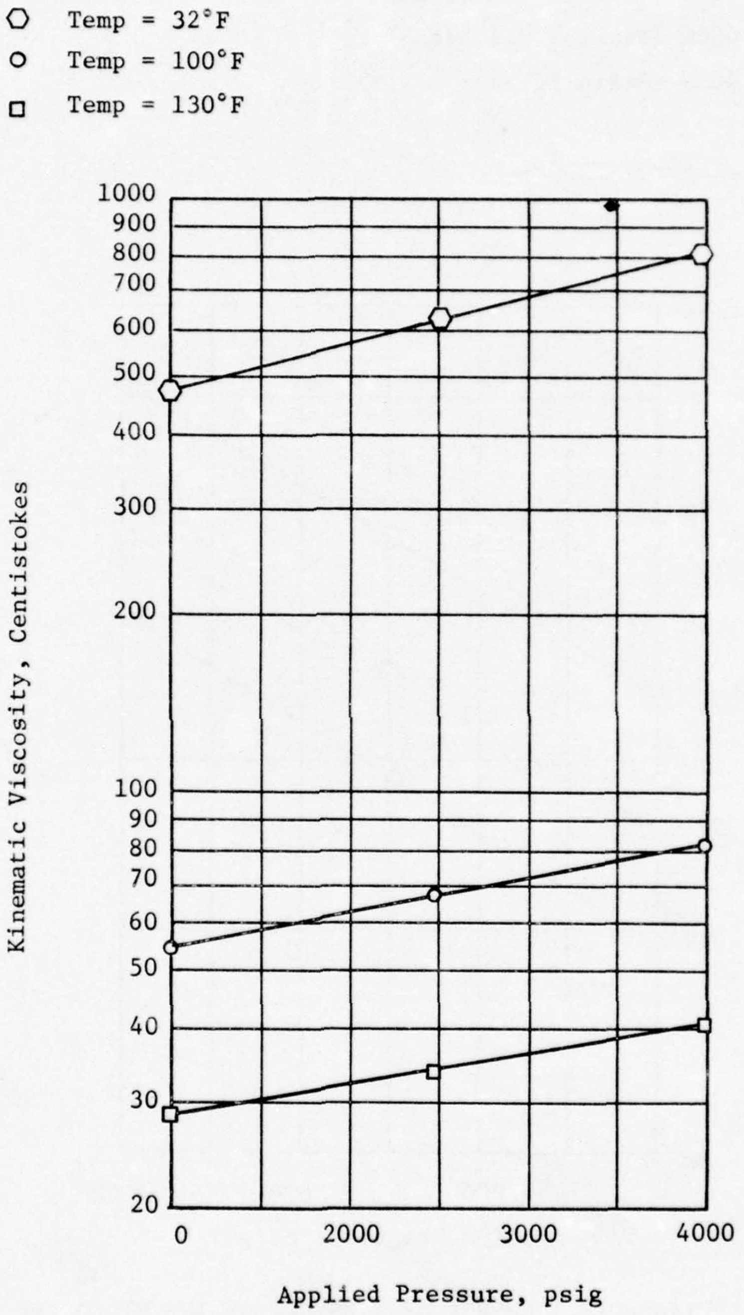

Figure 12. EFFECT OF PRESSURE ON THE VISCOSITY OF RESIN-MINERAL OIL BLEND (PRL 4559)

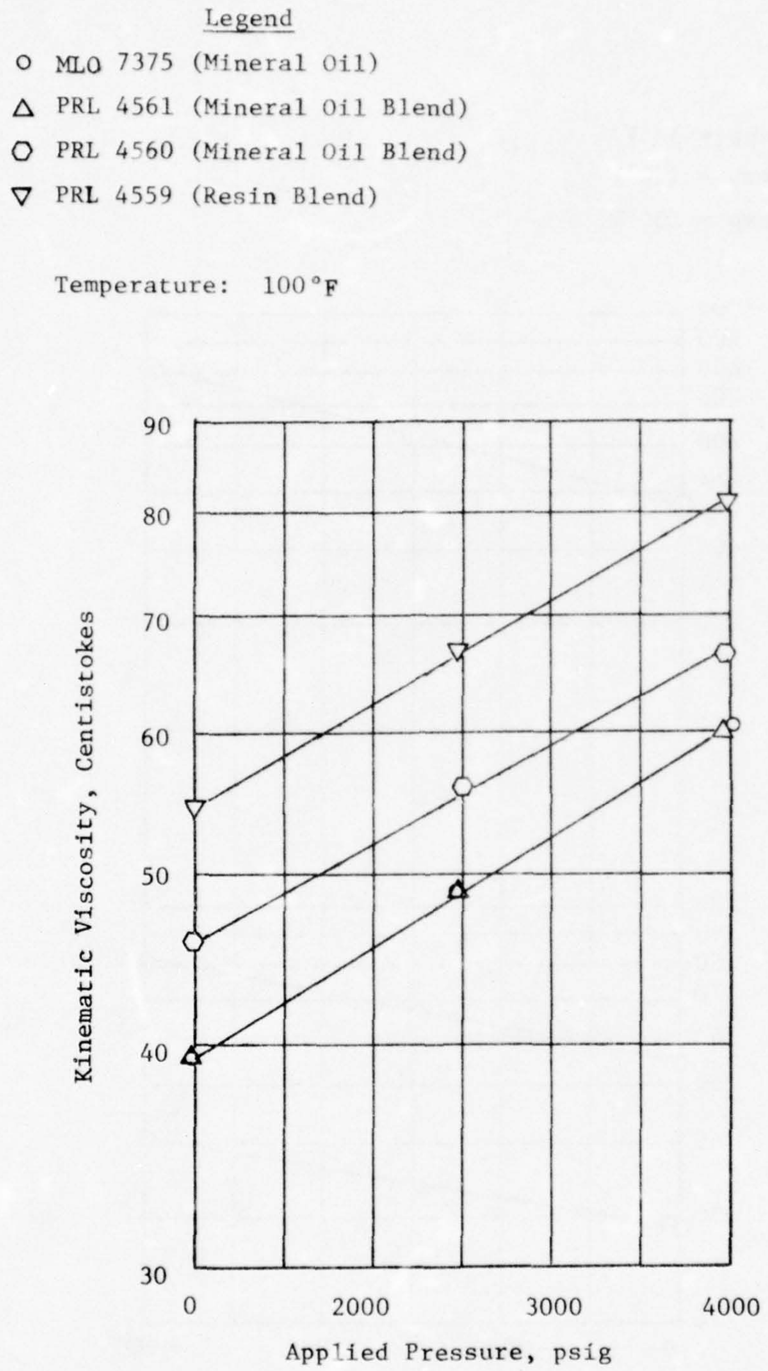

Figure 13. EFFECT OF PRESSURE ON THE VISCOSITY OF A MINERAL OIL, MINERAL OIL BLENDS AND A RESIN BLEND AT SIMILAR VISCOSITY LEVEL

Table 4

BRIEF DESCRIPTIONS AND PHYSICAL PROPERTIES OF THE FLUIDS USED IN THE CURRENT INVESTIGATION

Fluid Designation	Description	Atmospheric Viscosity, Centistokes 100 °F	ASTM Slope	Density, gm/cc 100 °F	Pressure Coefficient* (1/psig)x(10^4)
O-266	Paraffinic Gas Oil	4.844	0.821	0.8159	1.153
MLO 7372	Paraffinic Neutral	9.902	0.800	0.8416	1.333
MLO 7375	Paraffinic Neutral	39.34	0.748	0.8562	1.686
MLO 7120	Paraffinic Neutral	99.33	0.710	0.8710	1.770
MLO 7246	Paraffinic Bright Stock	438.2	0.640	0.8756	1.988
PRL 4561	65.07 wt. % MLO 7372 + 34.93 wt. % MLO 7120	39.32	0.734	0.8571	1.649
PRL 4560	53.71 wt. % MLO 7372 + 46.83 wt. % MLO 7246	45.82	0.703	0.8553	1.482
PRL 4559	68.08 wt. % MLO 7372 + 31.92 wt. % MLO 3915**	54.61	0.659	0.8552	1.566

* Based on pressure viscosity measurements at 1,500 psig and 3,000 psig

** Pennsylvania Resin, 8,360 cs. at 100°F and 228.7 cs. at 210°F

Table 5

BRIEF DESCRIPTIONS AND PHYSICAL PROPERTIES OF SEVERAL** FLUIDS USED TO DEVELOP THE CORRELATIONS

Fluid Designation	Description	Atmospheric Viscosity, Centistokes 100 °F	ASTM Slope	Density gm/cc 100 °F	Pressure Coefficient,* (1/psig)x(10^4)
MLO 7519	Super-refined paraffinic M.O.	12.78	0.764	0.8250	1.332
MLO 7557	Deep-dewaxed, Super-refined M.O.	14.00	0.783	0.8315	1.386
MLO 7558	Deep-dewaxed, Super-refined M.O.	20.13	0.710	0.8368	1.413
MLO 7661	Super-refined Paraffinic Bright Stock	146.4	0.676	0.8567	1.767
MLO 7094	Paraffinic Bright Stock	480.6	0.633	0.8743	1.875
PRL 2858	Naphthenic M.O. (API Oil 102)	8.811	0.840	0.8643	1.359
MLO 7516	Super-refined Naphthenic M.O.	78.69	0.762	0.8765	1.873
MLO 7754	Oligomer of α Olefins	79.99	0.639	0.8206	1.523
MLO 7123	Polybutene	124.4	0.734	0.8374	2.473
MLO 7124	Hydrogenated Polybutene	115.7	0.728	0.8285	2.473
MLO 7112	Di-2-ethylhexyl Sebacate	12.56	0.701	0.9015	1.060
MLO 7684	Polyester	88.64	0.596	0.9575	1.413

* Based on pressure viscosity measurements up to 10,000 psig.

If the plot of log viscosity versus pressure isn't a straight line, pressure coefficient is calculated based on the lowest pressure viscosity measurement.

** Fluids used in studies included in Annual Report AFML-TR-67-107, Part I.

Table 6

BRIEF DESCRIPTIONS AND PHYSICAL PROPERTIES OF SEVERAL**** FLUIDS USED TO DEVELOP THE CORRELATIONS

PRL Number	Solvent* used	Thickener** used	Atmospheric Viscosity centistokes 100 °F	ASTM Slope	Density gm/cc. 100 °F	Pressure Coefficient*** (1/psig)x(10^4)
2906	Napthenic Gas Oil	Acryloid 25	1293.	0.366	0.9090	1.574
2924	PRL 2859	Paratone CX2	33.90	0.583	0.8630	1.449
2924A			223.19	0.432	0.8625	1.767
2924B			1984.	0.361	0.8650	1.973
4025	PRL 2859	PRL 2905	33.09	0.499	0.8682	1.405
4027			227.0	0.330	0.8770	1.514
4028			1917.	0.280	0.8980	1.590
4029	PRL 2859	PRL 2906	34.70	0.526	0.8735	1.413
4032			227.4	0.397	0.8920	1.579
4033	MLO 7710	AC 307	33.60	0.576	0.9110	1.106
4034			226.8	0.446	0.9280	1.367
4036	PRL 2859	MLO 7760	34.84	0.689	0.8690	1.473
4037			222.9	0.597	0.8750	1.862
4038			1875.	0.548	0.8840	2.028
4039	MLO 7710	MLO 7760	34.78	0.623	0.8990	1.163
4041			225.7	0.558	0.8920	1.547
4042			1915.	0.536	0.8865	1.903
4043	MLO 7710	Paratone CX2	35.29	0.521	0.8965	1.158
4044			224.7	0.409	0.8860	1.541
4045			1268.	0.359	0.8770	1.759
4046	MLO 7685	Paratone CX2	9.61	0.587	0.8340	1.125
4047			18.70	0.499	0.8360	1.212
4048			28.56	0.462	0.8390	1.296
4049	PRL 2859	Paratone CX2	55.58	0.529	0.8640	1.525
4050			90.92	0.487	0.8645	1.620
4051	MLO 7516	Paratone CX2	232.7	0.601	0.8695	2.223
4052			460.4	0.524	0.8692	2.305
4053			743.8	0.477	0.8700	2.389
4054	MLO 7788	Paratone CX2	493.1	0.537	0.8670	1.911
4055			1014.	0.466	0.8650	2.003

* Brief descriptions and physical properties of the solvents are listed in Table 7.

** Brief descriptions and physical properties of the thickerners are listed in Table 8.

*** Based on pressure viscosity measurements up to 10,000 psig.

**** Fluids used in studies included in Annual Report AFML-TR-70-304, Part II.

Table 7

SOLVENTS USED IN EARLIER* VISCOSITY-PRESSURE STUDIES

Fluid Designation	Solvent Description	Centistoke Viscosity 100°F	Centistoke Viscosity 210°F	ASTM Slope
7685	Naphthenic Gas Oil	3.27	1.24	0.865
2859	Naphthenic Mineral Oil	8.80	2.28	0.849
7516	Naphthenic White Oil	78.86	8.20	0.769
7788	Paraffinic Mineral Oil	164.7	15.26	0.675
7710	Di-2-ethylhexyl Sebacate	12.57	3.32	0.700

---

*AFML-TR-70-304, Part II.

Table 8

BRIEF DESCRIPTION OF THICKENERS USED IN EARLIER* VISCOSITY-PRESSURE STUDIES

Thickener Designation	Description
PRL 2905	High molecular weight polymethacrylate (50.4 wt. per cent Acryloid-160 in a naphthenic gas oil).
PRL 2906	Low molecular weight polymethacrylate (47.7 wt. per cent Acryloid-25 in a naphthenic gas oil).
Ac-307	Low molecular weight polymethacrylate (52.3 wt. per cent Acryloid-25 in di-2-ethylhexyl sebacate).
Paratone cx-2	Polysiobutylene. (33.6 wt. per cent in a naphthenic white oil).
MLO 7760	Super-refined heavy resin with molecular weight of approximately 2000 to 3000 and basically paraffinic hydrocarbon.

---

*AFML-TR-70-304, Part II.

Table 9

BRIEF DESCRIPTIONS AND PHYSICAL PROPERTIES OF API PROJECT 42's (8) FLUIDS USED TO DEVELOP THE CORRELATIONS

Fluid Designation	Description	Atmospheric Viscosity, Centistokes 100°F	ASTM Slope	Density, gm/cc 100°F	Pressure Coefficient *, (1/psig)x(10^4)
PSU 532	n-C_{15} n-Pentadecane	2.592	0.815	0.7562	0.949
PSU 500	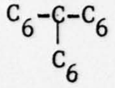 $C_6-\underset{C_6}{\overset{}{C}}-C_6$ 7-n-Hexyltridecane	4.551	0.865	0.7756	1.112
PSU 25	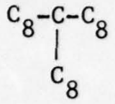 $C_8-\underset{C_8}{\overset{}{C}}-C_8$ 9-n-Octylheptadecane	8.931	0.766	0.7905	1.113

(Continued on next page.)

Table 9 (Continued)

Fluid Designation	Description	Atmospheric Viscosity, Centistokes 100°F	ASTM Slope	Density, gm/cc 100°F	Pressure Coefficient*, (1/psig)x(10^4)
PSU 8	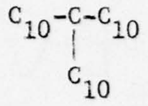 $C_{10}-C(C_{10})-C_{10}$ 11-n-Decylhencicesane	15.12	0.707	0.8005	1.199
PSU 134	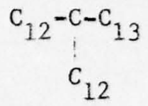 $C_{12}-C(C_{12})-C_{13}$ 13-n-Dodecylhexacosane	25.63	0.647	0.8077	1.186
PSU 516	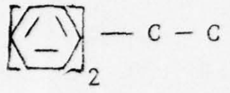 1,1-Diphenylethane	2.890	0.865	0.9860	0.912
PSU 503	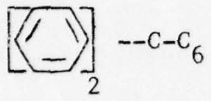 1,1-Diphenylheptane	8.512	0.925	0.9375	1.159
PSU 12	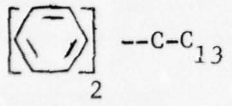 1,1-Diphenlytetradecane	18.62	0.777	0.9069	1.396

(Continued on next page.)

Table 9 (Continued)

Fluid Designation	Description	Atmospheric Viscosity, Centistokes 100°F	ASTM Slope	Density, gm/cc 100°F	Pressure Coefficient*, (1/psig)x(10^4)
PSU 18	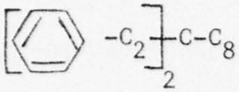 1-Phenyl-3(2-Phenyl-ethyl)-hendecane	12.61	0.803	0.9094	1.124
PSU 87	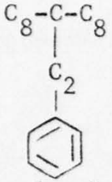 9(2-Phenyl-ethyl) heptadecane	9.383	0.777	0.8441	1.211
PSU 113	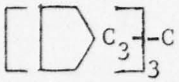 1,7-Dicyclopentyl-4 (3-cyclopentyl-propyl) heptane	25.68	0.751	0.8774	1.507
PSU 19	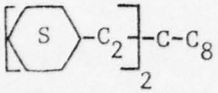 1-Cyclohexyl-3(2-Cyclohexylethyl) hendecane	33.53	0.793	0.8548	1.812

(Continued on next page.)

Table 9 (Continued)

Fluid Designation	Description	Atmospheric Viscosity, Centistokes 100°F	ASTM Slope	Density, gm/cc 100°F	Pressure Coefficient*, (1/psig)x(10^4)
PSU 111	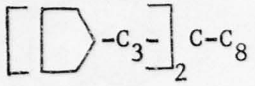 1-Cyclopentyl-4(3-Cyclopentylpropyl) dodecane	16.05	0.748	0.8469	1.281
PSU 88	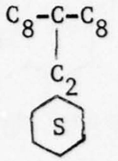 9(2-Cyclohexylethyl) heptadecane	14.73	0.772	0.8216	1.381
PSU 110	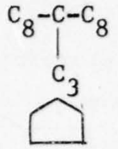 1-Cyclo-pentyl-4(3-Cyclopentylpropyl) dodecane	11.53	0.759	0.8187	1.088
PSU 122	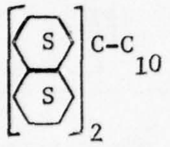 1,1-Di(alphadecayly)-hendecane	817.0	0.884	0.9204	3.813

(Continued on next page.)

Table 9 (Continued)

Fluid Designation	Description	Atmospheric Viscosity, Centistokes 100°F	ASTM Slope	Density, gm/cc 100°F	Pressure Coefficient*, (1/psig)x(10^4)
PSU 656	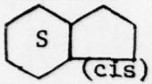 (cis) cis-Bicyclo(4,3,0)nonane	1.975	0.902	0.8707	0.948
PSU 657	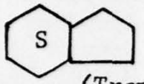 (Trans) trans-Bicyclo(4,3,0) nonane	1.438	0.915	0.8484	0.819
PSU 620	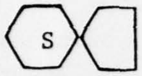 Spiro (4,5)decane	1.874	0.795	0.8646	0.868
PSU 569	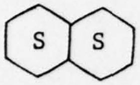 (cis) cis-Decahydronaphthalene	2.615	0.846	0.8834	0.942
PSU 570	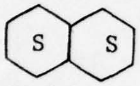 (Trans) trans-Decahydronaphthalene	1.810	0.843	0.8565	0.877

(Continued on next page.)

Table 9 (Continued)

Fluid Designation	Description	Atmospheric Viscosity, Centistokes 100°F	ASTM Slope	Density, gm/cc 100°F	Pressure Coefficient*, (1/psig)x(10^4)
PSU 622	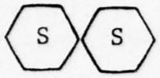 Spiro (5,5) undecane	2.522	0.810	0.8763	0.930
PSU 597	 5-Decylinden	6.851	0.773	0.8846	1.075
PSU 598	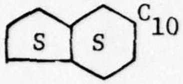 5-Decylhydrindan	8.549	0.730	0.8510	1.105
PSU 604	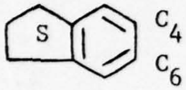 5-Butyl-6-hexylindan	8.911	0.857	0.8888	1.309
PSU 638	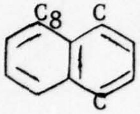 1,4-Dimethyl-5-Octylnaphthalene	13.86	0.879	0.9389	1.320

(Concluded on next page.)

Table 9 (Concluded)

Fluid Designation	Description	Atmospheric Viscosity, Centistokes 100°F	ASTM Slope	Density, gm/cc 100°F	Pressure Coefficient*, (1/psig)x(10^4)
PSU 639	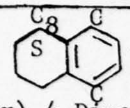 1(ar),4-Dimethyl-5-Octyltetralin	16.76	0.839	0.9098	1.566
PSU 640	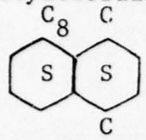 1,4-Dimethyl-5-Octyldecalin	10.99	0.810	0.8641	1.455
PSU 613	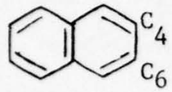 2-n-Butyl-3-n hexylnaphthalene	12.49	0.881	0.9209	1.379
PSU 614	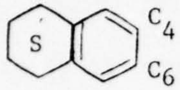 2(ar)-n-Bytyl-3(ar)n-hexyltetralin	14.83	0.857	0.8967	1.458
PSU 615	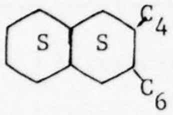 2-n-Butyl-3-n-hexyldecalin	15.28	0.885	0.8639	1.640

Table 10

PSEUDO LINEAR VARIABLES USED IN THE MULTIPLE LINEAR REGRESSION ANALYSIS

Order	Variables
First	ASTM^{*}, V^{**}, D^{***}
Second	ASTM^2, V^2, D^2, (ASTM)(V), (ASTM)(D), (D)(V)
Third	ASTM^3, V^3, D^3, $(\text{ASTM})(\text{V}^2)$, $(\text{D})(\text{V}^2)$, $(\text{ASTM})(\text{D}^2)$, $(\text{ASTM}^2)(\text{V})$, $(\text{D}^2)(\text{V})$, $(\text{ASTM}^2)(\text{D})$, (ASTM)(V)(D)
Fourth	ASTM^4, V^4, D^4, $(\text{ASTM})(\text{V}^3)$, $(\text{D})(\text{V}^3)$, $(\text{ASTM})(\text{D}^3)$, $(\text{ASTM}^2)(\text{V}^2)$, $(\text{D}^2)(\text{V}^2)$, $(\text{ASTM}^2)(\text{D}^2)$, $(\text{ASTM}^3)(\text{V})$, $(\text{D}^3)(\text{V})$, $(\text{ASTM}^3)(\text{D})$, $(\text{ASTM}^2)(\text{V})(\text{D})$, $(\text{ASTM})(\text{V}^2)(\text{D})$, $(\text{ASTM})(\text{V})(\text{D}^2)$

[*] ASTM = ASTM Slope

[**] V = log (Atmospheric viscosity)

[***] D = Atmospheric Density

Table 11

DEFINITION OF ABSOLUTE DEVIATION TERMS USED IN THE ANALYSIS OF THE DIFFERENT CORRELATIONS

Dev = Experimental Value - Calculated Value

$$\text{Avg} = \frac{1}{n} \Sigma \left|\text{Dev}\right|$$

$$\text{Bias} = \frac{1}{n} \Sigma \text{ Dev}$$

$$\text{RMS} = \sqrt{\frac{1}{n} \Sigma \text{ Dev}^2}$$

n = Number of points

$$\text{Sum of Residual Squares} = \Sigma \text{ Dev}^2$$

$$\text{Standard Error of Estimate} = \sqrt{\frac{1}{(n-k)} \Sigma \text{ Dev}^2}$$

k = Number of parameters

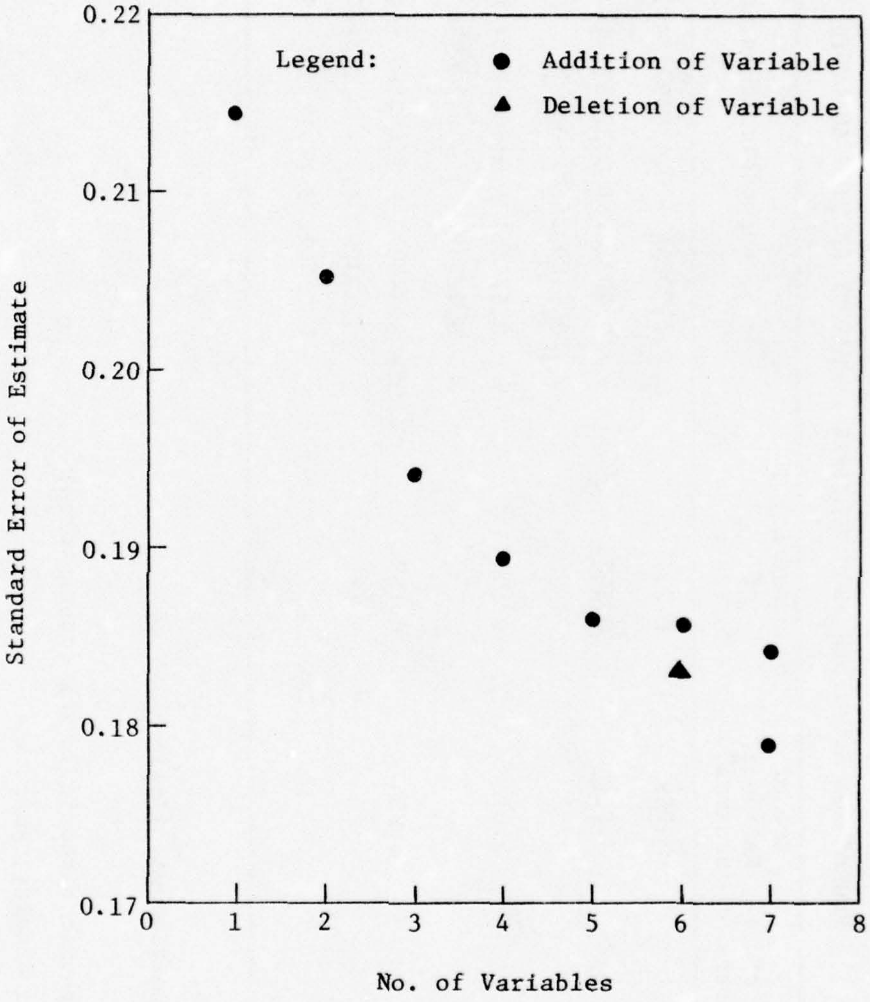

Figure 14. STANDARD ERROR OF ESTIMATE VERSUS NUMBER OF VARIABLES FROM THE MULTIPLE LINEAR REGRESSION ANALYSIS

Table 12

REGRESSION EQUATIONS FROM MULTIPLE LINEAR REGRESSION ANALYSIS

Number of Variables	Number of Parameters	Sum of Residual Squares*	Standard Error of Estimate*	Regression Equations**
1	2	3.769	0.2144	$\alpha = 1.00646 + 0.438590\ (ASTM^2)\ (V^2)$ [38]
2	3	3.414	0.2053	$\alpha = 0.902167 + 0.370822\ (ASTM^2)(V^2) + 0.112922\ (V)$ [39]
3	4	3.011	0.1940	$\alpha = 0.674811 + 0.660906 + (ASTM^2)(V^2) + 0.42739\ (V) - 0.376938\ (ASTM)(V^2)(D)$ [40]
4	5	2.834	0.1894	$\alpha = 0.390873 + 0.643182\ (ASTM^2)(V^2) + 0.593290\ (V) - 0.42884\ (ASTM^2)(V^2)\ (D) + 0.442273\ (ASTM^4)$ [41]

* See Table 13

** α = pressure coefficient, 1/psig

ASTM = ASTM Slope

V = log (Atmospheric Viscosity), log (centistokes)

D = Atmospheric Density, gm/c.c.

Table 13

REGRESSION EQUATIONS FROM MULTIPLE NON-LINEAR REGRESSION ANALYSIS

Number of Variables	Number of Parameters	Sum of Residual Squares*	Standard Error of Estimate*	Regression Equations**	
2	6	2.917	0.1921	$\alpha = 0.7236 + 0.2919\ V^{1.0459}$ $+ 0.5859\ ASTM^{3.5371}\ V^{1.6700}$	[42]
3	10	2.144	0.1691	$\alpha = 0.8396 + 1.2783\ V^{3.0656}$ $+ 0.8252\ ASTM^{5.0897}\ V^{1.6107}$ $- 1.1826\ ASTM^{0.0012}\ V^{3.1441}\ D^{0.2647}$	[43]
4	12	2.142	0.1713	$\alpha = -5.7183 + 1.7333\ V^{3.1873}$ $+ 0.8573\ ASTM^{4.8547}\ V^{1.5732}$ $- 1.6530\ ASTM^{0.0004}\ V^{3.2364}\ D^{0.1723}$ $+ 6.5361\ ASTM^{-0.0119}$	[44]
3	9	2.144	0.1679	$\alpha = 0.8381 + 2.8563\ V^{3.0627}$ $+ 0.3338\ ASTM^{5.1903}\ V^{1.5976}$ $- 2.7574\ V^{3.0974}\ D^{0.1161}$	[45]
3	9	2.849	0.1936	$\alpha = 1.4499 + 0.2583\ V^{0.9883}$ $- 3.9202\ ASTM^{1.3343}\ V^{0.5547}$ $+ 3.8111\ V^{1.959}\ ASTM^{0.8825}$	[46]

* See Table 13

** α = Pressure Coefficient
ASTM = ASTM Slope
V = log (atmospheric viscosity)
D = atmospheric density

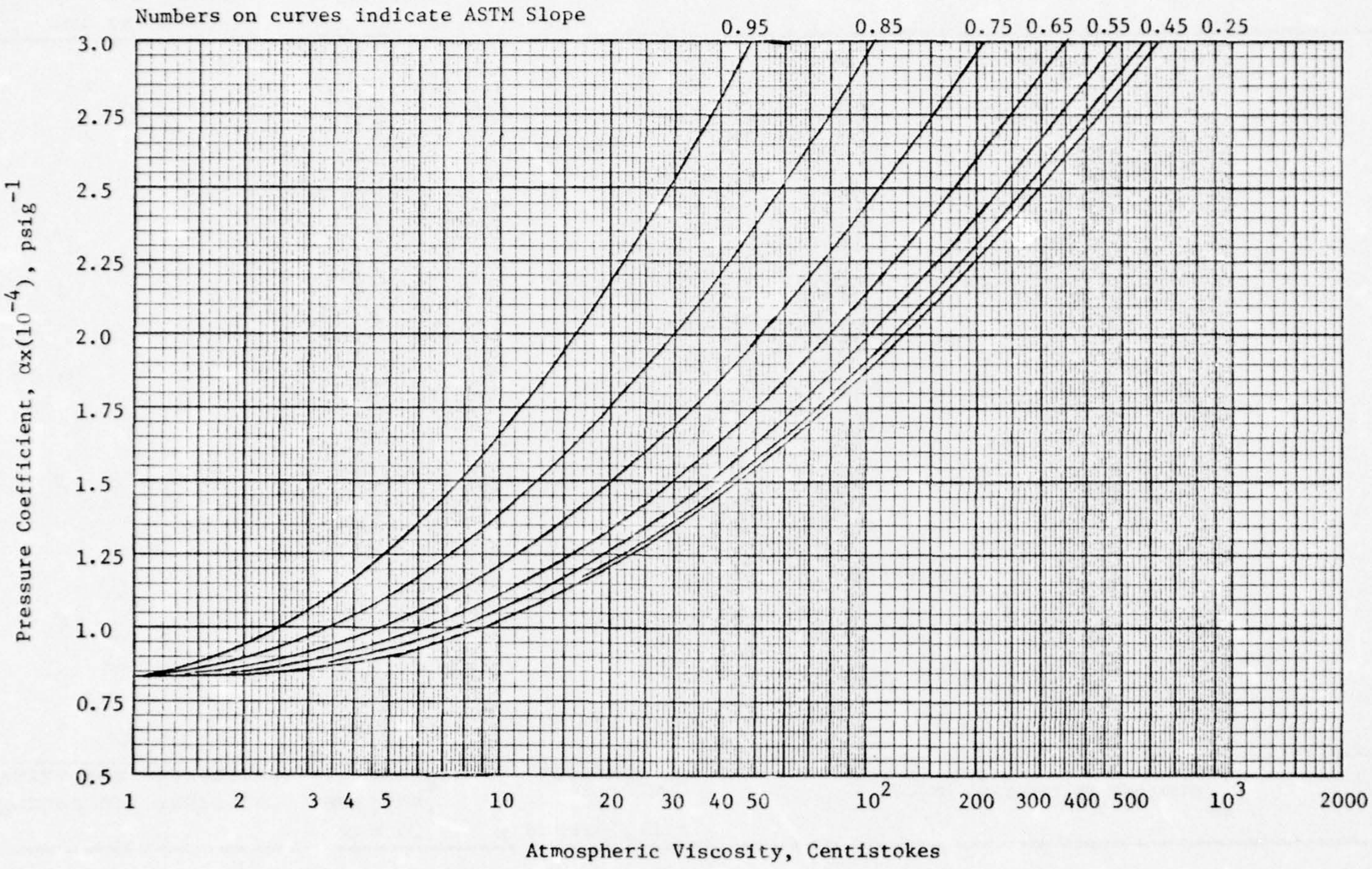

Figure 15. LIQUID PRESSURE COEFFICIENT PREDICTION CHART BASED ON EQUATION [45] AT ATMOSPHERIC DENSITY LEVEL OF 0.75 gm/cc (Concluded on next page.)

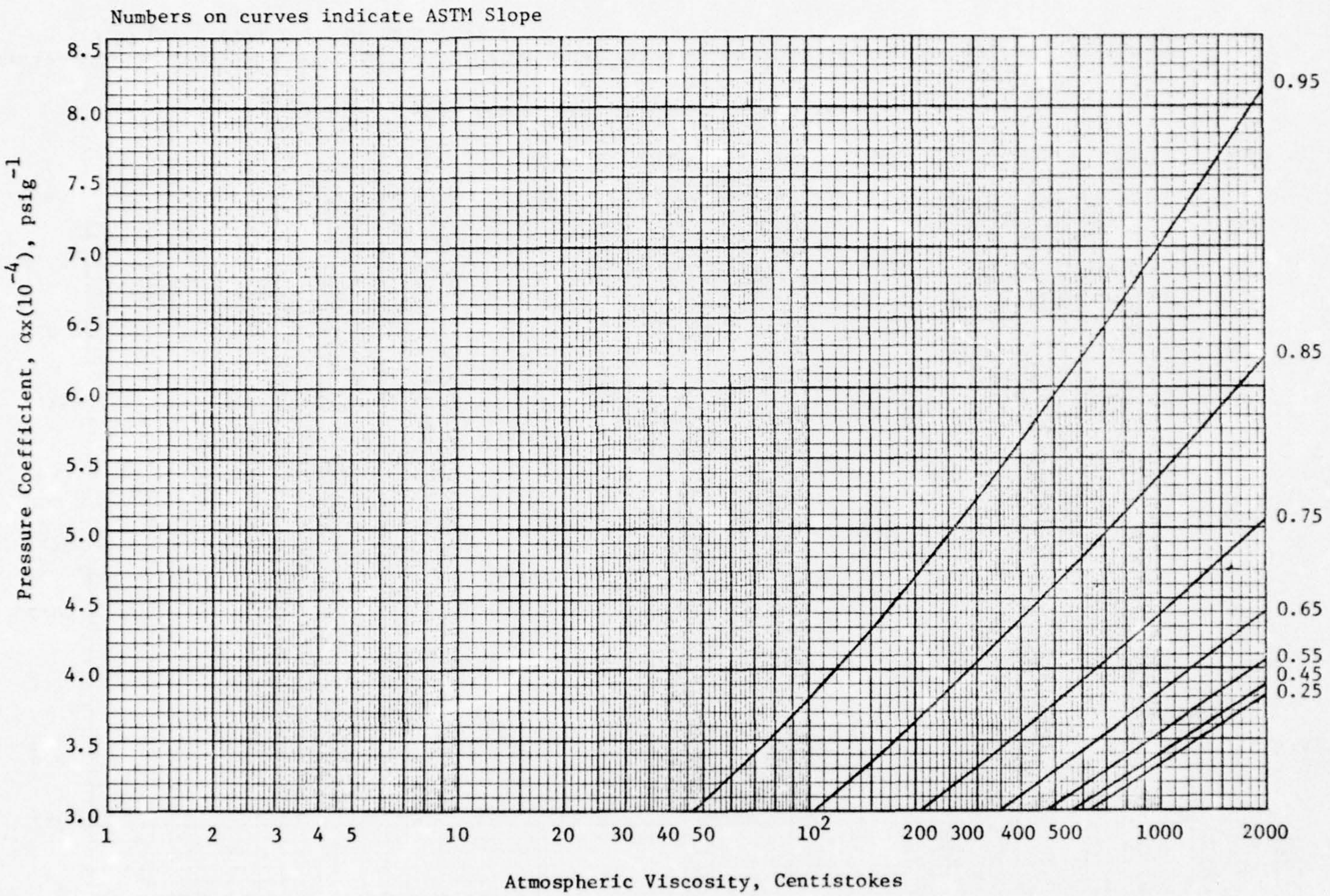

Figure 15. LIQUID PRESSURE COEFFICIENT PREDICTION CHART BASED ON EQUATION [45] AT ATMOSPHERIC DENSITY LEVEL OF 0.75 gm/cc (Concluded)

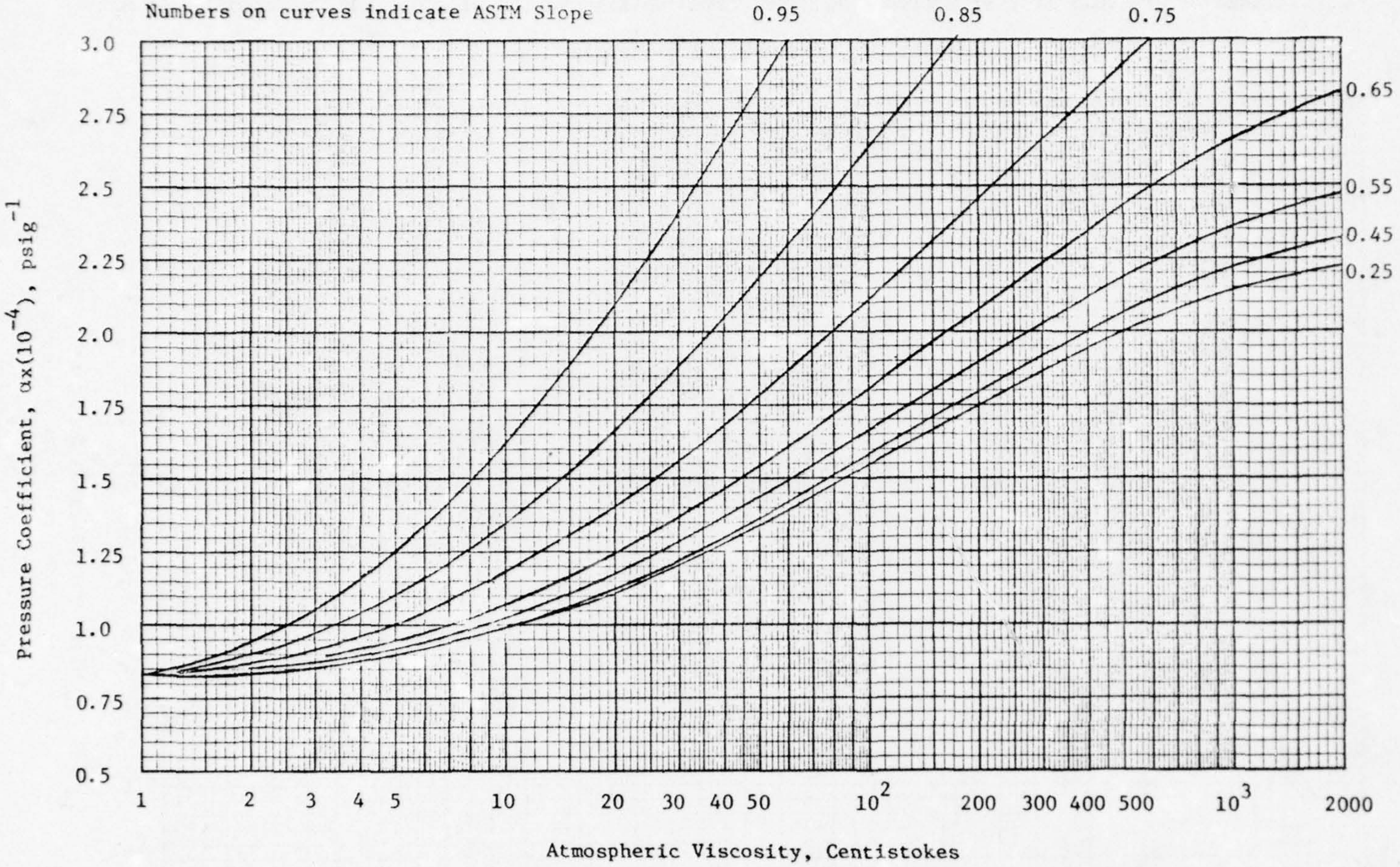

Figure 16. LIQUID PRESSURE COEFFICIENT PREDICTION CHART BASED ON EQUATION [45] AT ATMOSPHERIC DENSITY OF 0.85 gm/cc (Concluded on next page.)

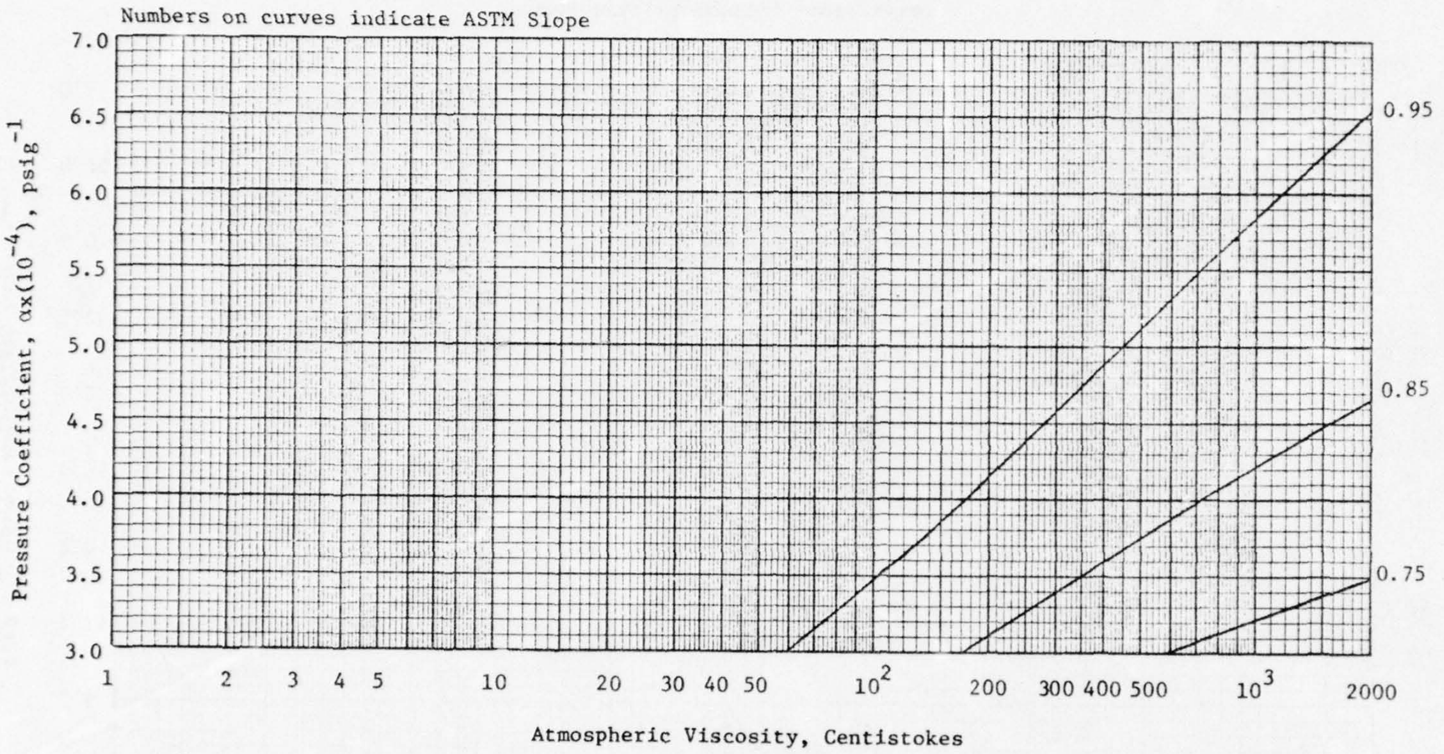

Figure 16. LIQUID PRESSURE COEFFICIENT PREDICTION CHART BASED ON EQUATION [45] AT ATMOSPHERIC DENSITY LEVEL OF 0.85 gm/cc (Concluded.)

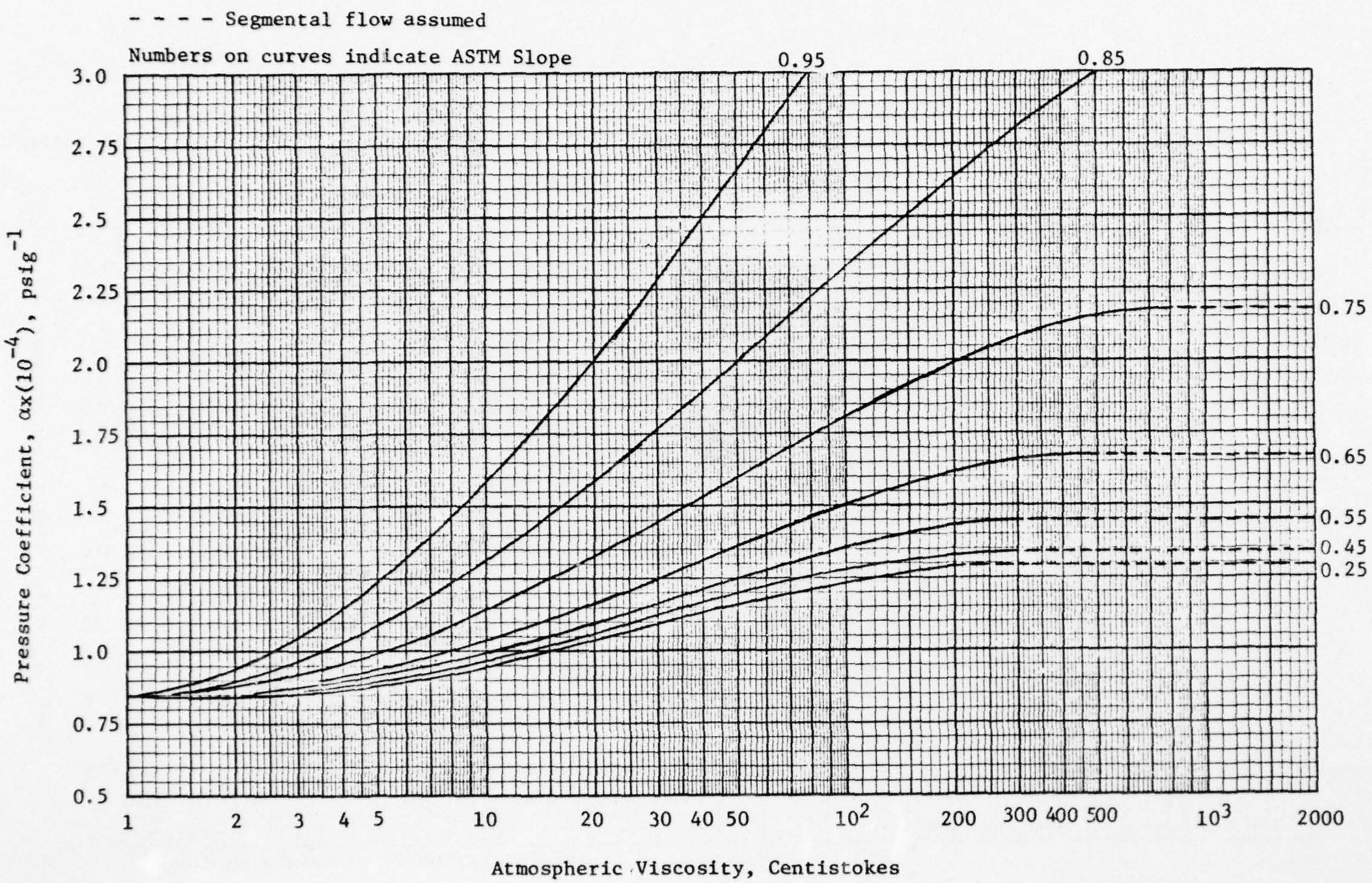

Figure 17. LIQUID PRESSURE COEFFICIENT PREDICTION CHART BASED ON EQUATION [45] AT ATMOSPHERIC DENSITY LEVEL OF 0.95 gm/cc (Concluded on next page.)

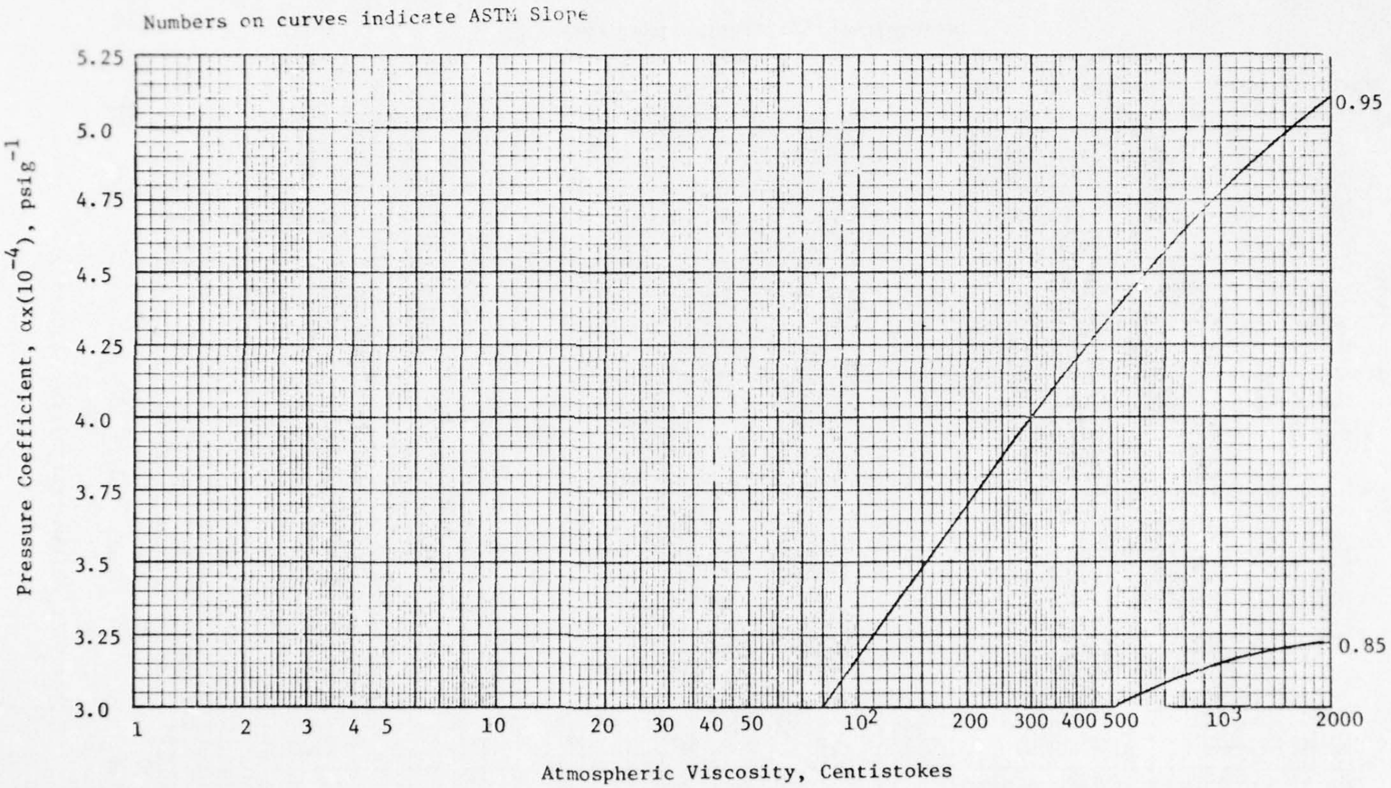

Figure 17. LIQUID PRESSURE COEFFICIENT PREDICTION CHART BASED ON EQUATION [45] AT ATMOSPHERIC DENSITY LEVEL OF 0.95 gm/sec (Concluded)

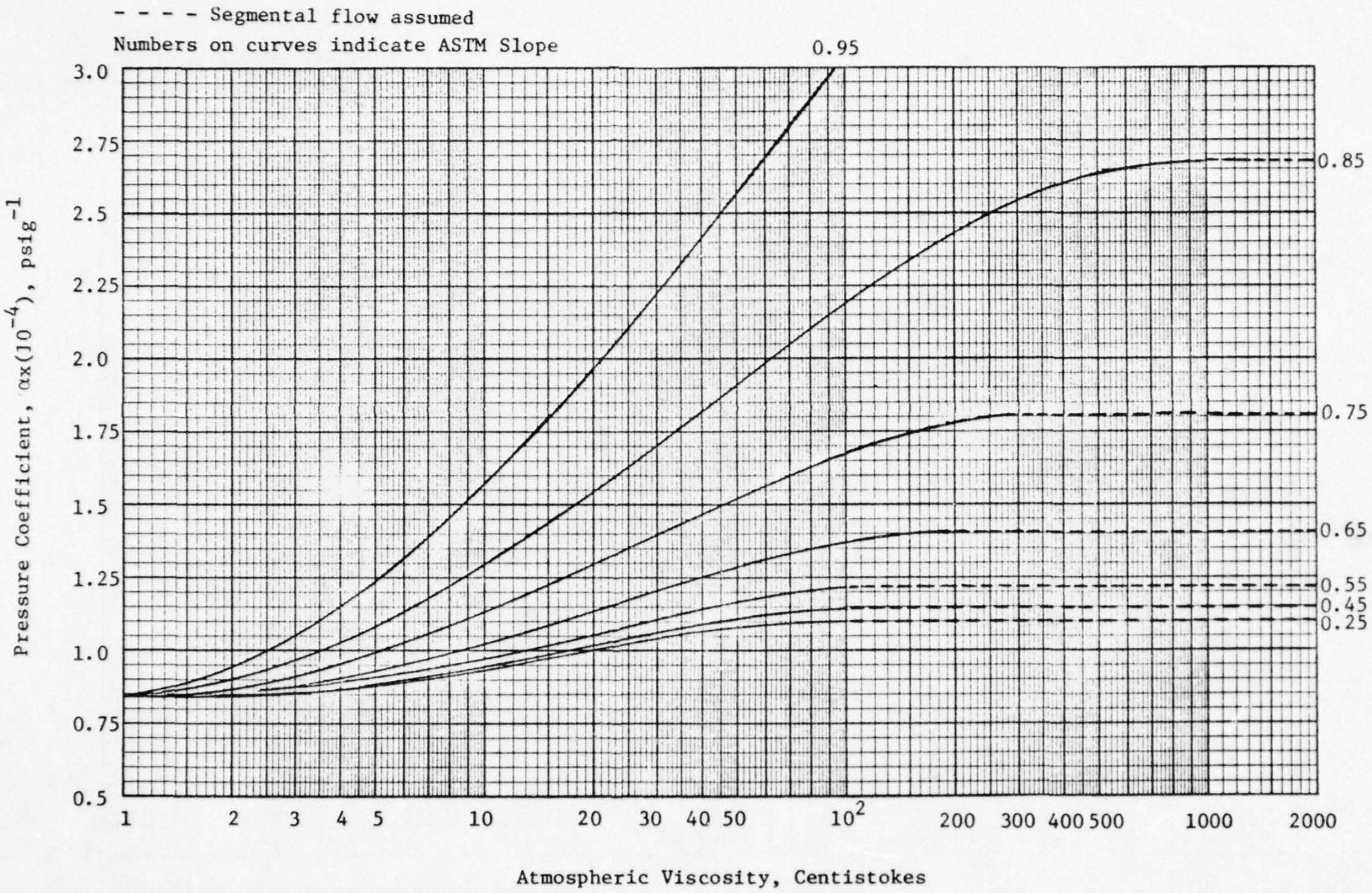

Figure 18. LIQUID PRESSURE COEFFICIENT PREDICTION CHART BASED ON EQUATION [45] AT ATMOSPHERIC DENSITY LEVEL OF 1.00 gm/cc (Concluded on next page.)

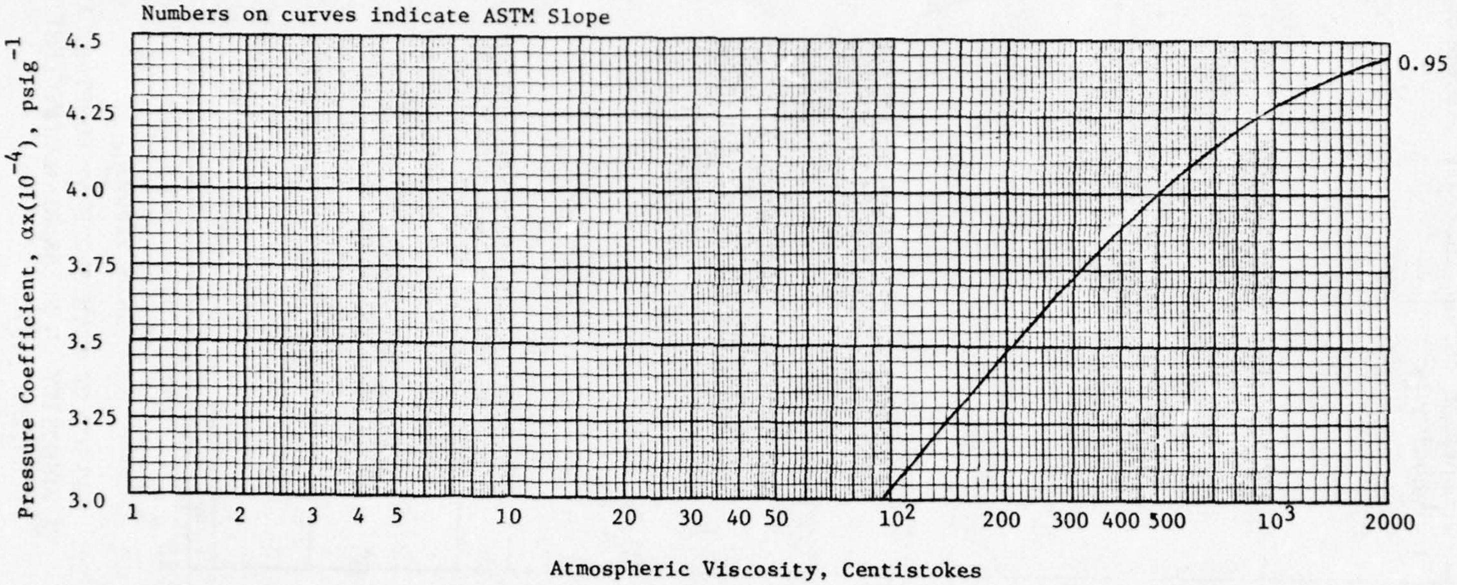

Figure 18. LIQUID PRESSURE COEFFICIENT PREDICTION CHART BASED ON EQUATION [45] AT ATMOSPHERIC DENSITY LEVEL OF 1.00 gm/cc (Concluded)

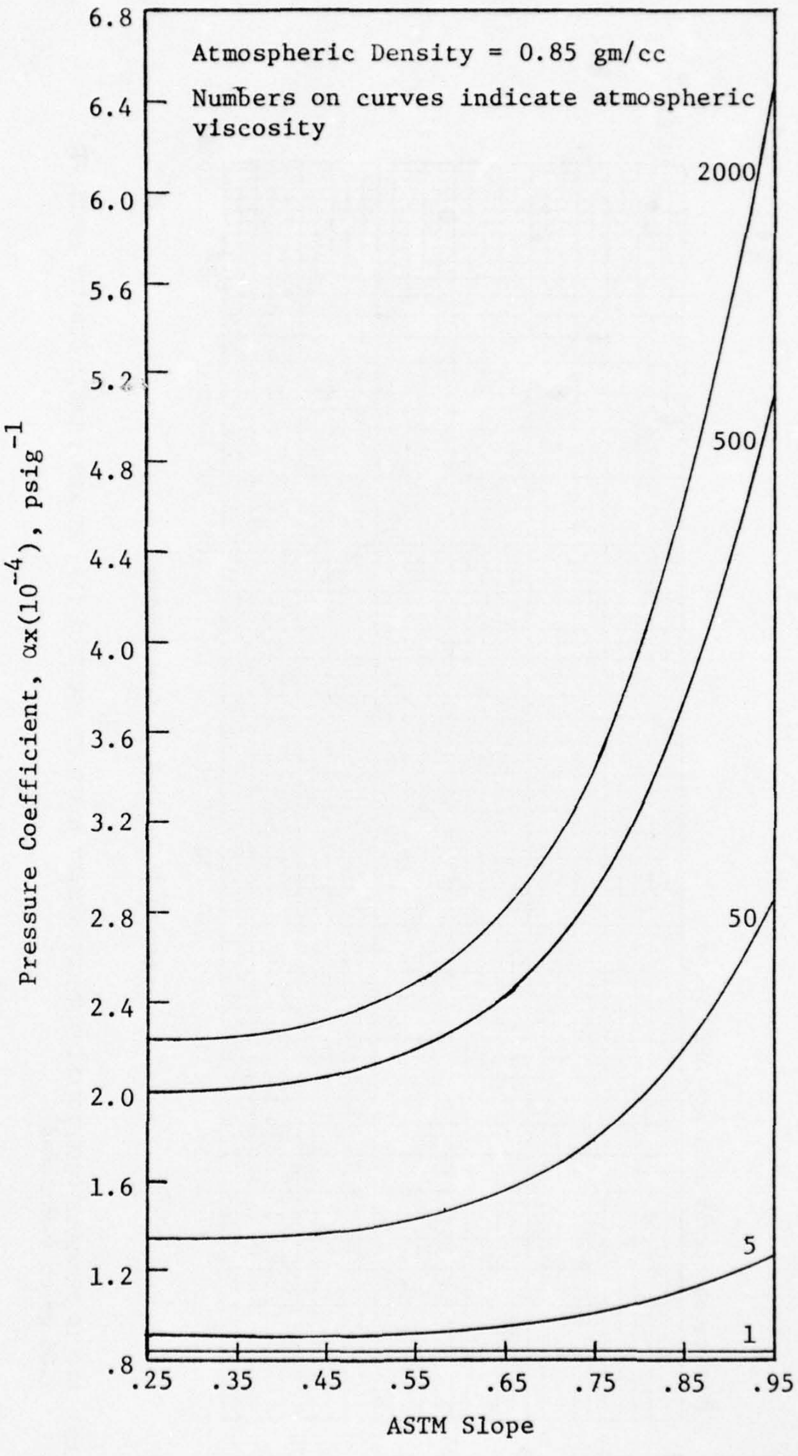

Figure 19. EFFECT OF ASTM SLOPE AT CONSTANT ATMOSPHERIC VISCOSITY ON PRESSURE COEFFICIENT BASED EQUATION [45]

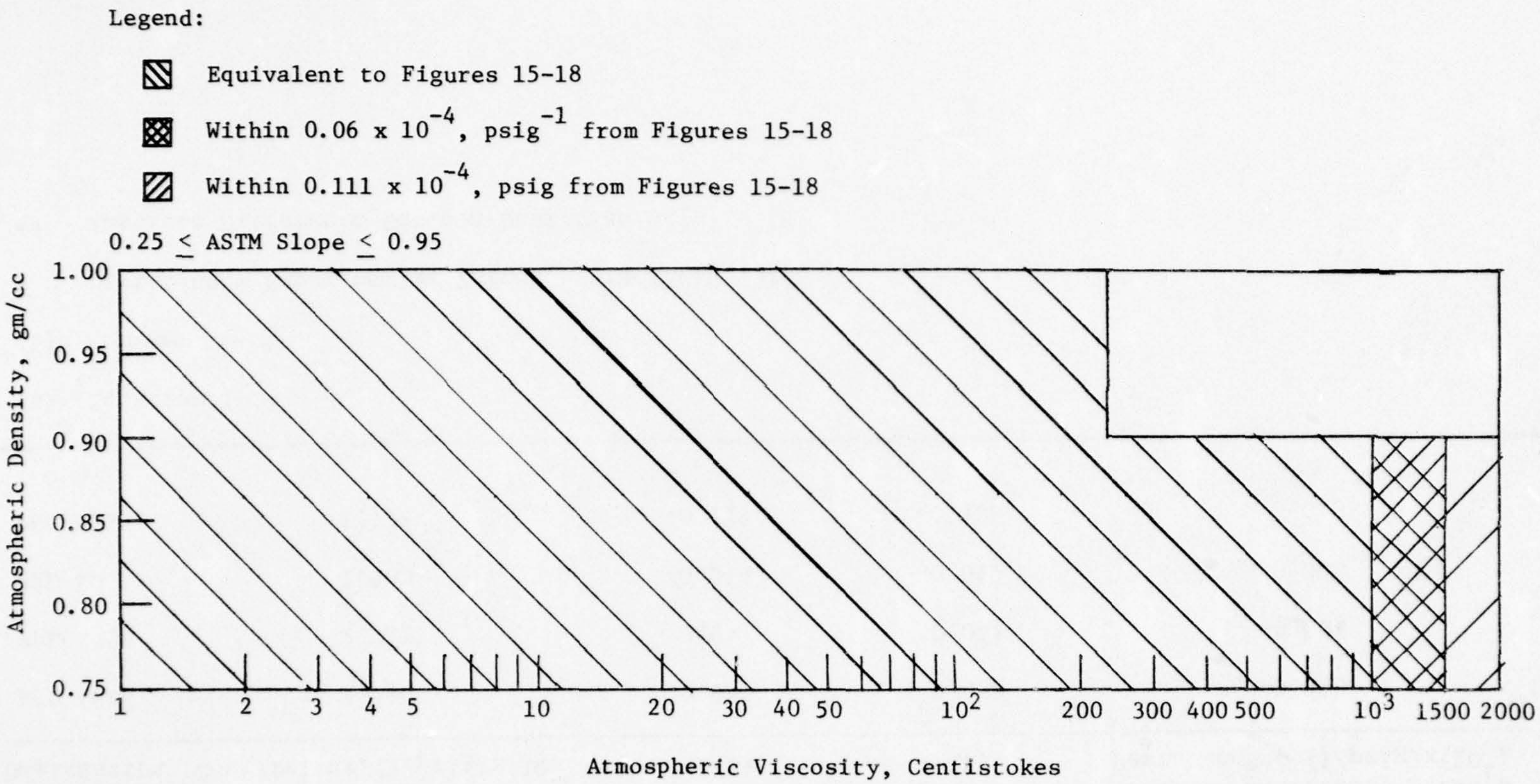

Figure 20. OPERATIONAL REGIONS OF EQUATION [45]

Table 14

COMPARISON OF EQUATION [45] AND FIGURES 15-18

Data Source: AFML-TR-70-304, Part II
Temperature: 100°F

Fluid Designation	Experimental Pressure Coefficient, (1/psig) x(10^{-4})	Deviation*, (1/psig) x(10^{-4}) (a)	Deviation*, (1/psig) x(10^{-4}) (b)	Absolute Difference Between Deviation**, (1/psig) x(10^{4})
PRL 4028	1.590	0.047	-0.050	-0.003
PRL 4038	2.028	0.047	0.048	-0.001
PRL 4042	1.903	-0.014	-0.022	-0.008
PRL 4045	1.759	-0.119	-0.106	0.013

(a) Equation [45]

(b) Figures 15-18

* Deviation = Experimental Values - Predicted Value

** Absolute Difference Between Deviation = $|a| - |b|$

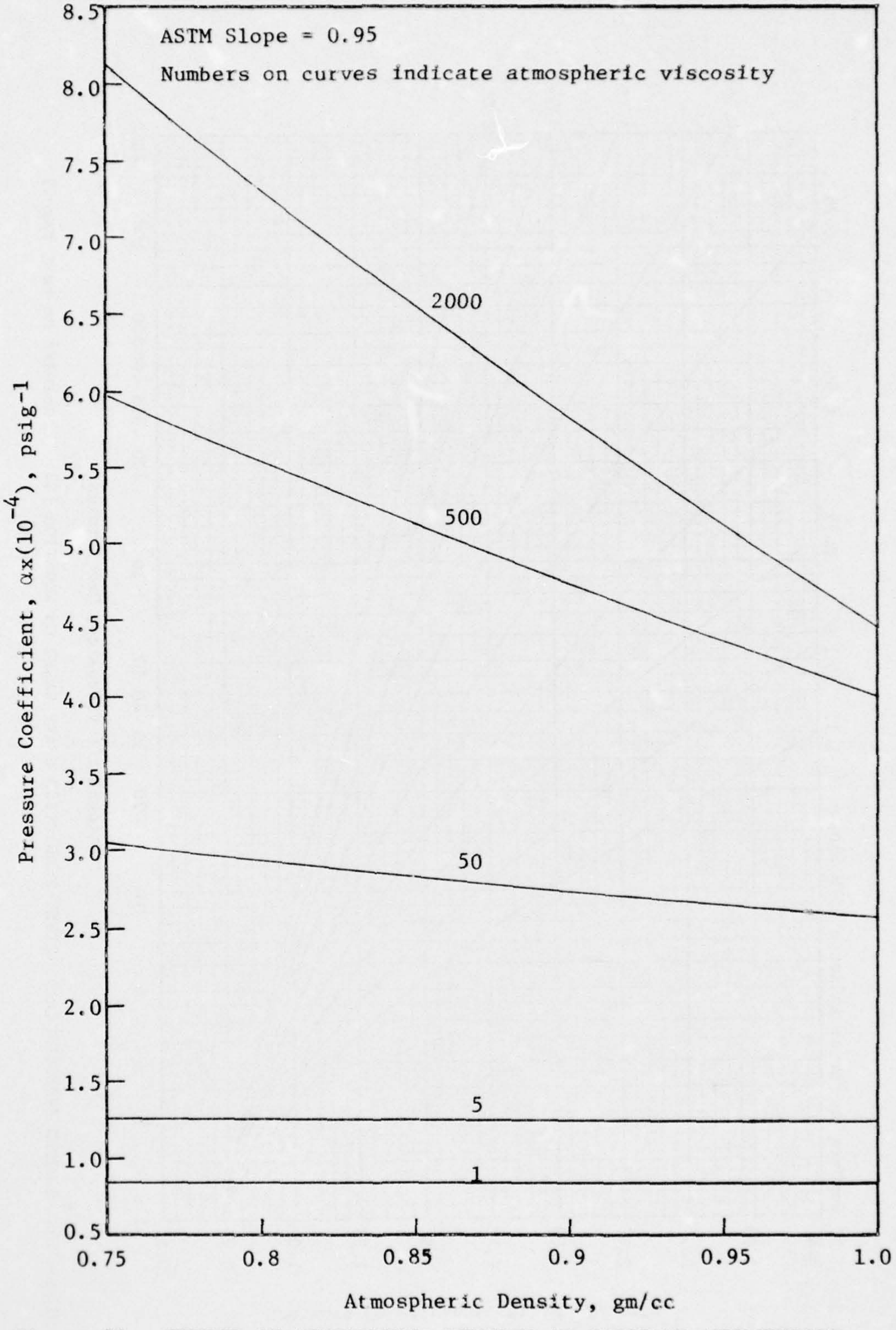

Figure 21. EFFECT OF ATMOSPHERIC DENSITY AT CONSTANT ATMOSPHERIC VISCOSITY AND ASTM SLOPE ON PRESSURE COEFFICIENT BASED ON EQUATION [45]

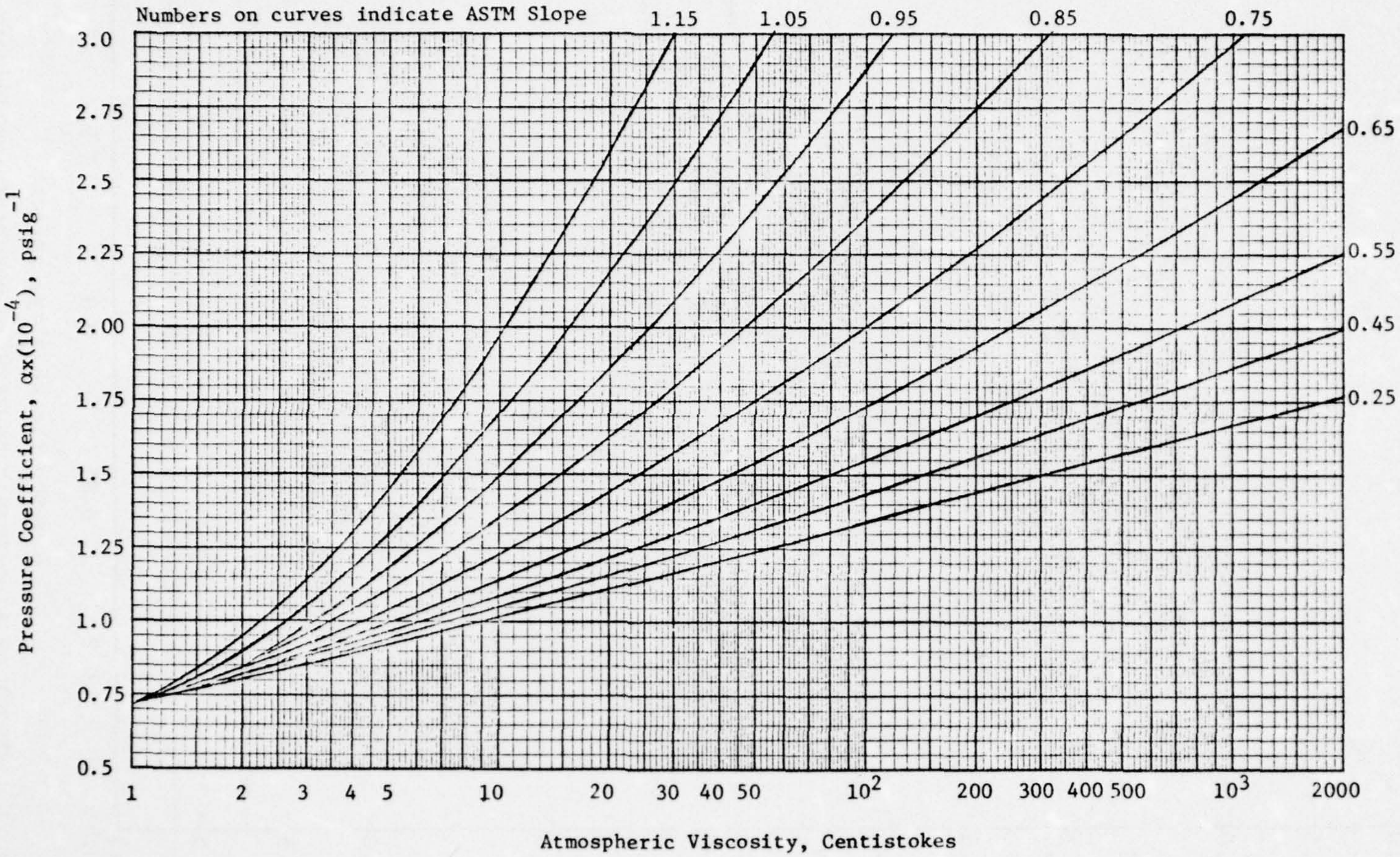

Figure 22. LIQUID PRESSURE COEFFICIENT PREDICTION CHART BASED ON EQUATION [42] (Concluded on next page.)

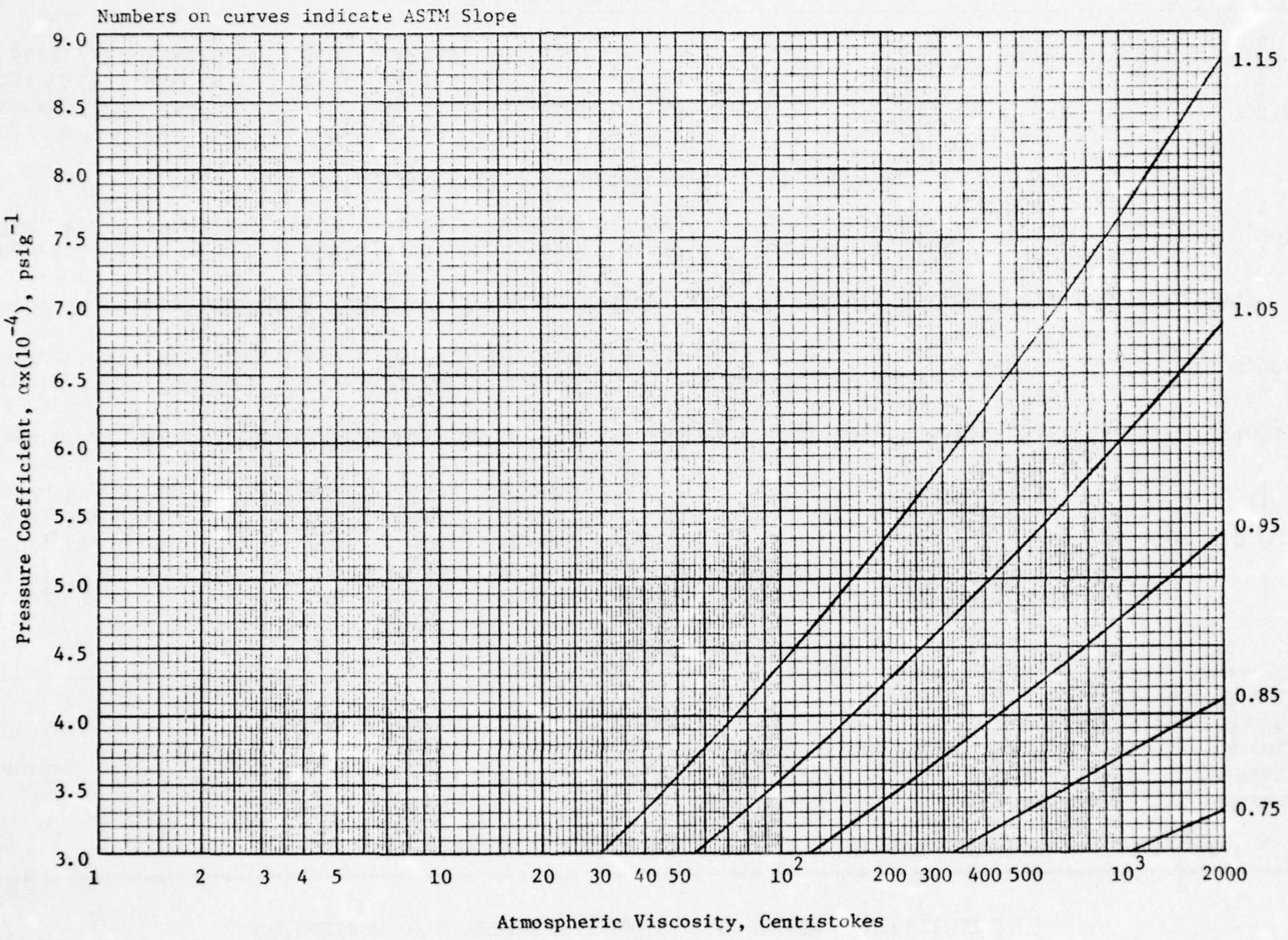

Figure 22. LIQUID-PRESSURE COEFFICIENT PREDICTION CHART BASED ON EQUATION [42] (Concluded)

Table 15

COMPARISON OF EXPERIMENTAL DATA OF DIFFERENT INVESTIGATORS

		Atmospheric Pressure					Pressure Coefficient, (1/psig) x (10^4)			
Data Source	Fluid Designation	Temp., °F	Viscosity, Centistokes	Density, gm/cc	ASTM Slope	Pressure, psig	Reported	Maximum Deviation Among Reported Values	Predicted Values*	Maximum Deviation Among Pred. Values*
Di-2-Ethylhexyl Sebecate										
ASME Report (12)	1A	100	12.45	0.9030	0.701	10,400	1.075	0.086	1.153	0.023
Winer (37)	A	100	12.15	0.9015	0.687	10,000	1.063		1.133	
TR-67-107, Pt. I	MLO 7112	100	12.56	0.9015	0.701	a	1.060		1.156	
TR-70-304, Pt. II	MLO 7710	100	12.57	0.9015	0.700	a	0.989		1.155	
Current Work	MLO 7710	100	12.52	0.9015	0.701	b	1.060		1.155	
Naphthenic Mineral Oil (PRL 2859) + 10.2 Weight % Low Molecular Weight Polymethacrylate (PRL 2906)										
ASME Report (12)	26E	100	33.60	0.8720	0.517	10,400	1.536	0.145	1.265	0.008
TR-70-304, Pt. II	PRL 2913	100	32.96	0.8720	0.539	2	1.391		1.273	
Naphthenic Mineral Oil (PRL 2859) + 4.7 Weight % High Molecular Weight Polymethacrylate (PRL 2905)										
ASME Report (12)	27E	100	32.50	0.8690	0.497	9,640	1.551	0.152	1.251	0.008
TR-70-304, Pt. II	PRL 2914	100	33.26	0.8690	0.503	a	1.399		1.259	
1-Cyclohexyl-3 (2-Cyclohexylethyl) Hendecane										
API Proj. 42 (13)	PSU 19	100	33.53	0.8548	0.793	5,000	1.812	0.003	1.723	0.053
ASME Report (12)	8-C	100	33.95	0.8550	0.807	5,110	1.809		1.776	
API Proj. 42 (13)	PSU 19	210	4.977	0.8158	0.793	5,000	1.322	0.067	1.044	0.009
ASME Report (12)	8-C	210	4.900	0.8170	0.807	7,520	1.255		1.053	

(Concluded on next page.)

Table 15 (Concluded)

		Atmospheric Pressure					Pressure Coefficient, (1/psig) x (10^4)			
Data Source	Fluid Designation	Temp., °F	Viscosity, Centistokes	Density, gm/cc	ASTM Slopes	Pressure, psig	Reported	Maximum Deviation Among Reported Values	Predicted Values*	Maximum Deviation Among Pred. Values*
1-Cyclopentyl-4(3-Cyclopentylpropyl) Dodecane										
API Proj. 42 (13)	PSU 111	100	16.05	0.8469	0.748	5,000	1.281	0.063	1.324	0.023
ASME Report (12)	10-C	100	15.50	0.8460	0.767	7,000	1.344		1.347	
API Proj. 42 (13)	PSU 111	210	3.571	0.8065	0.748	20,000	0.885	0.016	0.746	0.098
ASME Report (12)	10-C	210	3.400	0.8080	0.767	21,300	0.869		0.844	
Oligomer of α Olefins										
TR-67-107, Pt I	MLO 7754	100	79.99	0.8206	0.639	a	1.523	0.088	1.788	0.002
Current Work	MLO 7754	100	80.34	0.8206	0.639	3,000	1.435		1.790	
Di-2-Ethylhexyl Sebacate (MLO 7710) + 32.6 Weight % Low Molecular Wt. Polymethacrylate (AC 307)										
TR-70-304, PtII	PRL 4034	100	226.8	0.9280	0.446	a	1.367	0.125	1.441	0.003
Current Work	PRL 4034	100	229.1	0.9289	0.446	3,000	1.492		1.438	
Napthenic White Oil (MLO 7516) + 12.5 Weight % Polyisobutylene (Paratone Cx 2)										
TR-70-304, PtII	PRL 4053	100	743.8	0.8700	0.477	a	2.389	0.053	1.993	0.059
Current Work	PRL 4053	100	741.3	0.8762	0.477	3,000	2.336		1.934	

* Based on Equation [45]

a Based on Pressure Viscosity Measurements up to 10,000 psig

b Based on Pressure Viscosity Measurements up to 3,000 psig

Table 16

COMPARISON OF EQUATION [45] AND [42] IN PREDICTING PRESSURE COEFFICIENTS USED TO DEVELOP THE EQUATIONS AT ATMOSPHERIC VISCOSITY RANGE OF 1 TO 10 CENTISTOKES

Fluid Designation	Atmospheric Viscosity, cs. 100°F	Atmospheric Density, gm/cc 100°F	ASTM Slope	Experimental Pressure Coefficient, (1/psig)x(10^4)	Deviation*, (1/psig) x (10^4) Equation(45)	Deviation*, (1/psig) x (10^4) Equation(42)
0-266	4.844	0.8159	0.820	1.153	0.089	0.078
MLO 7372	9.902	0.8416	0.800	1.333	0.082	0.054
PRL 2858	8.811	0.8643	0.840	1.359	0.086	0.072
PRL 4046	9.610	0.8340	0.587	1.125	0.086	0.029
PSU 532	2.592	0.7562	0.815	0.949	0.022	0.044
PSU 500	4.551	0.7756	0.866	1.112	0.011	0.025
PSU 25	8.931	0.7905	0.766	1.113	-0.070	-0.097
PSU 516	2.890	0.9860	0.865	0.912	-0.056	-0.038
PSU 503	8.512	0.9375	0.925	1.159	-0.276	-0.229
PSU 87	9.383	0.8441	0.777	1.211	0.015	-0.025
PSU 656	1.975	0.8707	0.902	0.948	0.034	0.090
PSU 657	1.438	0.8484	0.915	0.819	-0.047	0.034
PSU 620	1.874	0.8646	0.795	0.868	-0.007	0.040
PSU 569	2.615	0.8834	0.846	0.942	0.002	0.026
PSU 570	1.810	0.8565	0.843	0.877	-0.005	0.050
PSU 622	2.522	0.8763	0.810	0.930	0.013	0.033
PSU 597	6.851	0.8846	0.773	1.075	-0.017	-0.065
PSU 598	8.549	0.8510	0.730	1.105	-0.005	-0.061
PSU 604	8.911	0.8888	0.857	1.309	0.006	-0.003

* Deviation = Experimental Value - Predicted Value

Table 17

COMPARISON OF EQUATION [45] AND [42] IN PREDICTING PRESSURE COEFFICIENTS USED TO DEVELOP THE EQUATION AT ATMOSPHERIC VISCOSITY RANGE OF 10 TO 100 CENTISTOKES

Fluid Designation	Atmospheric		ASTM Slope	Experimental Pressure Coefficient, (1/psig) x (10^4)	Deviation*, (1/psig) x (10^4)	
	Viscosity, cs. 100°F	Density, gm/cc 100°F			Equation [45]	Equation [42]
MLO 7375	39.34	0.8562	0.748	1.686	0.025	0.030
MLO 7120	99.33	0.8710	0.710	1.770	-0.133	-0.110
PRL 4561	39.32	0.8571	0.734	1.649	0.026	0.023
PRL 4560	45.82	0.8553	0.703	1.482	-0.132	-0.131
PRL 4559	54.61	0.8552	0.659	1.566	-0.024	-0.014
MLO 7519	12.78	0.8250	0.764	1.332	0.046	0.016
MLO 7557	14.00	0.8315	0.783	1.386	0.037	0.016
MLO 7558	20.13	0.8368	0.710	1.413	0.066	0.033
MLO 7516	78.69	0.8765	0.762	1.873	-0.096	-0.072
MLO 7754	79.99	0.8206	0.639	1.523	-0.265	-0.125
MLO 7112	12.56	0.9015	0.701	1.060	-0.096	-0.181
MLO 7684	88.64	0.9575	0.596	1.413	0.037	-0.183
PRL 2924	33.90	0.8630	0.583	1.449	0.123	0.093
PRL 4025	33.09	0.8682	0.499	1.405	0.148	0.129
PRL 4029	34.70	0.8735	0.526	1.413	0.137	0.107
PRL 4033	33.60	0.9110	0.576	1.106	-0.148	-0.240
PRL 4036	34.84	0.8690	0.689	1.473	0.008	-0.033
PRL 4039	34.78	0.8990	0.623	1.163	-0.162	-0.246
PRL 4043	35.29	0.8965	0.521	1.158	-0.088	-0.148
PRL 4047	18.70	0.8360	0.499	1.212	0.063	0.038
PRL 4048	28.56	0.8390	0.462	1.296	0.055	0.069
PRL 4049	55.58	0.8640	0.529	1.525	0.104	0.122
PRL 4050	90.92	0.8645	0.487	1.620	0.088	0.165
PSU 8	15.12	0.8005	0.707	1.199	-0.073	-0.097
PSU 134	25.63	0.8077	0.647	1.186	-0.186	-0.178
PSU 12	18.62	0.9069	0.777	1.396	0.005	-0.060

(Concluded on next page.)

Table 17 (Concluded)

Fluid Designation	Atmospheric		ASTM Slope	Experimental Pressure Coefficient, (1/psig) x (10^4)	Deviation*, (1/psig) x (10^4)	
	Viscosity, cs. 100°F	Density, gm/cc 100°F			Equation [45]	Equation [42]
PSU 18	12.61	0.9094	0.803	1.124	-0.186	-0.239
PSU 113	25.68	0.8774	0.751	1.507	0.034	-0.012
PSU 19	33.53	0.8548	0.793	1.812	0.087	0.112
PSU 111	16.05	0.8469	0.748	1.281	-0.044	-0.084
PSU 88	14.73	0.8216	0.772	1.381	0.028	0.010
PSU 110	11.53	0.8178	0.759	1.088	-0.158	-0.190
PSU 638	13.86	0.9389	0.879	1.320	-0.206	-0.203
PSU 639	16.76	0.9098	0.839	1.566	0.061	0.040
PSU 640	10.99	0.8641	0.810	1.455	0.159	0.130
PSU 613	12.49	0.9209	0.881	1.379	-0.114	-0.103
PSU 614	14.83	0.8967	0.857	1.458	-0.055	-0.052
PSU 615	15.28	0.8639	0.885	1.640	0.004	0.063

* Deviation = Experimental Value - Predicted Value

AD-A031 621 PENNSYLVANIA STATE UNIV UNIVERSITY PARK PETROLEUM RE--ETC F/G 11/8
FLUIDS, LUBRICANTS, FUELS AND RELATED MATERIALS. PART II.(U)
OCT 75 E E KLAUS, E J TEWKSBURY, B Y SO F33615-73-C-5101
UNCLASSIFIED AFML-TR-74-201-PT-2 NL

2 OF 3
AD
A031621

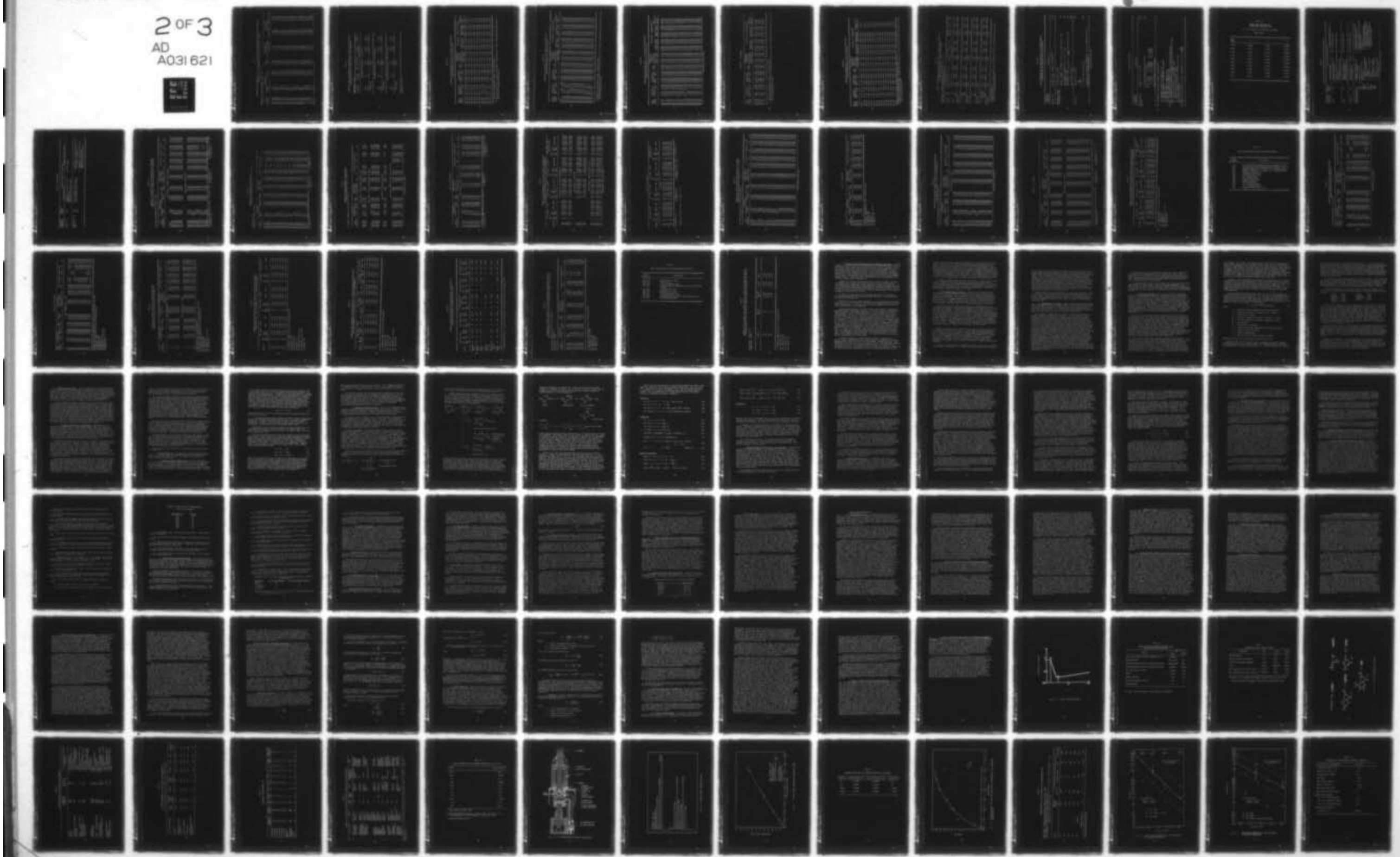

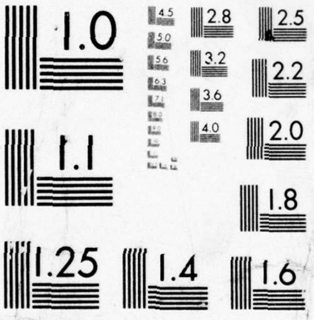
1.0
4.5
5.0
5.6
6.3
7.1
2.8
3.2
3.6
4.0
2.5
2.2
2.0
1.1
1.8
1.25
1.4
1.6

Table 18

COMPARISON OF EQUATIONS [45] AND [42] IN PREDICTING PRESSURE COEFFICIENTS USED TO DEVELOP THE EQUATION AT ATMOSPHERIC VISCOSITY RANGE 100 TO 2,000 CS.

Atmospheric Viscosity Range: 100 to 2,000 cs.

Fluid Designation	Atmospheric Viscosity, cs. 100°F	Atmospheric Density, gm/cc 100°F	ASTM Slope	Experimental Pressure Coefficient, (1/psig)x(10^4)	Deviation,* (1/psig)x(10^4) Equation [45]	Deviation,* (1/psig)x(10^4) Equation [42]
PRL 2906	1293.	0.9090	0.366	1.574	0.075	-0.218
PRL 2924A	223.19	0.8625	0.432	1.767	0.008	0.205
PRL 2924B	1984.	0.8650	0.361	1.973	-0.060	0.116
PRL 4027	227.0	0.8770	0.330	1.514	-0.142	0.026
PRL 4028	1917.	0.8980	0.280	1.590	0.047	-0.193
PRL 4032	227.4	0.8920	0.397	1.579	-0.018	0.046
PRL 4034	226.8	0.9280	0.446	1.367	-0.074	-0.213
PRL 4037	222.9	0.8750	0.597	1.862	-0.015	0.032
PRL 4038	1875.	0.8840	0.548	2.028	0.047	-0.211
PRL 4041	225.7	0.8920	0.558	1.547	-0.181	-0.202
PRL 4042	1915.	0.8865	0.536	1.903	-0.014	-0.303
PRL 4044	224.7	0.8860	0.409	1.541	-0.089	0.000
PRL 4045	1628.	0.8770	0.359	1.759	-0.119	-0.023
PRL 4051	232.7	0.8695	0.601	2.223	0.298	0.373
PRL 4052	460.4	0.8692	0.524	2.305	0.333	0.462
PRL 4053	743.8	0.8700	0.477	2.389	0.396	0.537
PRL 4054	493.1	0.8670	0.537	1.911	-0.112	0.025
PRL 4055	1014.	0.8650	0.466	2.003	-0.070	0.109
MLO 7246	438.2	0.8756	0.640	1.988	-0.178	-0.155
MLO 7661	146.4	0.8567	0.676	1.767	-0.239	-0.145
MLO 7094	480.6	0.8743	0.633	1.875	-0.301	-0.271
MLO 7123	124.4	0.8374	0.734	2.473	0.272	0.442
MLO 7124	115.7	0.8285	0.728	2.473	0.300	0.488
PSU 122	817.0	0.9204	0.884	3.813	-0.037	-0.065

*Deviation = Experimental Value - Predicted Value.

Table 19

SUMMARY OF THE COMPARISONS OF EQUATIONS [45] AND [42] IN PREDICTING PRESSURE COEFFICIENTS USED TO DEVELOP THE EQUATIONS

Temperature: 100°F

Equation	No. of Fluids	Avg. Abs. Dev.*,	Bias*,	RMS*,
		- - - - - - - -	(1/psig)x(10^4)	- - - - - - - -
Atmospheric Viscosity: 1 to 10 CS.				
[45]	19	0.049	-0.002	0.079
[42]	19	0.057	0.003	0.074
Difference		-0.008		
Atmospheric Viscosity: 10 to 100 CS.				
[45]	38	0.092	-0.022	0.111
[42]	38	0.102	-0.040	0.124
Difference		-0.010		
Atmospheric Viscosity: 100 to 2,000 CS.				
[45]	24	0.143	0.005	0.184
[42]	24	0.202	0.036	0.256
Difference		-0.059		

*Defined in Table 11.

Table 20

COMPARISON OF EQUATIONS [45], [42] AND [49] IN PREDICTING PRESSURE COEFFICIENTS AT 32°F AND 100°F

Fluid Designation	Atmospheric Viscosity, cs.		Atmospheric Density, gm/cc		ASTM Slope	Experimental Pressure Coefficient, (1/psig)x(10^4)		Deviation*, (1/psig) x (10^4)				
								Equation [45]		Equation [42]		Equation [49]**
	32°F	100°F	32°F	100°F		32°F	100°F	32°F	100°F	32°F	100°F	32°F
MLO 7372	51.19	9.902	0.8663	0.8416	0.800	1.764	1.333	-0.174	0.082	-0.123	0.054	0.341
MLO 7375	377.8	39.34	0.8807	0.8562	0.748	2.464	1.686	-0.090	0.025	-0.063	0.030	0.574
PRL 4559	485.7	54.61	0.8797	0.8552	0.659	2.018	1.566	-0.205	-0.024	-0.222	-0.014	0.208
PRL 2924	219.5	33.90	0.8880	0.8630	0.583	2.030	1.449	0.249	0.123	0.236	0.093	0.521
PRL 4025	180.3	33.09	0.8923	0.8682	0.499	1.924	1.405	0.313	0.148	0.322	0.129	0.493
PRL 4036	314.3	34.84	0.8910	0.8690	0.689	1.992	1.473	-0.153	0.008	-0.215	-0.033	0.325
PRL 4046	34.62	9.610	0.8580	0.8340	0.587	1.383	1.125	0.041	0.086	0.019	0.029	0.200
PRL 4047	70.50	18.70	0.8600	0.8360	0.499	1.536	1.212	0.058	0.063	0.117	0.038	0.502
PRL 4048	120.0	28.56	0.8630	0.8390	0.462	1.810	1.296	0.209	0.055	0.329	0.069	0.396
PRL 4049	425.5	55.58	0.880	0.8640	0.529	2.044	1.525	0.217	0.104	0.208	0.122	0.427

* Deviation = Experimental Value - Predicted Value

** Equation [45] was used to predict the pressure coefficients at 100°F, and Equation [49] was used to correct for the temperature effects.

Table 21

COMPARISON OF EQUATION [45], [42], AND [49] IN PREDICTING PRESSURE COEFFICIENTS AT 130°F and 100°F.

Fluid Desig-nation	Atmospheric Viscosity, cs.		Atmospheric Density, gm/cc		ASTM Slope	Experimental Pressure Coefficient, (1/psig)x(10^4)		Deviation*, (1/psig)x(10^4)				
								Equation 45		Equation [42]		Equa-tion [49]**
	130°F	100°F	130°F	100°F		130°F	100°F	130°F	100°F	130°F	100°F	130°F
0 266	3.319	4.844	0.8047	0.8159	0.820	1.076	1.153	0.101	0.089	0.107	0.078	0.066
MLO 7372	6.114	9.902	0.8306	0.8416	0.800	1.185	1.333	0.081	0.082	0.056	0.054	-0.002
MLO 7375	19.97	39.34	0.8454	0.8562	0.748	1.522	1.686	0.118	0.025	0.089	0.030	-0.024
MLO 7120	44.67	99.33	0.8604	0.8710	0.710	1.698	1.770	0.086	-0.133	0.078	-0.110	-0.109
MLO 7246	170.5	438.2	0.8647	0.8756	0.640	1.824	1.988	-0.111	-0.178	-0.038	-0.155	-0.230
PRL 4559	28.48	54.61	0.8443	0.8552	0.659	1.381	1.566	-0.000	-0.024	-0.025	-0.014	-0.129
MLO 7557	8.200	14.00	0.8204	0.8315	0.783	1.250	1.386	0.080	0.037	0.049	0.016	-0.030
MLO 7112	7.900	12.56	0.8910	0.9015	0.701	0.978	1.060	-0.075	-0.096	-0.145	-0.181	-0.119
PRL 4036	18.68	34.84	0.8580	0.8690	0.689	1.386	1.473	0.111	0.008	0.053	-0.033	-0.004
PRL 4046	6.660	9.610	0.8215	0.8340	0.587	1.074	1.125	0.098	0.086	0.047	0.029	0.088
PRL 4047	12.60	18.70	0.8250	0.8360	0.499	1.136	1.212	0.069	0.063	0.031	0.038	0.045
PRL 4048	18.92	28.56	0.8280	0.8390	0.462	1.212	1.296	0.065	0.055	0.054	0.069	0.033
PRL 4049	31.87	55.58	0.8540	0.8640	0.529	1.438	1.525	0.146	0.104	0.132	0.122	0.089
PRL 4050	51.04	90.92	0.8540	0.8645	0.487	1.571	1.620	0.180	0.088	0.224	0.165	0.117
PRL 4051	101.5	232.7	0.8600	0.8695	0.601	1.943	2.223	0.246	0.298	0.305	0.373	0.116
PRL 4052	199.6	460.4	0.8600	0.8692	0.524	2.028	2.305	0.217	0.333	0.367	0.462	0.156
PRL 4053	322.4	743.8	0.8600	0.8700	0.477	2.022	2.389	0.123	0.396	0.336	0.537	0.110
PRL 4054	211.4	493.1	0.8500	0.8670	0.537	1.843	1.911	-0.050	-0.112	0.148	0.025	-0.077
PRL 4055	434.1	1014.	0.8550	0.8650	0.466	1.938	2.003	-0.063	-0.070	0.210	0.109	-0.029

* Deviation = Experimental Value - Predicted Value

** Equation [45] was used to predict the pressure coefficients at 100°F and Equation 49 was used to correct for the temperature effects

Table 22

COMPARISON OF EQUATIONS [45], [42] AND [49] IN PREDICTING PRESSURE COEFFICIENTS AT 140°F AND 100°F

Fluid Designation	Atmospheric Viscosity, cs.		Atmospheric Density, gm/cc		ASTM Slope	Experimental Pressure Coefficient, (1/psig)x(10^4)		Deviation*, (1/psig)x(10^4)				
								Equation [45]		Equation [42]		Equation [49]**
	140°F	100°F	140°F	100°F		140°F	100°F	140°F	100°F	140°F	100°F	140°F
PSU 500	2.800	4.551	0.7606	0.7756	0.866	0.948	1.112	-0.021	0.011	0.007	0.025	-0.079
PSU 25	5.038	8.931	0.7761	0.7905	0.766	1.025	1.113	-0.004	-0.070	-0.027	-0.097	-0.079
PSU 8	8.077	15.120	0.7862	0.8005	0.707	1.057	1.199	-0.035	-0.073	-0.076	-0.097	-0.131
PSU 134	12.980	25.630	0.7938	0.8077	0.647	1.124	1.186	-0.042	-0.186	-0.076	-0.178	-0.157
PSU 516	1.899	2.890	0.9690	0.9860	0.865	0.822	0.912	-0.072	-0.056	-0.020	-0.038	-0.082
PSU 503	4.384	8.512	0.9215	0.9375	0.925	1.005	1.159	-0.150	-0.276	-0.114	-0.229	-0.335
PSU 12	8.871	18.620	0.8917	0.9069	0.777	1.226	1.396	0.062	0.005	0.007	-0.060	-0.072
PSU 18	6.459	12.610	0.8949	0.9094	0.803	1.049	1.124	-0.061	-0.186	-0.099	-0.239	-0.174
PSU 87	5.243	9.383	0.8296	0.8441	0.777	1.045	1.211	0.005	0.015	-0.024	-0.025	-0.071
PSU 113	11.770	25.680	0.8635	0.8774	0.751	1.312	1.507	0.092	0.034	0.036	-0.012	-0.063
PSU 19	13.940	33.530	0.8405	0.8548	0.793	1.550	1.812	0.189	0.087	0.168	0.112	-0.060
PSU 111	8.156	16.050	0.8324	0.8469	0.748	1.144	1.281	0.022	-0.044	-0.024	-0.084	-0.092
PSU 88	7.486	14.730	0.8068	0.8216	0.772	1.205	1.381	0.072	0.028	0.040	0.010	-0.058
PSU 110	6.215	11.530	0.8029	0.8178	0.759	0.963	1.088	-0.106	-0.158	-0.139	-0.190	-0.200
PSU 122	133.5	817.000	0.9067	0.9204	0.884	2.895	3.813	0.005	-0.037	0.192	-0.065	0.699
PSU 656	1.396	1.975	0.8525	0.8707	0.902	0.881	0.948	0.020	0.034	0.103	0.090	0.028
PSU 657	1.060	1.438	0.8299	0.8484	0.915	0.806	0.819	-0.034	-0.047	0.075	0.034	0.003
PSU 620	1.369	1.874	0.8475	0.8646	0.795	0.831	0.868	-0.019	-0.007	0.062	0.040	0.014
PSU 569	1.812	2.615	0.8665	0.8834	0.846	0.946	0.942	0.063	0.002	0.117	0.026	0.069
PSU 570	1.235	1.810	0.8399	0.8565	0.843	0.874	0.877	0.028	-0.005	0.120	0.050	0.051
PSU 622	1.778	2.522	0.8606	0.8763	0.811	0.868	0.930	-0.005	0.013	0.049	0.033	0.012
PSU 597	4.025	6.851	0.8695	0.8846	0.773	0.989	1.075	0.012	-0.017	-0.009	-0.065	-0.030
PSU 598	4.880	8.549	0.8361	0.8510	0.730	1.018	1.105	0.030	-0.005	-0.006	-0.061	-0.018
PSU 604	4.796	8.911	0.8737	0.8888	0.857	1.177	1.309	0.081	0.006	0.079	-0.003	-0.039

(Concluded on next page.)

Table 22 (Concluded)

Fluid Desig-nation	Atmospheric Viscosity, cs.		Atmospheric Density, gm/cc		ASTM Slope	Experimental Pressure Coefficient, (1/psig)x(10^4)		Deviation*, (1/psig)x(10^4)				
								Equation [45]		Equation [42]		Equation [49]**
	140°F	100°F	140°F	100°F		140°F	100°F	140°F	100°F	140°f	100°F	140°F
PSU 638	6.697	13.860	0.9243	0.9389	0.879	1.078	1.320	-0.154	-0.206	-0.154	-0.203	-0.346
PSU 639	7.798	16.760	0.8951	0.9098	0.839	1.137	1.566	-0.082	0.061	-0.106	0.040	-0.267
PSU 640	5.742	10.990	0.8499	0.8641	0.810	1.275	1.455	0.180	0.159	0.157	0.130	0.065
PSU 613	6.083	12.490	0.9058	0.9209	0.881	1.187	1.379	-0.017	-0.114	-0.012	-0.103	-0.208
PSU 614	7.133	14.830	0.8818	0.8967	0.857	1.301	1.458	0.077	-0.055	0.069	-0.052	-0.112
PSU 615	7.040	15.280	0.8494	0.8639	0.885	1.364	1.640	0.086	0.004	0.106	0.063	-0.163

* Deviation = Experimental Value - Predicted Value

** Equation [45] was used to predict the pressure coefficient at 100°F, and equation 49 was used to correct for the temperature effects.

Table 23

COMPARISON OF EQUATION [45], [42], AND [49] IN PREDICTING PRESSURE COEFFICIENTS AT 275°F AND 100°F

Fluid Desig-nation	Atmospheric Viscosity, cs.		Atmospheric Density, gm/cc		ASTM Slope	Experimental Pressure Coefficient, (1/psig)x(10^4)		Deviation,* (1/psig)x10^4				
	275°F	100°F	275°F	275°F		275°F	100°F	Equation [45] 275°F	Equation [45] 100°F	Equation [42] 275°F	Equation [42] 100°F	Equation [49] 275°F
PSU 8	2.167	15.12	0.7385	0.8005	0.707	0.820	1.199	-0.053	-0.073	-0.025	-0.097	-0.150
PSU 134	3.172	25.63	0.7471	0.8077	0.647	0.845	1.186	-0.053	-0.186	-0.060	-0.178	-0.2
PSU 503	1.324	8.512	0.8684	0.9375	0.925	0.675	1.159	-0.183	-0.276	-0.094	-0.229	-0.419
PSU 12	2.163	18.62	0.8415	0.9069	0.777	0.892	1.396	0.006	0.005	0.037	-0.060	-0.167
PSU 87	1.581	9.383	0.7781	0.8441	0.777	0.879	1.211	0.021	0.015	0.085	-0.025	-0.032
PSU 113	2.615	25.68	0.8145	0.8774	0.751	0.967	1.507	0.065	0.034	0.077	-0.012	-0.155
PSU 19	2.611	33.53	0.7928	0.8548	0.793	1.096	1.812	0.179	0.087	0.196	0.112	-0.218
PSU 88	1.928	14.73	0.7574	0.8216	0.772	0.947	1.381	0.073	0.028	0.116	0.010	-0.084
PSU 110	1.830	11.53	0.7539	0.8178	0.759	0.792	1.088	-0.075	-0.158	-0.028	-0.190	-0.157
PSU 597	1.369	6.851	0.8182	0.8846	0.773	0.894	1.075	0.046	-0.017	0.126	-0.065	0.062
PSU 598	1.540	8.549	0.7856	0.8510	0.730	0.930	1.105	0.078	-0.005	0.144	-0.061	0.084
PSU 604	1.363	8.911	0.8217	0.8888	0.857	1.026	1.309	0.172	0.006	0.255	-0.003	0.033
PSU 613	1.509	12.49	0.8550	0.9209	0.881	0.959	1.379	0.092	-0.114	0.166	-0.103	-0.178
PSU 614	1.708	14.83	0.8312	0.8967	0.857	1.034	1.458	0.156	-0.055	0.217	-0.052	-0.119
PSU 615	1.626	15.28	0.7996	0.8639	0.885	1.096	1.640	0.218	0.004	0.287	0.063	-0.151

* Deviation = Experimental Value - Predicted Value

** Equation [45] was used to predict the pressure coefficients at 100°F, and equation [49] was used to correct for the temperature effects.

Table 24

SUMMARY OF THE COMPARISON OF EQUATIONS [45], [42] and [49] IN PREDICTING THE PRESSURE COEFFICIENTS AT VARIOUS TEMPERATURES

Data Source: Current Investigation, AFML-TR-67-107, Part I, AFML-TR-70-304, Pt II and API Project 42 (13).

		Equation [45]			Equation [42]			Equations [45] and [49]**		
No. of Points	Temp., °F	Avg. Abs. Dev.*,	Bias*,	RMS*,	Avg. Abs. Dev.*,	Bias*,	RMS*,	Avg. Abs. Dev.*,	Bias*,	RMS*,
		(1/psig)x(10^4)								
10	32	0.171	0.046	0.190	0.186	0.061	0.210	0.399	0.399	0.417
	100	0.072	0.067	0.084	0.061	0.052	0.072	0.072	0.067	0.084
Difference		0.099			0.125			0.327		
49	130 or 140	0.079	0.034	0.098	0.097	0.053	0.127	0.110	-0.067	0.175
	100	0.087	-0.001	0.125	0.103	0.010	0.151	0.087	-0.001	0.125
Difference		-0.008			-0.006			-0.023		
15	275	0.098	0.049	0.117	0.127	0.100	0.150	0.147	-0.123	0.173
	100	0.071	-0.047	0.106	0.084	-0.059	0.107	0.071	-0.047	0.106
Difference		0.027			0.043			0.076		
74	32, 130 140 or 275	0.095	0.039	0.118	0.115	0.063	0.146	0.157	-0.015	0.223
	100	0.082	-0.001	0.117	0.093	0.001	0.134	0.082	-0.001	0.117
Difference		0.013			0.022			0.075		

*Defined in Table 11

**Equation [45] was used to predict the pressure coefficients at 100°F, and equation [49] was used to correct for the temperature effects

Table 25

VARIOUS METHODS USED IN THE COMPARISON OF THE EFFECTIVENESS IN PREDICTING THE PRESSURE EFFECTS ON VISCOSITY

Developer (Reference)	Correlation	
Kouzel (31)	$\log \frac{\eta_p}{\eta_o} = \frac{p}{1,000} \; (0.0239 + 0.01638 \eta_o^{0.278})$	[8]
Roelands, Vlugter, and Waterman (28)	For non-polymer fluids	
	$\log \frac{\eta_p}{\eta_o} = \left(\frac{p}{5,000}\right)^y \; [(0.002 C_A + 0.003\ C_N + 0.055) \log \eta_o + 0.228]$	[4]
	$\log (y - 0.890) = 0.00955\ (C_A + 1.5\ C_N) - 1.930$	[5]
	For polymer fluids	
	$\log (\log \eta_p + 1.200) = Z_{B1} \log \left(1 + \frac{p}{28,400}\right) + \log (\log \eta_o + 1.200)$	[11]
	$Z_{B1} = 0.6 Z_{or} + 0.4 Z^*_{B1}$	[10]
Fresco (27)	$\log \frac{\mu_p}{\mu_o} = p\ \alpha'^a\ (10^{-4})$	[9]
	$a = \frac{560}{°R}$	
	$\alpha' = A + B \log \mu_o + C (\log \mu_o)^2$	[50]
	A, B, and C are function of ASTM Slope. For its values see Table 26. Graphical method is also available.	

(Concluded on next page.)

Table 25 (Concluded)

Developer (Reference)	Correlation	
AFML-TR-70-304, Part II	$\log \frac{\mu_p}{\mu_o} = p\,(\alpha' + \beta)\,(10^{-4})$	[51]
	α' is calculated from Fresco's Method $\beta = A' \log \mu_r + B' (\log \mu_r)^2$	[52]
	For $T = 100°F$ $A' = 0.02064$ $B' = 0.0763$ $T = 130°F$ $A' = 0.02916$ $B' = 0.0628$ $T = 32°F$ $A' = 0.01670$ $B' = 0.1157$	
	Graphical method is also available	

The variables for the above equations are defined as:

η_p = absolute viscosity at pressure p, cp.
η_o = absolute viscosity at temperature of interest
p = pressure, psig
C_A = per cent carbon in aromatic ring
C_N = per cent carbon in naphthenic ring
Z or Z_{B1} = viscosity-pressure indexes of base oil and blend respectively
Z^*_{B1} = hypothetical viscosity-pressure index of the blend read from the chart
α' = pressure coefficient, α, times $\frac{(10^4)}{2.718}$, 1/psig
β = polymer pressure coefficient, 1/psig
μ_r = ratio of viscosity of blend to viscosity of solvent
log = base 10 logarithm

For polymer and resin blend pressure coefficient, $\alpha = (\alpha' + \beta) \times \frac{(10^4)}{2.718}$

Table 26

COEFFICIENTS FOR FRESCO'S CORRELATION (EQUATION [50])

$\alpha' = A + B \log v_o + C (\log v_o)^2$ At Various

ASTM Slopes

ASTM Slope	A	B	C
0.600	0.0878	0.2187	-0.0009
0.650	0.0578	0.2953	-0.0176
0.700	0.0425	0.3760	-0.0395
0.750	0.0379	0.4519	-0.0626
0.800	0.0546	0.5045	-0.0809
0.850	0.0720	0.5630	-0.1046
0.900	0.0947	0.6319	-0.1368
0.950	0.1064	0.7290	-0.1863
1.000	0.1384	0.8042	-0.2364
1.070	0.1423	1.0490	-0.4186

Table 27

PHYSICAL PROPERTIES REQUIRED FOR THE DIFFERENT CORRELATIONS

Developer (Reference)	Equation Number	Physical Properties Required Non-Polymer Fluids	 Polymer and Resin Fluids
Author	[45]	1) Atmospheric Viscosities at two different temperatures	same as non-polymer fluid
		2) Atmospheric Density at temperature of interest (also need ASTM Slope Table)	same as non-polymer fluid
Author	[42]	Atmospheric Viscosity at two different temperatures (also need ASTM Slope Table)	same as non-polymer fluid
Kouzel (31)	[8]	Atmospheric Viscosity at temperature of interest	same as non-polymer fluid
Roelands, Vlugter and Waterman (28)	[4] and [5] for non-polymer fluid; [10] and [11] for polymer and resin fluid	1) Atmospheric viscosity at two different temperatures 2) Atmospheric density 3) refractive index at 20°C (also need: a) correlation for temperature effects on atmospheric viscosity b) correlation for molecular weight c) correlation for temperature effect on atmospheric density d) n-d-m method of structural group analysis (21))	1) atmospheric viscosity of base oil a two different temperatures 2) Atmospheric viscosity of blend at two different temperature (also need: a) Correlation for temperature effects on atmospheric viscosity b) Correlation to predict viscosity pressure index for base oil c) Correlation to predict viscosity pressure index for blend)

(Concluded on next page.)

Table 27 (Concluded)

Developer (Reference)	Equation Number	Physical Properties Required	
		Non-Poylmer Fluid	Polymer and Resin Fluids
Fresco (27)	[50]	Atmospheric viscosity at two temperatures (Also need ASTM Slope Chart)	Does not apply
AFML-TR-70-304, Part II	[50] and [52]	For non-polymer fluid, this method becomes Fresco's Method	1) Atmospheric viscosity of base oil at two different temperatures 2) Atmospheric viscosity of blend at temperature of interest (Also need ASTM Slope Chart)

Table 28

COMPARISON OF VARIOUS METHODS IN PREDICTING PRL PRESSURE COEFFICIENT DATA FROM CURRENT INVESTIGATION AND FRESCO(27)

For Fluid Description See Table 4 and 5

Fluid Designation	Atmospheric Viscosity, cs. 100°F	Atmospheric Density, gm/cc 100°F	ASTM Slope	Experimental Press. Coeff., (1/psig) x (10^4)	Deviation*, (1/psig) x (10^4) (a)	(b)	(c)	(d)	(e)
				Data Source: Current Investigation					
0-266	4.844	0.8159	0.820	1.153	0.089	0.078	0.117	-0.004	-0.157
MLO 7372	9.902	0.8416	0.800	1.333	0.082	0.054	0.037	-0.067	-0.135
MLO 7375	39.34	0.8562	0.748	1.686	0.025	0.030	0.064	0.041	-0.187
MLO 7120	99.33	0.8710	0.710	1.770	-0.133	-0.110	0.011	-0.166	-0.476
MLO 7246	438.2	0.8756	0.640	1.988	-0.178	-0.155	0.074	-0.136	-1.096
PRL 4561	39.32	0.8571	0.734	1.649	0.026	0.023	0.071	0.014	-0.223
PRL 4560	45.82	0.8553	0.703	1.482	-0.132	-0.131	-0.044	-0.024	-0.446
PRL 4559	54.61	0.8552	0.659	1.566	-0.024	-0.014	0.132	-0.020	-0.428
				Data Source: Fresco (27)					
MLO 7519	12.78	0.8250	0.764	1.332	0.046	0.016	0.038	-0.064	-0.198
MLO 7557	14.00	0.8315	0.783	1.386	0.037	0.016	0.004	-0.066	-0.168
MLO 7558	20.13	0.8368	0.710	1.413	0.066	0.033	0.118	-0.054	-0.242
MLO 7661	146.4	0.8576	0.676	1.767	-0.239	-0.145	0.016	-0.098	-0.665
MLO 7094	480.6	0.8743	0.633	1.875	-0.301	-0.271	-0.039	-0.320	-1.273
PRL 2858	8.811	0.8643	0.840	1.359	0.086	0.072	-0.001	-0.105	-0.083
MLO 7516	78.69	0.8765	0.762	1.873	-0.096	-0.072	0.020	-0.284	-0.271
MLO 7754	79.99	0.8206	0.639	1.523	-0.265	-0.125	0.044	-	-0.623
MLO 7123	124.4	0.8374	0.734	2.473	0.272	0.442	0.590	-	0.124
MLO 7124	115.7	0.8285	0.728	2.473	0.300	0.488	0.625	1.226	0.160
MLO 7112	12.56	0.9015	0.701	1.060	-0.096	-0.181	-0.052	-	-0.472
MLO 7684	88.64	0.9575	0.596	1.413	0.037	-0.183	0.026	-	-0.788

*Deviation = Experimental value - Predicted value
(a) Equation [45]
(b) Equation [42]
(c) Fresco (27)
(d) Roelands, et. al. (23)
(e) Kouzel (26)

Table 29

COMPARISON OF VARIOUS METHODS IN PREDICTING
PRL PRESSURE COEFFICIENT DATA FROM AFML-TR-70-304, Part II

Temperature: 100°F
For Fluid Descriptions See Table 6

Fluid Designation	Atmospheric Viscosity, cs. 100°F	Density, gm/cc 100°F	ASTM Slope	Experimental Press. Coeff., (1/psig) x (10^4)	Deviation*, (1/psig) x (10^4)				
					(a)	(b)	(c)	(d)	(e)
PRL 2906	1293	0.9090	0.366	1.574	0.075	-0.218	-	-	-2.382
PRL 2924	33.90	0.8630	0.583	1.449	0.123	0.093	-0.040	-0.114	-0.373
PRL 2924A	223.19	0.8625	0.432	1.767	0.008	0.205	-	-0.019	-0.893
PRL 2924B	1984	0.8650	0.361	1.973	-0.060	0.116	-	0.024	-2.402
PRL 4025	33.09	0.8682	0.499	1.405	0.148	0.129	-0.080	-0.050	-0.409
PRL 4027	227.0	0.8770	0.330	1.514	-0.142	0.026	-	-0.047	-1.156
PRL 4028	1917	0.8980	0.280	1.590	0.047	-0.193	-	-	-2.752
PRL 4029	34.70	0.8735	0.526	1.413	0.137	0.107	-0.078	-0.136	-0.417
PRL 4032	227.4	0.8920	0.397	1.579	-0.018	0.046	-	-0.086	-1.093
PRL 4033	33.60	0.9110	0.576	1.106	-0.148	-0.240	-0.065	-0.279	-0.717
PRL 4034	226.8	0.9280	0.446	1.367	-0.074	-0.213	-	-0.240	-1.306
PRL 4036	34.84	0.8690	0.689	1.473	0.008	-0.033	-0.018	-0.206	-0.359
PRL 4037	222.9	0.8750	0.597	1.862	-0.015	0.032	-	-0.199	-0.798
PRL 4038	1875	0.8840	0.548	2.028	0.047	-0.211	-	-0.509	-2.291
PRL 4039	34.78	0.8990	0.623	1.163	-0.162	-0.246	-0.011	-0.285	-0.670
PRL 4041	225.7	0.8920	0.558	1.547	-0.181	-0.202	-	-0.266	-1.122
PRL 4042	1915	0.8865	0.536	1.903	-0.014	-0.303	-	-0.279	-2.438
PRL 4043	35.29	0.8965	0.521	1.158	-0.088	-0.148	-0.018	-0.191	-0.680
PRL 4044	224.7	0.8860	0.409	1.541	-0.089	0.000	-	0.034	-1.124
PRL 4045	1268	0.8770	0.359	1.759	-0.119	-0.023	-	0.280	-2.177
PRL 4046	9.61	0.8340	0.587	1.125	0.086	0.029	0.015	-0.118	-0.335
PRL 4047	18.70	0.8360	0.499	1.212	0.063	0.038	0.102	-0.139	-0.422
PRL 4048	28.56	0.8390	0.462	1.296	0.055	0.069	0.112	-0.112	-0.467
PRL 4049	55.58	0.8640	0.529	1.525	0.104	0.122	-0.038	-0.087	-0.476
PRL 4050	90.92	0.8645	0.487	1.620	0.088	0.165	-0.035	-0.025	-0.586
PRL 4051	232.7	0.8695	0.601	2.223	0.298	0.373	0.279	0.091	-0.461
PRL 4052	460.4	0.8692	0.524	2.305	0.333	0.462	0.268	0.121	-0.813
PRL 4053	743.8	0.8700	0.477	2.389	0.396	0.537	0.265	0.214	-1.087
PRL 4054	493.1	0.8670	0.537	1.911	-0.112	0.025	0.060	-0.025	-1.255
PRL 4055	1014	0.8650	0.466	2.003	-0.070	0.109	0.052	0.101	-1.731

* Deviation = Experimental Value - Predicted Value
(a) Equation [45]
(b) Equation [42]
(c) AFML-TR-70-304-Part II
(d) Roelands, et al (23)
(e) Kouzel (26)

Table 30

COMPARISON OF VARIOUS METHODS IN PREDICTING PRL
PRESSURE COEFFICIENT DATA AT 32 AND 130°F

For Fluid Descriptions, See Table 3, 4 and 5

Fluid Designation	Atmospheric Viscosity, cs.	Atmospheric Density, gm/cc	ASTM Slope	Experimental Press. Coeff., (1/psig)x(10^4)	Deviation*, (1/psig)x(10^4)					
					(a)	(b)	(c)	(d)	(e)	(f)
Data Source: Current Investigation at 32°F										
MLO 7372	51.19	0.8663	0.800	1.764	-0.174	-0.123	0.010	-	-0.098	-0.210
MLO 7375	377.80	0.8807	0.748	2.464	-0.090	-0.063	0.401	-	0.280	-0.524
PRL 4559	485.7	0.8797	0.659	2.018	-0.205	-0.223	0.114	-	-0.011	-1.143
Data Source: Current Investigation at 130°F										
O 266	3.319	0.8047	0.820	1.076	0.101	0.107	0.175	-	0.018	-0.160
MLO 7372	6.114	0.8306	0.800	1.185	0.081	0.056	0.041	-	-0.076	-0.172
MLO 7375	19.97	0.8454	0.748	1.522	0.118	0.087	0.068	-	0.041	-0.130
MLO 7120	44.67	0.8604	0.710	1.698	0.086	0.078	0.111	-	-0.033	-0.218
MLO 7246	170.5	0.8647	0.640	1.824	-0.111	-0.038	0.103	-	-0.088	-0.685
PRL 4559	28.48	0.8443	0.659	1.381	-0.000	-0.025	0.081	-	-0.071	-0.380
Data Source: Fresco (27) at 130°F										
MLO 7557	8.200	0.8204	0.783	1.250	0.080	0.049	0.027	-	-0.058	-0.169
MLO 7112	7.900	0.8910	0.701	0.979	-0.076	-0.145	-0.022	-	-	-0.439
Data Source: AFML-TR-70-304, Part II at 32°F.										
PRL 2924	219.5	0.8880	0.583	2.030	0.249	0.236	-	-0.017	-0.315	-0.626
PRL 4025	180.3	0.8923	0.499	1.924	0.313	0.322	-	-0.087	-0.259	-0.623
PRL 4036	314.3	0.8910	0.689	1.992	-0.153	-0.215	-	-0.132	-0.623	-0.879
PRL 4046	34.62	0.8580	0.587	1.384	0.041	0.019	-	-0.114	-0.616	-0.450
PRL 4047	70.50	0.8600	0.499	1.536	0.058	0.117	-	-0.107	-0.563	-0.565
PRL 4048	120.0	0.8630	0.462	1.810	0.209	0.329	-	-	-0.350	-0.528
PRL 4049	425.5	0.8880	0.529	2.044	0.217	0.209	-	-0.157	-0.287	-1.025

(Concluded on next page.)

Table 30 (Concluded)

Fluid Designation	Atmospheric Viscosity cs.	Density gm/cc	ASTM Slope	Experimental Press. Coeff., (1/psig)x(10^4)	Deviation*, (1/psig)x(10^4) (a)	(b)	(c)	(d)	(e)	(f)
Data Source: AFML-TR-70-304, Pt. II										
PRL 4036	18.68	0.8580	0.689	1.386	0.111	0.053	-	0.091	-0.112	-0.247
PRL 4046	6.660	0.8215	0.587	1.074	0.098	0.047	-	0.191	-0.065	-0.300
PRL 4047	12.60	0.8250	0.499	1.136	0.069	0.031	-	0.176	-0.108	-0.388
PRL 4048	18.92	0.8280	0.462	1.212	0.065	0.054	-	0.189	-0.092	-0.422
PRL 4049	31.87	0.8540	0.545	1.438	0.146	0.132	-	0.071	-0.027	-0.360
PRL 4050	51.04	0.8540	0.487	1.571	0.180	0.224	-	0.126	0.071	-0.394
PRL 4051	101.5	0.8600	0.601	1.943	0.246	0.305	-	0.180	0.278	-0.310
PRL 4052	199.6	0.8600	0.524	2.028	0.217	0.367	-	0.179	-0.293	-0.566
PRL 4053	322.4	0.8600	0.477	2.022	0.123	0.336	-	0.096	-0.563	-0.856
PRL 4054	211.4	0.8500	0.537	1.843	-0.050	0.148	-	0.163	-0.115	-0.782
PRL 4055	434.1	0.8550	0.466	1.938	-0.063	0.211	-	0.166	-0.252	-1.136

* Deviation = Experimental Value - Predicted

(a) Equation [45]

[b] Equation 42

[c] Fresco (27)

[d] AFML-TR-70-304, Pt. II

[e] Roelands et. al. (23)

[f] Kouzel (26)

Table 31

SUMMARY OF THE COMPARISONS OF VARIOUS METHODS IN PREDICTING PRL PRESSURE COEFFICIENT DATA AT VARIOUS TEMPERATURES

	Test Temp.: 32°F				Test Temp.: 100°F				Test Temp.: 130°F				Test Temp.: 32, 100 and 130°F			
Method	No. of Flu-ids	Avg. Abs. Dev.*	Bias*	RMS*	No. of Flu-ids	Avg. Abs. Dev.*	Bias*	RMS*	No. of Flu-ids	Avg. Abs. Dev.*	Bias*	RMS*	No. of Flu-ids	Avg. Abs. Dev.*	Bias*	RMS*
Data Source: Current Investigation																
(a)	3	0.157	-0.157	0.164	8	0.086	-0.031	0.102	6	0.083	0.046	0.092	17	0.097	-0.052	0.0113
(b)	3	0.137	-0.136	0.151	8	0.074	-0.028	0.089	6	0.066	0.044	0.071	17	0.082	-0.022	0.092
(c)	3	0.175	0.175	0.241	8	0.069	0.058	0.078	6	0.096	0.096	0.105	17	0.097	0.092	0.130
(d)	-	-	-	-	-	-	-	-	-	-	-	-	-	-	-	-
(e)	3	0.130	0.057	0.171	8	0.059	-0.045	0.082	6	0.055	-0.035	0.060	17	0.070	-0.023	0.098
(f)	3	0.626	-0.626	0.736	8	0.393	-0.393	0.492	6	0.291	-0.291	0.350	17	0.398	-0.398	0.485
Data Source: Fresco (27)																
(a)					12	0.154	-0.013	0.186	2	0.078	0.002	0.078	14	0.123	-0.011	0.175
(b)					12	0.170	-0.008	0.228	2	0.097	-0.048	0.108	14	0.155	-0.000	0.215
(c)					11	0.141	0.124	0.263	2	0.025	0.002	0.025	13	0.123	0.105	0.242
(d)					-	-	-	-	-	-	-	-	-	-	-	-
(e)					8	0.277	0.030	0.463	1	0.058	-0.058	0.058	9	0.253	0.020	0.437
(f)					12	0.422	-0.375	0.543	2	0.304	-0.304	0.333	14	0.405	-0.365	0.518
Data Source: AFML-TR-70-304, Pt. II																
(a)	7	0.177	0.133	0.200	30	0.110	0.024	0.143	11	0.124	0.104	0.139	48	0.123	0.058	0.152
(b)	7	0.207	0.145	0.230	30	0.157	0.022	0.204	11	0.173	0.173	0.210	48	0.168	0.074	0.209
(c)	-	-	-	-	-	-	-	-	-	-	-	-	-	-	-	-
(d)	6	0.102	-0.102	0.111	17	0.096	0.051	0.129	11	0.148	0.148	0.154	34	0.114	0.055	0.128
(e)	7	0.430	-0.430	0.456	28	0.153	-0.091	0.182	11	0.180	-0.173	0.233	46	0.202	-0.162	0.255
(f)	7	0.671	-0.671	0.697	30	1.106	-1.106	1.328	11	0.524	-0.524	0.589	48	0.909	-0.909	1.119

(Concluded on the next page.)

Table 31 (Concluded)

	Test Temp.: 32°F				Test Temp.: 100°F				Test Temp.: 130°F				Test Temp.: 32, 100 and 130°F			
Method	No. of Fluids	Avg. Abs. Dev.*	Bias*	RMS*	No. of Fluids	Avg. Abs Dev.*	Bias*	RMS*	No. of Fluids	Abs Dev.*	Bias*	RMS*	No. of Fluids	Avg. Abs Dev.*	Bias*	RMS*
								All Data								
(a)	10	0.171	0.046	0.190	50	0.117	0.007	0.149	19	0.107	0.075	0.121	79	0.121	0.023	0.149
(b)	10	0.185	0.061	0.210	50	0.147	0.010	0.1 7	19	0.131	0.109	0.168	79	0.147	0.040	0.191
(c)	3	0.175	0.175	0.241	19	0.110	0.096	0.206	8	0.079	0.073	0.092	30	0.108	0.093	0.187
(d)	6	0.102	-0.102	0.111	17	0.096	0.051	0.129	11	0.148	0.148	0.154	34	0.114	0.055	0.128
(e)	10	0.340	-0.284	0.393	44	0.158	-0.061	0.248	18	0.132	-0.121	0.186	72	0.177	-0.106	0.252
(f)	10	0.657	-0.657	0.709	50	0.828	-0.816	1.081	19	0.427	-0.427	0.501	79	0.710	-0.703	0.927

(a) Equation [45]
(b) Equation [42]
(c) Fresco (27)
(d) AFML-TR-70-304, Pt. LI
(e) Roelands, et. al. (23)
(f) Kouzel (26)

* Defined in Table 11; units are (1/psig) x (10^4)

Table 32

COMPARISON OF VARIOUS METHODS IN PREDICTING PRESSURE
COEFFICIENT DATA FROM API PROJECT 42 (8) AT 100°F

For Brief Descriptions of Fluids, See Table 9

Fluid Designation	Atmospheric Viscosity, cs. 100°F	Atmospheric Density, gm/cc 100°F	ASTM Slope	Experimental Press. Coeff., (1/psig) x (10^4)	Deviation*, (1/psig) x (10^4) (a)	(b)	(c)	(d)	(e)
PSU 532	2.592	0.7562	0.815	0.949	0.022	0.044	0.241	0.065	-0.242
PSU 500	4.551	0.7756	0.866	1.112	0.011	0.025	-0.014	0.172	-0.181
PSU 25	8.931	0.7905	0.766	1.113	-0.070	-0.097	-0.047	0.108	-0.326
PSU 8	15.12	0.8005	0.707	1.119	-0.073	-0.097	0.008	0.144	-0.372
PSU 134	25.63	0.8077	0.647	1.186	-0.186	-0.178	0.000	0.080	-0.540
PSU 516	2.890	0.9860	0.865	0.912	-0.056	-0.038	0.033	-0.293	-0.316
PSU 503	8.512	0.9375	0.925	1.159	-0.276	-0.229	-0.455	-0.287	-0.280
PSU 12	18.62	0.9069	0.777	1.396	0.005	-0.060	-0.071	-0.123	-0.243
PSU 18	12.61	0.9094	0.803	1.124	-0.186	-0.239	-0.276	-0.314	-0.409
PSU 87	9.383	0.8441	0.777	1.211	0.015	-0.025	0.001	0.029	-0.244
PSU 113	25.68	0.8774	0.751	1.507	0.034	-0.012	0.008	-0.489	-0.225
PSU 19	33.53	0.8548	0.793	1.812	0.087	0.112	0.105	-0.099	-0.005
PSU 111	16.05	0.8469	0.748	1.281	-0.044	-0.084	-0.049	-0.292	-0.312
PSU 88	14.73	0.8216	0.772	1.381	0.028	0.010	0.012	0.032	-0.186
PSU 110	11.53	0.8178	0.759	1.088	-0.158	-0.190	-0.152	-0.165	-0.415
PSU 122	817.0	0.9204	0.884	3.813	-0.037	-0.065	1.665	0.350	0.257
PSU 656	1.975	0.8707	0.902	0.948	0.034	0.090	0.212	-0.073	-0.210
PSU 657	1.438	0.8484	0.915	0.819	-0.047	0.034	0.280	-0.019	-0.290
PSU 620	1.874	0.8646	0.795	0.868	-0.007	0.040	0.371	-0.121	-0.282
PSU 569	2.615	0.8834	0.846	0.942	0.002	0.026	0.165	-0.235	-0.263
PSU 570	1.810	0.8565	0.843	0.877	-0.005	0.050	0.317	-0.088	-0.267
PSU 622	2.522	0.8763	0.810	0.930	0.013	0.033	0.246	-0.223	-0.267
PSU 597	6.851	0.8846	0.773	1.075	-0.017	-0.065	0.005	-0.255	-0.312
PSU 598	8.549	0.8510	0.730	1.105	-0.005	-0.061	0.055	-0.353	-0.329
PSU 604	8.911	0.8888	0.857	1.309	0.006	-0.003	-0.106	-0.098	-0.138
PSU 638	13.86	0.9389	0.879	1.320	-0.206	-0.203	-0.347	-0.168	-0.240

(Concluded on next page.)

Table 32 (Concluded)

Fluid Designation	Atmospheric Viscosity, cs. 100°F	Atmospheric Density, gm/cc 100°F	ASTM Slope	Experimental Press. Coeff., (1/psig) x (10^4)	Deviation*, (1/psig) x (10^4) (a)	(b)	(c)	(d)	(e)
PSU 639	16.76	0.9098	0.839	1.566	0.061	0.040	-0.044	-0.066	-0.044
PSU 640	10.99	0.8641	0.810	1.455	0.519	0.130	0.088	-0.116	-0.040
PSU 613	12.49	0.9209	0.881	1.379	-0.114	-0.103	-0.253	-0.076	-0.153
PSU 614	14.83	0.8967	0.857	1.458	-0.055	-0.052	-0.163	-0.132	-0.117
PSU 615	15.28	0.8639	0.885	1.640	0.004	0.063	-0.083	-0.041	0.060

* Deviation = Experimental Value - Predicted Value

(a) Equation [45]

(b) Equation [42]

(c) Fresco (27)

(d) Roelands, et. al (23)

(e) Kouzel (26)

Table 33

COMPARISON OF VARIOUS METHODS IN PREDICTING PRESSURE COEFFICIENT DATA FROM API PROJECT 42 (8) AT 140 AND 275°F

For Brief Descriptions of Fluids, See Table 9

	Atmospheric								
Fluid Designation	Viscosity, cs.	Density, gm/cc	ASTM Slope	Experimental Press. Coeff., (1/psig)x(10^4)	Deviation*, (1/psig)x(10^4) (a)	(b)	(c)	(d)	(e)
Test Temperature: 140°F									
PSU 500	2.800	0.7606	0.866	0.948	-0.021	0.007	0.016	0.060	-0.252
PSU 25	5.038	0.7761	0.766	1.025	-0.004	-0.027	0.036	0.079	-0.285
PSU 8	8.077	0.7862	0.707	1.057	-0.035	-0.076	0.017	0.066	-0.354
PSU 134	12.98	0.7938	0.647	1.124	-0.042	-0.076	0.070	0.088	-0.403
PSU 516	1.899	0.9690	0.865	0.822	-0.072	-0.020	0.126	-0.218	-0.335
PSU 503	4.384	0.9215	0.925	1.005	-0.150	-0.114	-0.341	-0.234	-0.291
PSU 12	8.871	0.8917	0.777	1.226	0.062	0.007	-0.029	-0.103	-0.217
PSU 18	6.459	0.8949	0.803	1.049	-0.061	-0.099	-0.142	-0.214	-0.324
PSU 87	5.243	0.8296	0.777	1.045	0.005	-0.024	0.012	-0.030	-0.278
PSU 113	11.77	0.8635	0.751	1.312	0.092	0.036	0.019	-0.377	-0.197
PSU 19	13.94	0.8405	0.793	1.550	0.189	0.168	0.078	-0.064	-0.000
PSU 111	8.156	0.8324	0.748	1.144	0.022	-0.024	-0.000	-0.224	-0.274
PSU 88	7.486	0.8068	0.772	1.205	0.073	0.040	0.032	0.007	-0.192
PSU 110	6.215	0.8029	0.759	0.963	-0.106	-0.139	-0.098	-0.164	-0.393
PSU 122	133.5	0.9067	0.884	2.895	0.005	0.192	0.656	0.168	0.508
PSU 656	1.396	0.8525	0.902	0.881	0.020	0.103	0.321	0.059	-0.222
PSU 657	1.060	0.8299	0.915	0.806	-0.034	0.075	0.445	0.144	-0.258
PSU 620	1.369	0.8475	0.795	0.831	-0.019	0.062	0.457	0.022	-0.269
PSU 569	1.812	0.8665	0.846	0.946	0.063	0.117	0.319	-0.024	-0.196
PSU 570	1.235	0.8399	0.843	0.874	0.028	0.120	0.499	0.125	-0.211
PSU 622	1.778	0.8606	0.811	0.868	-0.005	0.049	0.313	-0.087	-0.270
PSU 597	4.025	0.8695	0.773	0.989	0.012	-0.009	0.085	-0.183	-0.287
PSU 598	4.880	0.8361	0.730	1.018	0.030	-0.006	0.122	-0.248	-0.291

(Concluded on next page.)

Table 33 (Concluded)

Fluid Designation	Atmospheric Viscosity, cs.	Atmospheric Density, gm/cc	ASTM Slope	Experimental Press. Coeff., (1/psig)x(10^4)	Deviation*, (1/psig)x(10^4) (a)	(b)	(c)	(d)	(e)
Test Temperature: 140°F (cont'd)									
PSU 604	4.796	0.8737	0.857	1.177	0.081	0.079	-0.017	-0.046	-0.133
PSU 638	6.697	0.9243	0.879	1.078	-0.154	-0.154	-0.343	-0.215	-0.305
PSU 639	7.798	0.8951	0.839	1.137	-0.082	-0.106	-0.232	-0.259	-0.277
PSU 640	5.742	0.8499	0.810	1.275	0.181	0.157	0.116	-0.069	-0.069
PSU 613	6.083	0.9058	0.881	1.187	-0.017	-0.012	-0.194	-0.075	-0.174
PSU 614	7.133	0.8818	0.857	1.301	0.077	0.069	-0.082	-0.063	-0.092
PSU 615	7.040	0.8494	0.885	1.364	0.086	0.106	-0.099	-0.047	-0.023
Test Temperature: 275°F									
PSU 8	2.167	0.7385	0.707	0.820	-0.053	-0.025	0.125	-0.024	-0.320
PSU 134	3.172	0.7471	0.647	0.845	-0.053	-0.060	0.044	-0.036	-0.360
PSU 503	1.324	0.8684	0.925	0.675	-0.183	-0.094	-0.064	-0.173	-0.410
PSU 12	2.163	0.8415	0.777	0.892	0.006	0.037	0.096	-0.062	-0.262
PSU 87	1.581	0.7781	0.777	0.879	0.021	0.085	0.273	0.040	-0.220
PSU 113	2.615	0.8145	0.751	0.967	0.065	0.077	0.120	-0.108	-0.215
PSU 19	2.611	0.7928	0.793	1.096	0.179	0.196	0.163	0.066	-0.082
PSU 88	1.928	0.7574	0.772	0.947	0.073	0.116	0.227	0.069	-0.178
PSU 110	1.830	0.7539	0.759	0.792	-0.075	-0.028	0.128	-0.069	-0.325
PSU 597	1.369	0.8182	0.773	0.894	0.046	0.126	0.391	0.060	-0.190
PSU 598	1.540	0.7856	0.730	0.930	0.079	0.144	0.400	0.076	-0.166
PSU 604	1.363	0.8217	0.859	1.026	0.172	0.255	0.382	0.192	-0.058
PSU 613	1.509	0.8550	0.881	0.959	0.092	0.166	0.192	0.085	-0.143
PSU 614	1.708	0.8312	0.857	1.034	0.156	0.217	0.228	0.128	-0.083
PSU 615	1.626	0.7996	0.885	1.096	0.218	0.287	0.264	0.215	-0.010

* Deviation = Experimental Value - Projected Value
(a) Equation [45]
(b) Equation [42]
(c) Fresco (27)
(d) Roelands, et al. (23)
(e) Kouzel (26)

Table 34

SUMMARY OF THE COMPARISONS OF VARIOUS METHODS IN PREDICTING PRESSURE COEFFICIENT DATA FROM API PROJECT 42 (11) AT VARIOUS TEMPERATURES

Method	Test Temp.: 100°F				Test Temp.: 140°F				Test Temp.: 275°F				Test Temp.: 100,140 and 275°F			
	No. of Comp.	Avg. Abs. Dev.*	Bias*	RMS*	No. of Comp.	Avg. Abs. Dev.*	Bias*	RMS*	No. of Comp.	Avg. Abs. Dev.*	Bias*	RMS*	No. of Pts.	Avg. Abs. Dev.*	Bias*	RMS*
(a)	31	0.065	-0.034	0.096	30	0.061	0.007	0.08	15	0.098	0.049	0.117	76	0.070	-0.001	0.095
(b)	31	0.080	-0.036	0.103	30	0.076	0.017	0.092	15	0.127	0.100	0.150	76	0.088	0.012	0.110
(c)	31	0.189	0.057	0.353	30	0.177	0.072	0.247	15	0.207	0.198	0.235	76	0.188	0.091	0.293
(d)	31	0.165	-0.101	0.200	30	0.123	-0.071	0.154	15	0.094	0.031	0.109	76	0.134	-0.063	0.167
(e)	31	0.244	-0.224	0.270	30	0.246	-0.212	0.269	15	0.202	-0.206	0.231	76	0.237	-0.216	0.262

* Defined in Table 11; units are (1/psig)x(10^4)

(a) Equation 45
(b) Equation 42
(c) Fresco (27)
(d) Roelands, et. al (23)
(e) Kouzel (26)

Table 35

BRIEF DESCRIPTIONS OF FLUIDS FROM ASME REPORT (7)

Fluid Designation	Description
8C	1-Cyclohexyl-3(2-Cyclohexylethyl) Hendecane = PSU 19
10C	1-Cyclopentyl-4(5-Cyclopentylpropyl) Dodecane = PSU 111
26E	Naphenic Mineral Oil + Low Mol. Wt. Polymethacrylate
27E	Naphenic Mineral Oil + High Mol. Wt. Polymethacrylate
31G	Paraffinic Mineral Oil
32G	Paraffinic Mineral Oil
33G	Paraffinic Mineral Oil
36G	31G + Bright Stock
37G	Naphenic Mineral Oil
38G	Naphenic Mineral Oil
42G	37G Dearomatized
44G	31G + Polyisobutylene
45G	31 + Polymethacrylate
52G	Aromatic Fraction from 37G

Table 36

COMPARISON OF VARIOUS METHODS IN PREDICTING PRESSURE COEFFICIENT DATA FROM ASME REPORT (7)

For Fluid Descriptions, See Table 34

Fluid Designation	Atmospheric Viscosity, cs.	Atmospheric Density, g./cc	ASTM Slope	Pressure*, psig	Experimental Press. Coeff.,** (1/psig)x(10^4)	Deviation**,(1/psig)x(10^4) (a)	(b)	(c)	(d)	(e)	(f)
Test Temperature: 100°F											
8C	33.95	0.8550	0.807	5,110	1.809	0.033	0.072	0.059	-	-0.106	-0.012
10C	15.50	0.8460	0.767	7,000	1.344	-0.003	-0.036	-0.029	-	-0.218	-0.238
26E	33.60	0.8720	0.517	10,400	1.536	0.271	0.243	-	0.052	-	-0.283
27E	32.50	0.8690	0.497	9,640	1.551	0.300	0.279	-	0.064	-	-0.258
31G	52.50	0.8685	0.756	5,555	1.847	0.059	0.069	0.117	-	0.042	-0.133
32G	166.8	0.8720	0.683	5,440	1.894	-0.118	-0.079	0.090	-	-0.346	-0.607
33G	567.6	0.8910	0.646	5,040	2.138	0.015	-0.106	0.145	-	-0.602	-1.132
36G	55.40	0.9030	0.854	5,410	2.248	0.087	0.154	0.239	-	0.047	0.245
37G	145.9	0.9160	0.847	7,110	2.645	0.039	0.085	0.475	-	0.112	0.210
38G	511.1	0.9320	0.847	9,520	3.476	0.375	0.202	1.222	-	0.388	0.280
42G	74.60	0.8810	0.808	5,480	2.211	0.080	0.139	0.247	-	0.066	0.089
44G	151.1	0.8679	0.607	11,260	1.805	-0.005	0.054	0.260	0.006	-0.089	-0.643
45G	156.3	0.8720	0.525	10,030	1.691	0.003	0.081	-	0.111	-0.084	-0.775
52G	536.7	0.9790	0.930	9,670	4.115	0.253	0.129	2.092	-	0.729	0.880

(Concluded on next page.)

Table 36 (Concluded)

Fluid Desig- nation	Atmospheric Viscosity, cs.	Atmospheric Density, gm./cc	ASTM Slope	Pressure*, psig	Experimental Press. Coeff.,** (1/psig)x(10^4)	Deviation**, (1/psig)x(10^4) (a)	(b)	(c)	(d)	(e)	(f)
Test Temperature: 210°F											
8C	4.90	0.8170	0.807	7,520	1.255	0.202	0.186	0.070	-	-0.001	-0.048
10C	3.40	0.8080	0.767	21,300	0.869	-0.079	-0.085	-0.052	-	-0.229	-0.364
26E	8.50	0.8320	0.517	14,180	0.995	0.002	-0.049	-	0.029	-	-0.426
27E	8.70	0.8290	0.497	20,200	0.968	-0.026	-0.074	-	-0.013	-	-0.459
31G	6.80	0.8310	0.756	21,400	1.073	-0.010	-0.052	0.128	-	-0.183	-0.298
32G	15.10	0.8360	0.683	10,790	1.325	0.105	0.055	0.025	-	-0.207	-0.240
33G	33.50	0.8550	0.646	10,520	1,440	0.037	0.010	0.011	-	-0.404	-0.368
36G	5.80	0.8640	0.854	16,480	1.341	0.189	0.183	-0.042	-	-0.034	-0.001
37G	9.50	0.8780	0.847	10,150	1.575	0.264	0.253	0.003	-	0.025	0.122
38G	17.40	0.8940	0.847	10,890	1.854	0.297	0.298	0.065	-	0.038	0.244
42G	7.40	0.8430	0.808	20,640	1.348	0.181	0.154	-0.021	-	-0.039	-0.044
44G	17.44	0.8280	0.607	20,740	1.197	0.002	-0.037	0.030	-0.064	-0.124	-0.408
45G	22.40	0.8360	0.525	20,430	1.131	-0.074	-0.091	-	-0.160	-0.159	-0.547
52G	14.30	0.9400	0.930	7,741	1.927	0.204	0.286	-0.035	-	0.059	0.366

*Pressure where the calculation of pressure coefficient was based

** Deviation = Experimental Value - Predicted Value

(a) Equation [45]
(b) Equation [42]
(c) Fresco (27)
(d) AFML-TR-70-304, Pt. II
(e) Roelands, et. al. (23)
(f) Kouzel (26)

Table 37

COMPARISON OF VARIOUS METHODS IN PREDICTING PRESSURE COEFFICIENT DATA FROM ROELANDS-VLUGTER-WATERMAN (23)

Fluid Designation	Atmospheric Viscosity, cs.	Density, gm/cc	ASTM Slope	n-d-n Analysis* C_A-C_N-C_P	Experimental Pressure Coeff.,** (1/psig)x(10^4)	Deviation,***(1/psig)x(10^4) (a)	(b)	(c)	(d)	(e)
				Test Temperature:	104°F					
1	10.38	0.8472	0.778	13-21-66	1.362	0.134	0.094	0.102	0.020	-0.117
4	9.790	0.9316	0.732	35-34-31	1.619	0.500	0.415	0.507	-0.012	0.147
5	8.048	0.8822	0.840	0-69-31	1.606	0.370	0.351	0.278	-0.017	0.184
8	3.995	0.8260	0.807	15-22-63	1.078	0.075	0.065	0.161	-0.042	-0.196
9	8.181	0.8728	0.804	21-27-52	1.420	0.236	0.199	0.186	0.023	-0.005
10	7.665	0.8480	0.801	0-48-52	1.423	0.256	0.224	0.223	-0.003	0.014
20	4.067	0.8188	0.829	11-22-67	1.110	0.084	0.081	0.132	0.004	-0.166
				Test Temperature:	194°F					
1	3.215	0.8150	0.778	13-21-66	1.035	0.092	0.090	0.142	-0.008	-0.190
4	2.737	0.9011	0.732	35-34-31	1.090	0.191	0.194	0.361	-0.050	-0.117
5	2.565	0.8510	0.841	0-69-31	1.154	0.220	0.245	0.246	0.037	-0.036
8	1.702	0.7931	0.807	15-22-63	0.861	-0.007	0.051	0.263	-0.023	-0.259
9	2.692	0.8414	0.804	21-27-52	1.025	0.100	0.114	0.169	-0.026	-0.173
10	2.590	0.8157	0.801	0-48-52	1.062	0.143	0.161	0.232	0.013	-0.127
20	1.693	0.7855	0.827	11-22-67	0.891	0.020	0.080	0.261	0.014	-0.227

* Method of Van Nes and Van Westen

** Calculated based on pressure viscosity data at 7360 psig

***Deviation = Experimental Value - Predicted Value

(a) Equation [45]
(b) Equation [42]
(c) Fresco (27)
(d) Roeland, et. al. (23)
(e) Kouzel (26)

Table 38

SUMMARY OF THE COMPARISONS OF VARIOUS METHODS IN PREDICTING PRESSURE COEFFICIENT DATA FROM ASME REPORTS (7) AT VARIOUS TEMPERATURES

	Test Temp.: 100°F				Test Temp.: 210°F				Test Temp.: 100 and 210°F			
Method	No. of Fluids	Avg. Abs. Dev.*	Bias*	RMS*	No. of Fluids	Avg. Abs. Dev.*	Bias*	RMS*	No. of Pts.	Avg. Abs. Dev.*	Bias*	RMS*
(a)	14	0.117	0.099	0.169	14	0.119	0.092	0.154	28	0.118	0.096	0.162
(b)	14	0.123	0.092	0.142	14	0.129	0.074	0.160	28	0.126	0.083	0.151
(c)	11	0.452	0.447	0.758	11	0.044	-0.007	0.055	22	0.248	0.220	0.538
(d)	4	0.058	0.058	0.069	4	0.066	-0.208	0.088	8	0.063	-0.075	0.079
(e)	12	0.236	-0.005	0.324	12	0.125	-0.104	0.168	24	0.181	-0.055	0.258
(f)	14	0.413	-0.170	0.524	14	0.281	-0.177	0.326	28	0.347	-0.174	0.436

* Defined in Table 11; units are (1/psig)x(10^4)

(a) Equation [45]

(b) Equation [42]

(c) Fresco (27)

(d) AFML-TR-70-304, Pt. II

(e) Roelands, et..al (23)

(f) Kouzel (26)

Table 39

SUMMARY OF THE COMPARISONS OF VARIOUS METHODS IN PREDICTING PRESSURE COEFFICIENTS
DATA FROM ROELANDS-VLUGTER-WATERMAN (23) AT VARIOUS TEMPERATURES

	Test Temp.: 104°F				Test Temp.: 194°F				Test Temp.: 104 and 194°F			
Method	No. of Fluids	Avg. Abs. Dev.*	Bias*	RMS*	No. of Fluids	Avg. Abs. Dev.*	Bias*	RMS*	No. of Points	Avg. Abs. Dev.*	Bias*	RMS*
(a)	7	0.236	0.236	0.277	7	0.110	0.108	0.133	14	0.173	0.173	0.217
(b)	7	0.204	0.204	0.241	7	0.134	0.134	0.149	14	0.169	0.169	0.200
(c)	7	0.227	0.277	0.260	7	0.239	0.239	0.248	14	0.233	0.233	0.254
(d)	7	0.017	-0.004	0.021	7	0.024	-0.006	0.028	14	0.021	-0.005	0.025
(e)	7	0.119	-0.020	0.139	7	0.161	-0.161	0.176	14	0.140	-0.091	0.159

* Defined in Table 11; units are (1/psig)x(10^4)

(a) Equation [45]

(b) Equation [42]

(c) Fresco (27)

(d) Roelands, et. al (23)

(e) Kouzel (26)

Table 40

SUMMARY OF THE EFFECTIVENESS OF VARIOUS METHODS IN PREDICTING PRESSURE COEFFICIENTS OF DIFFERENT FLUID TYPES

	Mineral Oils			Pure Hydrocarbons			Polymer and Resin Blends			Non-hydrocarbons			All Fluids Studied		
Method	No. of Fluids	No. of Pts.	Avg. Abs. Dev.*	No. of Fluids	No. of Pts.	Avg. Abs. Dev.,*	No. of Fluids	No. of Pts.	Avg. Abs. Dev.,*	No. of Fluids	No. of Pts.	Avg. Abs. Dev.,*	No. of Fluids	No. of Pts.	Avg. Abs. Dev.,*
Equation [45]	23	55	0.134	33	80	0.070	34	56	0.118	5	6	0.174	95	197	0.105
Equation [42]	23	55	0.122	33	80	0.088	34	56	0.163	5	6	0.260	95	197	0.123
Fresco (27)	23	55	0.184	33	80	0.182	-	-	-	4	5	0.267	60	140	0.186
AFML-TR-70-304, Pt. II	-	-	-	-	-	-	17	42	0.105	-	-	-	17	42	0.105
Roelands, et. al. (23)	23	55	0.132	33	80	0.136	32	50	0.200	-	-	-	88	185	0.152
Kouzel (26)	23	55	0.310	33	80	0.233	34	56	0.847	5	6	0.435	95	197	0.435

* (|Experimental Value| - |Predicted Value|)/No. of Points; units are (1/psig) $x(10^4)$

Table 41

COMPARISON OF VARIOUS METHODS IN PREDICTING PRESSURE COEFFICIENT DATA OF NON-HYDROCARBONS LYING OUTSIDE THE LIMITS DESIGNED FOR EQUATION [45] AND [42]

For Brief Descriptions of Fluids, See Table 42
Data Source: Fresco (27)
Temperature: 100°F

Fluid Designation	Atmospheric Viscosity, cs.	Atmospheric Density, gm/cc	ASTM Slope	Experimental Press. Coeff., $(1/psig)x(10^4)$	Deviations,* $(1/psig)x(10^4)$			
					(a)	(b)	(c)	(d)
MLO 7742	980.9	1.9580	0.895	2.869	1.646**	-1.240	0.786	-0.873
MLO 7723	302.1	1.8640	0.584	2.881	1.957**	1.004	-	0.005
MLO 7428	75.66	1.1610	0.884	1.864	-0.099	-0.510	-0.274	-0.281
MLO 7017	55.80	1.0140	0.325	1.410	0.343	0.135	-	-0.603
MLO 7756	2.303	1.8080	0.961	0.924	-0.048	0.006	-0.048	-0.293
MLO 7743	26.80	1.9060	1.075	2.337	-0.191	-0.182	-	0.556
MLO 7741	6.225	1.8720	1.068	1.930	0.322	0.473	0.003	0.528
MLO 7668	355.1	1.1860	0.892	3.654	1.549**	0.286	1.430	0.692
MLO 7639	11.75	1.0470	0.563	0.815	-0.166	-0.308	-	-0.709
MLO 7061	46.69	1.4360	1.157	2.800	-1.727	-0.732	-	0.836

* Deviation = Experimental Value - Predicted Values
** Segmental Flow Assumed
(a) Equation [45]
(b) Equation [42]
(c) Fresco (27)
(d) Kouzel (26)

Table 42

BRIEF DESCRIPTIONS OF NON-HYDROCARBONS IN TABLE 41

Fluid Designation	Description
MLO 7742	Halocarbon Oil 14-25
MLO 7723	DuPont PR 143
MLO 7428	4-ring polyphenyl ether
MLO 7017	Improved Lubricity Silicone Fluid (G.E. Silicone 81406)
MLO 7756	Halocarbon Oil 208
MLO 7743	Halocarbon Oil 11-21
MLO 7741	Halocarbon Oil 11-14
MLO 7668	5-ring polyphenyl ether
MLO 7639	Phosphate Ester Hydraulic Fluid (Skydrol 500 1)
MLO 7061	Chlorinated Biphenyl

Table 43

SUMMARY OF THE COMPARISON OF VARIOUS METHODS IN PREDICTING COEFFICIENT DATA OF NON-HYDROCARBONS LYING OUTSIDE THE LIMITS DESIGNED FOR EQUATION [45] AND [42]

Data Source: Fresco (27)
Temperature: 100°F

Method	No. of Fluids	Avg. Abs. Dev.*	Bias*	RMS*
(a)	10	0.805	0.359	1.105
(b)	10	0.489	-0.106	0.617
(c)	5	0.508	0.139	0.739
(d)	10	0.538	-0.014	0.597

* Defined in Table 11, units are $(1/\text{psig})x(10^4)$

(a) Equation [45]

(b) Equation [42]

(c) Fresco (27)

(d) Kouzel (26)

C. The Effects of Chemical Reactions in Boundary Lubrication. The term "boundary lubrication" was first introduced by Sir William Hardy (45) in 1922 in describing a region where "the solid faces are near enough to influence directly the physical properties of the lubricant, and the friction depends not only on the lubricant but on the chemical nature of the solid boundaries." Recently, Dowson (46) defined boundary lubrication as the "surface interaction between a monomolecular layer of boundary lubricant and the solids dominate the operation of the contact. Hydrodynamic effects are negligible, and there is considerable asperity contact." While the words "monomolecular layer" are debatable, this definition is more precise than Hardy's.

Campbell (47) further clarified the term by stating, "Boundary lubrication is lubrication by a liquid under conditions where the solid surfaces are so close together that appreciable contact takes place between the asperities. The friction and wear are influenced predominantly by interaction between the lubricant and the solid, and the bulk flow properties of the lubricant play little or no part in friction and wear behavior." The word "interaction" will be qualified as "chemical interaction" in this work.

The object of this study is to investigate the effects of the chemical interactions between the solid surfaces and the lubricant. The lubricant will be restricted to mineral oils.

Lubrication is a very complex phenomenon. It is the reduction of friction and/or wear by a solid, liquid, or gas film existing between two surfaces moving against one another. In this work, only lubrication between metal surfaces by liquid hydrocarbons will be considered.

Lubrication can generally be classified into three regions: hydrodynamic, elastohydrodynamic, and boundary region. A classical Stribeck (48) diagram, as shown in Figure 23, illustrates these regions. At the minimum of the curve corresponding to point A, the coefficient of friction is about 0.002 and $\mu N/P$ quotient (where μ is the oil viscosity in centipoises, N the journal speed in rpm, and P the normal load per projected bearing area in psi.) varies from 1 to 10 according to the oil type, bearing geometry and material, and surface finish. For values of $\mu N/P$ above the minimum, the curve is quite linear. In this region, the oil film is thick enough so that the solid surfaces are completely separated from one another. The coefficient of friction depends on the fluid viscosity, sliding speed, and bearing geometry. This region is the most desirable state of lubrication due to its inherent protection of the solid surfaces by the fluid. There is no wear on the bearings. The lubrication mechanism in this region is fairly well explained by the hydrodynamic theory which is summarized by Hersey (49). Its development can be traced from Sir Issac Newton (1687) to Petroff (1883), Tower (1883) and Reynolds (1886). The journal bearing in an automobile operates hydrodynamically at high speeds.

According to Stribeck, the lubricating film begins to break down and asperity contact between the surfaces occurs at point A (Figure 23). The region between points A and B in Figure 23 has many names: elastohydrodynamic, quasi-hydrodynamic, partial fluid, and thin film lubrication. All these names indicate one thing, that is the solid boundaries begin to exert an influence on the lubrication at point A. Classically, it has been said that the load in region AB is supported partly by hydrodynamic action of the lubricant and partly by the boundary films. Recently, Dowson (46) proposed that in this region, the local elastic distortion of the solids provided coherent hydrodynamic films; and asperity interaction was prevented. The thin oil film was subjected to very high pressure and, as a result, the local viscosity increased greatly. Experimental data from Archard and Kirk (50) was used to demonstrate this theory. As N/P decreases below A, the proportion of hydrodynamic support decreases until at and below point B, lubrication is pure boundary. In region BC, the coefficient of friction is independent of the load; this is called Amonton's Law. It should be stressed that the curve shown in Figure 23 is only a representation of a set of data. For any other system, the points A and B may change their positions.

The regions discussed above are not very clear cut. In the context of this study, the boundary lubrication region has been previously defined as the conditions under which the distance between the solid boundaries is close enough that chemical interactions (as well as physical) between the solids and the lubricant play an important role in the lubrication mechanism. Thus the region ABC in Figure 23 would be included in this study.

1. Solid Surfaces and Dry Friction. Since the solid surface plays an important role in the mechanisms of boundary lubrication, the nature of the surface will be examined. On a microscopic scale, all metal surfaces used in lubrication are extremely rough no matter how finely they have been polished. An indication of the roughness generated by the various machining operations is shown in Table 44. Roughness characteristics have been studied by Shaw and Macks (51). With the most careful polishing, flatness can be carried to about 5 μ in. (1270Å). The atomic spacing in a metal is about 0.01 μ in. (2.5Å).

There have been many attempts both theoretically and experimentally to characterize the surface. The resulting knowledge is valuable but a satisfactory model has yet to emerge. As Moore (52) pointed out, most models failed in characterizing the surface using only one parameter such as the average height of the asperities or the root mean square (RMS) of the distance from a mean plane. In order to describe the surface fully, one has to take into account the height of the asperities; the void volume of the surface (the density of the asperities); and the sharpness of the peaks given by the second derivative of the surface profile. There are many experimental techniques that can be used to determine a surface profile. Excellent reviews in this area are given by Green (53), and Brown et al. (54). An indication of the surface roughness of a metal has been determined by Furey (55) using a stylus instrument on 52-100 steel.

When two dry surfaces meet, the contact area therefore is not equal to the corresponding surface area of the metal. The problem of determining contact areas for metal surfaces with idealized asperity shapes and distributions has been investigated by many researchers. Greenwood (56) showed that if the real area of contact between surfaces was determined by ideal plastic flow of the microcontacts, the area of contact was proportional to load. For elastic deformation, the average size of a microcontact was almost constant and independent of the load if the statistical distribution of asperity heights were considered.

The nature of the surface also depends on its past history (57). A surface being polished is different from a surface being ground using the same material.

One can study the surface topography with LEED (low energy electron diffraction) method using electrons whose range in the solid may be only a few tenths of an Angstrom unit. The resulting diffraction pattern is primarily that of the surface region. Using this method, one finds grinding leads to primarily mechanical attrition of the surface without changing its molecular crystallinity while polishing leaves a fairly deep and nearly amorphous surface layer, known as the Beilby layer. Beilby (58) showed that such a layer appeared amorphous under the microscope and had the general appearance of a film of viscous liquid that not only had covered the surface smoothly but had flowed into the surface irregularities such as cracks and scratch marks. Raether (59) concluded that the Beilby layer was actually microcrystalline. The formation of this layer may be due to the high temperature generated from the polishing operation and the subsequent metal softening if not actually melting.

Surface defects constitute another aspect of the surface condition. Actual crystals are not perfect; they may consist of microcrystalline domains bounded by slip planes, or they may have lattice irregularities surrounded by good crystals. The irregularities may involve a screw or spiral dislocation (60, 61). It is not uncommon for 20 percent of the volume of a crystal to be occupied by dislocations (62).

a. Thermodynamics of Surfaces. Surface tension is defined as the work spent in forming a unit area of surface (alternatively called surface free energy). The surface stress is defined as the work spent in stretching the surface. In a liquid, the surface mobility of the atoms is great and the surface tension is equal to the surface stress. In a solid, these two quantities are not necessarily equal due to the relative immobility of the atoms at the surface.

It is helpful to imagine that the process of forming a fresh surface of a monatomic substance is divided into two steps: first, the solid or liquid is cleared so as to expose a new surface, keeping the atoms fixed in the same positions that they occupied when in the bulk phase; second, the atoms in the surface region are allowed to rearrange to their final equilibrium positions. In the case of liquid, the two steps occur as one, but with the solid, the second step may occur only slowly through surface diffusion. Thus it may be possible to stretch or to compress the solid surfaces without changing the number of atoms in it, only their distances apart. Under this condition, a surface stress would be present. Dunning (60) postulated that the dilatant stress in small crystals could be relieved by the appearance of dislocations. A cube of ideal crystal subjected to compressive surface stress suffers deformation equivalent to applying traction to each edge of the cube. This stress could be relieved by rows of dislocations in which lines of atoms are missing, or by means of vacancies in surface planes (63). It thus appears that with a non-equilibrium surface whose surface stress and surface free energy values are not equal, there is a source of surface imperfections in addition to those representing the surface eruption of bulk imperfections. The ability of a surface to relieve a nonequilibrium stress may be very temperature dependent. At temperatures near the metal's melting point, both bulk and surface diffusion generally become appreciable. For copper (58) at 725°C, it takes 0.1 sec. for a copper atom in the bulk to diffuse 100 Å. At room temperature, it will take 10^{27} sec. The field emission microscope has shown that surface migration can be observed at as low as half the evaporation temperature of the solid.

At the surface, not all atoms possess the same energy level. Those atoms or molecules at the rugged asperity tips or the edge of a surface crack or imperfections of the crystal lattice possess higher energy and surface mobility than the average surface atom which has a normal number of nearest neighboring atoms. These high energy atoms are much more reactive and provide the most active adsorption sites for polar molecules.

In a situation where constant surface contact and rubbing take place, large shear stresses are always present. The resulting high temperatures at the asperity tips from the frictional energy will increase a surface atom's mobility and accelerate the rate to relieve the surface stress by creating more dislocations or imperfections. This results in more chemically active sites for adsorption and reaction.

b. Dry Friction of Metals. When two solid surfaces rub against one another, frictional heating is generated. Depending on the load and sliding speed, very high temperatures can occur at the surface. Because of the surface roughness, the real contact area is smaller than the surface area of the two surfaces. Therefore the heating is further localized around the asperities. The surface temperature had been measured (64) by measuring the electrical potential difference between the rubbing surfaces. In the case of a steel rider gliding over different metals, it can be shown that a temperature rise of several hundred degrees can occur. The temperature rise levels off at the melting temperature of the lower melting metal. If one of the surfaces is transparent, i.e., glass, the local temperature can be determined by infrared spectrophotometry. In this way, local temperatures as high as 1200°C have been measured for a steel on glass system (65).

The oxide film and the Beilby layer are the top most surface layers of a typical metal surface (66). These layers actually define the surface properties of the solid surface. The oxide film is usually of low mechanical strength and can be sheared off under high shear stress. The Beilby layer may be harder than the bulk material. Moore (67) measured the thermo-electric output between a wear pin (ingot iron) and a rough α-silicon carbide surface. The temperature at the junction was found to range from 300° to 900°C. The peak temperatures found are high enough to cause ferrite-austenite transformation in a pearlitic steel and the subsequent cooling rate fast enough to cause austenite to transform to martensite, which is harder than steel. Due to the fact that the hot spot temperature exists only at the site of real contact and the different temperatures reached at different asperity contacts, the martensite formation exists only at a few spots. This may explain plowing and scratching sometimes observed in boundary lubrication in wear tests under severe conditions.

There have been many attempts to predict theoretically the hot spot temperatures in dry sliding. Blok (68) and Jaeger (69) analyzed the heat transfer problem and derived several expressions to estimate the hot-spot temperature at the junction. They assumed adiabetic heating in different geometries with different simplifying assumptions. Archard (70) summarized the equations and popularized their usage. However, due to the extremely short duration of the contact and the small contact region involved, accurate experimental measurement has been very difficult to obtain. The accuracy of the theoretical prediction is still open to question. Several assumptions used in the theoretical analysis are, at best, quite crude. The temperatures are calculated on the assumption that the heat is generated at the area of true contact (i.e., a single area of contact is regarded as a plane source of heat). The estimation of the true area of contact again depends on whether plastic deformation or elastic deformation is assumed. On the other hand, the theoretical result indicates a maximum possible temperature rise, at least, qualitatively. The predicated temperatures are always much higher than the experimentally measured temperatures in dry sliding. The temperature rise is predicted to be from 700°C to 1200°C (70) for the dry wear of steel (0.52 percent carbon steel, V.P.N. 250).

Archard (70) also pointed out the effect of a surface film of low thermal conductivity on the flash temperatures. A protective film such as an oxide or a boundary lubricant would increase the surface hot-spot temperature and if the surface film thickness was large compared with molecular dimensions, the temperature gradient existing in the film could be easily the largest transient temperature in the contact zone and might be several times greater than the flash temperature.

In the unlubricated wear of steel, Quinn (71, 72, 73, 74) proposed an oxidative wear model. He assumed all of the mild wear of unlubricated steel-on-steel was due to oxidation of the steel, i.e., the steel surface oxidized to a critical thickness at which, under high shear, produced wear particles. The temperatures at which the steel oxidized were those hot spot temperatures at the junction. Quinn's wear equation is shown below:

$$W = [d\ A\ Ap\ e^{-(Qp/RT_O)}]/[\xi^2 \rho^2 V f^2] \qquad [53]$$

where:

W = wear rate, volume removed per unit sliding distance,

d = distance along which a wearing contact is made,

A = real area of contact,

Ap = Arrhenius constant for parabolic oxidation of steel,

Qp = activation energy for parabolic oxidation of steel,

R = gas constant,

T_O = temperature of oxidation,

ξ = critical oxide film thickness at each asperity contact,

ρ = density of the oxide film,

V = speed of sliding, and

f = mass fraction of oxide film which is oxygen.

Detailed derivation of this equation is shown in Ref. (71).

Equation [53] can be criticized that it contains too many ill-defined parameters such as d, ξ, A, and T_O. Quinn (71) recognized this but he agreed that independent estimates could be made on d, ξ, and A; therefore, T_O could be calculated from equation [53] with some wear rate data. Ap and Qp values were obtained from the static oxidation data on high purity steel by Kubaschewski (75) Quinn compared the oxidation temperature calculated from equation [53], 830°C (1526°F) with Archard's (70) flash temperature theory, 1250°C, and also with Furey's (77) experimental measurement of the contact temperature, 350°C (662°F) from dynamic thermocouples which Quinn (73) himself also obtained experimentally using x-ray diffraction patterns analyzing wear product composition (Fe_x0_y) as function of temperatures.

The discrepancy among the temperatures is not surprising. Static oxidation data may not be compatible with dynamic wear-oxidation. In the wearing process, new surfaces and the thickness of the oxide film are constantly changing. With three parameters d, ξ, A crudely estimated, one is surprised to see that the calculated temperature falls within the reasonable limits (350°C - 1250°C).

The steel Quinn used was a low alloy medium carbon steel similar to the steel used in large marine turbine shaft bearings. The steel composition is as follows:

Carbon	0.42%	Nickel	2.54%
Silicon	0.28%	Chromium	0.71%
Manganese	0.62%	Molybdenum	0.55%
Sulfur	0.16%	Copper	0.16%
Phosphorus	0.015%		

Earles (78, 79, 80, 81) and his coworkers also studied the wear characteristics of steels in relation to surface temperatures and oxidation. While the linear sliding speeds in Quinn's work ranged from 1 m/sec. to 8 m/sec., Earles (81) used much higher sliding speeds, 20-100 m/sec. Earles showed that at the same load, when the sliding speeds varied, the coefficient of friction and wear went through a transition from one type of behavior to another, which were related to temperature dependent changes in the metal and oxide properties. He showed that at higher sliding speeds, hence higher contact temperatures, FeO instead of Fe_2O_3, Fe_3O_4 was formed at the surface. Fe_2O_3 and Fe_3O_4 are known to have good friction and wear properties, while FeO does not. The properties of the oxides are presented in Table 45.

Tenwick and Earles (80) derived an equation correlating the average surface temperature (not the contact or flash temperature as in Quinn's work), load, sliding speed with oxidative wear of steels. Also instead of using a parabolic oxidation model to describe the oxidation mechanism, they used a linear oxidation model. However, as Berry (82, 83) pointed out, the two models were essentially identical except for the interpretation of the temperatures at which oxidation occurs.

Recently, Amsallem et al. (84) studied the wear of sintered iron in dry sliding both in air and in a nitrogen atmosphere. The result showed that different oxides having different wear characteristics were formed as the load varied under constant sliding speed. The wear debris were analyzed with x-ray and electron diffraction techniques. From the composition of the wear debris, the temperature was estimated to be 570°C at 80 N loading.

2. Chemistry of Lubrication. The wear resulting from lubricated contacts differs from that of dry frictional wear. The nature and the composition of the lubricant play a major role in the wear characteristics of the contact junction. The wear also depends on other parameters such as the relative speed of the moving parts, load, metal compositions, oxygen concentration in the oil and the environment, water concentration, operating temperature and geometric configuration of the contact surfaces. In this section, the plausible or probable chemical reactions that could take place in boundary lubrication are discussed.

There are hundreds of chemical species in a typical lubricating oil. Many of them have been identified only in the past twenty years. In an investigation which started in 1927, the American Petroleum Institute Research Project 6 has isolated 264 chemical compounds from one petroleum oil. When the lubricating oil is subjected to high local temperatures and extreme pressures in boundary lubrication, the possible chemical reactions that could result are literally numerous. In addition to the severe environment that the oil encounters, the clean metal surface generated in the wear process and the chemical additives usually added in commercial oils further complicate the situation. Therefore it would be futile, if not impossible, to study the elementary mechanisms of the chemical reactions that are taking place in boundary lubrication. However, some groups of reactions that play a key role in wear could be examined and the overall chemical effects in boundary lubrication, hopefully can be assessed accordingly.

a. The Chemical Composition of Lubricants. Lubricating oils from petroleum are composed mainly of hydrocarbons together with small amounts of organic compounds of sulfur, nitrogen, and oxygen and traces of organometallic compounds of vanadium, nickel, iron and copper. The hydrocarbons can be classified into three groups: paraffins (saturated straight or branched chains), naphthenes (saturated cycloparaffins), and aromatics (with benzene rings). Some typical structures in lube oils are illustrated in Figure 24. The petroleum oil fractions used in lubrication comprise principally compounds containing from 20 to 40 carbon atoms per molecule, especially from C_{20} to C_{25}.

The number of possible chemical compounds, according to stereochemistry for C_{20} is almost infinite (20^{20} possible variations). Chemical composition analysis on a number of lubricants in a recent study (86) indicate the approximate composition according to the classes of compounds. There are many molecular species in each of the classes. As is indicated, molecules sometimes have paraffinic structures together with aromatic rings or one single molecule can have all three classes of compounds. Therefore, from a chemical point of view, it is important to realize that in a "paraffinic" oil, all three classes of compounds exist, although the physical properties are influenced most strongly by the paraffinic portions.

During the past twenty years, high temperature mass spectrometry has become a powerful tool in analyzing complex petroleum fractions. Some of these studies were done by Hood (89), Melpolder (90), Lumpkin (91, 92). In another approach, developed largely by Waterman and Associates (93, 94) in Holland and Kurtz and Associates (95) in this country, analyses of petroleum oils were made by correlating physical properties of pure components to the oil being analyzed. The physical properties chosen are refractive index, density, and molecular weight (n-d-m method). Methods so based give the percentage of the total number of carbon atoms that occur in aromatic rings, and in paraffins plus paraffinic side chains. All of the information obtained with these methods is in accord with the picture of lubricating oils presented above. The individual hydrocarbon species and their properties identified thus far have been compiled by the American Petroleum Institute (API) Research Projects 6 and 42.

After carbon and hydrogen, sulfur is the next prominent element present in base oils. The most complete investigation of the sulfur compounds in petroleum have been done by the API Research Project 48, which has isolated 166 sulfur compounds from four crude oils. The types identified are alkyl, cyclic and aromatic thiols; alkyl sulfides, alkyl-cycloalkyl sulfides and cyclic sulfides; thiophenes and aromatic thiophenes. The content of thiols decreases rapidly with increasing boiling point material. The alkyl sulfides, as the boiling point increases are replaced by cyclic sulfides. From a mass spectrometric examination of a lubricating oil fraction. Lumpkin and Johnson (91) concluded that the majority of sulfur compounds in the higher boiling fraction were of the condensed aromatic type. Later, Lumpkin (92) found that the trinuclear aromatic portion from the 347°-460°C (656°-680°F) boiling range of a high-sulfur crude contained the following: indanothiophenes 4.2%; indenothiophenes, 1.8%; dibenzothiophenes, 39.7%; acenaphthenothiophenes, 1.5%; and benzodithiophenes, 2.8%.

The early work of Bailey and Lochte (1955) showed that the nitrogen compounds which were extractable with dilute mineral acids, arbitrarily classified as "basic", contain both quinolines and pyridines carrying alkyl substituents. In 1954, a study on the identity of the "non-basic" nitrogen compounds (cannot be titrated with perchloric acid) in petroleum was undertaken by the API Research Project 52. The results indicate that pyrroles, indoles, and carbazoles are the principal constituents. Phenazines, benzonitriles, and amides have been detected in cracked oils. The results were summarized by Lathan (97).

The oxygen compounds in petroleum can be divided into two classes: acidic which can be extracted with bases, and neutral non-extractable components. The acids include normal and branched chain acids, and acids containing a cyclic group in the molecule, e.g., 2, 3-dimethylcyclohexane carboxylic acid. The presence of myristic, palmitic, stearic, and arachidic acids has also been reported (98). Four neutral oxygen-containing compounds, 1-, 2- or 3-, and 4-methyldibenzofurans and 4, 6- dimethyldibenzofuran, have been isolated from the reference petroleum of API Research Project 6.

Excellent reviews in the compositions of petroleum oils are given by Mair (99), Bondi (88).

b. Oxidation Reactions. The oxidation of the metal surfaces and the lubricants plays a prominent role in boundary lubrication. Analysis of wear debris in the boundary regime indicates the presence of metal oxides and oxidation products of hydrocarbon.

1. Oxidation of Metals, Especially Iron: Let the clean surface of a metal or an alloy be exposed to oxygen, chemical reaction will begin at the metal-gas interface. If the oxides formed are not volatile, they immediately form an intermediate layer between the alloy and the gas. The layers may be compact or interpersed with pores or cracks, so that further reaction may involve atomic diffusion or simply passage of gas molecules through the pores. Diffusion

may be through the grains, along grain boundaries or surfaces of the metal. When an alloy reacts, either one or all the component metals may form compounds with oxygen, the resulting layer may be a conglomerate of different particles or clearly subdivided into individual layers. Therefore, the characteristics of the oxidation layers for the metal-gas pair are vital in studying the oxidation of the metal. Since the energy states at an interface or surface differ from those in the bulk material, metallic compounds that are otherwise unstable may be formed at the interface. Gulbransen (100) found that Wustite, FeO was normally unstable below 570°C (1058°F) but an iron oxidized below this temperature formed a thin film of FeO underneath an Fe_3O_4 scale. The thickness of the film became less as the temperature of formation was lowered but it was still detected at 400°C (762°F). The energy required for four moles of FeO according to the equation

$$Fe_3O_4 + Fe \rightarrow 4FeO \qquad (2)$$

amounts to 2500 cal. at 400°C; it was suggested that this energy was supplied by the surface of the iron.

If a metal has several oxidation states and forms a number of compounds with oxygen, these compounds are arranged in layers with the one richest in oxygen at the oxide-air interface, and the one richest in metal in contact with the metallic base. Paidassi (101) has studied the oxide layers of cobalt and iron and discusses the observed positions of the various oxides formed.

If two metals of an alloy react with oxygen, the reaction products may exist as a heterogeneous mixture on the metal surface or as separate layers. The formation of solid solutions may also be present, e.g., Fe_3O_4 - Mn_3O_4, FeO - MgO, Fe_3O_4 - $MgFe_2O_4$, FeO - MnO.

Iron forms three stable oxides: Wustite, FeO, magnetite, Fe_3O_4 and hematite, Fe_2O_3. FeO is a p-type conductor, has an unusually high concentration of lattice defects which consist of vacant cation sites and an equivalent number of electron defects represented chemically by trivalent Fe or Fe^{3+} ions. Consequently diffusion is mainly cationic via vacant cation sites. Magnetite, Fe_3O_4 has a lower defect concentration. Diffusion is both cationic and anionic. Hematite, Fe_2O_3 is an n-type conductor in which anions largely diffuse. Their chemical reaction equations are as follows:

$$Fe + \tfrac{1}{2} O_2 \rightarrow FeO \qquad [55]$$

$$3Fe + 2\ O_2 \rightarrow Fe_3O_4 \qquad [56]$$

$$2Fe + 3\ O_2 \rightarrow 2\ Fe_2O_3 \qquad [57]$$

Quinn (74) in studying the dry wear of steel in air, determined the composition of the wear debris in a pin and disc system using a x-ray diffraction technique. His work shows clearly the volume percentages of α-iron, Fe_2O_3 and Fe_3O_4 for externally induced temperature experiments. The work was conducted at a relatively low sliding speed of five centimeters per second and at a high sliding speed of 625 centimeters per second. From these results, Quinn demonstrated that at low temperature, the major reaction product was Fe_2O_3 between the two rubbing surfaces in air. As the temperature goes up, the amount of

Fe_2O_3 decreases and the amount of Fe_3O_4 increases. FeO is shown to be absent in this temperature region. The amount of α-iron i.e. due to mechanical wear, is low and drops to an insignificant amount when the bulk temperature rises above 100°C.

Tao (102, 103) proposed that all wear was due to chemical corrosion, i.e., the growth of an oxide layer and its subsequent removing by rubbing. He found that a mathematical model based on this assumption performed quite well in correlating his wear test results with a ball-on-cylinder device (56 cm/sec). The analytical results showed that the rate of metal oxidation was the important factor in determining the wear rate. Since the oxidation rate depends heavily on the temperature at the contact zone, Tao's results also imply the importance of temperature in boundary lubrication.

2. Oxidation of Lubricating Oils. Very little is known about the oxidation mechanism of lubricating oils, largely because of the extremely complex chemical compositions involved. Voluminous literature, however exists on oxidation of simpler hydrocarbons. Several excellent reviews on the oxidation of lubricating oils have been written by Zuidema (104) and Bondi (88).

Lubricating oils are composed of such a complex mixture of hydrocarbons that it is extremely difficult to identify specific compounds in their oxidation products, except for such degradation products as water, carbon dioxide, and some of the lower carboxylic acids. Since lubricating oils are composed of mainly three groups of hydrocarbons, paraffin, naphthene, and aromatic, it would be appropriate to examine the nature of the chemical reactions of pure hydrocarbons of these three types under oxidation conditions.

Chavanne and coworkers (105, 106, 107) studied the oxidation of a few paraffins and naphthenes. They oxidized n-decane, n-nonane, and n-octane with oxygen at atmospheric pressure and a temperature of 120°C. The gaseous oxidation products, which account for 10 percent or so of the total, were similar in all three cases: 30-40% CO_2; 5-7% H_2; 1-2% saturated hydrocarbons. The liquid products contained water, succinic acid, and formaldehyde. The three hydrocarbons produced a significant amount of methyl-octyl, methyl-heptyl and methyl-hexyl ketones, respectively, together with series of carboxylic acids ranging from formic to Cn_{-1} (n is the number of carbon atoms in the hydrocarbon). Octanol was formed from n-octane. From these data, one would conclude that the beta carbon was attacked primarily, the gamma secondarily, and so on toward the center of the molecule. The view was substantiated by other workers later.

Several investigators have shown that water is one of the principal oxidation products of lubricating oils (108, 109, 110). Zuidema (104) proposed the following mechanism for the oxidation of paraffins at temperatures between 100° to 200°C:

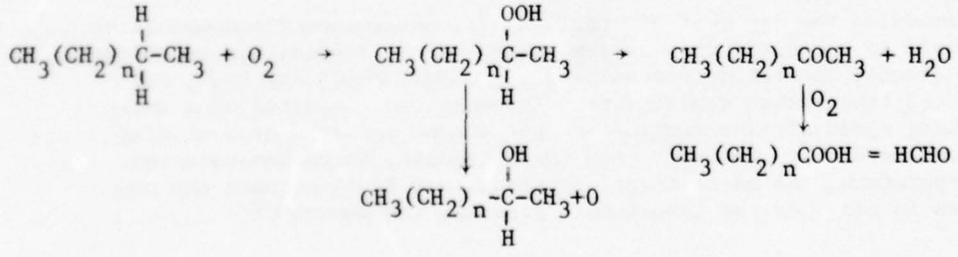

$$CH_3(CH_2)_n\overset{H}{\underset{H}{C}}-CH_3 + O_2 \rightarrow CH_3(CH_2)_n\overset{OOH}{\underset{H}{C}}-CH_3 \rightarrow CH_3(CH_2)_nCOCH_3 + H_2O$$

$$CH_3(CH_2)_nCOCH_3 \xrightarrow{O_2} CH_3(CH_2)_nCOOH = HCHO$$

$$CH_3(CH_2)_n\overset{OOH}{\underset{H}{C}}-CH_3 \rightarrow CH_3(CH_2)_n-\overset{OH}{\underset{H}{C}}-CH_3+O$$

Since Engler (111) and Bakh (112) first proposed the formation of a peroxide, this scheme of oxidation has been called the Engler-Bakh peroxide theory.

Chavanne and Bode (105) made an extensive study of the oxidation products of 1,4- dimethylcyclohexane under atmospheric pressures and at 100°C. The principal oxidation products were 1,4- dimethylcyclohexanol, with water, carbon dioxide, β-methyl-δ-acetylvaleric acid, glycolic acid, acetic acid, β-methylvaleric acid, dimethylcyclohexanediol, and acetonylacetone. Small amounts of hydrogen, carbon monoxide, methane, ethane, and formic acid were also detected. The authors postulated the following mechanism:

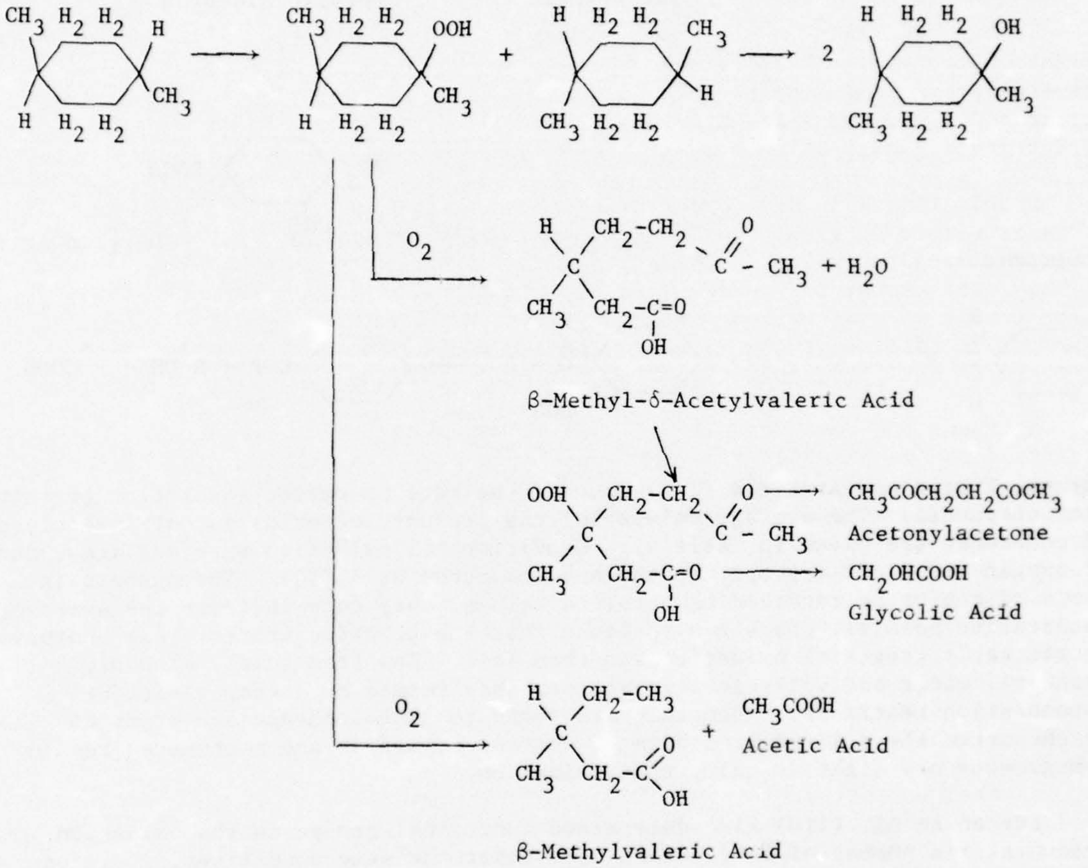

Stevens and Roduta (113) made a study of the slow oxidation of a series of benzene derivatives. They bubbled oxygen through the hydrocarbon for a number of days at temperatures from 80° to 140°C. Their results are summarized in Table 46. Zuidema (104) again proposed the formation of hydroperoxide to explain Stevens' data. He pointed out that oxidation always centered about a carbon atom attached to the benzene ring. The methylbenzenes all formed aldehydes with the same number of carbon atoms as the parent molecule. The substituted benzenes containing larger groups all formed ketones containing a phenyl group plus the other R group originally attached to the benzene ring. Acids, resulting from the further oxidation of aldehydes or ketones, were also formed. Acids were formed from the fragments split off in the formation of ketones from secondary compounds. Zuidema proposed the following mechanism:

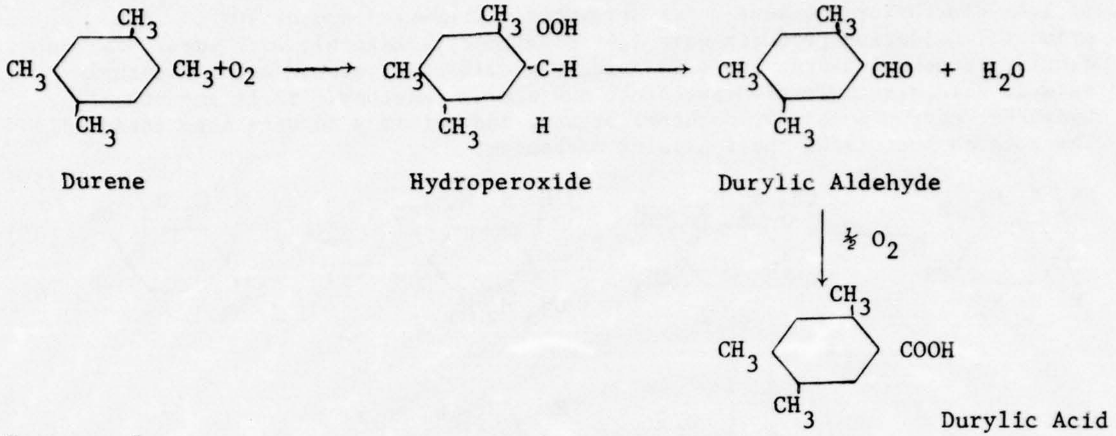

In general:

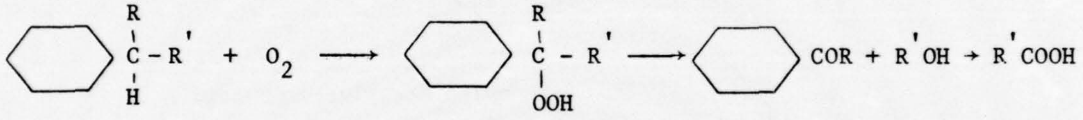

Larsen, Thorpe and Armfield (114) studied the rate of oxygen absorption of thirty-nine compounds. The average values for the products of oxidation of five classes of compounds are given in Table 47. Conditions of oxidation were one atmosphere of oxygen and 110°C (except naphthalene compounds at 150°C). The numbers in Table 47 cannot be regarded as absolute values, they only indicate the average, qualitative results. Larsen also found that the peroxide content rose sharply in the early stages of oxidation and then fell. The free acids, alcohol, carbonyl, water and volatile acid are probably formed by decomposition or condensation reactions. Aromatics are found to give condensation products which darken the oil and precipitate, whereas paraffins and naphthenes remain homogeneous and light in color upon oxidation.

Larsen et al. (110) also determined functional groups in the oxidation products of a number of lubricating oils under the same conditions, i.e., one atmosphere of oxygen, and 110° or 150°C. The results for nine oils are shown in Table 48. The first seven are lubricating oil fractions, while the eighth is a synthetic oil made by polymerization of cracked-wax olefins. The last is a white oil. Both of the last two oils are aromatic-free. The first six are California furfural raffinates of various stages of extraction, as indicated by the progressively increasing viscosity index. It can be seen that as the aromatics are removed, there is a marked tendency toward a lower asphaltene content in the oxidized oil. This observation is consistent with the conclusion based upon work on pure hydrocarbons that aromatics give dark insoluble condensation products.

Recent theory on the oxidation of hydrocarbons proposes free radical chain reactions. Excellent reviews have been made by Emanuel (114, 115, 116), Boss (117), Agabekov et al. (118), and Boudart (119). The radical chain mechanism is consistent with Zuidema's hydroperoxide theory but more sophisticated in concept. The chain mechanism can be roughly classified into four stages: initiation, propagation, branching, termination.

Initiation:

$RH + HR \longrightarrow 2R' + H_2$ (weak C-H bond) [58]

$RH + O_2 \longrightarrow + HOO'$ [59]

$RH + RH + O_2 \longrightarrow 2R + HOOH$ (lowest energy required) [60]

$RH + \text{Energy} \longrightarrow R' + H'$ (high temperature required) [61]

Propagation:

$R' + O_2 \longrightarrow ROO$ [62]

$ROO + RH \longrightarrow ROOH + R$ [63]

$R'H + ROO \longrightarrow ROOH + R'$ [64]

$R' + ROOH \longrightarrow ROH + RO'$ [65]

$R_1CH(OO)R_2 + R_1CH(OOH)R_2 \rightarrow R_1COHR_2 + R_1CH(OH)R_2 + O_2$ [66]

$R_1COHR_2 + RH \longrightarrow R_1CH(OH)R_2 + R$ [67]

$ROO + >=< \longrightarrow ROO\text{-}C\text{-}C\text{-} \longrightarrow RO_2\text{-}C\text{-}C\text{-}OO$ (Olefins)

$RO + >C \overset{O}{-} C<$ [68]

$ROO + O = \longrightarrow ROO\text{-}\overset{O}{C}$ (aromatics) [69]

Degenerate Branching

$ROOH \longrightarrow RO + OH$ [70]

$ROOH + R'H \longrightarrow RO + H_2O + R$ [71]

$ROOH + >C = C< \longrightarrow RO + >\overset{OH}{C}C\text{-}C<$ [72]

$ROOH + R'\overset{O}{C}OH \rightleftarrows [ROOH \ldots HOOCR] \rightarrow RO + OH + R'COOH$ [73]

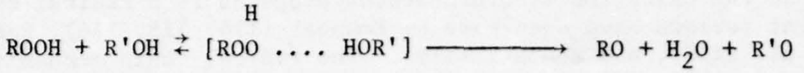

$$ROOH + R'OH \rightleftarrows [ROO \overset{H}{....} HOR'] \longrightarrow RO + H_2O + R'O \qquad [74]$$

$$ROOH + R_1COR_2 \rightleftarrows [R_1C(OH)(ROO)R_2] \longrightarrow RO + R_1C(O)(OH)R_2 \qquad [75]$$

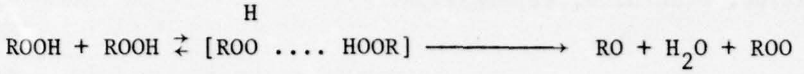

$$ROOH + ROOH \rightleftarrows [ROO \overset{H}{....} HOOR] \longrightarrow RO + H_2O + ROO \qquad [76]$$

Termination

$$R + R \longrightarrow R\text{-}R \qquad [77]$$

$$R + ROO \longrightarrow ROOR \qquad [78]$$

$$RO + RO \longrightarrow ROOR \qquad [79]$$

Equations [58] and [79] represent some of the chain reactions that can take place in hydrocarbon oxidation. Different starting chemical composition, different temperatures and pressures will make some of the reactions dominate the system.

In summary, the oxidation reactions of lubricating oils are numerous and complex. Peroxides or hydroperoxides play an important role in the early stage of oxidation. For paraffins, the main oxidation products are: alcohols, aldehydes, ketones, and acids. For naphthenes, alcohols, ketones, dicarboxylic acids are formed. For aromatics, phenol, aromatic monocarboxylic acids, dicarboxylic acids, and unsaturated dicarboxylic acids are formed. Comparatively, aromatic hydrocarbons are more stable toward oxidation than naphthenes, which, in turn, are more stable than paraffins.

In this section, the nature of the oxidation reactions, intermediate compounds, final products of the lubricating oils have been examined. The possible chemical effects of these reaction products on boundary lubrication will be discussed in a later section.

c. Thermal Decomposition Reactions of the Lubricants. Petroleum hydrocarbons, upon heating, decompose to form smaller or more reactive species. Secondary reactions from these initial products may result in the formation of larger than, smaller than, or the same size as the molecules present in the starting material. The temperature at which this phenomenon occurs depends on the bond energies of the weakest bond in the molecule. In this respect, the carbon-hydrogen bond is stronger than the carbon-carbon bond. Recent studies (120, 121) have shown that triple bonds are more thermally stable than the double bonds which are more stable than the single bonds. Within the carbon-carbon bonds, a naphthenic ring is stronger than a straight chain hydrocarbon. Among the paraffins, the straight chain molecules are more stable than the branched ones. In a given class of hydrocarbons, the susceptibility to cracking increases with the molecular weight.

The breakdown of paraffinic hydrocarbons occurs at any carbon-carbon bond with some predominance at the middle of the chain.

The rupture of naphthenic rings takes place only under severe conditions. Temperatures of 1000°F are required to achieve extensive ring rupture. In complex organic molecules, the decomposition of paraffinic side chains attached to naphthenic rings constitute the major reactions. The alkylated naphthenes crack to yield a paraffin, naphthene with olefinic side chain, or an olefin and a naphthene with paraffinic side chain. Naphthenes with very short side chains are more stable thermally than those with long side chains.

Olefins, upon cracking, decompose as well as polymerize through condensation reactions. Under moderately high temperature, both types of reactions occur simultaneously. Generally, however, under conditions of gradually increasing temperatures, the polymerization or formation of high molecular weight hydrocarbons would be the first reaction. With slightly more heat, isomerization and decomposition reactions set in. The simple mono-olefins are found to polymerize to higher hydrocarbons at 300°C with sufficient contact time. High pressure enhances the polymerization.

The thermal stability of aromatic hydrocarbons depends on the nature of its side chains. The benzene ring by itself is similar to a naphthenic ring requiring high temperatures (1000°F) to obtain substantive ring breakage. High boiling fractions from petroleum contain aromatic hydrocarbons having long paraffinic side chains. These side chains exhibit stabilities similar to those of paraffinic hydrocarbons. A number of studies (123, 124) have been conducted on the stability of alkylated aromatic hydrocarbons. The methylated aromatics are the most thermally stable compounds at the same carbon number as compared to other hydrocarbons.

The most widely accepted mechanism of the thermal decomposition of hydrocarbons is the free radical theory. Rice and Herzfeld (125) proposed that the reactions were initiated by the generation of free radicals by splitting the molecule at its weakest bond. One of these radicals abstracted the hydrogen atom from the parent compound to form a small saturated molecule and a new free radical. Both radicals could react this way. The rates of removing the hydrogen atom are 1:3.2:10.3 for primary, secondary, and tertiary hydrogens at 600°C respectively. A comprehensive monograph has been written on free radical reactions by Steacie (126).

The effects of the thermal decomposition on the rate of oxidation are not clear. The two kinds of reaction usually occur simultaneously. The generation of free radicals by thermal degradation would certainly increase the amount of free radical concentration. The free radicals, being very active chemically, would seem to increase the oxidation rate.

d. Boundary Surface Reactions. In hydrodynamic lubrication, the surfaces in relative motion are separated by a lubricant layer of considerable thickness and under ideal conditions, there is no wear of the solid surface. If the sliding speeds are low and the loads are high, the lubricant layer breaks down and the surfaces are separated by lubricant films of only molecular dimensions. Under these conditions, the friction is influenced by the nature and the chemical constitutions of the boundary surface and the lubricant. The bulk viscosity plays little or no part in the frictional behavior.

Since the effectiveness of the lubricant depends on the nature of the boundary film, there have been many attempts (127 through 132) to determine the chemical compositions and the physical characteristics of the film. Tabor and Willis (131) studied the lubrication of heavily-loaded sliding copper contacts (100 kg/mm^2 at contact) by a low viscosity (10 cs.) dimethylsilicone fluid containing 0.5 percent by weight of stearic acid. At temperatures above 100°C, electrical resistance measurements showed that the film was nonconducting. Infrared spectroscopic analysis showed the film to consist of a high concentration of copper stearate embedded in a cross-linked polysiloxane matrix. The molecular structure of the metal soap was very complex. They further suggested that the load-bearing properties of the film were dependent on the high concentration of copper stearate, the polysiloxane network simply served as a matrix. In the absence of the fatty acid, the polymer was readily worn away by the sliding process.

Materials such as fatty acids which have a polar OH group at one end of the molecule have been studied extensively in boundary lubrication. They have been considered to adsorb on the metal surfaces forming well-defined "boundary films" which are oriented monomolecular adsorbed layers attached to the metal via the polar head (OH group). These films are considered to break up and lose their effectiveness when their melting points are exceeded. Recent researchers using radioactive tracers, electron microscope, and x-ray diffraction have shown the main constituents of the film to be a mixture of hydrocarbons, surfactants (polar molecules), metals and their oxides. The complexity and the possible interactions among these constituents of the film have been recognized only in the last decade.

Summers-Smith (132) studied the chemical reactions on bearings in lubricated industrial machines. The temperatures reached in the bearings of high speed machines are such that chemical reactions, at times leading to bearing failure, can occur. A summary of the chemical reactions involving sulphur is presented in Table 49. In item 1, the metals involved are tin-rich alloys (typical composition: 80% Sn, 15% Sb, 5% Cu). There are two points worthy of comment in these examples. The reaction products were identified by x-ray diffraction as a mixture of a basic copper sulphate, $CuSO_4 \cdot 2Cu(OH)_2$, and a copper sulphide, $4Cu_2S.CuS$. Both of these were confirmed as reaction products by the deficiency of copper in the underlying white metal and evidence of intergranular attack. The chemical reaction appears to be closely temperature dependent. On a thrust pad, the thickness of the reaction layer followed the temperature profile on the pad. The second point is that after numerous bearing failures with the machines the bearing metal was changed to a copper free, lead-rich white metal (10% Sn, 15% Sb, 75% Pb). No failure occurred within the normal useful life of the bearing in the same environment.

Godfrey (128) reported that the major constituent of the boundary lubricating film in a steel-on-steel system was Fe_3O_4 with small amount of FeS and FeO. The tests were conducted with a SAE extreme-pressure machine and a sulfurized mineral oil (sulfur saturated USP mineral oil) under 200 pounds or more loading. An iron carbide (77.4% Fe, and 17.4% C) was identified in a few cases. The test cups were made of SAE 4615 steel (60-62 Rockwell hardness).

Ever since Hermance and Egan (133) described the amorphous organic solid, they found on the palladium contacts as "friction polymer", the term has been used to describe the resinous-like wear debris. Fein and Kreuz (134) analyzed the compositions of this amorphous solid in the contact region with infrared spectroscopy and found 72.7% C, 6.6% H and 4.1% Fe. The solid analyzed was obtained from a four-ball machine with 52100 steel ball bearings at 0.35 cm/sec sliding velocity with benzene as the lubricant. This material was insoluble in common solvents and appeared to gradually char on heating. The infrared spectrum as well as its chemical analysis, showed that it was organic in character. When cyclohexane vapor was used instead of benzene, the "polymer" generated was partially soluble in cyclohexane and completely soluble in chloroform. Both "polymers" indicated the existence of carbonyl (C=0) and probably carboxylate soap (COO) bonds. Besides these resinous solids, Fe_2O_3 and Fe_3O_4 were also present. They also found that if oxygen was excluded from the system, the wear product consisted of black ferromagnetic particles, identified as "FeC" by x-ray diffraction.

Oxygen seems to play an important role in these reactions involving the boundary surfaces. Brown and Burton (135) studied the frictional behavior of 52100 steel as a function of oxygen partial pressure and found at extremely low oxygen concentration, 10^{-9} torr, the friction was very high and severe wear resulted. At high oxygen pressure, the oxide formed acted as a boundary lubricant, hence reducing the friction. Appeldoorn, Goldman and Tao (136, 137) studied the effects of water and oxygen on scuffing and found that water and oxygen caused significant increases in wear. The tests were conducted on a four-ball wear machine with 52100 steel at 1200 rpm and 77°F. The authors explained the observations with a corrosive wear mechanism of forming and subsequent removal of metal oxides. The white oil used was acid-treated to remove all polar and aromatic impurities. They also contended that air or moisture was not necessary for successful additive action as stated by Tingle (138), Godfrey (139, 140), and Barcroft and Daniel (141). This apparent contradiction is probably due to different operating conditions as will be explained later.

The results of these studies demonstrate that the sliding behavior of metal lubricated by hydrocarbons under boundary conditions can be related to chemical reactions at the sliding surfaces involving metal, hydrocarbon and the available oxygen and water. The following sections will examine the organometallic chemistry and the effect of temperature and pressure on such reactions.

All chemical reactions involve either the breaking or forming of a bond. The strength of a bond is directly proportional to the distance between the two molecules. The activation energy indicates how easy a particular reaction would occur, however, there are very few data available in the literature. An indirect indicator of the relative energy requirement of the formation or repture of a particular bond would be the heat of formation, ΔH_f. Table 50 lists some ΔH_f data on some bonds at 25°C.

From Table 50, it can be seen that the iron-oxygen bond has a large negative heat of formation, indicating that the iron is easily oxidized. Carbon-oxygen bond, which has a ΔH_f of -12 kcal/mole, is smaller than the CO-O bond forming olefinic peroxide (ΔH_f = -50 kcal/mole). The direct bonding between iron and carbon is relatively difficult but sulphur combines readily with iron. The low energy requirement of the iron-sul bond explains why some sulfur-containing oils exhibit beneficial effects in boundary lubrication. From these energy requirements of the various bonds, organic acids, peroxides (typical oxidation products) would be relatively easy to react with iron. A hypothetical RCOO-Fe bond would require a minimum amount of energy to form. In this respect, the hydrocarbons could be oxidized to give peroxides or acids which would react with the iron or iron oxides. If oxygen is not available, the iron may react with the more polar molecules like phosphate, chlorides or long chain hydrocarbons at a higher temperature to meet the higher energy requirements.

There are two types of organometallic compounds: one involves the direct bonding of metal-carbon bond; the other type contains both the metal and carbon atoms but does not have a direct carbon-metal bonding. The latter type consists mainly metal alkoxides, organometallic complexes and organometallic polymers. This type is quite difficult to analyze and some are very unstable. The postulated RCOOM (M=metal) bonding will be this type of compounds. The vast literature or organometallic chemistry considers mainly the compounds having a direct carbon-metal bonding.

Carbon is a fairly electro-negative element, hence might be expected to form ionic bonds only with the most electropositive elements, like sodium and potassium, and to form electron-pair covalent bonds with other elements, like iron, copper, nickle, and chromium. In boundary lubrication, only metals of the d-block transition elements in the periodic table are of interest. The properties of these organometallic compounds are heavily influenced by their organic ligands: alkyl, aryl. carbonyls, or hydrides. Most of the organometallic compounds would exhibit the following behavior: rapid oxidation; facile cleavage by protic agents; and complex formation.

$$\text{R-M} - \left[\begin{array}{lll} O_2 \longrightarrow & \text{R-O-M} & [80] \\ \text{H-S} \longrightarrow & \text{RH + M-S} & [81] \\ :\text{B} \longrightarrow & \text{R - M:B} & [81] \end{array}\right.$$

There are several relatively well-known iron organometallic compounds. Ferrocene, $(C_2H_5)_2Fe$, and its derivatives can be generated by heating cyclopentadiene with iron to 300°C (572°F) (145) in an inert atmosphere. Relatively speaking, ferrocene has exceptional thermal stability (300°C) as compared to most other organometallic compounds (100°- 200°C). It had been used as an anti-knock additive in automotive engines but was abandoned after it was found that the wear in the piston rings increased by as much as eight times (146) compared to the other anti-knock additives such as tetraethylead. Iron carbonyls, $Fe(CO)_5$, can be formed by passing carbon monoxide gas over heated iron. It is an active compound reacting with butadiene to give a complex. It is used as a catalyst in carbonylation (process in which carbon monoxide is introduced into a molecule) The hydrocarbonyls of cobalt and iron are efficient homogeneous hydrogenation catalysts. Also, iron carbonyls can isomerize olefins.

In summary, the oxganometallic compounds can be very complex. Their chemistry is not well-understood, many of them are being tested as a catalyst in hydrogenation and polymerization reactions of hydrocarbons. In general, they tend to react more readily with unsaturated hydrocarbons. Due to the catalytic properties of the transitional metals, the reaction products, sometimes, are not predictable. Whether these products are formed in boundary lubrication systems is not definite. A reasonable guess would be that two types of organometallic complexes are formed in boundary lubrication depending on the temperature at the junction and the oxygen concentration. If temperatures are high and oxygen is in short supply, carbon-metal bonds may form, if oxygen is plentiful, then some kind of metal alkoxides with hydrocarbon ligands may form preferentially due to the low energy requirement.

3. Experimental Technique Development. Since the chemical reactions in boundary lubrication are numerous and complex, it is not practical to study all of the reactions. In reality, chemical reactions that ultimately will affect the lubrication are those involving the boundary surface. The bulk fluid oxidation/degradation reactions are important only when their reaction products are adsorbed onto the surface and dominant the surface region. Therefore, the chemical reactions between the surfaces and the adsorbed molecules are the key reactions. Since the surface consists mainly of iron molecules, the key reactions to be considered can be further narrowed to chemical reactions between iron and polar hydrocarbons.

Of the many parameters affecting these reactions, temperature is the most important variable. The rates of chemical reactions sometimes vary exponentially with temperature. Also entirely different reactions may result if the temperature is changed over a large range. Therefore, the first step will be to define the temperature under which the chemical reactions occur.

The temperature at the lubricated junction, at present, is ill-defined. There have been many attempts to experimentally measure the junction temperature. But as can be seen from the previous discussion on the hot-spot temperature in dry sliding, large discrepancies exist among various calculations and experimental results. In lubricated contact, the picture is further complicated by the presence of lubricant, which is being pumped through the junction by the relative motion of the moving surfaces. From the standpoint of heat transfer, the overall average temperature at the junction will probably be lower than the dry sliding case since the frequency and contact of the surface asperities are reduced by the lubricant, hence less heat is generated by friction. The circulating lubricant acts also as a coolant to reduce the temperature. On the other hand, there will be an additional heat source due to the viscous dissipation of heat due to shear. The critical ramification due to the presence of the lubricant, however, is the localization of the hot-spots in the junction. Petroleum oils usually have very low thermal conductivity compared to metals. In the case of dry sliding, the heat generated at the junction is quickly conducted away. In lubricated contact, the lubricant acts like insulation. As asperity-asperity contact occurs, the heat generated will be dissipated at a much slower rate providing localized hot-spot temperatures. For the adsorbed molecules at the vicinity of the heat source, the localized hot-spot temperature provides the energy for chemical reactions.

With these considerations in mind, and with the aid of the results of the previous work carried out at this laboratory, an experimental program was put together to estimate the surface temperature in the lubricated junction.

a. Review of Previous Work. Boundary lubrication studies using activation analysis are discussed in Annual Report AFML-IR-67-107, Part II. The wear debris from a Shell Four-ball Wear Tester was separated into three fractions; namely, organic, insoluble metallic, and soluble metallic debris. The method of separating the organic and organometallic debris from the metallic particles in the sludge was developed using pyridine as the extracting solvent. Activation analysis was used to determine the metal content of both fractions. By assuming iron had the same reactivity as manganese, the amount of iron in the sludge could be determined by counting the gamma-rays emitted from the manganese-56 produced by the thermal neutrons reacting with maganese-55.

A continuation of studies of this type included in Annual Report AFML-TR-67-107, Part III, indicates that the assumption of equal reaction rates of iron and manganese was probably not valid. Atomic absorption spectroscopy was used to determine the metal content of the various fractions from wear debris.

Additional studies using atomic absorption spectroscopy are included in Annual Report AFML-TR-74-201, Part I. The wear debris was analyzed by washing the four ball assembly with naphtha and collecting the solids on a filter paper. The filter paper was dissolved in pyridine and the solution was filtered again to yield the organometallic fraction. The metal particles left on the second, different filter paper were dissolved in strong hydrochloric acid and the filtrate contained the insoluble metals in the wear debris.

Although these investigations were exploratory in nature, they demonstrated positively that successive solvent extraction coupled with atomic absorption spectroscopy was a viable way to analyze the wear debris and gained insight into the mechanism of lubrication.

b. Experimental Equipment and Operating Procedures. Two Four-Ball Wear Testers were used in this study. One is a Shell Four-ball Wear Tester which has been described in detail in previous reports. The majority of the data was obtained using the second, new four-ball wear tester which has been modified as proposed by Brown (147) of General Electric Company. This second wear tester will be referred to as the GE/Brown modified four-ball tester in this work.

1. Four-ball Wear Tester (GE/Brown Modification). A diagram illustrating the essential working parts of the wear tester is shown in Figure 25. It consists of an oil cup fitted with clamps to hold three balls in a planar configuration, and a precision chuck to hold the fourth spinning ball on top of the other three. The load on the ball contact points is controlled by air pistons which provide 0.1 to 180 kg. loads. Two interchangeable pistons were used. The low load piston supplied 0.1 to 18 kg. force, the high load 1 to 180 kg. force. An air bearing system supports the heating block (D) and ball-cup (H). This enables accurate measurement of the shear strain by a Statham force transducer with D.C. power supply. Both the transducer output and the temperature control system are continuously recorded on a Minneapolis-Honeywell strip chart recorder. The rotational speed of the top ball is provided by an eddy current motor connected by belt drive to the spindle giving stepless variable speed control under full torque from 30 to 3600 r.p.m. A speed reducer which supplied 60:1 reduction interchanges with the direct drive. The practical speed range of the machine is from 2 to 3300 r.p.m. Heat for the system is provided by a three-cartridge heating block which provides controlled temperatures to 1000°F. The thermocouple leads and heater connections dip into the mercury pools to give frictionless contacts. Provision for controlled atmosphere studies has been built-in in the system. As shown in Figure 25, the point P denotes the connection for controlled atmosphere gas inlet. In this study, either dry air or helium was supplied to the ball-pot all the time while running.

The wear tester is made by Roxana Machine Works, 1036 Hansom Drive, St. Louis 37, Missouri.

The following procedures were used in operating the GE/Brown modified four-ball wear tester:

1. The 52100 steel ½" diameter ball bearings (PRL Batch 15) were washed in naphtha and acetone and then wiped clean with a lintless tissue.

2. The ball-pot assembly was rinsed in naphtha, benzene and acetone successively. Then it was dissembled and each individual piece (ball pot, bottom piece, lock ring, clamp) were wiped with a white lintless tissue paper wetted with acetone. If any stain was detected on the tissue paper, the step was repeated until clean.

3. Three clean ball-bearings were then clamped into the ball-pot and locked tight.

4. The fourth ball was placed into the ball chuck which was cleaned as described in step 2.

5. The spindle which was to hold the ball chuck was cleaned with wet tissue paper with acetone until no stain could be observed on the white tissue paper.

6. The lubricant to be tested was poured into the ball-cup and its volume recorded.

7. The ball-pot was placed on the heater assembly and the chuck was placed in the spindle and tightened with drawbar (G).

8. Temperature was set on the Honeywell strip chart recorder. The thermocouple cold well was checked to see if additional ice was needed. The cold well was maintained at 0°C with an ice-distilled water mixture.

9. The valve on the controlled atmosphere inlet (P) was opened. The gas flow rate was set at 0.25 liter per minute for all runs.

10. The air bearing switch was turned on and its pressure was adjusted to 15 psi after loading the ball-pot.

11. The load switch was turned on and the air pressure was adjusted to desired pressure to give the proper load. (With the high load piston, 1 psi = 3 kg.; low load piston, 1 psi = 0.3 kg.).

12. The automatic timer was set to desired running time, usually 100 minutes.

13. The timer, heater, and motor switches were turned on.

14. The rheostat of the heater was set according to the following table:

RHEOSTAT SETTING FOR VARIOUS TEMPERATURES ON THE FOUR BALL MACHINE

Temperature, °F	Setting
100°	30
167°	35
200°	40
300°	50
400°	55
500°	60
600°	70
700°	80

15. The Honeywell chart recorder switches and the D.C. current supply switch were turned on.

16. The chain from the Statham transducer was hooked on the arm of the ball-pot.

17. When the ball-pot reached the set temperature, the motor was automatically turned on and the timer started. At the end of the set time, the motor would automatically be turned off.

18. With high temperature runs (500°F or up), the ball-pot should be retightened when hot to prevent rolling of the stationary balls.

19. At the end of the run, the ball-pot was unloaded. The air bearing and the switches turned off.

2. Atomic Absorption Spectrophotometer. The principle of atomic absorption spectroscopy and its application to analysis of elemental metals are described in detail by Slavin (148). Briefly stated, a liquid sample is converted into an atomic vapor by a hot flame (acetylene-air mixture) and irradiated by a monochromatic light source whose wave length is set to coincide with the emission lines of the metal. The absorption of the light by the vaporized sample is correlated to the metal concentration.

The atomic absorption spectrophotometer used in this study is a model 303 from Perkin-Elmer Corporation, Norwalk, Connecticut. It was used in conjunction with the Perkin-Elmer automatic null recorder readout and a Servo/Riter II Potentiometric recorder, model PS01W64 by Texas Instruments, Inc., Houston, Texas.

The operating procedures used in this study are similar to those presented in the manual. Some modifications were made to improve sensitivity and precision. The following procedures were used.

1. "Intensitron" source lamp from Perkin-Elmer for iron was used. It has approximately 10 percent higher sensitivity than an ordinary cathode lamp. The lamp was installed in the instrument.

2. Power switch was turned on. Half an hour was allowed to warm up the lamp. The lamp current was set at 30 ma. The wave length was set at 2483.

3. The lamp position was adjusted both vertically and horizontally to give maximum energy as indicated by the energy meter.

4. A three-slot burner head was used instead of the single-slot burner head. This gave higher sensitivity. The burner head was inspected for fouling. A razor blade was used to scrap it clean.

5. The burner head was adjusted so that the light would pass above the center of the burner head with a ¼" clearance.

6. Air was turned on. Its pressure set at 30 psi. Initial rotameter reading should be about 9 (at the center of the ball).

7. Acetylene was turned on after the exhaust fan of the hood was switched on. Initial rotameter set at 9 (the top plastic ball).

8. The flame was ignited and distilled water was aspirated for 15 minutes to warm up the burner head.

9. The aspiration rate for distilled water was adjusted to give 8 c.c./min. At this setting, maximum sensitivity was achieved for low concentrations.

10. The wavelength was adjusted to give maximum energy level as indicated by the energy meter by turning the fine control knob to about 2480 ± 10.

11. The energy meter indicating needle should always be inside the black region. During the course of analysis, if it fell outside the region, the wavelength could be adjusted to get it back into the black region without any adverse effect. However, if it was not adjusted, then the energy level would continuously fall off giving erroneous results.

12. The energy needle should be kept at the lowest possible level within the black region so that minimum gain could be used. This would reduce noise level significantly.

13. Depending on the sample fluid, the flame was adjusted by changing the air/fuel ratio to give a lean, hot flame. Caution should be taken not to make it too hot lest blow-back would occur damaging the burner. The following rotameter meter reading were used in this study:

ACETYLENE AIR RATIO FOR VARIOUS FLUIDS ON THE PERKIN-ELMER ATOMIC ABSORPTION SPECTROPHOTOMETER

Sample Fluid	Air Rotameter Reading	Acetylene Rotameter Reading
25% HNO_3	10	9
50% HCl	10	9
2:1 pyridine oil mixture	11	4.5
pyridine	11	5

NOTE: All readings were taken at the center of ball. The acetylene reading was for the top plastic ball.

14. At the end of the analysis, distilled water was aspirated for five minutes before shutdown. This would clear the burner chamber.

15. After every 30 hours of operation, the burner chamber should be taken apart and washed in warm water and soap and worn parts replaced. For some highly oxidized oils whose viscosity is high, the cleaning procedure should be followed after each analysis. Often times a widely fluctuating base-line was due to a dirty burner chamber.

3. Calibration of Standards. A calibration curve was developed by using a series of carefully prepared standard solutions whose metal concentration was known. These known standards were aspirated to give different levels of absorption. The level of absorption depended on such variables as the flame temperature, aspiration rate, electrical noise level, gas flowrate and recorder gain setting. It was difficult to reproduce consistently the same absorption level of a standard repeatedly. Therefore, a peak-height ratio calibration was developed. Instead of plotting the absorption levels of the standards versus concentrations, the ratio of the absorption level with respect to the same standard solution versus concentration was plotted. Thus, the effects of operating parameter variations were reduced to a minimum. In running unknown samples, the same standard solution was used after each unknown so that the ratio of the unknown peak height to the standard peak height could be measured. A typical trace is shown in Figure 26 and subsequent calibration chart is shown in Figure 27. By using the ratio of two peak heights, good precision was obtained. However, a new calibration was needed each time the machine was used.

c. Wear Debris Analysis. The wear debris in this study was separated into four portions: 1. Oil soluble organometallic iron; 2. Oil insoluble but pyridine soluble organometallic iron; 3. Solid iron particles dissolved in 3.92 N HNO_3; 4. Iron oxides dissolved in 5.06 N HCL inhibited with 0.014 M Acridine.

The filtration apparatus used in this study was a 47 mm diameter Millipore Pyrex filtering unit. The filter paper used was a 0.25 micron porosity Teflon membrane filter paper (Millipore Fluoropore) which contained no iron contaminants and resisted pyridine and acids. Due to its construction (the thin Teflon membrane was sandwiched between two polypropylene grids) leaks developed during filtration. This was solved by inserting a silicone rubber gasket between the filter and the filtering cup. A clean 25 c.c. sampling bottle was used to collect the filtrate inside the filtering flask. A Duo Seal vacuum pump was used to supply the vacuum.

1. Oil Soluble Organometallic Iron Sample. The oil from the ball-pot after a wear test was drained into the filtering apparatus. The oil sample collected was diluted with double-distilled pyridine. The mix ratio was 2:1 pyridine to oil. The purpose of this dilution was to reduce the viscosity of the oil so that samples with different degrees of oxidation, i.e., different viscosities, would end up approximately the same. On the other hand, too much dilution decreased the concentration of the metal in the sample. Since there was very little iron to start with, dilution above four would make the iron undetectable.

2. Pyridine Soluble Organometallic Iron Sample. The chuck holding the top ball was unscrewed from the spindle and put into the ball-pot. Fifteen cubic centimeters of double-distilled pyridine was added to the ball-pot and heated

until the temperature reached 180°F. This was followed by scrubbing the balls with a rubber policeman and the contents poured into the filtering cup. The hot pyridine was allowed two minutes on the filter paper before the vacuum was turned on. The filtrate was collected in a 25 ml. sample bottle. The ball-pot assembly and the chuck were then carefully rinsed with about 250 c.c. of prefiltered naphtha (0.25 μ) onto the filter to collect the solid wear debris. The same filter paper that filtered the oil now should have only a mixture of iron chips and iron oxide particles.

3. Iron Particles Sample. A method to separate the iron oxides from the iron particles generated during the wear process has been developed during the course of this study. Nitric acid, an oxidizing agent, has a very low solubility for any stable oxides. In fact, concentrated nitric oxide would not dissolve iron. Various concentrations of nitric acid were tested and a 3:1 mixture of concentrated nitric and distilled water (3.92 N) was selected. The following data were obtained when various components were mixed with 25 c.c. 3.92 N HNO_3 for two minutes and the mixture filtered through a 0.25 Millipore Solvinert filter paper and the filtrate analyzed for its iron content with the Atomic Absorption Spectrophotometer.

As can be seen from Table 51, the solution rate or selectivity between Fe_2O_3 and iron is about 800 times; 80 times for Fe_3O_4 and about 4 times for FeO. As discussed previously, FeO usually is formed at about 570°C (1026°F). Therefore unless the junction temperature reaches that high, very little FeO should exist in the wear debris. Therefore 3.92 N nitric acid was used to extract iron from the wear debris.

The filter and the filter holder containing the debris left after the pyridine extraction was rinsed with 20 c.c. acetone to remove entrained oil and to wet the filter paper which is hydrophobic. Ten cubic centimeters of 3.92 N nitric acid was measured into the filtering cup and was allowed 10 minutes contact time. At the end of ten minutes, the vacuum line was opened and the filtrate collected in the sample bottle ready for analysis.

4. Iron Oxides. Work reported previously in AFML-TR-74-201, Part I, involved the use of acridine-inhibited hydrochloric acid to separate iron and iron oxides. Those data are shown in Figure 28. It can be seen that the selectivity in solution is fairly good, ranging from 3 to 16 times. In this work, 5.06 N HCl (50:50 mixture of concentrated HCl and distilled water) inhibited with 0.014 M acridine was used to dissolve oxides left on the filter paper.

Before the addition of the acid, the filter paper and the filtering cup were rinsed with 20 c.c. acetone so that the nitric acid with its iron concentration would not mix with the HCl and affect the result. Ten cubic centimeters of inhibited HCl was introduced onto the filter paper and ten minutes contact time was allowed.

In these procedures, only one filter paper was used and the various solvents were allowed to contact the debris on a fixed time basis. No claim will be made that all of the iron or organometallic iron was extracted from the wear debris. Under the same conditions, the rate of solution should be identical. Therefore these fixed time extractions when compared relatively to each other, provided a valid basis for comparison.

d. Wear Scar Diameter Determination. Wear scar diameters were measured with a microscope containing a calibrated scale in the ocular lens. The measurements were made on the three stationary balls both parallel and perpendicular to the striations. All readings were averaged. In case the wear scar was highly irregular, either an imaginery square or rectangle would be superimposed such that the wear scar area outside the square will be equal to the unworn area inside the square. Then the following equation was used to calculate the diameter.

$$d = 2\sqrt{ab/\pi} \qquad [83]$$

The equation can be derived by equating $\pi\gamma^2 = ab$ where a,b are the length of the sides of a rectangle.

e. Precision and Consistency of Data. The wear debris analysis procedure has gone through several stages of development in this work. Accordingly, the data can be divided into three sets. Within each set, the data are internally consistent. Care must be taken when comparing runs from different sets.

One set consists of forty-one runs. These runs were made at the early stage of the experimental program, some difficulties in analysis were encountered. The operating parameters were not clearly defined. Hence not much significant data were generated. A second set consists of fifty runs. These runs were made in the Shell Four-Ball Wear Tester with various additives. Except for the first couple runs, this set of data represent a major improvement over the first set.

A third set of seventy-four constitute the best set of data. By this time, the analysis procedures were firmly set and the operating parameters well-defined. Hence, most of the conclusions are drawn from sets two and three. Set one and three used the same machine, the G.E./Brown Modified Wear Tester while set two was run on a different machine, the Shell Four-Ball Wear Tester. Both machines are similar in construction but different in sophistication. The resulting data from these two machines are compatible. All experimental data obtained from this study together with some pertinent results from previous workers have been used in this study. Whenever there was a change in procedure or material, the change is noted.

The precision and repeatability of the results were checked by repeating identical runs several times. The results are shown in Table 52. This actually represents the best set of data (set three) The variance of data is larger in set two and set one. Generally speaking, the wear scar diameters are quite reproducible. In this particular example, the average diameter can be reproduced to 0.90 ± 0.005 mm. The amount of iron recovered as oil soluble compounds is too small in this series to be determined in any certainty. The amount of pyridine-soluble iron compounds as determined by atomic absorption spectroscopy is quite consistent in the order of magnitude. Run 43 has a higher than average amount, 21 μg. The standard deviation, σ, for this set of data equals 4.387 and the normal error limit on the mean would be $\sigma_m = \sigma/\sqrt{n} = 4.387/\sqrt{4} = 2.19$, i.e., pyridine soluble iron = 13.5 ± 2.19 μg. If Run 21 is excluded according to the Chauvenet's criterion (149), i.e., a reading may be rejected if the probability of obtaining the particular deviation from the mean is less than ½ N, the standard deviation equals 0.816 and the average will be 11.0 ± 0.47 μg. Therefore, although the range of the data is large (10 to 21 μg), the normal deviation certainly is much smaller.

The amount of iron and iron oxides, due to the manner they are collected, is much less consistent. As described previously, these are washed out of the ball-pot and collected on the filter paper. Complete removal of wear particles from the ball-pot assembly each time is difficult to achieve, if not impossible. Therefore, although these samples can be measured with much higher accuracy by atomic absorption, they have a larger standard deviation, 24 for iron and 34.1 for iron oxides. In Figure 29, the amount of iron extracted by nitric acid for several series of experiments (same operating conditions) is plotted against the reciprocal of absolute temperatures. The general trend of the data is quite clear in spite of the obvious scatter. In Figure 30, the amount of iron as iron oxides is similarly plotted, the increased scatter of the data coincide with the higher standard deviation calculated.

4. Lubricating Characteristics of a Super-Refined Paraffinic Mineral Oil. The base fluid used in this study is a super-refined paraffinic mineral oil, designated as MLO 7789 Its physical properties are presented in Table 53. It contains no aromatic ring structures in the molecule and its chemical properties are dominated by the paraffinic portions. Generally speaking, the paraffinic side chains determine the thermal stability of the oil even in predominately naphthenic or aromatic oils.

The fluid was further purified by percolation through a glass column, 1" o.d. and 5 ft. long, filled with activated alumina. This removed oxygenated polar impurities in the oil. Only one gallon of oil was treated by one column. Thus, base fluid with the same level of purity was obtained. For comparison purpose, untreated oil (MLO 7789), treated oil (7789 A), and the first 50 c.c. of oil from percolation (7789 B) were run in the GE /Brown Modified Four-Ball Wear Tester under identical conditions. The results are presented in Table 54. As can be seen from the table, at 167°F, wear increases with fluid purity. This would indicate that the polar impurities removed by percolation act as lubricity additives. Therefore it is only logical that purer fluid would give better additive response since there will be less components to compete for the surface. This point is shown to be correct experimentally in this work. T e difference between 7789 A and 7789 B is small indicating that there is little difference between them.

a. Chemical Composition of the Ball-Bearing. The half inch 52-100 steel ball-bearings are supplied by SKF Industries. Its tolerance is controlled to 0.000025 inches. The chemical composition of the ball is shown in the following table.

CHEMICAL COMPOSITION OF THE 52-100·STEEL BALL BEARING

Element	Weight Percent
Carbon	0.95 - 1.10
Manganese	0.30 - 0.5
Phosphorus	0.025 max.
Sulfur	0.025 max.
Silicon	0.2 - 0.35
Chromium	1.2 - 1.5
Iron	96.5 - 97.3

b. Static Experiments. In order to provide a basis for comparison, a series of "static" tests were run as a function of temperature. The tests were conducted in the GE/Brown Modified Four-Ball Wear Tester. Identical procedures were used to clean and assemble the ball-pot. The air flow rates were set the same as the wear tests. The speed was set at 2.9 r.p.m. (0.108 cm/sec). In short, exact procedures were used as for the wear tests except that the load was set at zero. This was done to simulate the exact environment, the metallurgy, and the mass and heat transfer characteristics of the system. Since there was no wear, only the oil and pyridine phase were analyzed for iron content. The results are presented in Table 55 and Figure 31.

As can be seen in Figure 31, both the amount of iron in oil soluble compounds and in pyridine soluble (oil insoluble) compounds increase with temperature. The iron found in the oil phase is the product of the direct reaction between iron and hydrocarbon. The exact nature of these products is not known. Oxygen seems to play a very important role in the formation of these products, as illustrated in Table 56. As the temperature goes higher, the effect is more pronounced. At 500°F, the amount of oil soluble iron is ten times higher than the run with helium and at 700°F, it is about 200 times higher. From this evidence, it can be deduced that the oil oxidized and formed the various oxidation products, e.g., ketones, alcohols, carboxylic acids, aldhydes. These reaction products then react with the iron surface via adsorption-reaction-desorption processes. The reaction products may be metal soaps, ionized metal complexes, or soluble metal salts. From the bond energy consideration, as discussed before, direct C - Fe bonding requires a high activation energy. The lowest energy path is indirect bonding through oxygen, e.g., RCOO - Fe.

The iron-organic compounds extracted by pyridine are oil insoluble. Their formation appears to depend on temperature, oxygen concentration, chemicals present and the nature of the metal. Their oxygen dependence though not as strong as the oil soluble organometallics, is quite significant. Preliminary studies indicate that small amounts of polar additives also affect their formation significantly. A correlation between the amount of oil soluble iron and pyridine soluble iron under various conditions is not present. It seems that these two classes of compounds may be in some way related, or may actually have two distinctly different chemical reaction paths (mechanisms) in their formation. It has been known for sometime in plastic industries that iron in the presence of high molecular weight hydrocarbons may react to form oil insoluble resinous materials. Due to their high molecular weight and the presence of extremely chemically complex mixtures of different moieties, isolation and analysis are not practical. Few facts are known about their structure or chemical nature. In lubrication literature, reports abound about a "friction polymer" (151, 152, 153) and insoluble "metal soaps" (150, 152, 128, 131). Generally, they have been credited with the effectiveness of the lubrication system. Most recently, Zaslavsky et al. (154) and Sanin (155) studied the "friction polymers" in mineral oils with and without additives and both found iron reacting with the hydrocarbons and forming a part in the resulting polymers. Some of these polymers are oil soluble and some insoluble. Therefore it can be said that the pyridine soluble iron-organic materials are some kind of high molecular weight complexes of iron and oil oxidation products and are similar to the "friction polymers" found in the wear processes.

c. Dynamic Oxidation-Wear Study

1. Slow-Sliding Wear Tests. To assess the effects of a fresh iron surface, a series of experiments was conducted under conditions similar to the static tests except a 40 kg load was applied. To avert frictional energy build-up as heat in the conjunction, the sliding speed was kept at 2.9 r.p.m. Two fluids were used, the MLO 7789 and the MLO 7789A. These are super-refined paraffinic mineral oils. MLO 7789A is the oil which had been further treated by percolating through an activated alumina column.

The results for PRL 7789 and PRL 7789A are presented in Tables 57 and 58 respectively. As can be seen from Table 57, the wear increases with temperature as indicated by the mean wear scar diameter. As wear increases, the total amount of iron recovered also increases, but the percentage of the iron in the form of organometallics (oil soluble iron + pyridine soluble iron) increases drastically from 3 to 46 percent. This indicates that as temperature rises, chemical wear becomes increasingly important and effective lubrication will depend more heavily on the nature of the reaction products between the oil and the metal.

In Figure 32, the mean wear scar diameter is plotted against the bulk fluid temperatures. At a sliding speed of 2.9 r.p.m. or 1 mm/sec, very little heat builds up at the conjunction, hence it can be reasonably assumed that the temperature at the junction is approximately the same as the bulk fluid. As can be seen from Figure 32, the wear scar diameter undergoes two transition stages. There is a sudden increase in wear at 500°F; it then stays the same at 600°F. However, at 700°F, the wear increases again. The 7789A data are plotted on the same graph for comparison. In Figure 33, the iron in the oil soluble and oil insoluble organometallics is plotted against temperature. It can be seen that similar transition regions are present. The oil soluble iron increases rapidly with temperature. At 500°F, there is a surge in its formation and at 600°F, it begins to level off. The oil insoluble iron has the same transition point at 500°F, but continues to rise to 700°F. In the wear scar diameter plot, the two fluids, MLO 7789 and 7789A, behave the same in the overall wear as shown in Figure 33. In Figure 33, the amount of organic-iron produced from the two fluids shows different behavior. The purer fluid 7789A (polar impurities removed by percolating through activated alumina) generates the oil insoluble organic-iron compounds at a slower rate and in lower amounts at high temperatures. This phenomenon is much less pronounced in the case of the oil soluble organic iron. This indicates that the amount of polar impurities in the fluid, though not potent enough to modified the wear pattern, do exert considerable influence on the generation of oil insoluble organometallics, and to a lesser extent, oil soluble iron. Therefore, polar impurities must have adsorbed on the surface. This effect demonstrates that the generation of oil insoluble organic-iron compounds is more surface related.

The transition regions observed in Figure 33 are similar to the classical wear scar diameter versus load plot in which the wear goes through a sudden increase at certain loads, commonly referred to as the transition load. The friction level usually increases in this region. As further load is applied, depending on the lubricant, the wear either stays at the same level or increases slightly with additional load. Eventually as load increases to a certain point, seizure and welding will take place. This phenomenon has generally been explained as follows. Load increases the contact pressure at the conjunction. Higher pressure decreases the lubricant film to a minimum and more asperity-asperity contact are produced, hence higher friction. Higher friction produces more heat and higher temperatures result. At this point, the so-called incipient seizure with recovery takes place. This is the beginning of the transition region. The classical theory proposed by Blok, Bowden and Tabor is that the melting point of the lubricating film (reaction product of polar molecule with surface or pure chemical species adsorbed on the surfaces) has been reached, hence more contact and higher temperature result from the film breakdown until welding takes place. In the case of temperature versus wear, a similar situation exist except in this case, the heat source is not the dissipation of friction.

As discussed previously, iron and iron oxides data are less precise due to analytical difficulties. The results of MLO 7789 and MLO 7789A are presented in Figure 34 and Figure 35, respectively. For both fluids, there seems to be an increasing trend of iron and iron oxide generation as temperature rises. In the case of MLO 7789A, the amount of iron particles is always larger than the amount of iron oxides indicating less effective lubrication and higher frequency of metal-metal contact. The wear scar data in Figure 32 confirm this point. Another interesting observation is that whenever there is a large increase in the amount of oil soluble and/or oil insoluble iron, there is a corresponding drop in the amount of iron particles produced or a sudden increase in the oxides formation. The effect is more pronounced in MLO 7789A. This is reasonable. MLO 7789A is a purer fluid with many polar impurities removed. Therefore the polar oxidation products produced by the oil at certain temperatures have less competition to adsorb/reach the iron surface and react with iron forming oil soluble and insoluble organo-iron compounds which evidently serve as lubricant reducing metal-metal contact. In MLO 7789, the polar impurities in the fluid occupy the surface preferentially. The polar oxidation products have to compete with them for active metal surface. Apparently at higher temperatures, the oxidation products from the oil itself are able to reach the surface. This may explain the fact that for MLO 7789, the rise in oil soluble/insoluble iron does not take place until 500°F while for MLO 7789A, 400°F is sufficient.

2. Correlation Between Static and Slow-Sliding Wear Test Data. The difference between the static data and the slow-sliding wear test data is that one has wear and the other hasn't. Whether the freshly exposed metal surface from wearing processes exerts a major influence on the chemical reaction products and lubrication is the question. The differences, if any, of the two sets of data could also result from a higher temperature zone in the conjunction of the wear tests. It will be difficult to distinguish between the two factors from the data.

In Figure 36 the amount of oil soluble iron is plotted on a semi-log scale versus the reciprical of absolute temperature, °R. A straight line is drawn through the data points of the static experiments, indicating that the oil soluble iron in the static case obeys the Arrhenius type of relationship with temperatures. The slow-sliding wear test data for the two fluids are plotted on the same graph, and as can be seen, fall on the line pretty well. In fact, the correlation between the static and the slow-sliding wear tests for MLO 7789A is excellent. MLO 7789, on the other hand, does deviate more from the line. This may be due to the fact that MLO 7789 is chemically different from MLO 7789A. When the data is expressed as oil soluble iron per unit area and plotted against the reciprocal of absolute temperature as in Figure 37, a little more data scattering is observed. The definite trend of rising temperature with higher product concentration remains the same. The increased data scatter may be due to the inaccuracy of estimating the surface area or the chemically different systems of MLO 7789 and MLO 7789A. In spite of all these, and considering all the factors involved, the data are well correlated. This implies first that the static experiments are chemically compatible with the slow-sliding experiments. Secondly, the amount of reaction products is an exponential function of temperature. Generally, only for a relatively simple chemical reaction system, the kinetic rate data (initial rate of formation or steady state rates) can be correlated according to the Arrhenius equation which is usually expressed in the form as $k = Ae^{-E/RT}$. The fact that the amount of iron (product concentration = $_0\int^t r\,dt$ for each temperature) measured as oil soluble organo-metallic iron compounds obeys the Arrhenius equation suggests that these reactions, as a class, in forming these products, have rate(s) of formation with a constant functionality with the product concentration or the steady state rate(s) mask the rate changes in the system at each temperature. Also, a continuous chemical reaction system is indicated. There may be different reactions, each more predominant at different temperatures, but as far as the iron involvement, it is continuous.

In the case of the oil insoluble organic iron (pyridine soluble), similar treatment yields a little different results. In Figure 38 the oil insoluble iron is plotted against the reciprocal of the absolute temperature. The raw data indicate that MLO 7789 behaves quite differently from MLO 7789A and apparently there are some differences between the slow-sliding runs and the static experiments. The difference is small for the same fluid. In a broader view point, the fluids are the same class chemically and the general trend should correlate fairly well with temperature. This is shown in Figure 39, where the oil insoluble iron per unit area is used. The differences between the fluids and the load still exist, yet taken together, the general trend is quite obvious. Straight-line correlation with 1/T in this case is no longer observed. In the MLO 7789 slow-sliding case, the data can be correlated with two straight-lines with the abrupt change of slope at 500°F as shown in Figure 38. For MLO 7789A slow-sliding, the first big incremental change also occurs at 500°F. In the static system, the first big increase is at 400°F. These data indicate that there may be two different reaction regions in which the rates of formation of oil insoluble organic-iron compounds are different. One possible theory is that the observed behavior is due to bulk oil concentration effect. At 500°F, the bulk oil oxidation reaches a point that the rates of oxidation increase drastically. This could have two effects: the higher rates of oxidation increase the production rates of the active species for the formation of oil insoluble organometallics involving iron; or the bulk oil concentration of polar oxidation products reaches a stage that the bulk oil chemical composition is sufficiently changed to provide higher production of oil insoluble organic-iron compounds.

The amount of iron particles and iron oxides data are treated similarly. These results are shown in Figures 40 and 41. The production of iron particles depends on the frequency of contact and the effectiveness of the lubrication. The production of iron oxides will depend on the amount of oxygen available to the surface and the temperature. As explained before, the collection of these data was difficult and the resulting data scatter make any interpretation difficult. Nevertheless, the general trends are there. In Figure 40, a steady rise in the amount of iron particles produced per unit wear area can be seen, suggesting increasing amount of contact between the surfaces. In Figure 41, there is enough scatter in the data that virtually several lines can be drawn with equal validity. The lines drawn in Figure 40 are the lines that best correlate the MLO 7789 data.

3. Dynamic Wear Tests. Two series of experiments were made at moderate speed, 600 r.p.m. (linear velocity 22.8 cm/sec or 0.75 ft/sec) on the four-ball wear testers. The bulk fluid temperature was maintained at 167°F. The other operating parameters were maintained the same as the slow-sliding experiments namely: load = 40 kg., duration = 100 minutes, atmosphere = dry air. At the end of the run, the wear debris were analyzed. In Table 59, the results for MLO 7789A (percolated through activated alumina) are shown. There is very little oil soluble organic-iron generated but the oil insoluble organic-iron generation is quite significant. This demonstrates again that the production of these oil insoluble organometallic compounds are strongly surface related. The amount of iron in oxide form is greater than the amount of iron particles. This suggests iron oxidation plays quite important role in the lubrication. It is not clear whether the surface oxidizes first and then the oxides are removed by shear stresses or whether the surfaces produce small iron particles from contact fatique and these particles subsequently oxidize in the conjunction at elevated temperatures.

Table 60 shows the data obtained from the untreated oil, MLO 7789 in the Shell four-ball wear tester. Higher amounts of both oil soluble and oil insoluble organic-iron are produced. The mean wear scar diameters appear to fluctuate from 0.60 mm to 0.87 mm. It was later discovered that the particular wear tester, due to its design had different alignment when a different ball-pot was used. Runs K1A and K25 used the same ball-pot while Runs K1B and K26 had the other ball-pot. With this in mind, the precision of the wear scar diameters is actually quite good. Apparently, the other results were not affected by this problem.

d. Junction Hot-Spot Temperature Estimation with Chemical Conversion Data. When one considers the overall chemical reaction systems involved in boundary lubrication, one usually concludes that some kind of simplification is necessary in order that meaningful data can be obtained and interpreted. In this work, without going to an exhaustive and probably fruitless analytical route of separations and purifications, the numerous reaction systems are lumped into one gross chemical reaction system. The reactants in this system are, on the one hand, iron on the metal surface and numerous polar hydrocarbon species on the other. Because of the little known nature of the chemical products and the reaction mechanisms involved, the usual reaction kinetic analysis is difficult to apply here. The difficulties encountered in obtaining reproducible data add another restraint to the task. Ideally, if the concentration of the iron as organometallics can be measured at the initial stages of the rubbing process in the slow-sliding and the dynamic systems, a plot of linearized initial rates of such reaction at various temperatures can be used to correlate the rate data between the dynamic system and the static/slow-sliding system. This proves to be impractical. In the dynamic experiment, at the start of the rubbing process, due to the tremendously high pressure (very small load supporting area), a lot of wear is generated in a relatively short time and the concentration of organometallics is very low if at all detectable in the present experimental set-up. There are some questions as to whether or not this "wear-in" period is in the chemical lubrication regime, i.e., the lubricant is not functioning effectively, hence it may be more of a physical rubbing and tearing rather than chemical reactions controlling the lubricating mode. Next, the precision of data gathered in the early stages due to the low values, is of such quality that correlation built on such rate date is of dubious value. In the static or slow-sliding experiments, at high temperatures, this initial rate concept also encounters some problems. It takes about ten minutes for the ball-pot assembly to be heated up to the required temperature and as temperature rises, reactions occur. The same analytical problems present in the dynamic experiment are present here also except that the theoretical analysis of a transient temperature region complicates the interpretation unnecessarily.

1. Steady-State Concentration Correlation. One reasonable alternative to the initial rate method is the correlation based on the steady state conversion data. If the rates of formation of the products are constant (zero order reaction) or if the product concentration reaches a steady state at a fixed temperature, then at a fixed time or after enough time is allowed to reach the steady state concentration, the product concentration will be determined by the temperature alone. To investigate the validity of this assumption, a series of experiments was performed. In Table 61, data from dynamic experiments as a function of time at 167°F and 600 r.p.m. are presented. In Figure 42, the change of the mean wear scar diameter with time is plotted. As can be seen from the graph, after 30 minutes the rate of wear is essentially constant. During the first half hour, the wear rate can be approximated reasonably well with a straight line. In Figure 43, a similar conclusion can be drawn with respect to the oil insoluble iron concentration. It rises very quickly and levels off at a steady state concentration. Therefore, at least for the dynamic experiments, the steady state correlation is justifiable. In the slow-sliding or static experiments, since the temperature at the junction is constant throughout the run, the concentration of oil insoluble iron has to be the function of the particular temperature of that experiment.

2. Surface Area Considerations. In the high temperature region, the ball-pot assembly in the static and slow-sliding experiments was heated and maintained at high temperature throughout the run. The bulk oil reacted with the metal surfaces in the surrounding. In the dynamic run, only a small fraction of the oil was subjected to high temperatures at the junction and in terms of surface area, only the wearing areas and the wear metal particles existing at the conjunction were involved. To account for these differences, the oil insoluble iron has to be expressed in μg per unit area. For the static experiments, the total active area throughout the run is easily obtained by measuring and summing the total surface area of the ball-pot assembly. In the slow-sliding and dynamic systems, the surface area of the wear particles presents some problems. In the slow-sliding case, all of the wear particles generated are subjected to the same temperature at all times. Therefore, the total surface area will be the sum of all the particles and the ball-pot assembly. In AFML-TR-74-201, Part I, typical particle size distribution, measured under a microscope, is presented. Surface area can then be estimated from these data. The detailed calculations of the surface area are listed in Appendix I. In the dynamic case, only those wear particles which remained at the conjunction were subjected to high temperature. The particles that were removed from the junction would have a temperature of 167°F, the bulk oil temperature. And during a dynamic wear test, the wearing area increased with time, so the amount of particles at the junction would also increase with time. To simplify the situation, all wear particles are assumed to be active at all times. This assumption would reduce the average temperature somewhat. In view of the approximate nature of the correlation, and the precision of other data, a more accurate analysis is not warranted.

3. Estimation of the Temperature at the Conjunction. As discussed in the previous sections, the amount of oil insoluble organometallic iron per unit surface area is used to correlate the dynamic runs at 600 r.p.m. with the static and the slow-sliding runs. Table 62 tabulates all the pertinent data.

The correlation between the static and the dynamic runs with MLO 7789A is first considered. In Figure 44, the data from the static runs is plotted against temperature. The datum point at 500°F is weighted less significantly based on the general correlation presented in Figures 38 and 39. The dynamic test at 167°F, 40 kg. load and 600 r.p.m. for 100 minutes generated 7.76×10^{-3} $\mu g/mm^2$ of oil insoluble organometallic iron. The static test results showed that for the same amount of reaction products to be formed in 100 minutes, the temperature would have to be 715°F ± 50°F. For the same fluid, but instead of the static runs, the slow-sliding with 2.9 r.p.m., 40 kg. load results showed that the temperature would have to be 660°F ± 15°F as indicated in Figure 45. The difference between the two sets of data could be attributed to several factors. In the slow-sliding tests, fresh iron surfaces were continuously generated. The fresh iron surface would have a much higher surface energy hence higher reactivity. Another factor would be that in the slow-sliding, although according to theoretical calculations the temperatures at the junction would be the same as the bulk fluid temperature, in reality, it might be slightly higher than the bulk to generate more reaction products. Lastly, the surface area of the wear particles of the slow-sliding runs were estimated from approximate measured profiles in which all particles were assumed spherical. It is conceivable that the assumptions built-in the surface area calculations could produce some errors.

MLO 7789 is the untreated paraffinic mineral oil, which exhibits different behavior compared to the activated-alumina-percolated oil (MLO 7789A). In the same dynamic run at 167°F, 600 r.p.m. and 100 minutes duration, it has generated 12.34×10^{-3} $\mu g/mm^2$ of oil insoluble organic iron and at the same time generated 8.64×10^{-3} $\mu g/mm^2$ oil soluble organometallic iron. Therefore in this case, both the oil-soluble and the oil insoluble organometallic iron compounds can be used to correlate the temperature. The data on Figure 46 shows the oil-insoluble organic iron versus temperature. For the same amount of reaction products, the temperature at the junction would have to be 640 ± 25°F in the dynamic test. For the oil soluble iron, Figures 36 and 37 can be used. The result is 640°F ± 50°F. Thus, for different purity levels (different high temperature behavior) different correlating parameters, the answers all agree very well. The results are summarized in Table 63.

4. Consecutive Dynamic Test to Eliminate "Run-in" Effects. In the dynamic runs, for the first 30 minutes the wear rate was high as shown in Figure 42, then a constant wear rate set in. At the initial wearing stages, the temperature at the junction could get higher than the steady state temperature associated with the constant wear rate. To check this effect, a consecutive run was performed. In the first 100 minutes run, the wear scar reached certain dimensions. The ball-pot assembly was then thoroughly cleaned with naphtha, acetone and hot pyridine (180°F) without disturbing the locking positions of the ball-bearings. Then fresh oil was used and the second 100 minutes run commenced. The wear debris were analyzed and the results are shown in Table 64. It can be seen that the result falls right in the range of the four first 100 minutes runs, indicating that as far as the temperature correlation is concerned, the "wear-in" has very little effect.

e. Theoretical Analysis of Junction Temperatures. The frictional process, whether between lubricated or unlubricated surfaces, is always accompanied by dissipation of heat. This heating process raises the temperatures of the sliding surfaces and the surrounding environment. In the last decade, a great deal of research have been done both experimentally and theoretically studying the temperatures at the frictional junction. From the works of Earles (79, 80, 81), Powell (156, 78), Furey (77), Cameron (157) and others, it became increasingly clear that there are two temperatures at least, at the junction; θs, the sub-surface temperatures, and θ_F, the flash temperatures or hot-spot temperatures. In the lubricated junction, there possibly exists another temperature θ_L, the lubricant film temperatures. Since these temperatures play an important role in boundary lubrication, they are discussed below.

The flash temperature is the localized temperature of the flashes caused by the dissipation of frictional (and viscous if lubricated) energy at the asperities on one or both surfaces. The measurement of these temperatures, θ_F is extremely difficult as they are of only a few milli-seconds duration and occur over an extremely small area relative to the contact area. Most of the experimental investigations and theories are centered around dry wear systems. The addition of lubricant into an already complex system, at this point, has not been very fruitful. The sub-surface temperature is the steady state temperature existing just below the asperity (0.1 mm) surface. Usually the bulk of the metal in the system is large enough that the heat is treated as conducting away into a semi-infinite slab. The temperature at or near the surface interface is a dynamic steady state temperature established by the heat sources (flash temperatures) and heat transfer away from the surface by conduction into the bulk material. In the case of a lubricated junction, the hydrocarbon lubricant due to its relative high heat capacity and low heat conductivity will act as an insulating material. From the continuous generation of temperature flashes, the oil film temperature builds up near the surfaces very fast. This temperature gradient in the oil film has never been experimentally measured (the film may be only 100 to 500 Å thick), and it has only been qualitively analyzed from a mathematical point of view by Archard (70).

Furey (77) in his work studying the dry wear of metals, used both the dynamic thermocouple and imbedded thermocouple methods to measure θs and θ_F. The dynamic thermocouple consisted of rubbing the two dissimilar metals, e.g., iron and constantan, against one another and the junction temperatures measured by the e.m.f. generated. A ball-on-cylinder device was used in his study. An oscilloscope was also employed to monitor the temperature flashes. Before the temperature data obtained in Furey's work are examined, some discussion of the two temperature measuring devices (imbedded thermocouples and dynamic thermocouples) are in order. The use of imbedded thermocouples close to the contact region interferes with the heat flow and it is doubtful that they indicate any real temperatures reached at the tips of asperities in contact. They will give an estimation of the sub-surface temperatures. The dynamic thermocouples, by using dissimilar metals and measuring the thermoelectric voltages generated by contact, theoretically would give the true temperatures at contact. In reality, only a time average temperature is obtained. The measured e.m.f. is some average value pertaining to all the points in contact at any given instant. If all points in contact are at the same temperature, the e.m.f. generated will give a true response. However, if the points are at different temperatures, the measured e.m.f. will be a kind of average value which is not necessarily even an arithmetical average, it will depend on the relative ratio of the contact resistance. The temperature reading probably will approach the temperatures of the contacts that have the least electrical resistance. Since the electrical resistance increases in contacts at elevated temperatures, one may expect to read a temperature considerably below the mean temperature. The use of an oscilloscope only increases the response time of the equipment but the basic problem remains. Whether the asperities have uniform temperature across the contact area or not can be resolved from the following considerations. The area of contact is often formed by elastic deformation of curved bodies in nominal point contacts (as in 4-ball machine, pin-on-disc, ball-on-cylinder devices). In these cases, the contact pressure is exactly or approximately elliptically distributed over the contact area according to the classic equations of Hertz. Thus, the power density (rate of frictional heat production per unit area) in a sliding Hertzian contact will be likewise elliptically distributed. Therefore, different temperatures will result at areas under varying power density distribution. The hottest spot will be at the center of contact area. Also in a time frame, at any instant, different stages of contact will have different temperatures. With these considerations in mind, Furey's data will be examined below.

When the ball and rotating cylinder first come into contact at the start of a test, the surface temperature increases instantaneously to a high level and remains essentially at this level during a test at a given load and speed. Although there are variations in surface temperature with time, these are generally small and can be explained on the basis of frictional force change during the test. When the rotating cylinder is stopped, the surface temperature drops instantaneously to the original value. These temperatures are recorded as a recorder trace in the experiments using the dynamic thermocouple. The same temperatures are recorded with a high-speed camera taking a picture of the oscilloscope trace. It was found that although the average surface temperature is about 149°F, the maximum surface temperature is as high as 300°F. The system temperature is 77°F. These temperatures are obtained from a load of 250 gm and 56 cm/sec linear velocity. The duration of these temperature flashes or spikes revealed in the oscilloscope picture is about a 10^{-4} second. One important result of these data is the relatively constant temperature with time. Since wear is occurring throughout the test, this suggests that the temperature rise is affected very little by the gross wear area. Furey rechecked this point by running more experiments. For a total 58-fold increase in wear area, the surface temperatures remain relatively constant, 124.5°F versus 123.5°F. This is further evidence that the surface area does not appear to affect the temperature at the junction significantly.

Furey's work is with dry sliding. From his results, one gains the basic concept of the nature of surface temperature flashes. The temperatures measured or theoretically estimated are generally average temperatures over the contact area. In terms of chemical reactions localized at the asperity tips, the average temperature at the junction is irrelevant. It is the flash temperatures under which the chemical reactions (oxidation/degration/polymerization) and adsorption/desorption processes are initiated and/or terminated that are the key parameters in the system.

In the lubricated contact, one additional heat transfer consideration enters the picture. The oil film between the surfaces acts as an insulation. When heat-energy is continuously fed into the oil film inside which there is a net accumulation of energy until a steady state temperature is reached (at this point, the net gain of heat will be zero), the temperature gradient across the film could be several times the surface temperatures. Therefore, in lubricated contacts, the chemical reactions could take place at the surface where the temperature flashes are occurring or inside the oil film and the resultant polar species move toward the metal surfaces.

1. Theoretical Hot-Spot Temperature Calculations. Several theoretical studies have been made on surface temperatures generated by friction. In 1937, Blok (68) investigated the problem of stationary and moving source of heat in plane surfaces with infinite heat sinks. Jaeger (69) in 1942 similarly studied the problem and included considerable numerical detail. Holm (158) in 1948 and Bowden & Tabor (64) in 1950 presented a simplified version of Blok's theory. Archard (70) in 1959 simplified and reorganized Blok's temperature theory and included such considerations as elastic and plastic deformation. This is often called the Blok-Archard flash temperature theory. The basic assumptions involved are a) the heat is generated at the area of true contact, considering a single area of contact as a plane heat source, and that b) this heat is conducted away into the bulk of the rubbing members. The theory required the determination of the heat flow into each body which must result in the same average surface temperature over the contact area. The surface temperatures are expressed in terms of the rate of supply of heat, the size and speed of the heat source, and the heat capacities and thermal conductivities of the surface materials. Barber (159) in 1967, and Francis (160) in 1970 both derived equations to calculate the surface temperature with further refinements of the Blok-Archard theory. However, the existence of a layer of low thermoconductivity material, i.e., the lubricant is not allowed for. Therefore the theory will only predict the temperature in a dry sliding case.

There are several equations which can be used in calculating the flash temperatures based on different or varying degree of assumptions. Fein (161) derived an equation for the Shell four-ball wear tester based on the Blok-Archard theory. Furey (77) derived simplified equations using Archard's results. Most recently, in 1975, Bos (162) compared several simplified mathematical models with his experimental work in determining the temperature at the wear scars of the four-ball apparatus. In the following sections, various equations for calculating the surface temperature rise are discussed.

a. Blok-Archard Equations. The model is based on a protuberance on the surface of body B which forms a circular area of contact $A = \pi\gamma^2$, which moves with a velocity V over the flat surface of body C. Body B therefore receives heat from a stationary heat source and body C from a moving heat source. Let Q_B be the quantity of heat supplied per second to body B and Q_C be the quantity of heat supplied per second to body C. k_B and k_C are the thermal conductivities, C_B and C_C the specific heats and ρ_B and ρ_C the densities of the two bodies. The mean rise in temperature over the contact area, θ_m for a stationary heat source can be calculated from the following equation:

$$\theta_m = \frac{Q_B}{4rk_B} \qquad [84]$$

It can be seen that the mean rise in temperature is directly proportional to the rate of heat supplied and inversely proportional to the radius of the contact area and thermal conductivity.

For a slow moving heat source, the contact time is long enough for temperature distribution of a stationary contact to be established in C, and thus

$$\theta_m = \frac{Q_C}{4rk_C} \qquad [85]$$

At high speeds, the contact time is insufficient to establish a temperature distribution and the temperature rise is given by:

$$\theta_m = \frac{0.31}{k_C r} Q_C \left(\frac{\alpha_C}{Vr}\right)^{\frac{1}{2}} \qquad [86]$$

The speed criterion is established by the dimensionless parameter developed by Jaeger (69), $L = (Vr)/(2\alpha)$. Equation [85] applies when $L < 0.1$ and Equation [86] for $L > 5$. For intermediate values of L, Archard presents a graphical procedure. In these equations, the rate of heat supply is related to the total energy input to the system by:

$$Q = fWgV/J = Q_B + Q_C \qquad [87]$$

The distribution of the energy between the contact members in dry sliding is assumed by Archard to be divided as follows. For $L < 0.1$ (low speeds), and for bodies made of the same material, the heat supply is divided equally, i.e., $Q_B = Q_C = \frac{1}{2}Q$. At $L > 100$ (high speeds) essentially all the heat is supplied to body C and $Q = Q_C$. For intermediate speeds, the following criterion applies:

$$\frac{1}{\theta_m} = \frac{1}{\theta_B} + \frac{1}{\theta_C} \qquad [88]$$

Where the temperature rise for each body B and C is calculated on the assumption that all of the heat is supplied to it and the mean temperature rise θ_m calculated from Equation [88].

For contacts whose size is determined by the applied load, the mean temperature rise is given by the following equations:

With plastic deformation at low speeds ($L < 0.1$)

$$\theta_m = 0.25\ N\ L \qquad [89]$$

where:

$$N = \frac{fg\pi P_m}{J\rho C} \qquad [90]$$

$$L = \frac{Vr}{2\alpha} = \frac{F_N^{\frac{1}{2}}\ V}{2\alpha(\pi P_m)^{\frac{1}{2}}} \qquad [91]$$

With plastic deformation at high speeds $(L > 100)$

$$\theta_m = 0.435\ N\ L^{\frac{1}{2}} \qquad [92]$$

At moderately low speeds $(0.1 < L < 5)$,

$$\theta_m = 0.25\ N\ L \qquad [93]$$

Where θ_m ranges from a value of about 0.95 at $L = 0.1$ to about 0.5 at $L = 5$. At moderate speeds $(5 < L < 100)$

$$\theta_m = 0.435\ \gamma\ N\ L^{\frac{1}{2}} \qquad [94]$$

where

$$\gamma = 1/(1 + 0.87\ L^{-\frac{1}{2}} \qquad [95]$$

Generally, γ ranges from a value of 0.72 at $L = 5$ to 0.92 at $L = 100$. Since the maximum flash temperature occurs when the maximum possible load is concentrated at the smallest possible area, i.e., when the total load is borne by plastic deformation at a single area, Equations [89], [92], [93], and [94] can be used to calculate the maximum flash temperature in dry sliding. Using these formulas, the average junction temperature without taking into account the existence of the oil film for runs 42 through 45 (40 kg, 600 rpm, 167°F) is found to be 260°F and the maximum temperature, 353°F. Detailed calculations are shown in Appendix II.

Fein (161) in using Blok's formula to calculate the flash temperature in lubricated contacts in the four-ball wear tester, found the temperatures thus determined were too low to account for the observed transition temperature data. When he arbitrarily increased his calculated temperatures by 33 percent, a reasonable correlation of the data was obtained. Following his procedure, θ_m = 290°F and θ_{max} = 415°F.

b. Francis' Equations. Francis (160) derived an analytical expression for the steady-state interfacial temperature field in a sliding circular Hertzian contact. He accounted for the ellipsoidal distribution of the frictional power, hence heat generation in the contact area. Blok-Archard's equations assume uniform heat generation and equal temperatures of the two contacting bodies. In an apparatus such as the four-ball machine, this is not the case. The area of contact is formed by elastic/plastic deformation of curved bodies in nominal contact and the pressure is distributed elliptically according to the classical equations of Hertz. Thus, given that the friction force contributed by a differential element of area is proportional to the normal load on that element the power density (i.e., the rate of frictional heat production per unit area) in a sliding Hertzian contact will be elliptically distributed.

For the stationary surface, the average temperature rise is given by

$$\Delta\theta_s = \frac{9\pi\ Q}{32\ \pi r k} \qquad [96]$$

for the moving surface

$$\Delta\theta_V = \frac{1.016\ Q}{\pi r k B^{\frac{1}{2}}} \left[1 + \frac{1.047}{B} + \frac{0.774}{B^{3/2}}\right] \qquad [97]$$

where:

Q = rate of heat generation, cal/sec

k = thermal conductivity of the metal, cal/cm cal/cm-°C-sec.

B = dimensionless parameter = rV/α

For B = 10, Equation [97] simplifies to

$$\Delta\theta_V = 1.148 \left(\frac{Q}{\pi r k B^{\frac{1}{2}}}\right) \qquad [98]$$

The average interfacial temperature is given by

$$\Delta\theta_m = 1/\left(\frac{1}{\Delta\theta_s} + \frac{1}{\Delta\theta_V}\right) \qquad [99]$$

The maximum temperature can also be calculated by

$$\Delta\theta_{max} = \frac{1.852\ Q}{\pi r k} /(1.996 - 1.091B^{-0.818} - 0.537B^{-0.271} + B^{\frac{1}{2}}) \qquad [100]$$

The detail derivation for the above equation is given by Francis in Reference (160) The calculated temperatures from Francis' equations are higher than those calculated using the Blok-Archard equation by 33 to 38 percent. Thus the empirical adjustment by Fein to increase the temperatures by 33 percent are seemingly justified by Francis' theory. Using the above equations, the average temperatures at the junction in the four-ball machine is determined to be 338°F and the maximum temperature, 442°F. The detail calculations are shown in Appendix II.

c. Bos' Work. Bos (162) continued Francis' work and using a computer, obtained the solution for the whole region of B. From regression analysis, he obtained the following equation:

$$\Delta\theta_m = \frac{Q\ 0.281}{kr(B + 4)^{\frac{1}{2}}} \qquad [101]$$

where:

Q = rate of heat generation, Joules/sec.

k = thermal conductivity, Joules/m^2-sec-°K

r = radius of the heat source, m

B = dimensionless parameter = Vr/α

V = sliding velocity, m /sec.

α = thermal diffusivity, m^2/sec.

Which is good for $0 \leq B \leq 100$. Bos further carried out a series of experimental studies measuring the mean temperature at the wear scars of the four-ball machine. The technique used was an imbedded thermocouple 0.5 mm below the wear scar and 0.3 mm in diameter. The experiments were made with HVI oil containing one percent sulfur. In comparing the experimentally measured mean temperatures with Francis' theoretical model, the measured temperatures are always much higher than the calculated temperatures. Figure 47 presents Bos' data for 30 cm/sec linear velocity in a four-ball apparatus (FBA). It can be seen that at r = 0.15 mm, the difference between the two temperatures is about 83 percent, and at r = 0.4 mm, the difference is 300 percent. Bos theorizes that after the start of an FBA experiment, the distribution of frictional heat over the rotating and fixed balls changes rapidly, the heat flow into the lower balls increases because the bulk temperature of the upper ball, which is heated more intensively, rises more rapidly than that of the lower balls. To prove this hypothesis, Bos used an aluminum oxide upper ball which is non-heat conducting. The result gave a very good agreement between theory and measured temperature.

A different explanation of the observed phenomena is also possible. There is an oil film existing between the contact area and the conductivity of the oil is low enough that in the physical system, the oil film is equivalent to the non-conducting Al_2O_3 upper ball. Furthermore, the oil film will absorb enough heat in a very short while that the resulting temperature gradient across the oil film reaches such proportions that there will be heat flow towards both metal surfaces and this, in essence, would also create a situation similar to the non-conducting Al_2O_3 ball.

From Bos' work, the temperatures at the junction can be similarly adjusted and the resulting temperatures are tabulated in Table 65. Calculational details are compiled in Appendix II.

d. Discussion of the Junction Temperatures. From the previous discussions, it is evident that the temperatures at the lubricated junction are ill-defined both experimentally and theoretically. The experimental difficulties in physically measuring the actual temperatures are enormous and their interpretation equally arduous. The theories generally have too many assumptions and none of them account for the presence of the oil film and the heat transfer characteristics of the testing machines. Furthermore, the inability to predict the values of the physical properties of the oil and the physical condition and frequency of contact make it all but impossible to predict the temperatures.

This work, so far, has studied the temperature problem at great length. The nature, and the magnitude of the temperatures have been discussed in concert with other researcher's work. In the following sections, the validity of the results obtained in this study and the effects of several parameters on the results will be discussed at length.

1. Validity of Present Result. In this work, chemical reactions which by themselves are not clearly defined, are utilized to back calculate the average hot-spot temperatures over a fixed period of time in the junction.

This method avoids the many physical difficulties in actually measuring the temperature. On the other hand, this method relies on several factors to be successful: the ability of the solvent to extract a fixed percentage (100% would be the best) of the organometallic compounds that are formed during lubrication; the variation of temperatures in the junction throughout the dynamic run remain small; and same types of chemical reaction products are formed in the static experiments so that these products have the same solubility in the extracting solvent as the dynamic tests.

Pyridine is the solvent used in this study. From the repeat test data shown in Table 53, the solution rate of pyridine seems quite constant. Also from the temperature-organometallic formation relationship, it is quite obvious that at high temperatures much more organic-iron compound is formed. The exponential nature of the formation rate of organometallic compounds with temperature makes the constancy of pyridine solution rate less critical. The existence of these oil insoluble organic-iron materials is supported in part in that correspondent amounts are found in the oil phase as oil soluble compounds.

During a dynamic run, the pressure at the junction varies considerably. Initially, the load (16200 gm in 40 kg. load) is supported entirely on a single point and the mean specific pressure is about 300,000 psi. At the conclusion of the test, for a wear scar diameter of 0.9 mm, the same load produces about 30,000 psi average pressure at the junction. This is a tenfold decrease. Traditionally, people when considering the temperatures at the junction, logically assume that the temperatures will be proportional to load, i.e., large change in junction temperatures during wear tests. Two considerations point to the fact that there may be some temperature change during wear experiments, but the degree of change is quite small. Theoretically, it must be pointed out that the tenfold decrease in pressure relates only to the average or mean specific pressure at the junction. In reality, the pressure or the load is not uniformly distributed but ellipsoidal in nature as shown in Francis' work (160). This implies that even though the average pressure is changing, the maximum pressure at the center of the junction may change very little. Also, the wear-in process is very quick in this study, within a few minutes the wear scar is already in the 0.5-0.6 mm range. Experimentally, the consecutive run data presented in Table 64 certainly implies the existence of constant temperatures at the junction. The run was started after the normal 100 minutes of a wear experiment in which the wear scar diameter had reached 0.9 mm. The whole ball-pot assembly was carefully washed and run for another 100 minutes. The change in wear scar diameter, this way, is drastically reduced (from 0.9 mm to 0.995), and the corresponding average pressure change is from 30,000 psi to 28,000 psi, a change of seven percent. The amount of organometallic iron determined from this run, however, is about the same as from the first 100 minute run. Another supporting evidence is offered by Furey (77) in his work measuring surface temperatures in a ball-on-cylinder device (the load is also ellipsoidal distributed). He found that for a 58 fold variation of wear area, the temperatures (average temperatures) changed only 10°F. This is shown in Figure 47 It can be seen that the result is quite impressive. Another consideration is that the load is supported by the contacting surface. The real contact area may be only a fraction of the gross wear area. For an asperity which is supporting the load, the local pressure at that instant could be just as high as the very initial point of contact. One interesting point is that the flow pressure of the bearing is approximately 100,000 psi. The asperity which is load carrying when subjected to any pressure greater or equal to 100,000 psi will deform plastically. Below this pressure, the deformation is elastic. Theoretically, at least, elastohydrodynamic lubrication should produce little wear if any at all. From the average junction pressure consideration, when the wear scar diameter reaches 0.53 mm, the average pressure is about 100,000 psi and the wear rate after this should drop quite significantly. In Figure 43, where the wear scar diameter versus time is plotted, it can be seen that there is no sudden break in the wear curve and the wear increases at a constant rate. This indicates that from the previous considerations, such as the ellipsoidal pressure distribution, small actual real contact area and the experimental evidence of this work and that of Furey's, the temperatures at the junction of the 4-ball apparatus in the dynamic runs in this work change little.

To ensure that the same type of chemical reaction products are formed during the static experiments, the same apparatus and the same conditions are used so that the heat and mass transfer characteristics between the two sets of experiments are identical. Since impurities are excluded from the oil, the same reactants under similar conditions would lead to similar type of products.

The temperature determined in this study is the average mean temperature of the aggregate of hot flashes and mean surface temperatures. It is the temperature under which chemical reactions take place. If the temperature varies during a run, the temperature determined will be the integral average temperature under which the integral of the rate of reaction gives the total amount of reaction products. The theoretical calculated temperatures, on the other hand, are all equilibrium or steady state average temperatures at the junction. These two temperatures can be different and the fact that they agree (though only after the correction factor offered by Bos's measurements) lends support to one another's validity.

2. Effect of Surface Activity on Chemical Reactions. Iron has been known as a dehydrogenation catalyst under relative high temperature for a long time. The recent studies of Morecroft (150) and Buckley (163, 164) indicate that fresh iron surface produced by filament evaporation and condensation show catalytic activity when in contact with organic vapors. Whether the catalytic effect is important or not in boundary lubrication has long been a subject of conjecture and hypothesis. In this work, sets of experiments are designed to give some indications in this regard. The difference between the static experiments and the slow-sliding runs is the creation of wear or fresh iron surface throughout the run. The difference obtained in terms of the temperature determination by conversion data is small, about 55°F which lies within the precision range of the data. This indicates that catalytic effect may be present but is not significant. Further, in run K34 and 108, excellent contrast can be observed in this respect. The data are presented in Table 66. For an increase in surface area of 1800 percent, the total chemical reaction product changes 58 percent and the oil insoluble portion increases by 45 percent only. If catalytic effects are important in chemical reactions in boundary lubrication regime, the change in the integral conversion data should be much more pronounced. It appears that the iron surface, whether fresh or oxide covered, reacts directly with polar components rather than serving as a catalyst. In this respect, the reactivity between the two surfaces is about the same, while fresh iron surface may exhibit higher reactivity at high temperatures. Data from stop-and-go intermittent wear experiments included in AFML-TR-74-201, Part I, also suggest the above conclusion.

3. Effect of Bulk Fluid Concentration of Polar Species on Chemical Reactions. In the dynamic experiment, 167°F, 600 r.p.m., the bulk fluid temperature is low enough that very little oil soluble iron compounds are produced indicating that bulk oil oxidation is insignificant. Preliminary studies indicate that, in the same experiment, if a five percent octadecyl alcohol is added, the amount of oil soluble iron compounds and to a less extent, oil insoluble iron are increased drastically. In both the static and slow-sliding experiments, the bulk oil is subjected to constant high temperature at run temperatures of 600° and 700°F. The bulk oil oxidation is very significant producing polar species such as alcohols, ketones, etc. Whether this increased polar species concentration in the bulk oil will affect the resulting chemical reactions and what extent its influence has on the results is an important question.

First let the differences between MLO 7789 and MLO 7789A be examined in this regard. Two fluids, having quite different polar material concentration as evidenced by different amount of organometallic products at different temperatures, upon correlating, give the same junction temperature. This would indicate that within a single chemical system, this concentration effect is insignificant. When foreign materials which by themselves may initiate different reactions, are introduced, the effects are dramatic. At this, if the same chemical system is used for correlation, the effect may again be small. It can also be argued that the concentration of these polar species in the "valleys" of the lubricated junction may be just as high as the high temperature static runs. Furthermore, even if the concentration effect of oxidation products at high temperatures is significant, it would mean that for the dynamic test, where low concentration is observed, the temperature at the junction must be much higher than the present results in order to compensate for the concentration difference.

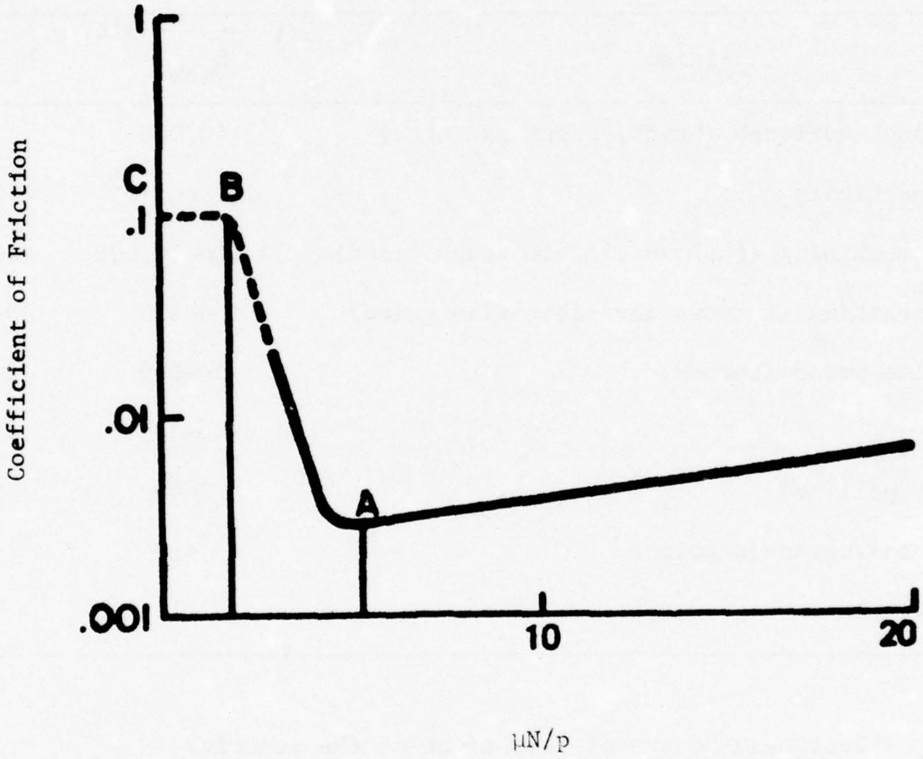

Figure 23. TYPICAL STRIBECK DIAGRAM.

Table 44

RANGE OF SURFACE ROUGHNESS OBTAINED WITH CERTAIN FINISHING OPERATIONS

Finish	- - - - µin. - - - - h_{max}	h_{rms}**
Very rough surfaces (brick, castings, etc.)	>40,000	
Rough machining	10^4 to 10^5	$>10^3$
Medium machining (furrows visible-rough grind)	2,000-10,000	>400
Fine machining (furrows invisible-fine grind)	200-400	30-100
Very fine grind (turned)	20-200	5-30
Honed	40-80	2-10
Lapped, polished	2-40	<4
Fine metallographic polish	<10	<2
Cleavage plane	<1	

** h_{rms} - Root Mean Square of the height of the asperity

Table 4

PROPERTIES OF THE OXIDES OF IRON*

Properties	FeO	Fe_2O_3	Fe_3O_4
Formula Weight	71.9	159.7	231.5
Heat of Formation, kcal/mole	-63.7	-196.5	-267.0
Gibb's Free Energy, kcal/mole	-58.4	-177.1	-242.4
Color	black	red/black	black
Min. Temperature at which formed, °C	570°C**	200°C	200°C
Min. Temperature at which formed, °F	1058°F**	392°F	392°F

** Bernard, J., L'oxydation de métaux, Gauthier Villars, Paris, 1964

* Lange's Handbook of Chemistry, 10th Edition, McGraw Hill, 1966

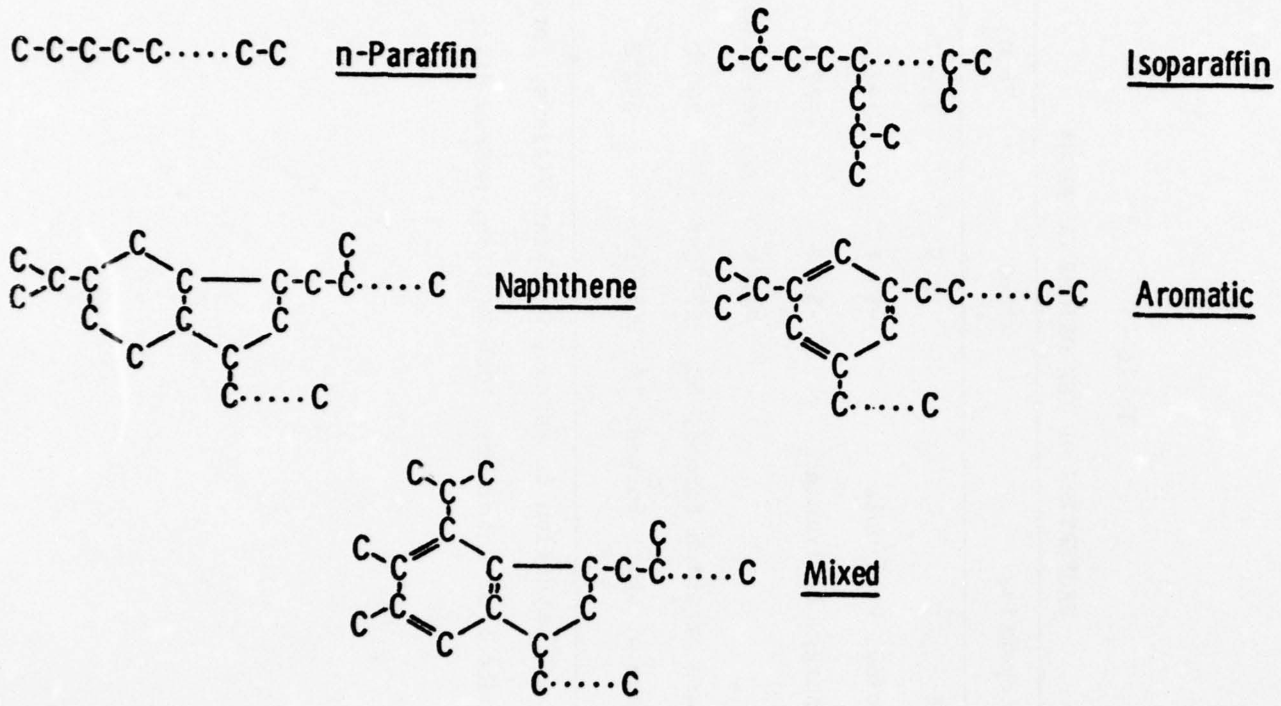

Figure 24. TYPICAL STRUCTURES IN LUBE OIL.

Table 46

OXIDATION PRODUCTS FROM AROMATIC HYDROCARBONS

	Oxidation Temperature, °C	Conditions (Time, hr)	Grams of Product per 100 g of Hydrocarbon
Toluene	100	48	Trace of aldehyde
m-Xylene	100	30	2.1 g toluic adlehyde; 1.1 g toluic acid
Mesitylene (1,3,5-trimethylbenzene)	100	24	2.1 g 1,3-dimethylbenzaldehyde; 1.4 g mesitylenic acid
Durene (1,2,4,5-tetramethylbenzene)	100	9	5.8 g durylic aldehyde; 4.9 g durylic acid
p-Cymene (1-methyl-4-isopropylbenzene)	85	14	1.2 g cumic aldehyde; 0.8 g cumic acid
	102-4	14	Cumic aldehyde; cumic acid; 2 g p-tolyl methyl ketone; formic acid
Ethylbenzene	110-15	24	19 g acetophenone
n-Propylbenzene	102-4	25	Resin
	78	36	Trace of propiophenone
Cumene (isopropylbenzene)	102-4	23	4 g acetophenone
	80	32	Formic acid
tert-Butylbenzene	102-4	25	Trace of nonvolatile residue
Ethylmethylphenylmethane	119	14-29	2-10 g acetophenone
	140	90	7.5 g acetophenone; 4.2 g benzoic acid
n-Butylmethylphenyl methane	119	14-29	2-10 g acetophenone; butyric acid identified by odor
Methyldiphenylmethane	119	14-29	2-10 g benzophenone; formic acid

Table 47

OXIDATION PRODUCTS OF FIVE CLASSES OF HYDROCARBONS

All Values Expressed as Percentage of Total Oxygen Consumed

Class of Hydrocarbon	Free Acid	Combined Acid (Ester)	Peroxide	Alcohol and Phenol	Carbonyl	H_2O	CO_2	Volatile Acids
Paraffin	14.3	16.3	4.1	1.9	46.0	43.9	4.7	---
Naphthene and alkyl-naphthene	11.2	17.0	13.5	8.9	51.4	21.9	3.8	0.6
Aromatic naphthene	6.1	23.1	4.3	8.5	27.2	16.7	1.2	0.4
Alkylbenzene	9.5	12.7	6.7	3.3	36.3	18.2	6.5	Trace
Naphthalene and alkyl-naphthalene	6.9	16.3	1.4	9.4	9.6	51.3	7.8	1.6

Table 48

OXIDATION OF LUBRICATING OILS

	Temperature of Oxidation, °C	O_2 Absorbed, cc per 100 g	Free Acid	Combined Acid	Peroxide	Alcohol	Carbonyl	H_2O	CO_2	Volatile Acids	Asphaltene, mg per 10 g oil
40 VI California	150	2826	5.0	11	0	2.9	1.5	36	21	2.4	135
50 VI California	150	3010	4.5	10	0	8.9	8.9	51	26	2.0	100
60 VI California	150	2853	4.7	12	0	2.5	1.4	56	12	1.7	65
70 VI California	150	2800	4.1	9.0	0	0.4	1.2	68	9.2	1.6	25
80 VI California	150	2803	3.8	10	0	0.6	—	60	16	1.4	6
85 VI California	150	2800	4.1	12	-	1.3	2.5	65	16	1.2	2
Mid-Continent Neutral	150	3233	4.5	12	<.1	0.7	5	49	—	1.1	—
Synthetic oil made from cracked wax olefins	150 110	2532 2980	5.9 6.6	16 15	<1 0.4	9 8	9 19	34 26	7 4.9	2.4 3.8	0 0
White Oil	110	1571	13	19	5.0	13	44	11	—	1.3	0

Table 49

INCIDENTS OF CHEMICAL REACTIONS INVOLVING SULPHUR AND THE BEARING METAL

Item	Lubricating System	Component	Speed (rev/min)	Specific Loading (bar)	Lubricant	Reaction Products (identified by X-ray diffraction)	Comments
1	Steam turbine and centrifugal ammonia syngas compressor	thrust bearing d_m=125 mm Sn 83, Sb 9, Cu 8	3,600	14.5	straight oil 32cS at 100°F S=0.65%	72% $CuSO_4 \cdot 2\ Cu(OH)_2$ 26% 4 $Cu_2S \cdot CuS$ 2% Cu_2O	Repeated thrust bearing failures on 6 machines until bearing metal changed
2	Electric motor gearbox and nitrous gas (10% NO + NO_2) axial flow compressor	thrust bearing d_m=185 mm Sn 85, Sb 10, Cu 5	6,300	22.7	turbine oil BS 489 medium	CuCNS	one, possibly two, failures
3	Electric motor, gearbox and centrifugal ammonia syngas compressor	thrust bearing d_m=110 mm Sn 85, Sb 8, Cu 7, Pb 0.5	14,800	17	turbine oil BS 489 heavy S=0.1%	4 $Cu_2S \cdot CuS$	one incident after 12 months on line. Oil sulphur at failure 0.19%
		journal bearing d=120 mm c_d=0.24 mm Sn 81, Sb 12.4, Cu 8.4, Pb 0.15	14,800		ditto	$(NH_4)_2SO_4 \cdot CuSO_4 \cdot H_2O$	
4	Crankcase of reciprocating ammonia syngas compressor	big-end bearing d=330 mm c_d=0.15 mm Sn 89, Sb 8, Cu 3	333	—	straight oil 140 cS at 100°F S=1.17%	4 $Cu_2S \cdot CuS$	occurred after severe overload
5	Crankcase of reciprocating ethylene compressor	big-end bearing d=145 mm Sn 87.5, Sb 7 Cu 5.5	585	80 max	straight oil 112 cS at 100°F	4 $Cu_2S \cdot CuS$	the bearing from this stage has suffered two fatigue failures
6a	Rotary carbamate pump gearbox and bearings	thrust bearing d_m=100 mm Ag-plated steel	20,500	30	(i) hydraulic oil with ZDDP 31.5 cS at 100°F	Ag_2S βZnS	failures occurred 400 and 800 hr
					(ii) hydraulic oil without ZDDP	Ag_2S	failures occurred 150 and 250 hrs
6b	Rotary carbamate pump gearbox and bearings	journal bearing d=57.5 mm c_d=0.1 mm Cu 80, Sn 10, Pb 10	20,500		31.5 cS at 100°F	copper sulphide	incipient corrosion appeared at 250 hr inspection
7	Shaft sealing oil hydrocarbon gas centrifugal compressor	floating bush seal d=115 mm c_d=0.07 mm Sn 85, Sb 8, Cu 7, Pb 0.5	8,900	—	straight oil 55 cS at 100°F	CuS βZnS $(NH_4)_2SO_4 \cdot CuSO_4 \cdot H_2O$	deposit also contained organic sulphur compounds
8	Steam turbine, centrifugal hydrocarbon gas compressor, shaft sealing oil	floating bush seal d=177.5 mm c_d=0.07 mm Sn 91, Sb 5, Cu 4	5,800	—	turbine oil BS 489 light with ZDDP S=0.81%	CuS βZnS	reaction product found after first 16 months on line

Summers-Smith, D., "Chemical Reactions on Bearings in Lubricated Industrial Machines." Wear, 18, 291-300, 1971.

Table 50

HEAT OF FORMATION DATA ON BONDS INVOLVING C, O_2, H, Fe, S

Bonds	ΔH_f kcal/mole*
>CO-O	-50.5
Fe-O	-39.0**
O-H	-27.0
Fe-S	-22.8**
>CO-H	-13.9
C-O	-12.0
C-H	- 3.8
S-H	- 0.8
Fe-C	+ 1.4**
C-S	+ 6.7
O-O	+21.5

* Data taken from Benson (98)

** Estimated from ΔH_f of Fe_2O_3 = - 196.3; FeS = -22.8; Fe_3C + 5.4 from Kubaschewski (100) as suggested by Mortimer (100)

> Indicates double bond C=C

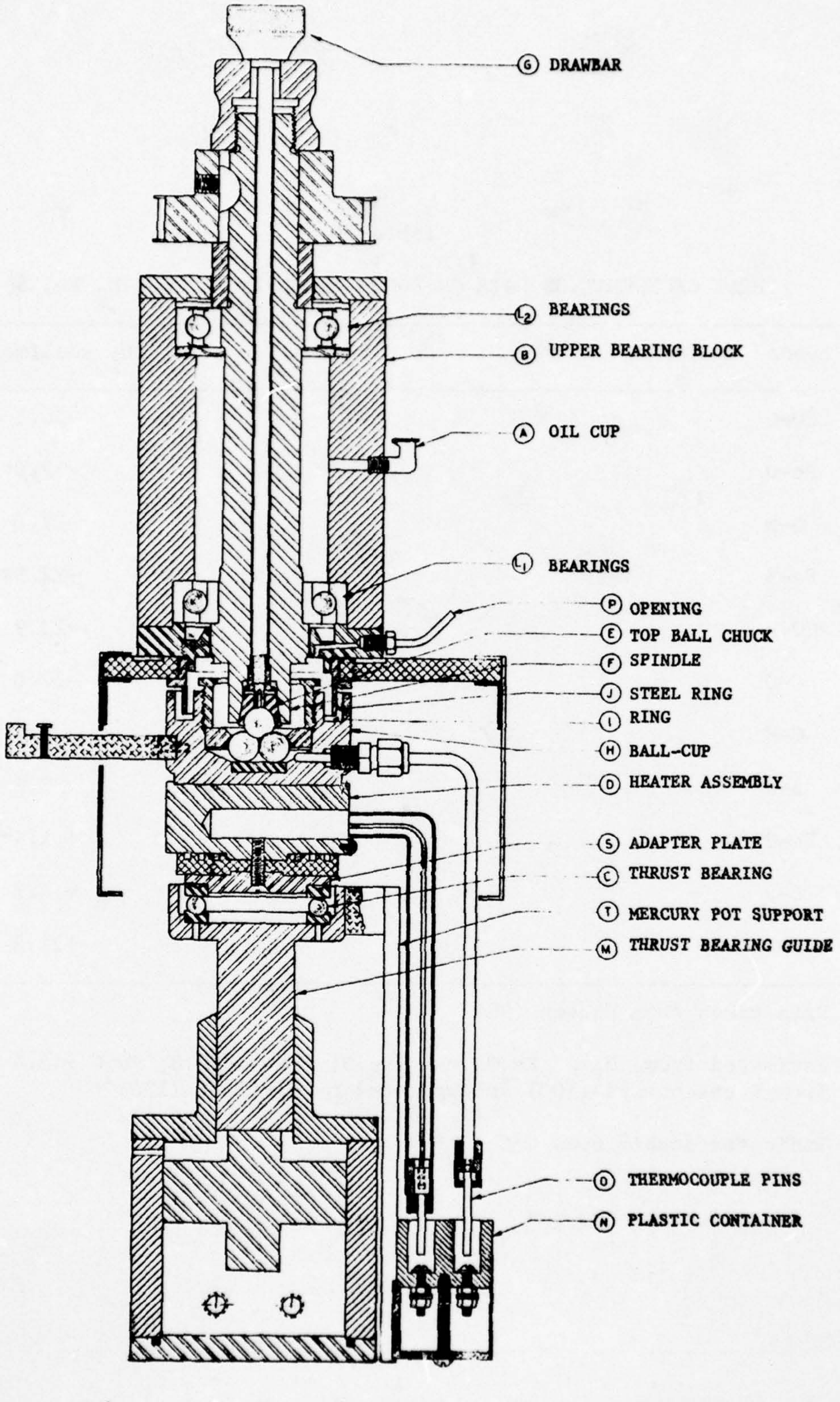

Figure 25. GE/BROWN MODIFIED FOUR-BALL WEAR TESTER.

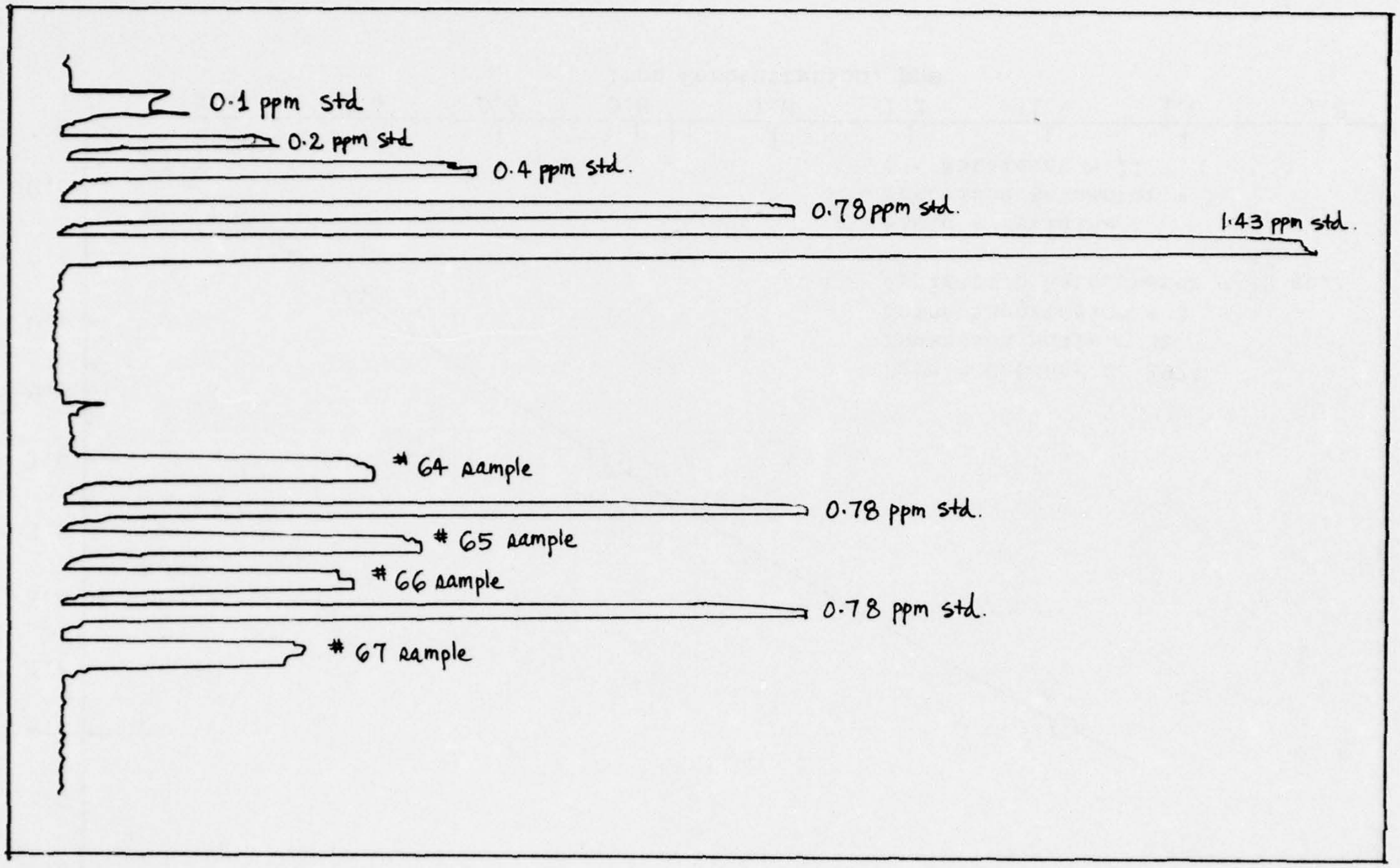

Figure 26. A TYPICAL ATOMIC ABSORPTION TRACE.

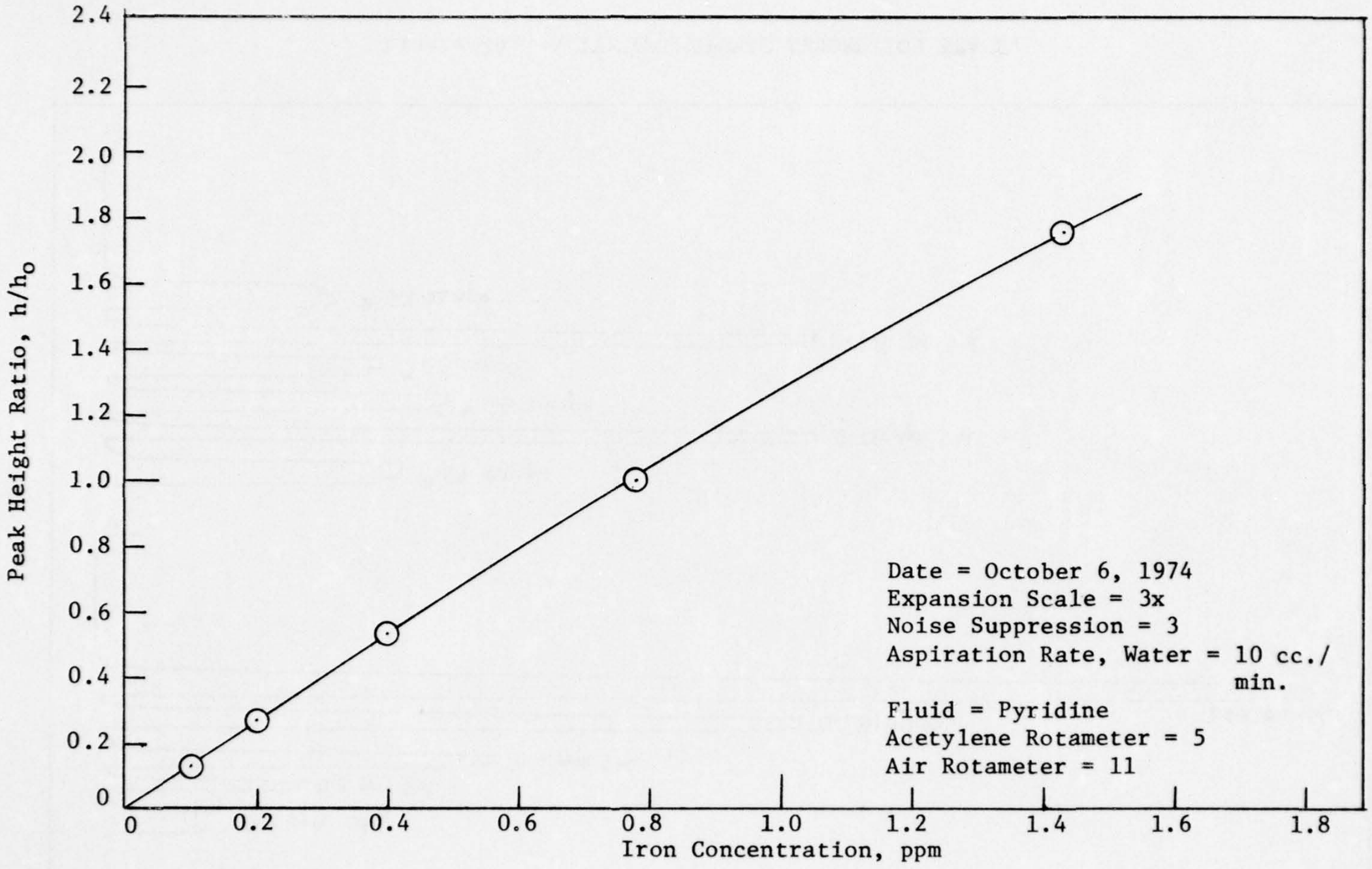

Figure 27. A TYPICAL ATOMIC ABSORPTION CALIBRATION CHART.

Table 51

PERCENTAGE IRON AND ITS OXIDES DISSOLVED IN 3.92N HNO_3

Substance	Sample Weight, gm	Iron in Filtrate, gm	Dissolved, %
Fe	0.02863	0.02360	83
FeO	0.68017	0.12780	19
Fe_2O_3	0.58606	0.00003	0.005
Fe_3O_4	0.71947	0.00300	0.038

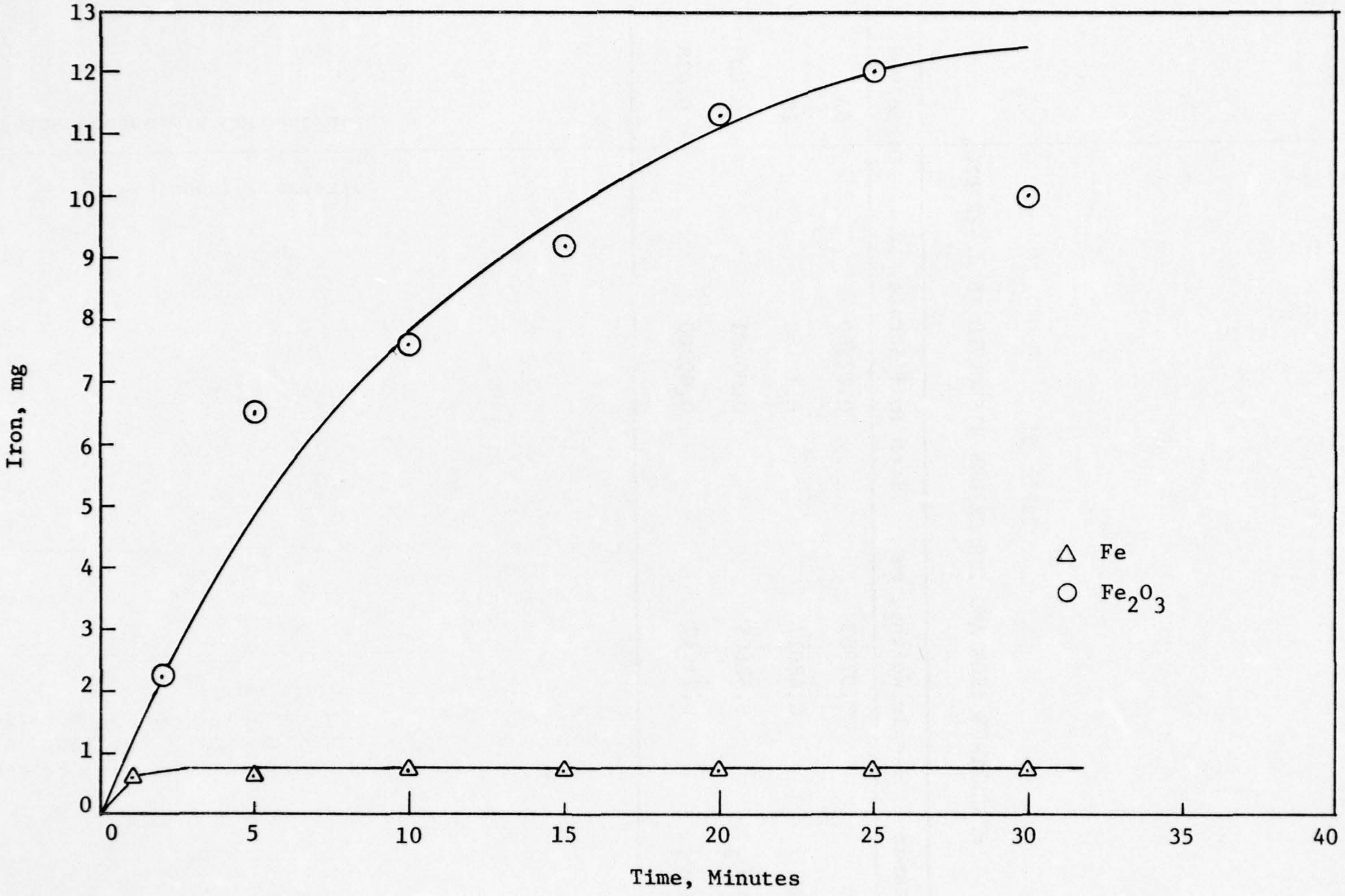

Figure 28. DISSOLUTION RATES FOR IRON AND IRON OXIDE IN HYDROCHLORIC ACID INHIBITED WITH ACRIDINE.

Table 52

REPRODUCIBILITY AND CONSISTENCY OF THE EXPERIMENTAL DATA

Test Fluid: Super-refined paraffinic mineral oil (MLO 7789A)
Test Machine: GE/Brown Modified Four-ball Wear Tester
Test Conditions: Load = 40 kg., Speed = 600 r.p.m., Duration = 100 min., Bulk Fluid Temp. = 167°F
Atmosphere = dry air at 0.25 ℓ/min

Run No.		Wear Scar Diameter mm.	- - - -Iron Recovered from Wear Debris in μg as - - - -			
			Oil Solu.	Pyridine Solu.	Iron	Iron Oxides
42		0.90	BDC*	12	101	209
43		0.90	1	21	99	139
44		0.90	BDC	11	108	231
45		0.90	BDC	10	48	186
BA	average	0.90	BDC	13.5	89	191
	standard deviation	0	---	4.39	24.0	34.1

* Below Detactable Concentration

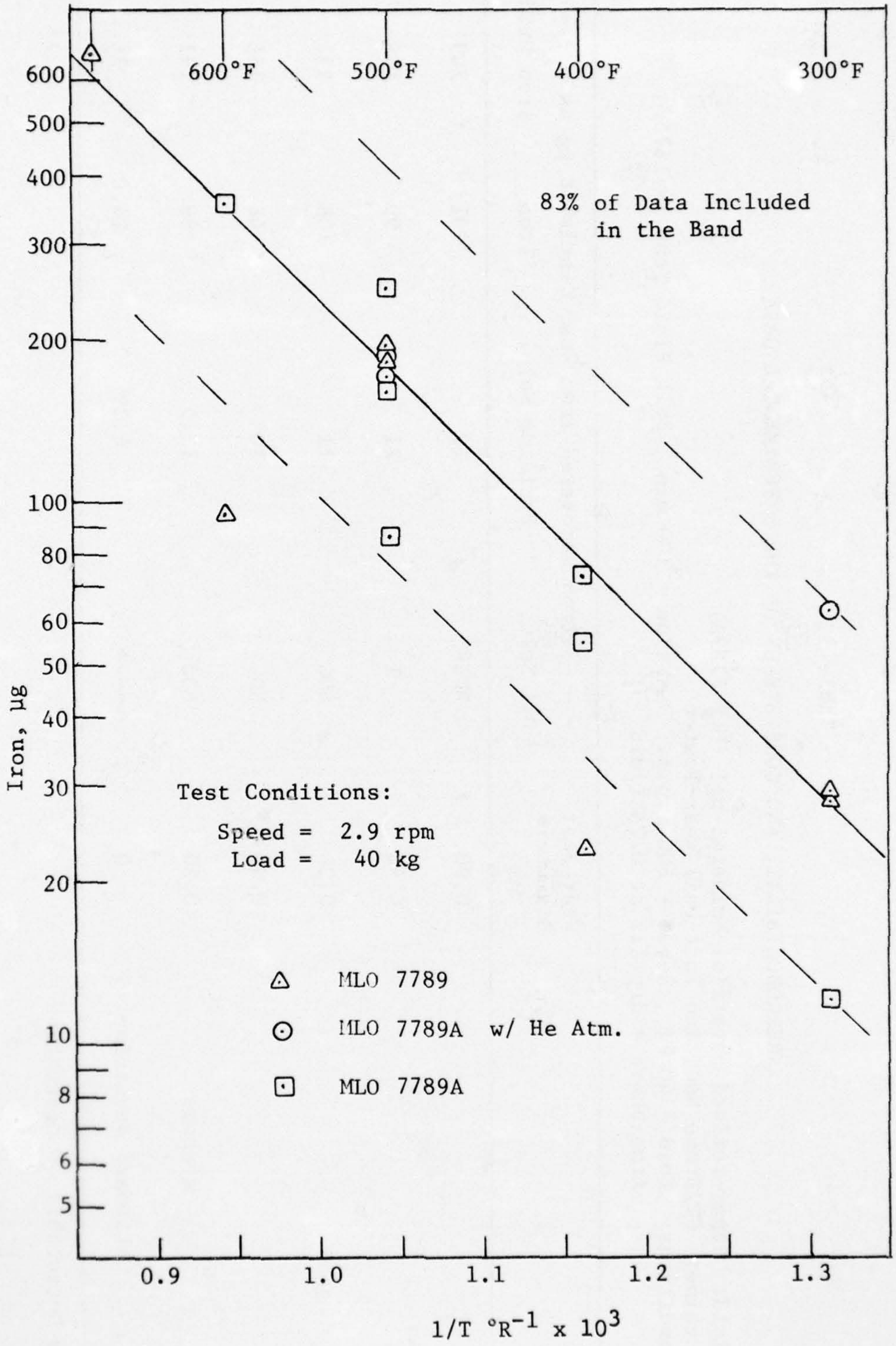

Figure 29. IRON PARTICLES GENERATION VS. THE RECIPROCAL OF ABSOLUTE TEMPERATURE.

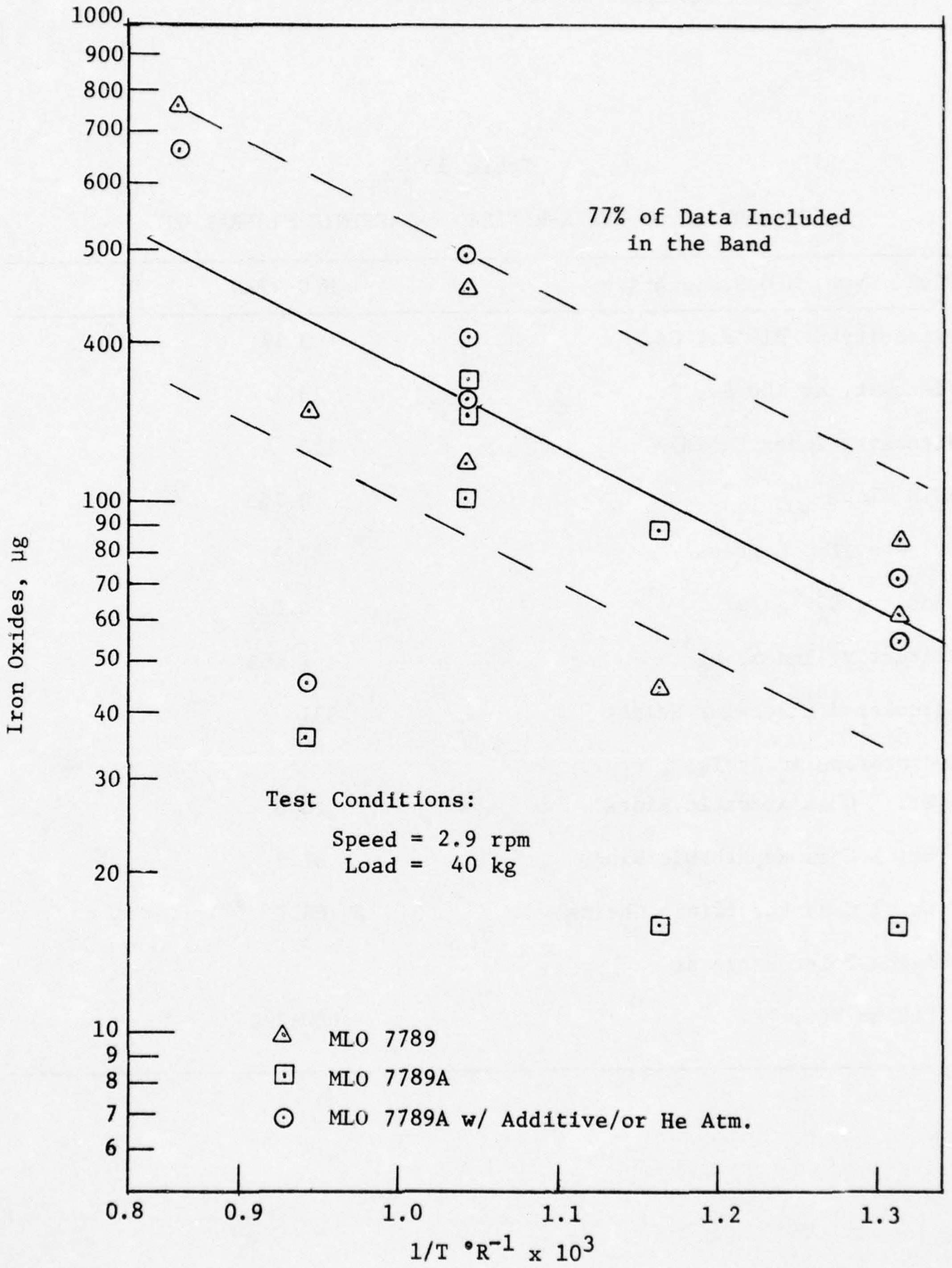

Figure 30. **IRON OXIDES GENERATION VS. THE RECIPROCAL OF ABSOLUTE TEMPERATURE.**

Table 53

PROPERTIES OF SUPER-REFINED PARAFFINIC MINERAL OIL

Fluid Type, MLO Designation	MLO 7789
Viscosity at 210°F., Cs.	3.11
Viscosity at 100°F., Cs.	13.1
Viscosity Index (ASTM)	110
ASTM Slope	0.763
API Gravity, Degrees	37.3
Density, D_4^{20} g./ml.	0.838
Refractive Index, n_D^{20}	1.4637
Calculated Molecular Weight	331
Hydrocarbon Analysis:	
Wt. % C as Aromatic Rings	0.0
Wt. % C as Naphthenic Rings	31.3
Wt. % C as Paraffinic Chains	68.7
Boiling Point Range at 760 mm Hg., °F.	600-770

AD-A031 621 PENNSYLVANIA STATE UNIV UNIVERSITY PARK PETROLEUM RE--ETC F/G 11/8
FLUIDS, LUBRICANTS, FUELS AND RELATED MATERIALS. PART II.(U)
OCT 75 E E KLAUS, E J TEWKSBURY, B Y SO F33615-73-C-5101

UNCLASSIFIED AFML-TR-74-201-PT-2 NL

3 OF 3
AD
A031621

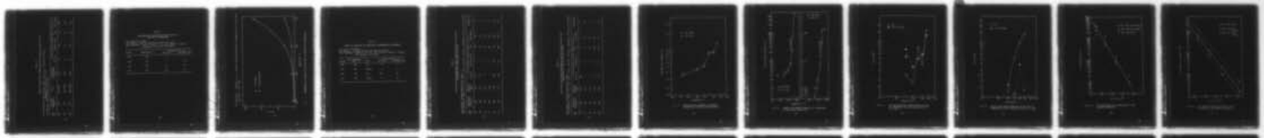

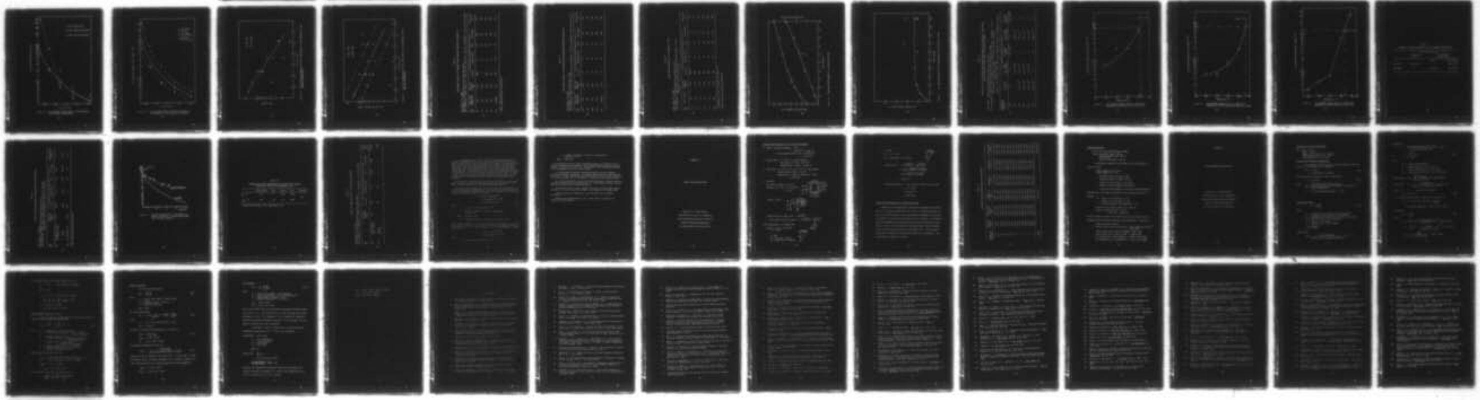

END

DATE
FILMED
12-76

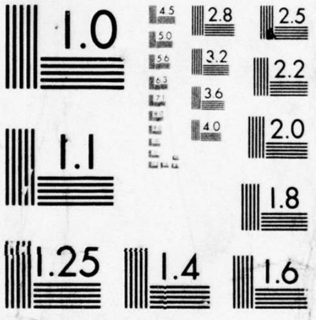

MICROCOPY RESOLUTION TEST CHART
NATIONAL BUREAU OF STANDARDS-1963-A

Table 54

EFFECT OF PERCOLATION THROUGH ACTIVATED ALUMINA ON WEAR AT 167°F

Test Conditions: Load = 40 kg., Speed = 630 r.p.m., Duration = 100 min.,
Atmosphere = dry air at 0.7 ℓ/hr
Test Machine: Sheel Four-ball Wear Tester

Run No.	Bulk Fluid Temperature, °F	Fluid	Average Wear Scar Diameter, mm.	- - Iron Recovered from Wear Debris in μg as - - -			
				Oil Solu.	Pyridine Solu.	Iron	Iron Oxides
BK	167°	MLO 7789	0.74	14	20	51	198
K23	167°	MLO 7789A	0.81	15	41	58	128
K24	167°	MLO 7789B	0.83	16	28	66	170

Table 55

ORGANOMETALLIC FORMATION IN STATIC TESTS AS A FUNCTION OF TEMPERATURES

Test Fluid: MLO 7789A
Test Machine: GE/Brown Modified Four-ball Wear Tester
Test Conditions: Load = 0, Speed = 2.9 r.p.m., Duration = 100 min.
Atmosphere = dry air at 0.25 ℓ/min.

Run No.	Temperature, °F	Organometallic, μg Oil Solu.	Organometallic, μg Pyridine Solu.
105	400	1	7
106	500	8	20
107	600	63	20
108	700	244	58

Test Conditions = Speed=2.9 r.p.m., Load=zero, Duration=100 minutes, Atmosphere=dry air at 0.25 LPM

Test Fluid = MLO 7789A

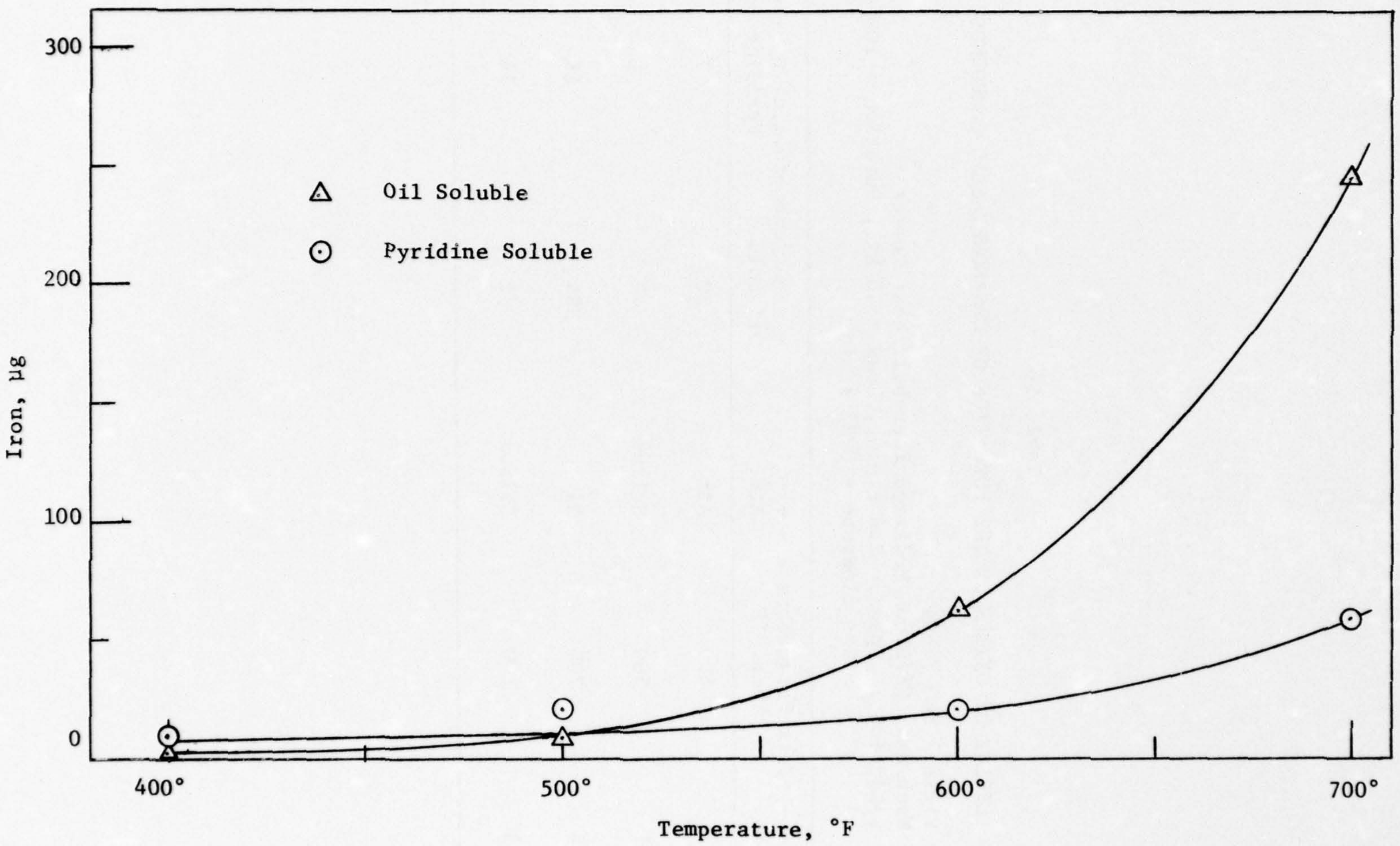

Figure 31. ORGANOMETALLIC FORMATION IN STATIC TESTS AS FUNCTION OF TEMPERATURE.

Table 56

EFFECT OF OXYGEN ON THE FORMATION OF ORGANOMETALLIC COMPOUNDS

Test Fluid: MLO 7789A
Test Machine: GE/Brown Modified Four-ball Wear Tester
Test Conditions: Speed = 2.9 r.p.m., Load = 40 kg., Duration = 100 min.
Gas flowrate = 0.25 ℓ/min

Test Parameters			Organometallic, μg	
Run No.	Temp. °F	Atm.	Oil Solu.	Pyridine Solu.
K28	500	Air	20	7
K31	500	Helium	2	3
K34	700	Air	394	84
K33	700	Helium	2	14

Table 57

THE RELATIONSHIP BETWEEN WEAR PRODUCT COMPOSITION AND THE BULK FLUID TEMPERATURES AT SLOW-SLIDING (MLO 7789)

Test Machine: GE/Brown Modified Wear Tester
Test Conditions: Speed = 2.9 r.p.m., Load = 40 kg., Duration = 100 min., Atmosphere = dry air at 0.25 ℓ/min

Run No.	Bulk Fluid Temperature, °F	Wear Scar Diameter, mm.	- - - Iron Recovered from Wear Debris in μg as - - -				Organic-Iron %
			Oil Solu.	Pyridine Solu.	Iron	Iron Oxides	
35	300	0.45	0.5	3	28	85	3
35A	300	0.45	0.5	3	29	61	3
36	400	0.51	2	5	23	45	9
37	500	0.86	7	7	196	119	4
38	600	0.89	128	80	94	149	46
39	700	1.36	150	517	690	563	35

Table 58

THE RELATIONSHIP BETWEEN WEAR PRODUCT COMPOSITION AND THE BULK FLUID TEMPERATURES AT SLOW-SLIDING (MLO 7789A)

Test Machine: GE/Brown Modified Wear Tester
Test Conditions: Speed = 2.9 r.p.m., Load = 40 kg., Duration = 100 min., Atmosphere = dry air at 0.24 ℓ/min

Run No.	Bulk Fluid Temperature, °F	Wear Scar Diameter, mm.	- - - Iron Recovered from Wear Debris in μg as - - -				Organic-Iron %
			Oil Solu.	Pyridine Solu.	Iron	Iron Oxides	
96	167	0.37	BDL	3	34	7	8
97	300	0.44	1	4	12	16	15
98	400	0.54	1	4	73	16	5
99	500	0.90	15	8	249	102	6
100	600	0.93	48	22	364	36	15

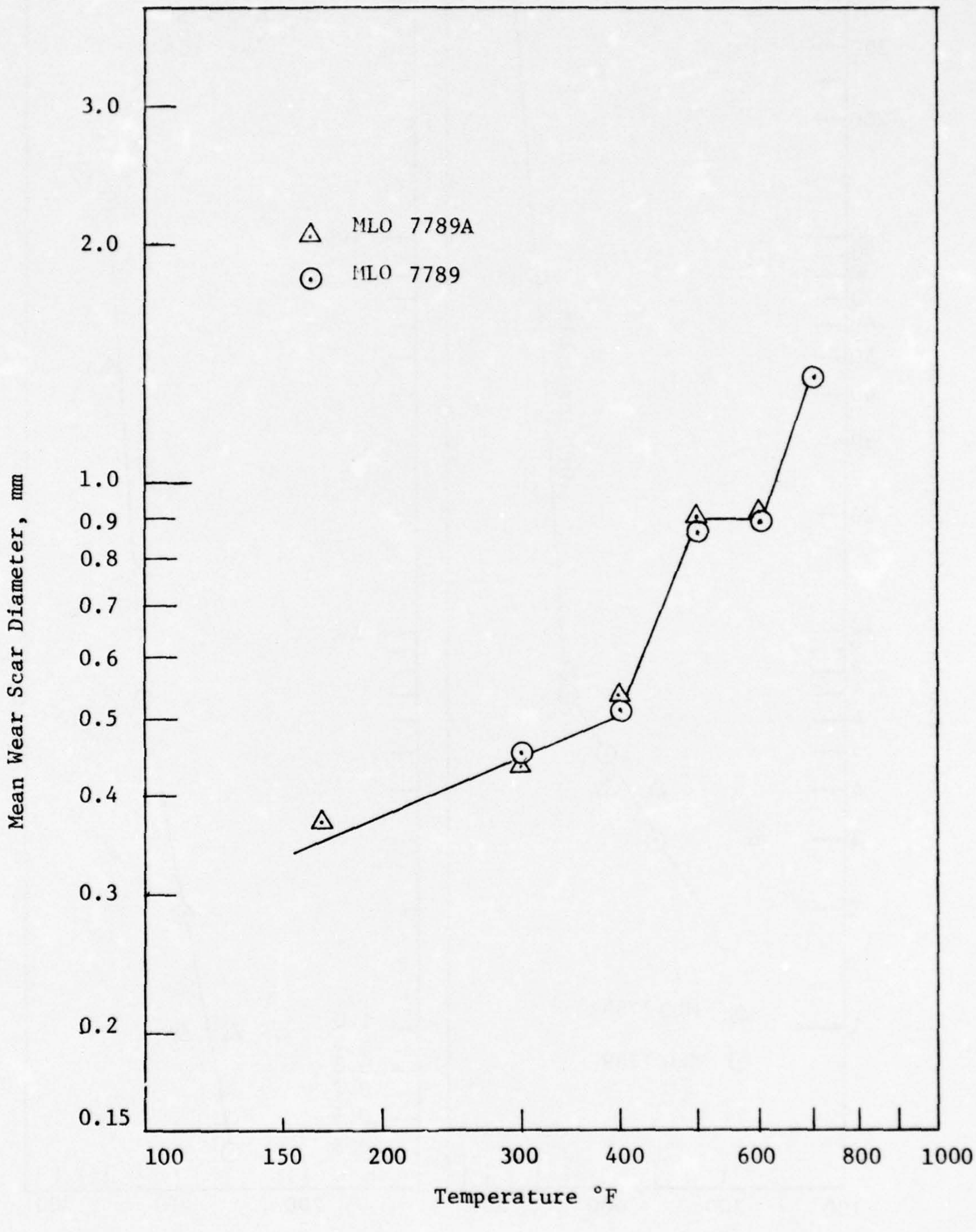

Figure 32. MEAN WEAR SCAR DIAMETERS AT DIFFERENT TEMPERATURES IN SLOW-SLIDING WEAR TESTS.

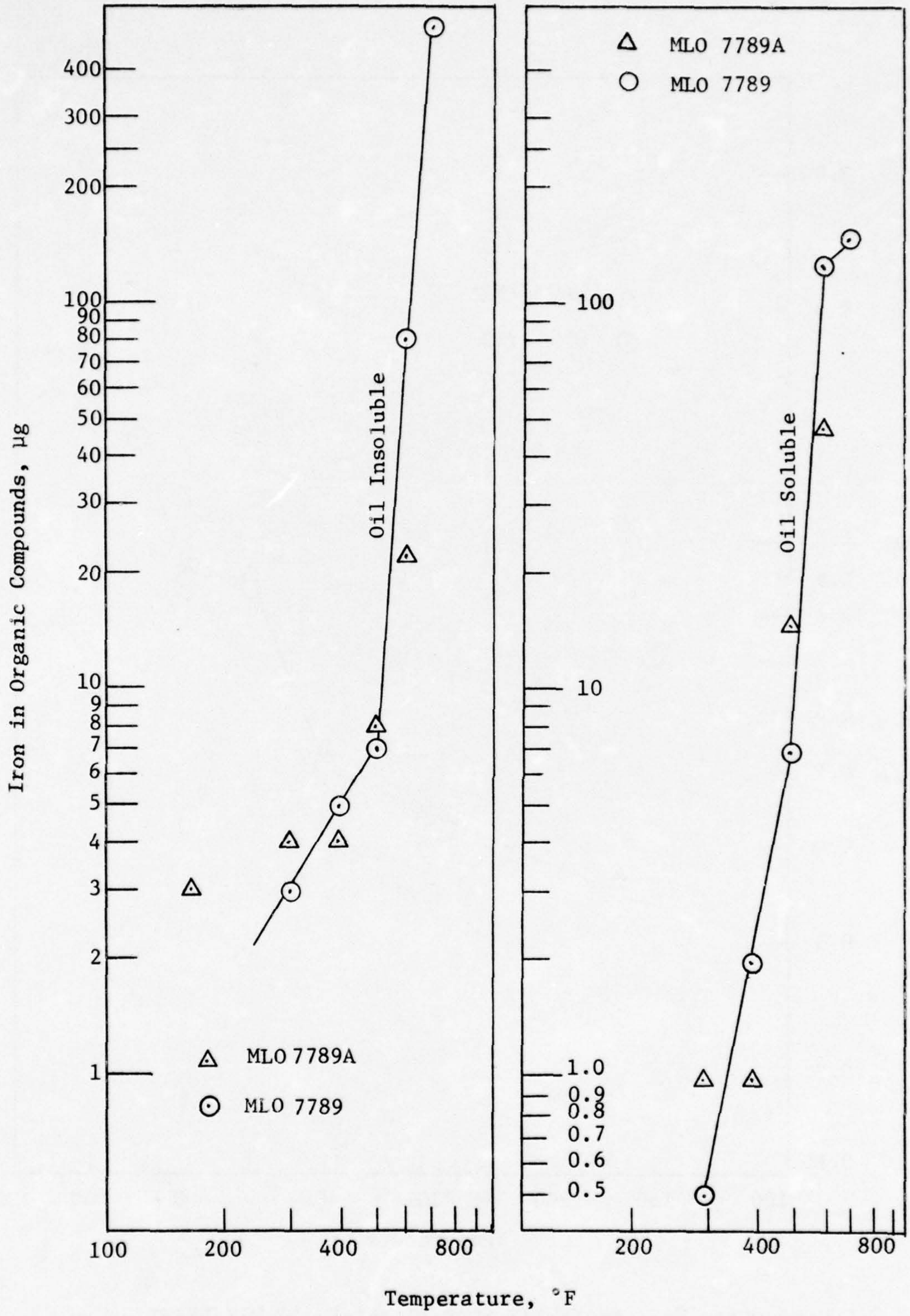

Figure 33. ORGANIC-IRON COMPOUND FORMATION VS. TEMPERATURE IN SLOW-SLIDING WEAR TESTS.

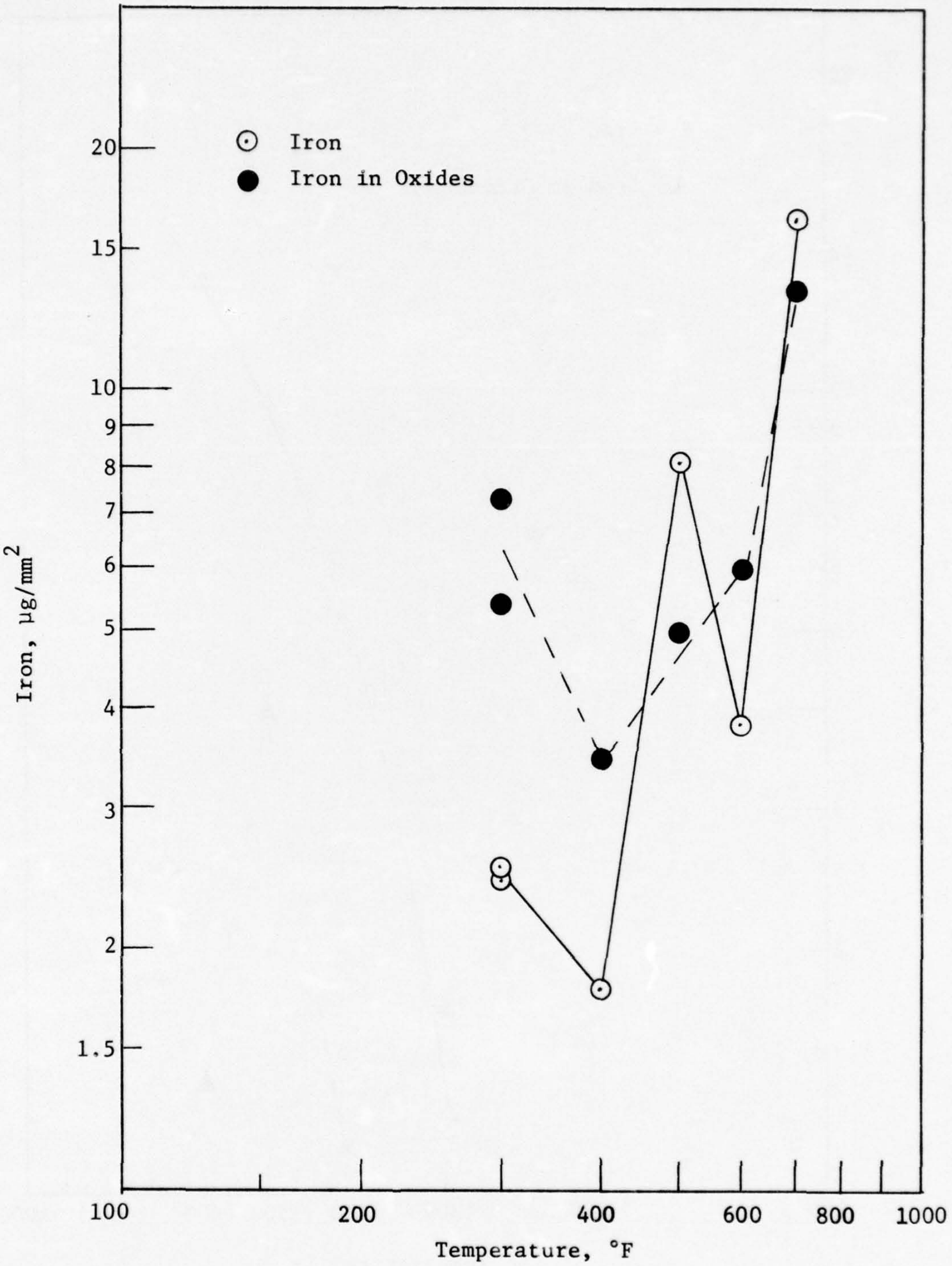

Figure 34. IRON AND IRON OXIDES FORMATION PER UNIT AREA VS. TEMPERATURE IN SLOW-SLIDING WEAR TESTS (MLO 7789).

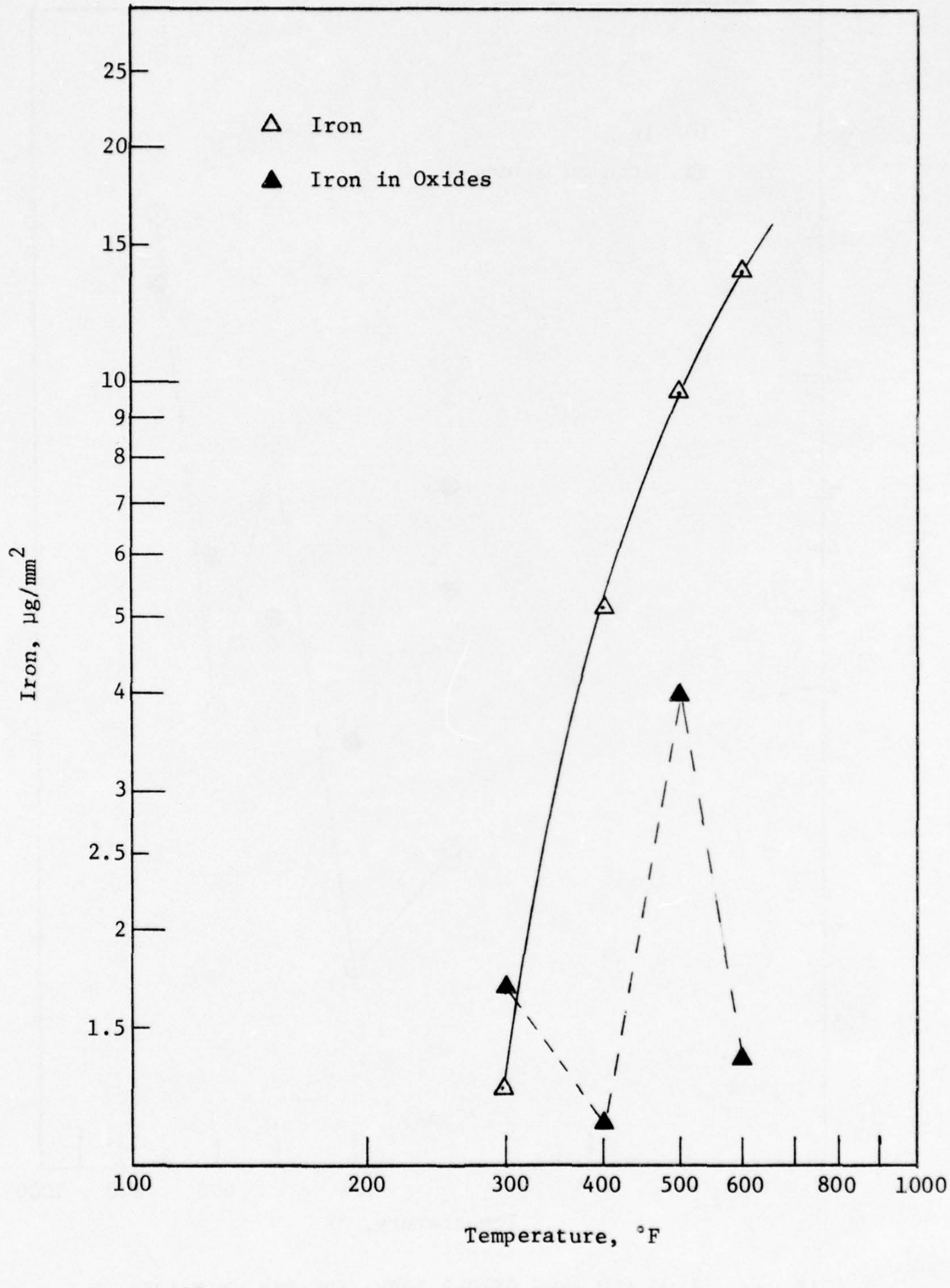

Figure 35. IRON AND IRON OXIDES FORMATION PER UNIT AREA VS. TEMPERATURE IN SLOW-SLIDING WEAR TESTS (MLO 7789A).

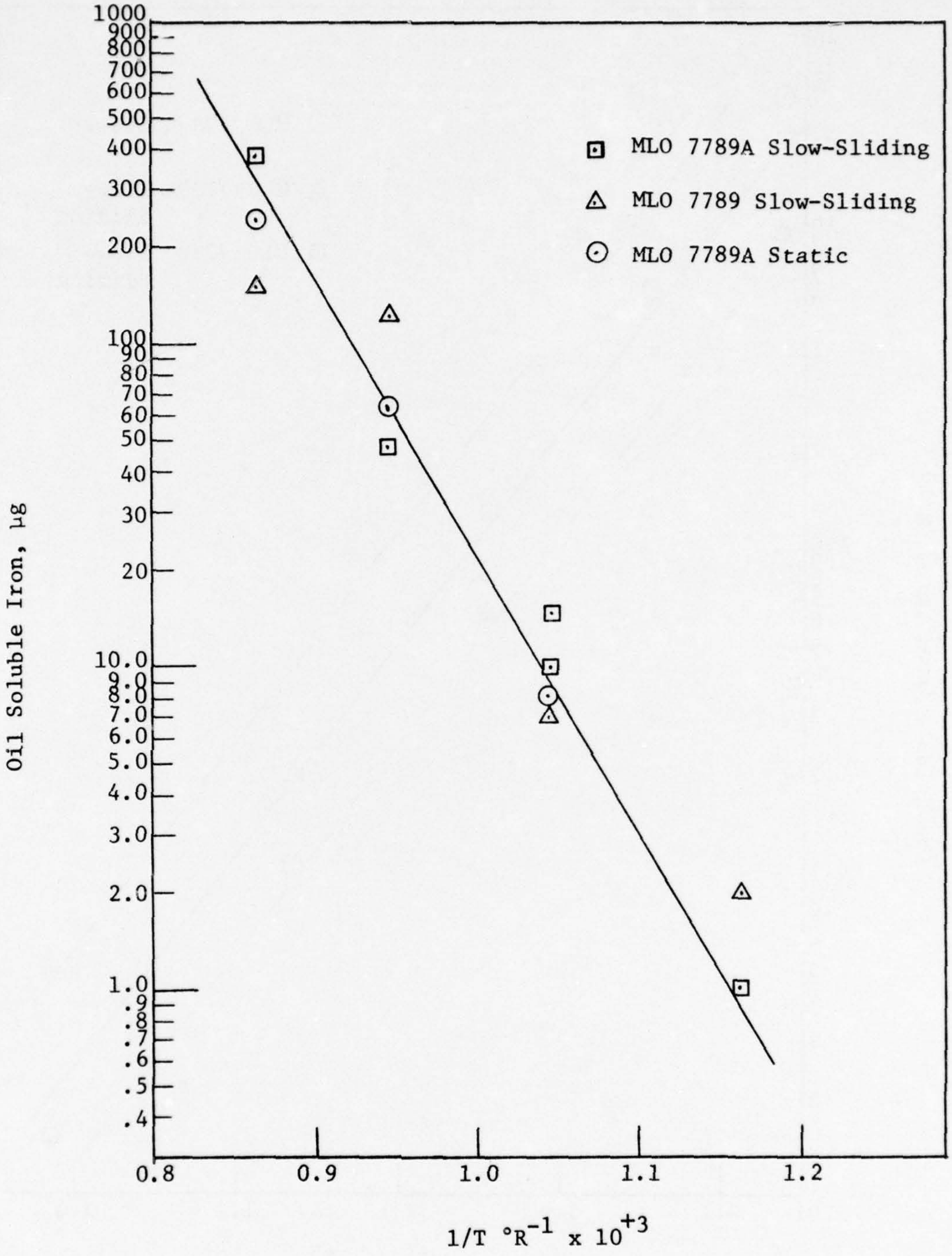

Figure 36. OIL SOLUBLE IRON VS. THE RECIPROCAL OF THE ABSOLUTE TEMPERATURE.

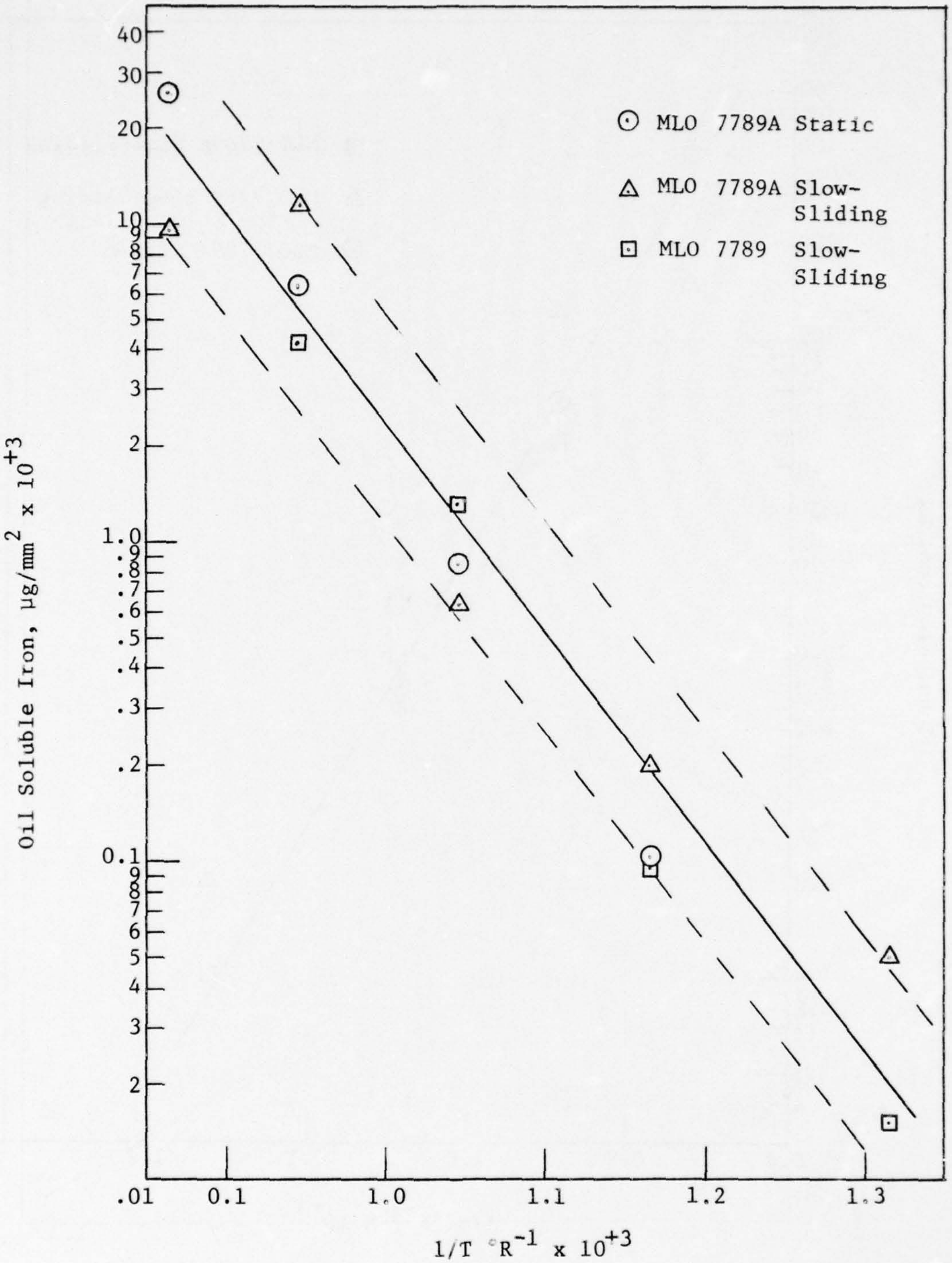

Figure 37. OIL SOLUBLE IRON PER UNIT AREA VS. THE RECIPROCAL OF THE ABSOLUTE TEMPERATURE.

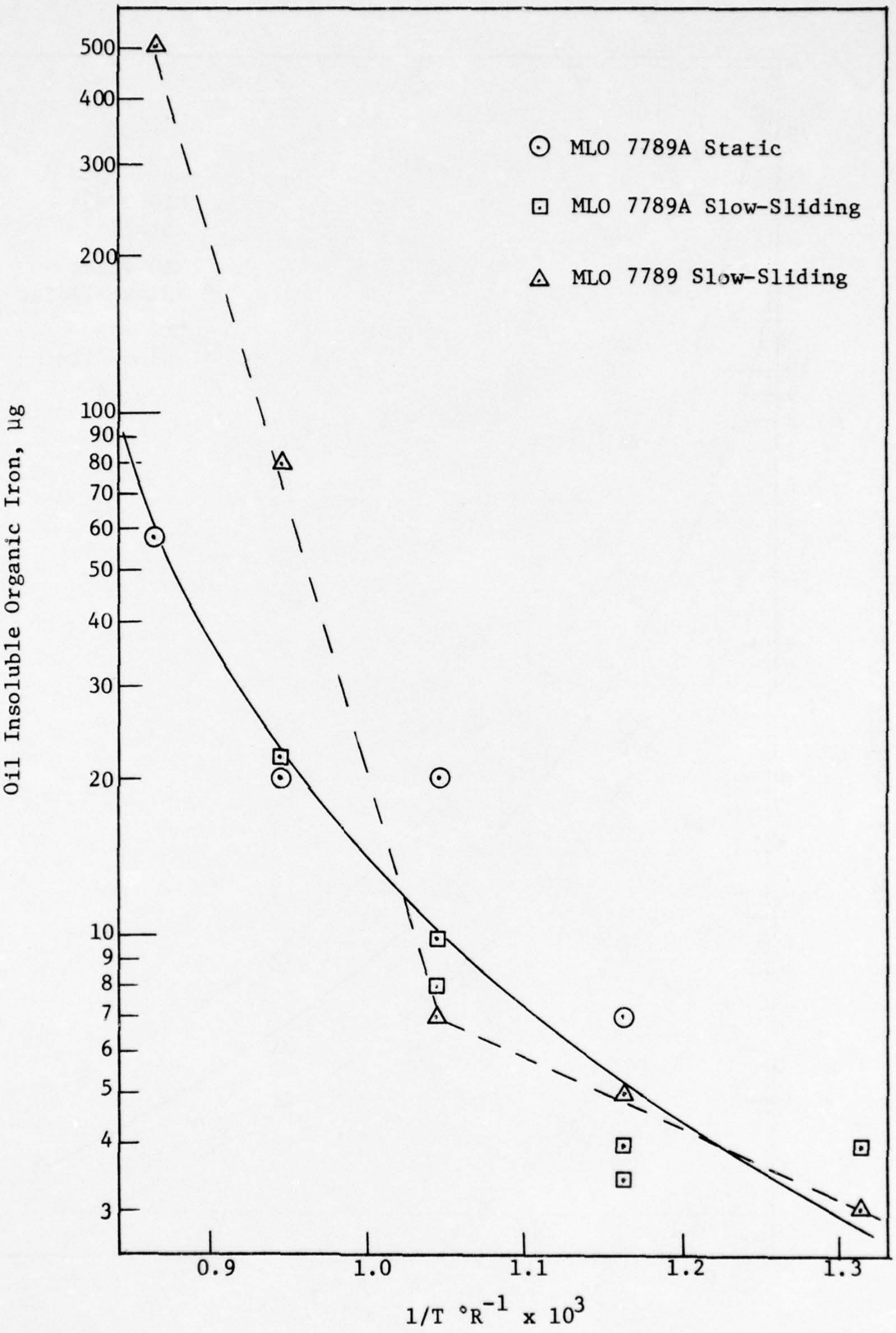

Figure 38. OIL INSOLUBLE ORGANIC IRON VS. THE RECIPROCAL OF THE ABSOLUTE TEMPERATURE.

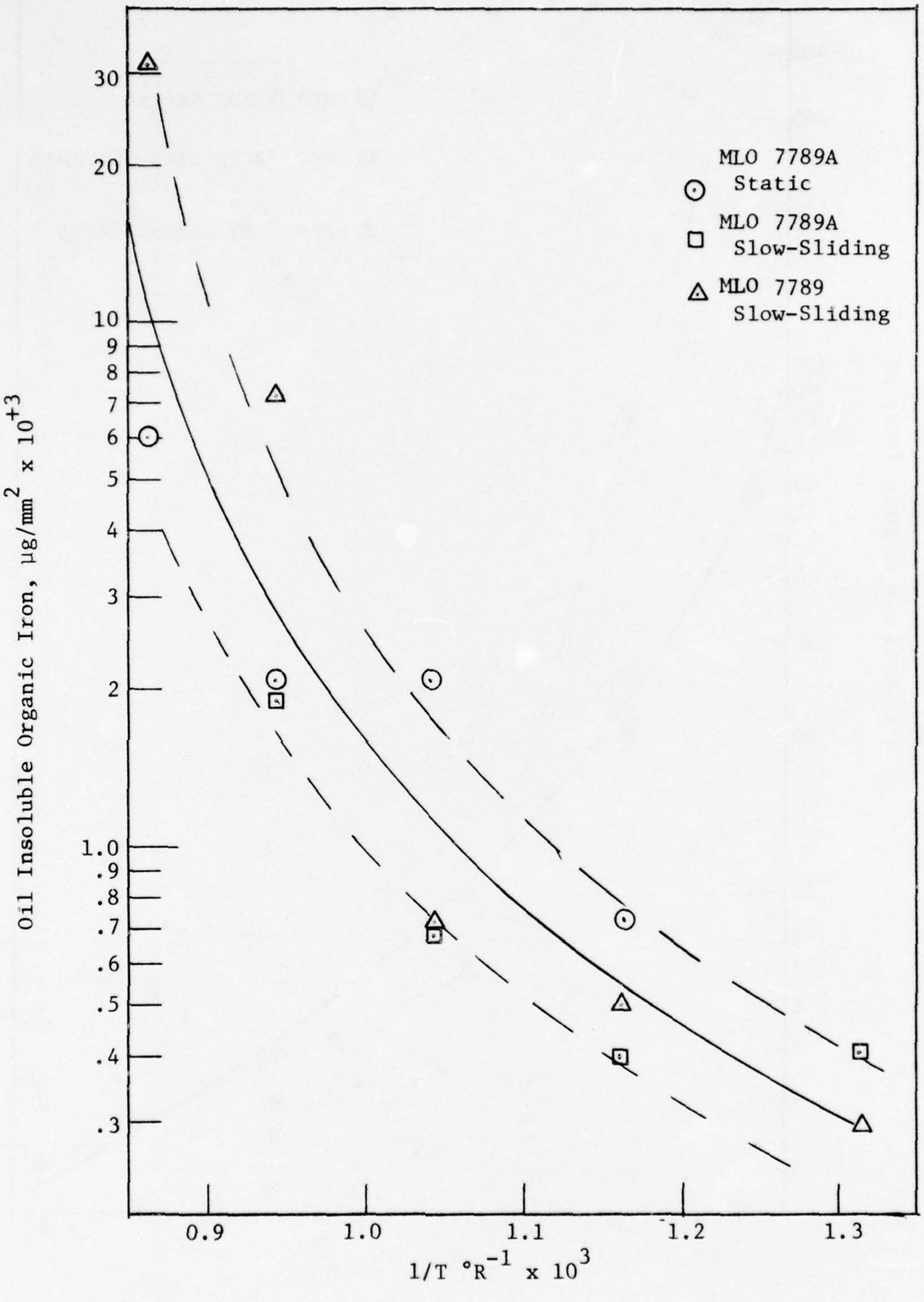

Figure 39. OIL INSOLUBLE ORGANIC IRON PER UNIT AREA VS. THE RECIPROCAL OF THE ABSOLUTE TEMPERATURE.

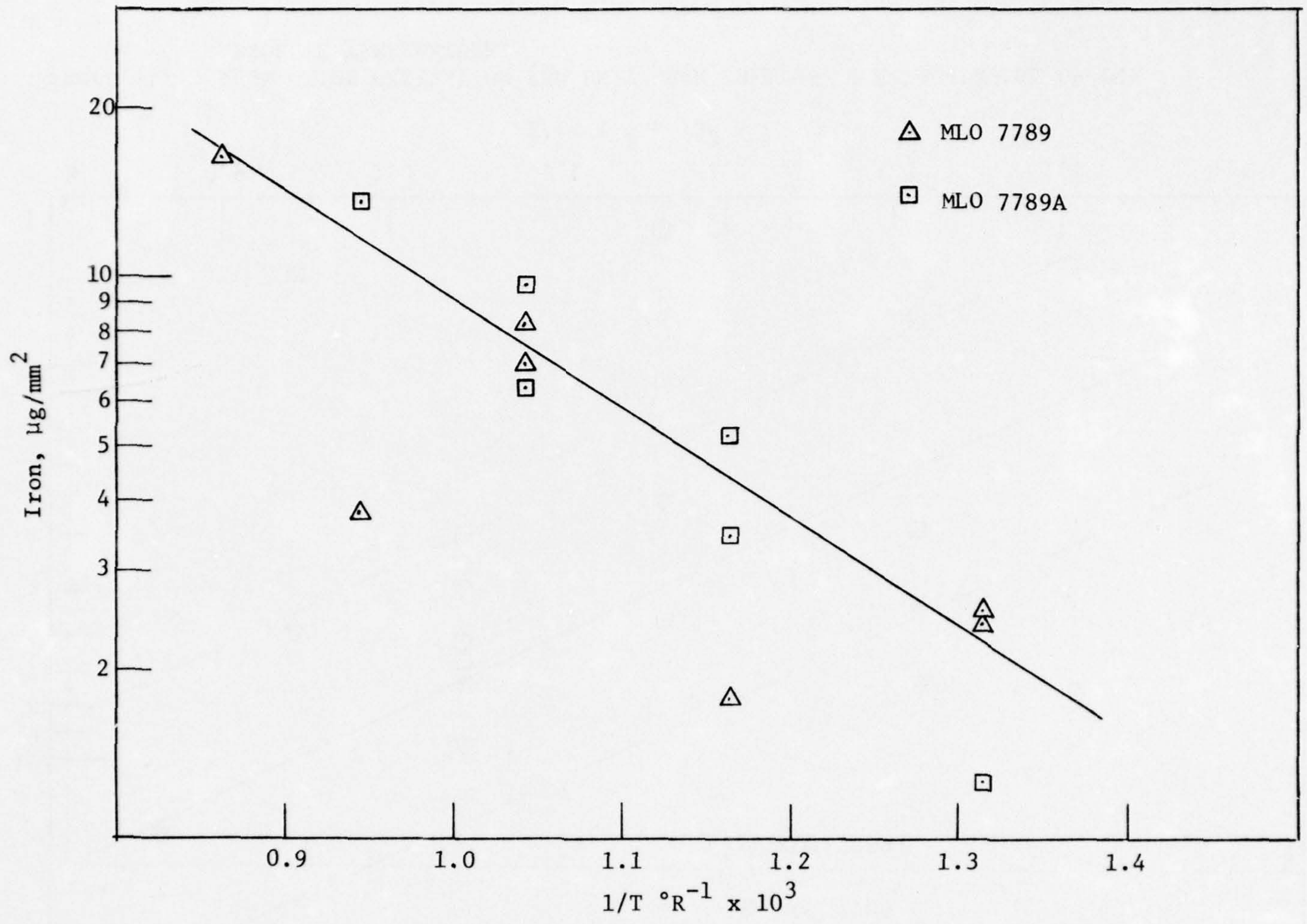

Figure 40. IRON PARTICLES GENERATED PER UNIT WEAR AREA VS. THE RECIPROCAL OF THE ABSOLUTE TEMPERATURE.

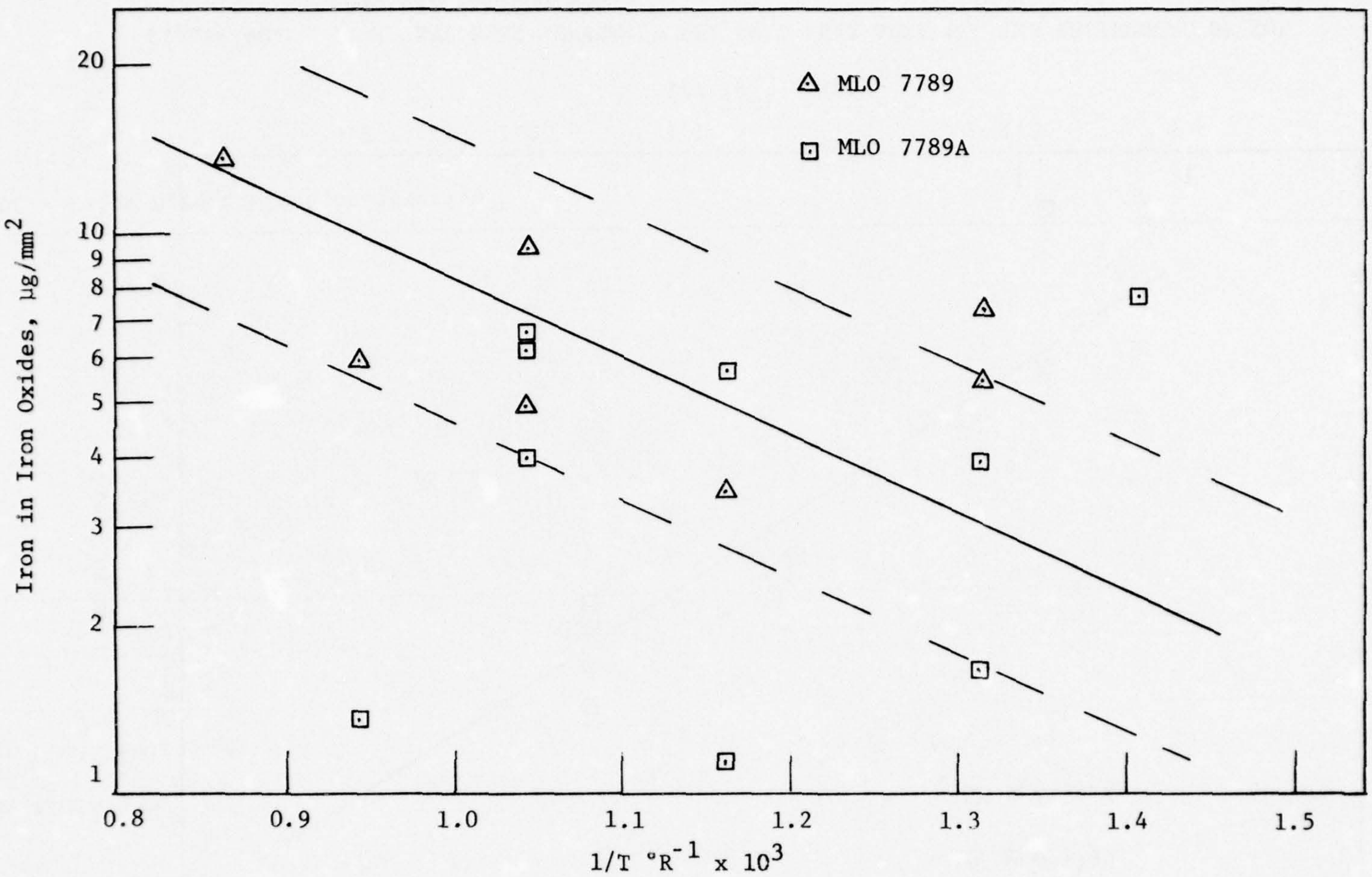

Figure 41. IRON OXIDE GENERATION PER UNIT WEAR AREA VS. THE RECIPROCAL OF THE ABSOLUTE TEMPERATURE.

Table 59

WEAR DEBRIS ANALYSIS OF TREATED SUPER-REFINED PARAFFINIC MINERAL OIL

Test Fluid: MLO 7789A
Test Machine: GE/Brown Modified Four-ball Wear Tester
Test Conditions: Speed = 600 r.p.m., Load = 40 kg., Duration = 100 min., Atmosphere = dry air at 0.25 ℓ/min

Run No.	Bulk Fluid Temperature, °F	Wear Scar Diameter, mm.	- - - Iron Recovered from Wear Debris in µg as - - -				Total Iron, µg
			Oil Solu.	Pyridine Solu.	Iron	Iron Oxides	
42	167	0.90	BDC*	12	101	209	322
43	167	0.90	1	21	99	139	260
44	167	0.90	BDC	11	108	231	350
45	167	0.90	BDC	10	48	186	244
BA	Average	0.90	BDC	13.5	89	191	294

* BDC = Below Detectable Concentration

Table 60

WEAR DEBRIS ANALYSIS OF UNTREATED SUPER-REFINED PARAFFINIC MINERAL OIL

Test Fluid: MLO 7789
Test Machine: Sheel Four-ball Wear Tester
Test Conditions: Speed = 600 r.p.m., Load = 40 kg., Duration = 100 min., Atmosphere = dry air at 0.7 ℓ/hr

Run No.	Bulk Fluid Temperature, °F	Wear Scar Diameter, mm.	- - - Iron Recovered from Wear Debris in μg as - - -				Total Iron, μg
			Oil Solu.	Pyridine Solu.	Iron	Iron Oxides	
K1A	167	0.60	12	13	38	241	241
K1B	167	0.85	10	32	52	197	197
K25	167	0.62	19	15	54	426	426
K26	167	0.87	16	19	60	266	266
BK	Average	0.74	14	20	51	198	283

Table 61

WEAR PRODUCT ANALYSIS AS A FUNCTION OF TIME

Test Fluid: MLO 7789A
Test Machine: GE/Brown Modified Four-ball Wear Tester
Test Conditions: Load = 40 kg., Speed = 600 r.p.m., Bulk Fluid Temp. = 167°F.,
Atmosphere = dry air @ 0.25 ℓ/min

Run No.	Time, Minutes	Wear Scar Diameter, mm.	- - - Iron Recovered from Wear Debris in μg as - - -				Total Iron, μg
			Oil Solu.	Pyridine Solu.	Iron	Iron Oxides	
76	10	0.44	BDC**	9	17	13	39
74	20	0.53	BDC	11	16	30	57
75	40	0.66	BDC	13	58	53	124
72	60	0.74	BDC	11	28	79	118
73	70	0.79	BDC	23	80	113	216
BA*	100	0.90	BDC	14	89	191	294

* Average of 4 runs, for detail see Table 58

** BDC = Below Detectable Concentration

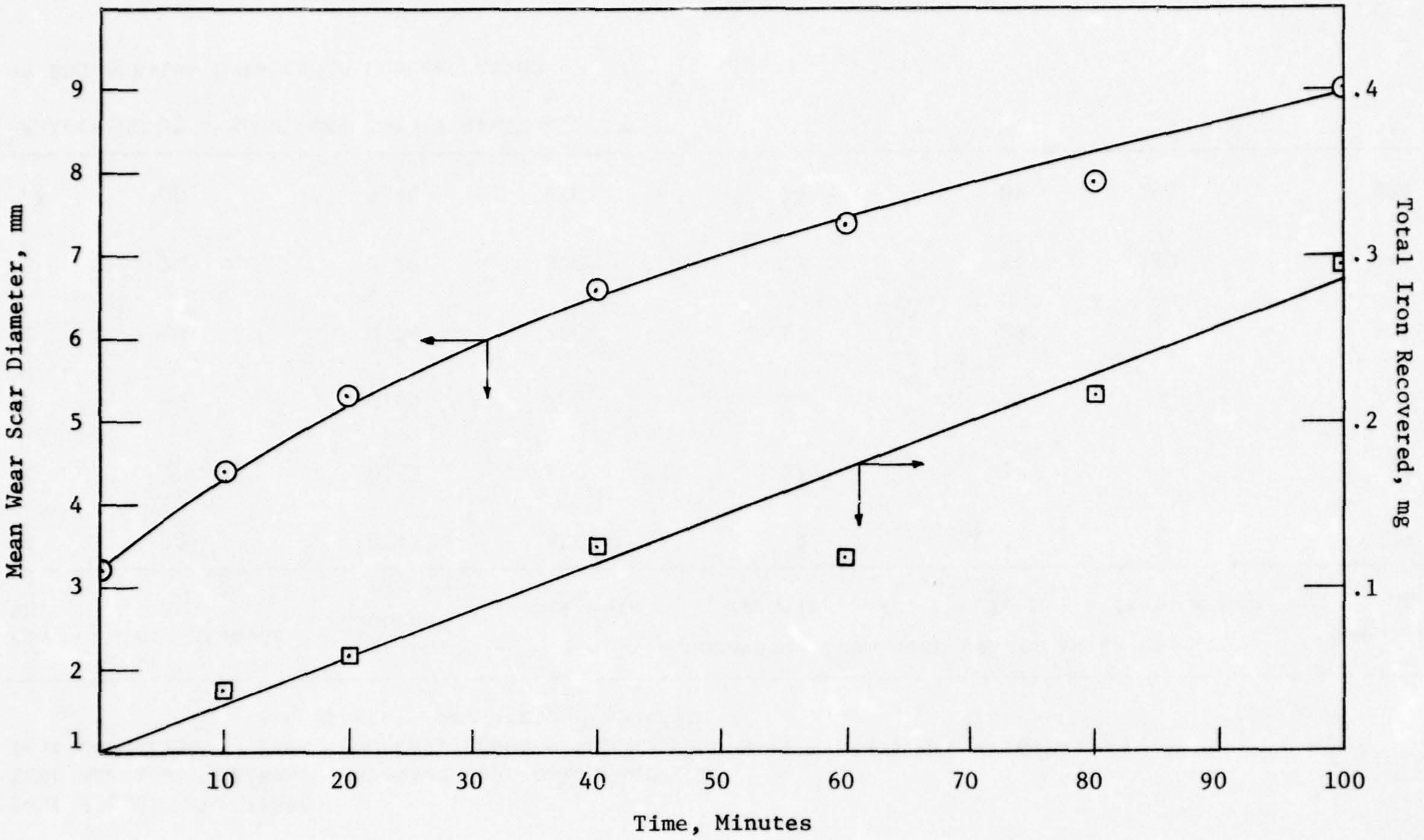

Figure 42. MEAN WEAR SCAR DIAMETER AS A FUNCTION OF TIME.

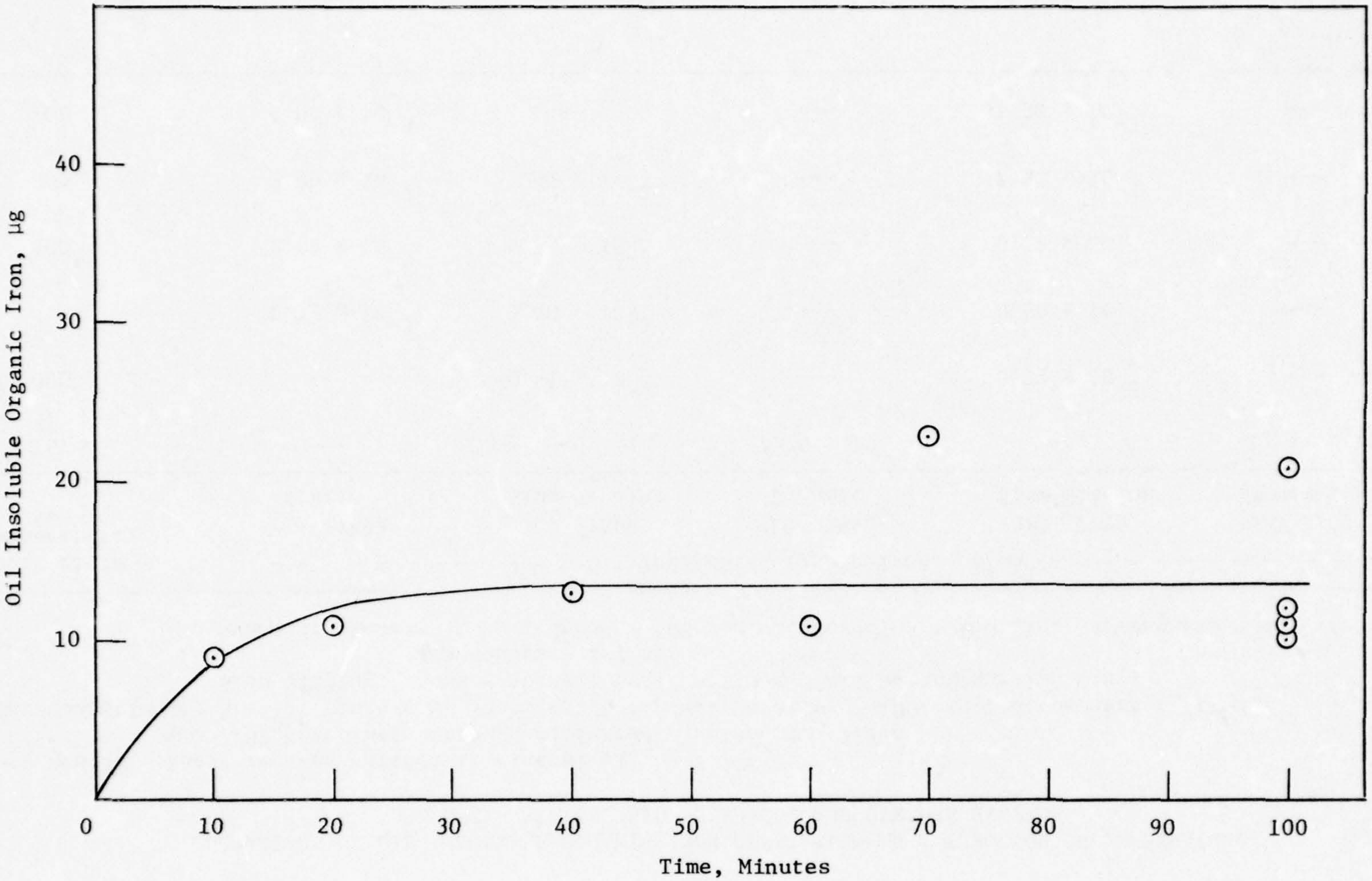

Figure 43. OIL INSOLUBLE ORGANIC IRON CONCENTRATION AS A FUNCTION OF TIME.

Table 62

COMPARISON OF OIL INSOLUBLE ORGANIC-IRON GENERATION AS A FUNCTION OF TEMPERATURE AMONG THE STATIC, SLOW-SLIDING, AND DYNAMIC SYSTEMS

Test Fluids: Super-refined paraffinic mineral oil, MLO 7789
MLO 7789 percolated through Activated Alumina, MLO 7789A

Test Conditions: Static: Load = 0, Speed = 2.9 r.p.m., Duration = 100 min., Atmosphere = dry air
Slow Sliding: Load = 40 kg., Speed = 2.9 r.p.m., Duration = 100 min., Atmosphere = dry air
Dynamic: Load = 40 kg., Speed = 600 r.p.m., Duration = 100 min., Atmosphere = dry air

Bulk Fluid Temperature, °F	Oil Insoluble Organic-Iron, µg/mm^2				
	MLO 7789A Static	MLO 7789A Slow-Sliding	MLO 7789A Dynamic	MLO 7789 Slow-Sliding	MLO 7789 Dynamic
167	---	---	7.76×10^{-3}	---	12.34×10^{-3}
300	---	0.41×10^{-3}	---	0.29×10^{-3}	---
400	0.73×10^{-3}	0.40×10^{-3}	---	0.50×10^{-3}	---
500	2.09×10^{-3}	0.70×10^{-3}	---	0.71×10^{-3}	---
600	2.09×10^{-3}	1.91×10^{-3}	---	7.30×10^{-3}	---
700	6.06×10^{-3}	---	---	31.30×10^{-3}	---

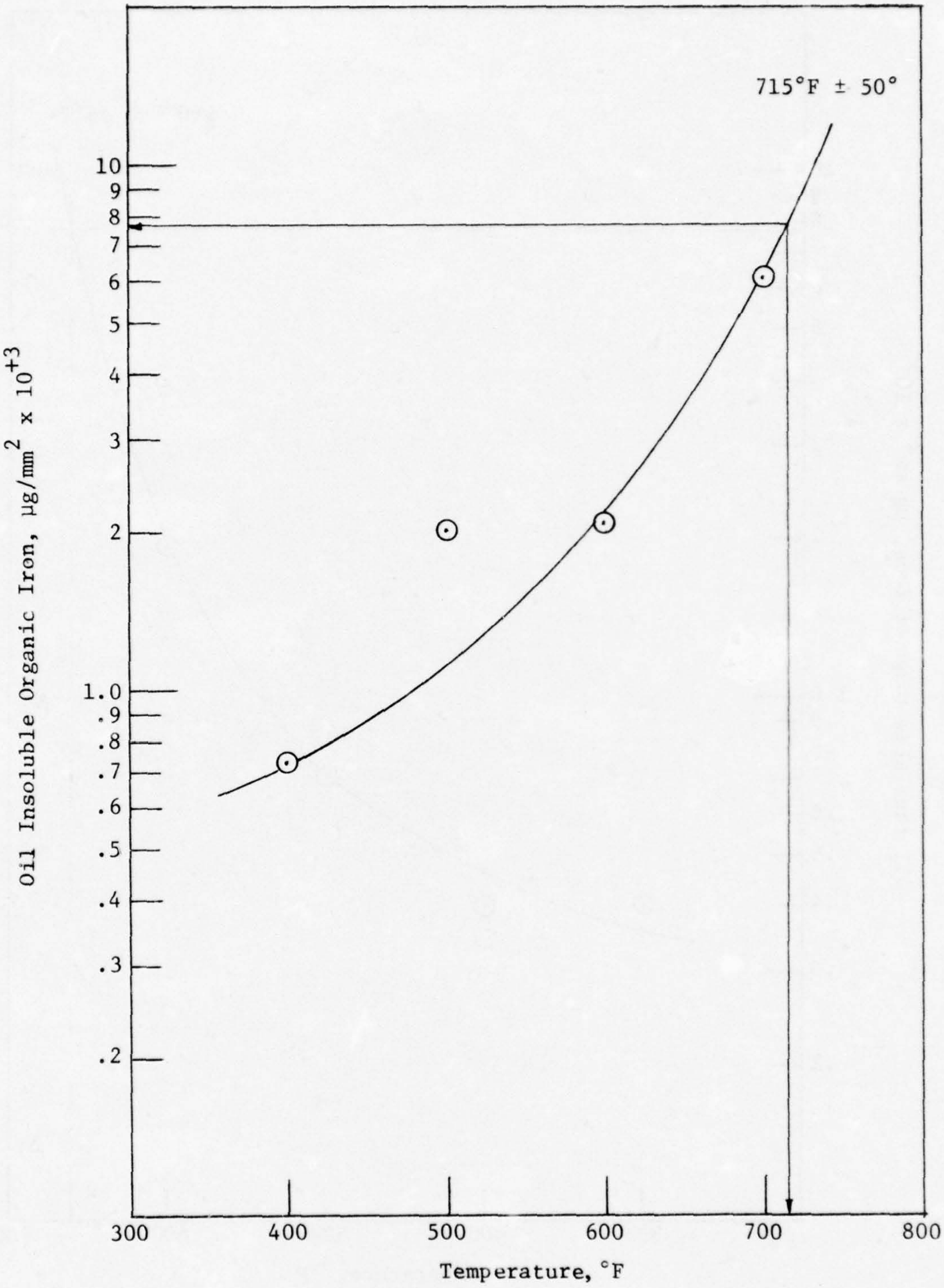

Figure 44. OIL INSOLUBLE ORGANIC IRON AS A FUNCTION OF TEMPERATURE IN THE STATIC TESTS (MLO 7789A).

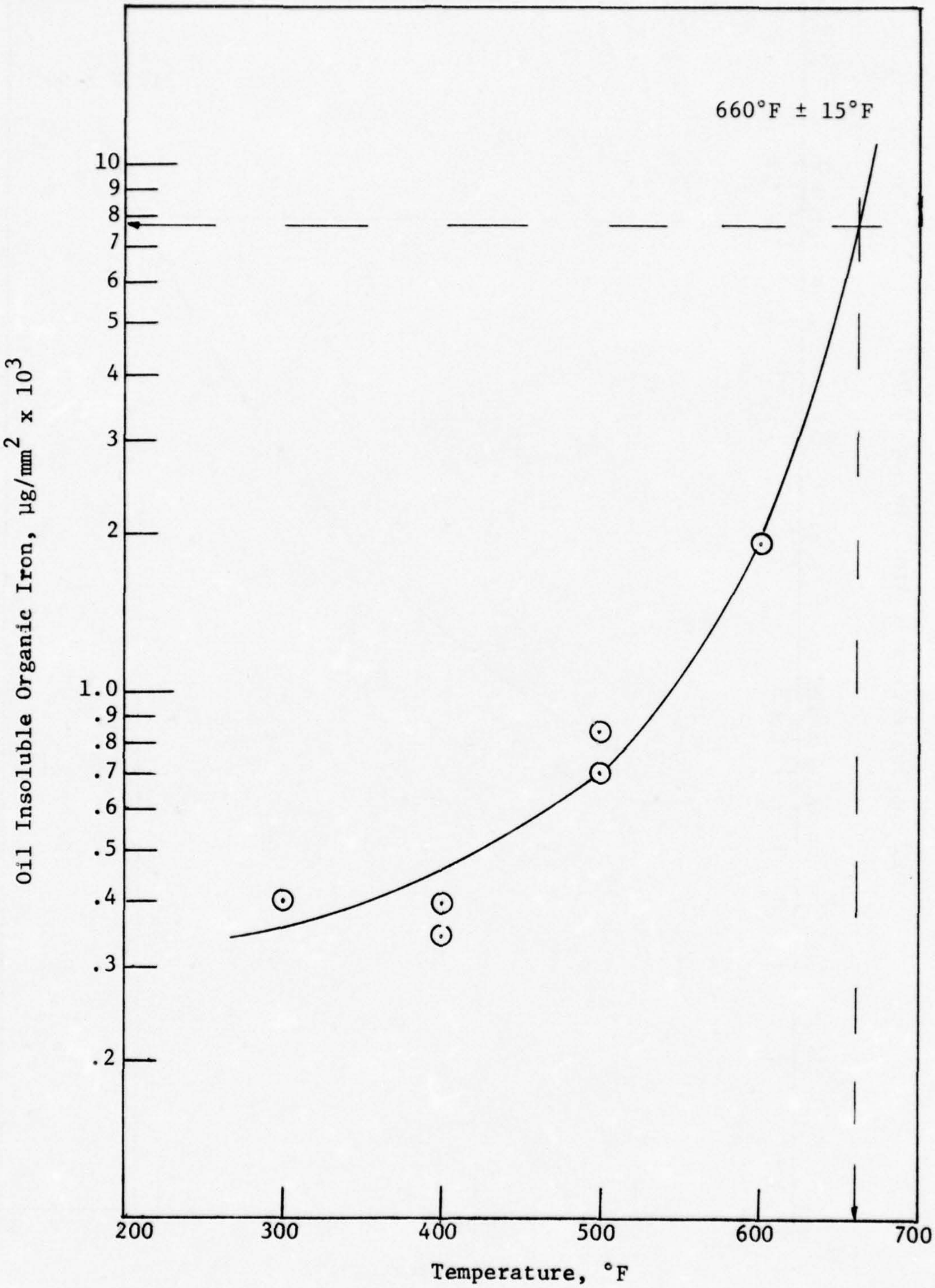

Figure 45. OIL INSOLUBLE ORGANIC IRON AS A FUNCTION OF TEMPERATURE IN THE SLOW-SLIDING TESTS (MLO 7789A).

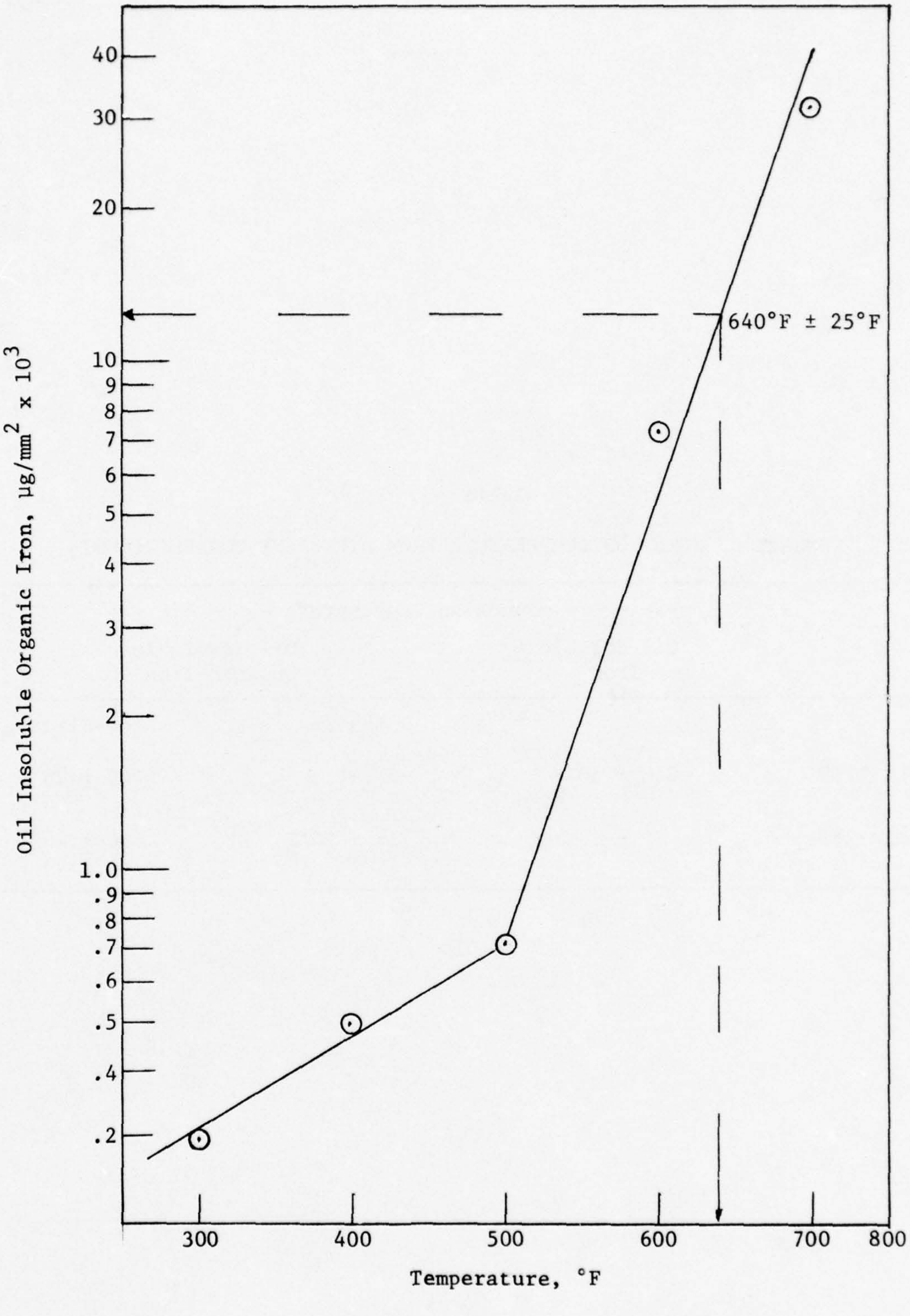

Figure 46. OIL INSOLUBLE ORGANIC IRON AS A FUNCTION OF TEMPERATURE IN SLOW-SLIDING TESTS (MLO 7789).

Table 63

SUMMARY OF JUNCTION TEMPERATURE FROM DIFFERENT CORRELATIONS

	Junction Temperature		
	Oil Soluble Iron	Oil Insoluble Organic-Iron	
		Static	Slow-Sliding
MLO 7789	640 ± 50°F	--	640 ± 25°F
MLO 7789A	--	715 ± 50°F	660 ± 15°F

Table 64

ANALYSIS OF WEAR PRODUCTS IN CONSECUTIVE 100 MINUTES RUN

Test Fluid: MLO 7789A
Test Machine: GE/Brown Modified Four-ball Wear Tester
Test Conditions: Load = 40 kg., Speed = 600 r.p.m., Duration = 100 min.
Temperature = 167°F, Atmosphere = dry air @ 0.25 ℓ/min.

Run No.		Wear Scar Diameter, mm.	- - Iron Recovered from Wear Debris in µg as - - -				Organometallic Iron, %
			Oil Solu.	Pyridine Solu.	Iron	Iron Oxides	
BA	Average of 4 runs 1st 100 min. run	0.90	BDC*	13.5	89	191	5
	Range		BDC-1	10-21	48-108	139-231	3.7-8.5
115	2nd 100 min. run	0.995	BDC	17	88	60	10

* BDC = Below Detectable Concentration

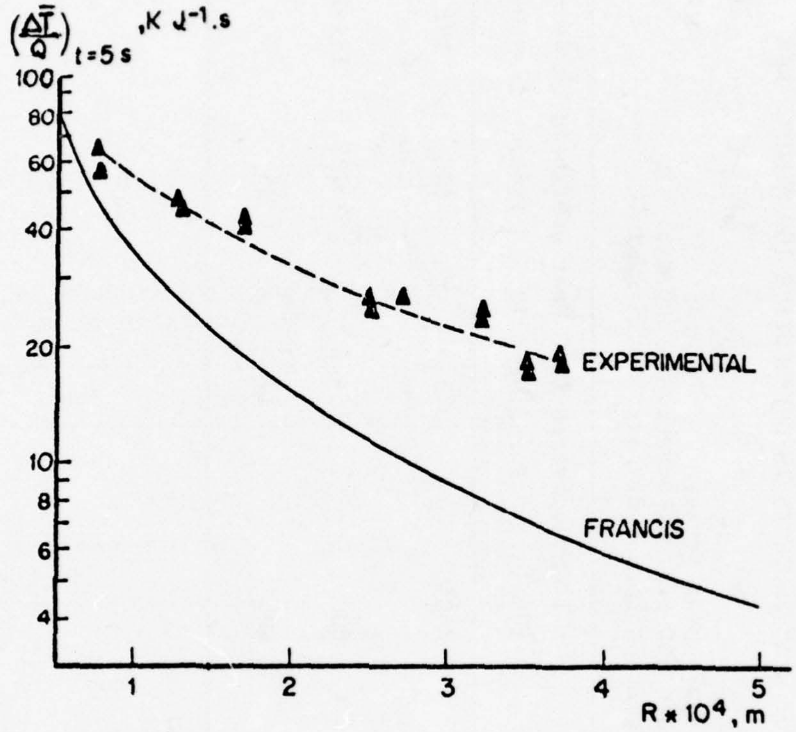

Figure 47. COMPARISON BETWEEN BOS' EXPERIMENTAL AND FRANCIS' THEORETICAL JUNCTION TEMPERATURES IN A FOUR-BALL APPARATUS.

Table 65

COMPARISON OF FLASH TEMPERATURE CALCULATIONS FROM VARIOUS THEORETICAL MODELS AND EXPERIMENTAL DATA

	Blok-Archard	Fein	Francis	Bos	This Work
θ_m, °F	270	--	364	422*	640
θ_{max}, °F	353	415	442	642*	

* Adjusted according to BOS' experimental data

Table 66

EFFECT OF SURFACE ACTIVITY ON CHEMICAL REACTIONS

Test Fluid: MLO 7789A
Test Machine: GE/Brown Modified Four-ball Wear Tester
Test Conditions: Temperature = 700°F., Speed = 2.9 r.p.m., Atmosphere = Air @ 0.25 ℓ/min

Run No.		Wear Scar Diameter, mm.	- - - -Iron Recovered from Wear Debris in μg as - - - -				Surface Area, mm^2
			Oil Solu.	Pyridine Solu.	Iron	Iron Oxides	
K34	Slow-sliding, Load = 40 kg	2.40	394	84	25,000	7,100	169,089
108	Static, no load	--	244	58	--	--	9,569

D. Conclusions. An analysis of the viscosity-pressure measurement in the PRL high pressure viscometer shows that gas solubility in the fluid, as a result of diffusion at the gas-liquid interface, represents the principal experimental problem. Studies show that diffusion rate of the gas into the liquid varies over a significant range and appears to be related to the fluid class. Significant errors can be shown after only one hour soak time at pressures as low as 3000 psig. The gas solubility results in too low a measured viscosity at a given pressure. Polyolefins which show a significant diffusion rate are among the hydrocarbons that show a poor predicted pressure-viscosity value. In order to reduce the error due to gas solubility, the limiting slope of the viscosity-pressure curve at 0 psig should be used to predict the viscosities at high pressures.

Two empirical correlations were developed from the 100°F viscosity-pressure data from the PRL pressure viscometer and the Penn State API Project 42. The final form of the equations was obtained by regression analysis.

For fluids with average of about 4.5 formula weights per atom, Equation [4] or Figures 16 through 18 adequately describe the pressure coefficient of mineral oils, pure hydrocarbons, nonhydrocarbons and blends of mineral oils, polymer, and resin at temperatures ranging from 32° to 275°F.

$$\begin{aligned}\alpha = {} & 0.8382 + 2.8563\,V^{3.0627} \\ & + 0.8338\,\mathrm{ASTM}^{5.1903}\,V^{1.5976} \\ & - 2.7574\,V^{3.0975}\,D^{0.1162}\end{aligned} \qquad [4\ ]$$

where:

α = pressure coefficient, $\mathrm{psig}^{-1} \times 10^{-4}$,

V = kinematic atmospheric viscosity at temperature of interest, cs,

ASTM = ASTM slope, and

D = atmospheric density at temperature of interest, gm./cc.

When atmospheric density is not available, Equation [4] or Figure 22 can be used for a close approximation. For fluids with average formula weights far from 4.5 per atom, Equation [4] is a better equation to use for approximating the pressure coefficient.

$$\begin{aligned}\alpha = {} & 0.7236 + 0.2919\,V^{1.0459} \\ & + 0.5860\,\mathrm{ASTM}^{3.5371}\,V^{1.6701}\end{aligned} \qquad [\ \ ]$$

where:

α = pressure coefficient, $\mathrm{psig}^{-1} \times 10^{-4}$, V = kinematic atmospheric viscosity at temperature of interest, cs, and

ASTM = ASTM slope.

The parameters used for these correlations appear to be related to such physical characteristics as molecular interlocking, molecular packing, molecular rigidity, and size of the flow unit. The behavior of the correlations was shown to be in agreement with the void volume theory.

A new experimental technique has been developed to study the chemical reactions in boundary lubrication. The method combines the use of the four-ball wear tester and atomic absorption spectroscopy with successive solvent extractions. It offers new insight into the mechanism of lubrication in the boundary regime.

The junction temperature rise has been determined using a chemical conversion correlation between static and dynamic runs. It is substantially higher than the generally used Blok-Archard flash temperatures.

The catalytic aspect of metal surfaces in chemical reactions under boundary lubrication, at least in paraffinic mineral oils, appears to be insignificant.

Chemical reactions do indeed play a very important role in boundary lubrication.

Oxygen has been demonstrated to have a large effect on the nature of chemical reaction products.

APPENDIX I

SURFACE AREA CALCULATIONS

Appendix I of Annual Report
AFML-TR-74-201, Part II, Prepared by
Petroleum Refining Laboratory Division,
Chemical Engineering Department
The Pennsylvania State University

Surface Area Calculation of the Ball-Pot Assembly

1. Balls: Surface area/ball = πd^2

   = $\pi(1/2)^{1/2}$ = 0.785 in^2

   $\therefore$ Total exposed surface area = (0.785)(3.5)

   = 2.75 in^2

2. Bottom piece: d = 0.85", h = 0.18" circular

   Top surface = $\pi d^2/4$ = 0.567 in^2

   Lateral sides = $2(\pi dh)$ = 0.961 in^2

3. Lock ring: di = 0.9", do = 1.73", h = 0.3" donut shape

   Lateral sides = $2\pi dh$ = 3.26 in^2

   Surface area = $2\pi(di/2 + do/2)(do/2 - di/2)$

   = 3.428 in^2

4. Ball-Pot:

   Top half = 0.68"/2 = 0.34" = h

   Surface area = πdh = π(1.5")(0.34")

   = 1.6 in^2

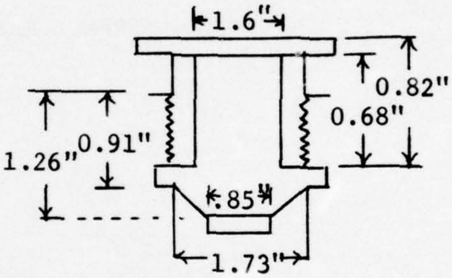

Incline surface:

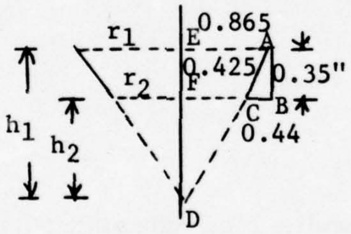

Surface area of a right cone = $\pi r\sqrt{r^2+h^2}$

$\therefore$ Net surface area of incline = $\pi r(\sqrt{r_1^2+h_1^2} - \sqrt{r_2^2+h_2^2})$

From trigonometry, in triangle ABC

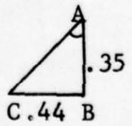

Angle A = tan A = 0.44/0.35

< A = 51.5°

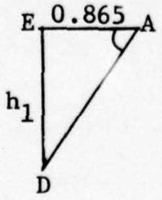

$\therefore$ in ΔADE

< A = 90°-51.5° = 38.5°

h_1 = 0.865 tan A = 0.688 in.

$\therefore$ in ΔCFD

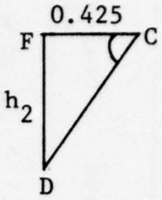

$< C = < A = 38.5°$

$h_2 = 0.425 \tan C = 0.338$ in.

$$\therefore \text{ Surface area } = \pi\left(r_1\sqrt{r_1^{\,2}+h_1^{\,2}} - r_2\sqrt{r_2^{\,2}+h_2^{\,2}}\right)$$

$$= \pi(0.865\sqrt{(0.865)^2 + (0.688)^2}$$

$$- 0.425\sqrt{(0.425^2 + (0.338)^2}$$

$$= 2.278 \text{ in}^2$$

$$\therefore \text{ Total surface area } = 2.75 + 0.567 + 0.961 + 3.26 + 3.428$$

$$+ 1.6 + 2.278$$

$$= 14.844 \text{ in}^2$$

$$= 9576.75 \text{ mm}^2$$

Surface Area Calculation of the Wear Particles

A method for the measurement of the particle diameters of the wear debris is discussed in AFML-TR-74-201, Part I. From this information, a particle size distribution can be calculated and assuming all particles are spheres, a surface area distribution can be estimated. From density data, by assuming the smallest particles are iron oxides and the layer particles iron, the total weight of the distribution can be calculated. The end result is surface area per unit weight ratio. This constant equals 4565.52 mm^2/mg for this particular particle distribution. The calculations are shown in Table 67.

Table 67

CALCULATION OF THE SURFACE AREA TO WEIGHT RATIO

Number of Particles	Particle Diameter mm	Surface Area/ Particle mm^2	Total Surface Area mm^2	Volume/Sphere mm^3	Weight/Sphere mg	Total Weight mg
105	0.003	2.827×10^{-5}	2.968×10^{-3}	1.22×10^{-14}	6.25×10^{-14}	6.56×10^{-12}
174	0.007	1.539×10^{-4}	2.678×10^{-2}	1.91×10^{-12}	9.77×10^{-12}	1.70×10^{-9}
78	0.012	4.524×10^{-4}	3.528×10^{-2}	4.85×10^{-11}	3.78×10^{-10}	2.96×10^{-8}
72	0.015	7.068×10^{-4}	5.089×10^{-2}	1.85×10^{-10}	1.45×10^{-9}	1.04×10^{-7}
18	0.019	1.134×10^{-3}	2.041×10^{-2}	7.64×10^{-10}	5.97×10^{-9}	1.07×10^{-7}
24	0.023	1.662×10^{-3}	3.988×10^{-2}	2.40×10^{-9}	1.88×10^{-8}	4.51×10^{-7}
12	0.027	2.290×10^{-3}	2.748×10^{-2}	6.29×10^{-9}	4.92×10^{-8}	6.39×10^{-7}
13	0.030	2.827×10^{-3}	3.675×10^{-2}	1.18×10^{-8}	9.25×10^{-8}	1.20×10^{-6}
5	0.034	3.632×10^{-3}	1.815×10^{-2}	2.51×10^{-8}	1.96×10^{-7}	9.81×10^{-7}
7	0.038	4.536×10^{-3}	3.175×10^{-2}	4.89×10^{-8}	3.82×10^{-7}	2.68×10^{-6}
3	0.042	5.542×10^{-3}	1.662×10^{-2}	8.91×10^{-8}	6.97×10^{-7}	2.09×10^{-6}
4	0.046	6.648×10^{-3}	2.659×10^{-2}	1.54×10^{-7}	1.20×10^{-6}	4.81×10^{-6}
2	0.049	7.543×10^{-3}	1.508×10^{-2}	2.25×10^{-7}	1.76×10^{-6}	3.51×10^{-6}
2	0.068	1.453×10^{-2}	2.905×10^{-2}	1.61×10^{-6}	1.26×10^{-5}	2.51×10^{-5}
2	0.076	1.815×10^{-2}	3.629×10^{-2}	3.13×10^{-6}	2.45×10^{-5}	4.89×10^{-5}
TOTAL			4.140×10^{-1}			9.069×10^{-5}

Sample Calculation

Run 38 (MLO 7789 slow-sliding at 600°F)

Data: Oil soluble iron = 128 µg
Pyridine soluble iron = 80 µg
Iron = 94 µg
Iron as iron oxides = 149 µg

Assuming the amount of iron oxides are a 50:50 mixture of Fe_2O_3 and Fe_3O_4

Atomic weight of Fe = 55.85
Atomic weight of O = 16

$\therefore$ Molecular weight of Fe_2O_3 = 159.7
Molecular weight of Fe_3O_4 = 231.55

$\therefore$ Amount of iron in Fe_2O_3 = 111.7/159.7
Amount of iron in Fe_3O_4 = 167.55/231.55

$\therefore$ To get the total weight of iron oxides from the weight of measured iron, one needs to multiply by the reciprocal of the percentage

For Fe_2O_3, it is 159.7/11.7 = 1.42
Fe_3O_4, it is 231.5/167.5 = 1.38
$\therefore$ For 50:50 mixture, the multiplier = 1.40

Amount of iron oxides = 149 x 1.4 = 208.6 µg
Amount of iron particles = 94.0 µg
Total iron = 302.6 µg

From the previous section, the surface area of the particles can be estimated from the measured particle size distribution. From Table 67

Surface area/mg = 4565.52

$\therefore$ Surface area of the iron particles = (317.5 µg)(4565.52)(10^{-3})
= 1381.5 mm^2

Surface area of the ball-pot assembly = 9569.7 mm^2

$\therefore$ Total surface area = 1381.5 + 9569.7 = 10951.2 mm^2

$\therefore$ Oil soluble iron = 128 µg/10951.2 = 11.688 x 10^{-3} µg/mm^2
Oil insoluble iron = 80 µg/10951.2 = 7.306 x 10^{-3} µg/mm^2

APPENDIX II

FLASH TEMPERATURE CALCULATIONS

Appendix II of Annual Report
AFML-TR-74-201, Part II, Prepared by
Petroleum Refining Laboratory Division
Chemical Engineering Department
The Pennsylvania State University

Calculation of Flash Temperatures

Data: Runs 42-45
Load = 40 kg.
Speed = 600 r.p.m. = 22.7 cm/sec.
Temperature, bulk fluid = 167°F
Strain gauge force = 215 gm

Coefficient of Friction Determination

From geometric considerations, the force normal to the wear scar F_N of a stationary ball is given by:

$$F_N = 0.408\ W \qquad (102)$$
$$= (0.408)(40\text{kg}) = 16320\ \text{gm}.$$

The coefficient of friction, f can be calculated by

$$f = 2.23\ F\ell/W \qquad (103)$$

where F = force measured by strain gauge, gm.
ℓ = lever arm distance from the center of rotation, cm.
W = machine loading, gm.

$$f = (2.23)(215)(10.48)/(40{,}000) = 0.117$$

Blok-Archard Theory

$$N = \frac{fg}{J}\frac{\pi P_m}{\rho C} \qquad (104)$$

where

f = coefficient of friction = 0.117 (from Run 42)
g = acceleration due to gravity = 980 cm/sec^2
J = mechanical equivalent of heat = 4.18×10^7 ergs/cal
P_m = flow pressure = $7.04 \times 10^6\ \text{gm/cm}^2$
ρ = density = 7.78 gm/cm^3
C = specific heat = 0.109 cal/gm°C

$$\text{erg}[=]\ \frac{\text{gm-cm}^2}{\text{sec}^2}$$

dimensionally

$$N[=]\ \frac{(\text{cm/sec}^2)(\text{gm/cm}^2)}{(\text{gm-cm}^2)/\text{sec}^2\ \text{-cal})(\text{gm/cm}^3)(\text{cal/gm-°C}}\ [=]\ °\text{C}$$

numerically

$$N = \frac{(0.117)(980)(3.1416)(7.04 \times 10^6)}{(4.18 \times 10^7)(7.78)(0.109)} = 71.54°C$$

$$L = \frac{P_N^{1/2} V}{2\alpha\ (\pi P_m)^{1/2}} \tag{105}$$

where

P_N = normal load = 16320 gm.

V = sliding velocity = 22.7 cm/sec.

α = thermal diffusitivity = 0.12 cm^2/sec.

P_m = flow pressure of steel = 7.04 x 10^6 gm/cm^2

dimensionally: $$L[=] \frac{(gm^{1/2})(cm/sec)}{(cm^2/sec)(gm^{1/2}/cm)} [=] \text{ dimensionless}$$

numerically: $$L = \frac{(16320)(22.7}{(2)(0.12)[(3.1416)(7.04 \times 10^6)]^{1/2}} = 2.57$$

Since $0.1 < L < 5$ $\therefore$ Equation (41) applies:

$$\Theta_m = 0.25\ \delta\ NL \tag{106}$$

δ is estimated from Archard's paper (26) to be about 0.75.

$$\Theta_m = (0.25)(0.75)(71.54)(2.57) = 34.5°C$$
$$= 94.1°F$$

$\therefore$ the average temperature = 167° + 94.1° = 261°F

Alternately

$$\Theta_B = \frac{Q}{4rk_B} \tag{107}$$

where

$$Q = \frac{fWgV}{J} = \frac{(0.117)(16200)(980)(22.7)}{4.18 \times 10^7} = 1.0087 \text{ cal/sec.}$$

$$r = \left(\frac{W}{\pi\ P_m}\right)^{1/2} = \left[\frac{16200}{(3.1416)(7.04 \times 10^6}\right]^{1/2} = 2.7 \times 10^{-2} \text{ cm}$$

$$\Theta_B = \frac{1.0087}{4(2.7 \times 10^{-2})(0.0546)} = 171°C = 340°F$$

Θ_c is given by Fig. 2 in Archard's paper [Ref. 70].

$$L_c = 2.57 \qquad \text{from previous calculation}$$

$$\frac{\Theta_c}{N} = 0.85$$

$$\therefore \Theta_c = 0.85\ N = 0.85\ (71.54) = 60.81°\text{C}$$

$$\therefore \frac{1}{\Theta_m} = \frac{1}{\Theta_B} + \frac{1}{\Theta_c} = \frac{1}{171} + \frac{1}{60.81} = 0.022$$

$$\Theta_m = 44.86°\text{C} = 112.7°\text{C}$$

$$\therefore \Theta_m = 167 + 112.7 = 279.7°\text{F}$$

Blok's formula used by R. S. Fein:

A spot of radius r rubbing against an extensive surface with uneven heat distribution between surfaces.

$$\Theta_{max} \approx \frac{2fP_1}{\rho c} \cdot \frac{(1 + \frac{1}{\sqrt{2}} \cdot \phi}{1 + \pi/2 \cdot \phi} + \Theta_o \tag{108}$$

where: f = coefficient of friction = 0.117
P_1 = junction pressure, $\text{kg/cm}^2 = 6.85 \times 10^3\ W^{1/3}$
$= 2.343 \times 10^4\ \text{kg/cm}^2$
W = machine load, kg = 40 kg.
k = thermal conductivity = 0.108 cal/cm-°C-sec
= 4.609 kg-cm/cm=°C-sec
c = specific heat = 0.109 cal/gm-°C
$= 4.652 \times 10^3$ kg-cm/kg-°C
ρ = density of steel = $7.78 \times 10^{-3}\ \text{kg/cm}^3$
ϕ = thermal diffusitivity = $0.127\ \text{cm}^2/\text{sec}$
Θ_o = ambient temperature = 167°F

substituting these values into (B-7)

$$\Theta_{max} \approx \frac{2(0.117)(2.343 \times 10^4)(1.707)(0.67)}{(7.78 \times 10^3)(4.652 \times 10^3)(1 + 1.0259)} + \Theta_o$$

$$\Theta_{max} - \Theta_o \approx 85.5°\text{C} = 186°\text{F}$$

$$\therefore \Theta_{max} = 167 + 186 = 353°\text{F}$$

or as in Fein's work, Θ_{max} is adjusted by 1.33

$$\therefore \Theta_{max} - \Theta_o \approx 186° \times 1.33 = 248°\text{F}$$
$$\Theta_{max} = 248 + 167° = 415°\text{F}$$

Francis' Equation:

For the stationary surface,

$$\Delta\Theta_s = \frac{9\pi}{32}\frac{Q}{\pi rk} \qquad (109)$$

where

Q = rate of heat supply = 1.0087 cal/sec
π = 3.1416
r = wear scar radius = 0.015 cm
k = 0.108 cal/cm-°C-sec

$\therefore \Delta\Theta_s = 175°C$

For the moving surface

$$\Delta\Theta_v = 1.016\frac{Q}{\pi rkB^{1.2}}\left[1 + \frac{1.047}{B} + \frac{0.774}{B^{3/2}}\right] \qquad (110)$$

where

$B = Vr/\alpha = (22.7)(0.15)/(0.127) = 2.68$

$\Delta\Theta_v = 192.8°C$

Therefore the mean surface temperature Θ_m is given by

$$\Delta\Theta_m = 1/\left(\frac{1}{\Theta_s} + \frac{1}{\Theta_v}\right) \qquad (111)$$

$$\Delta\Theta_m = 91.7°C = 197°F$$

$$\therefore \Theta_m = 167° + 197° = 364°F$$

The maximum temperature is given by

$$\Delta\Theta_{max} = \frac{(1.852)\left(\frac{Q}{\pi rk}\right)}{1.996-1.091B^{-0.818}-0.537B^{-0.271}+B^{1/2}} \qquad (112)$$

Equation (B-11) is suitable to use when $B \geq 10$. In this work, $B = 2.68$, so Equation (B-11), straightly speaking, is not suitable. However the error introduced this way is small compared with other assumptions.

$$\Delta\Theta_{max} = 137°C = 275°F$$

$$\therefore \Theta_{max} = 275 + 167 = 442°F$$

Bos' Equation:

$$\Delta\Theta_m = \frac{Q}{kr} \frac{0.281}{(B+4)^{1/2}} \qquad (113))$$

where

Q = rate of heat supply = 4.22 Joules/sec
k = thermal conductivity = 45.2 Joules/m^2-sec-°K
B = dimensionless parameter = 2.68
r = radius of wear scar = 1.5×10^{-4} m

$$\Delta\Theta_m = 68°K = 154°F$$

$$\therefore \Theta_m = 167 + 154 = 321°F$$

This result differs from that calculated from Francis' Equations (109), (110), and (111). Francis Equations are really limiting case studies and apply at $B \geq 10$. Bos' Equation (113) is obtained by regression analysis from complete numerical solutions. The two answers are close enough to justify both sets of equations.

From Figure 47 (Fig. 7 in Bos' work), the theoretical and experimental temperatures for r = 0.015 cm are estimated.

Experimental: EN 31 Steel

k = 26.6 J/m^2-sec-°K
ρ = 7.81×10^3 kg/m^3
c = 460 J/kg-°K
Q = 4.22 J/sec

$$\frac{\Delta\Theta}{Q} \cong 42$$

Theoretical: $\frac{\Delta\Theta}{Q} \cong 23$

$$\Delta\Theta \cong (23)(4.22) = 97°K$$

$$\frac{\Delta\Theta \text{ experimental}}{\Delta\Theta \text{ theoretical}} = \frac{177}{97} = 1.824$$

Therefore the temperatures calculated from previous equations are similarly adjusted to determine the kind of flash temperatures that would be obtained relying on Bos' findings.

$\Delta\Theta_m$ = 68°C (1.824) = 124°C = 255°F

Θ_m = 167 + 255 = 422°F

$\Delta\Theta_{max}$ = 475 + 167 = 642°F

E. REFERENCES

1. Cohen, M. H. and Turnbull, D., "Molecular Transport in Liquids and Glasses," J. of Chemical Physics, 31, p. 1164-9, (1959).

2. Bell, J. C. and Kannel, J. W., "Interpretations of the Thickness of Lubricant Films in Rolling Contact II - Influence of Possible Rheological Factors," Journal of Lubrication Technology, Trans. of ASME, 93 (4), p. 485-97, October (1971).

3. Cheng, H. S., "Isothermal Elastohydrodynamic Theory for the Full Range of Pressure-Viscosity Coefficient," Journal of Lubrication Technology, Trans. of ASME Series F, 94(1), p. 35-43, January (1972).

4. Westlake, F. J. and Cameron, A., "Optical Elastohydrodynamic Fluid Testing," ASLE Trans., 15(2), p. 81-95, (1972).

5. Bridgman, P. W., "The Effect of Pressure on the Viscosity of Forty-Three Pure Liquids," Proceedings of the American Academy of Arts and Science, Vol. 61, p. 57, (1926).

6. Kuss, E., "The Viscosity of 50 Lubricating Oils Under Pressure Up to 2000 Atmospheres," Report No. 17 on Sponsored Research (Germany), Department of Scientific and Industrial Research, London (1951).

7. ASME Pressure-Viscosity Report, ASME, New York (1953).

8. Dixon, J. A., Webb, W., and Steele, W. A., "Properties of Hydrocarbons of High Molecular Weight," Research Project 42, Report to Am. Petrol. Inst., The Pennsylvania State University, Sept. (1962).

9. Roth, W., and Rich, S. R., "A New Method for Continuous Viscosity Measurement. General Theory of the Ultra-Viscoson," J. App. Phys., 24, p. 940 (1953).

10. Novak, J. D. and Winer, W. O., "The Effect of Pressure on the Non-Newtonian Behavior of Polymer Blended Petroleum Oil," J. of Lub. Tech., 91(3), p. 459-463, (July 1969).

11. Appeldoorn, J. K., Okrent, E. H., and Philippoff, W., "Viscosity and Elasticity at High Pressure and High Shear Rate," Proceedings of Am. Pet. Inst., 42(III), (1962).

12. Mason, W. P., "Dispersion and Absorption of Sound in High Polymers," Encyclopedia of Physics, Springer, Berlin (1961).

13. Foord, C. A., Hamman, W. C., and Cameron, A., "Evaluation of Lubricants Using Optical Elastohydrodynamics," ASLE Trans., 11(1), p. 31-43, (1968).

14. Westlake, F. J. and Cameron, A., "Optical Elastohydrodynamic Fluid Testing," ASLE Trans., 15(2), p. 81-95, (1972).

15. Dow, R. B., "The Viscosity of Mixtures of Liquids at High Pressures," Physics, 6, p. 71-9, February (1935).

16. Griest, E. M., Webb, W., and Schiessler, R. W., "Effect of Pressure on Viscosity of High Molecular Weight Hydrocarbons and Their Mixtures," The J. of Chemical Physics, 29(4), p. 711, October (1958).

17. Worster, R. C., Discussion to Paper by Bingham, A. E., "Some Problems of Fluids for Hydraulic Power Transmission," Proceedings of the Institute of Mechanical Engineering, 165, p. 269, (1951).

18. Hartung, H. A., "Prediction of the Viscosity of Liquid Lubricants Under Pressure," Mech. Engr. 77, p. 1006, (1955).

19. Clark, O. H., "Prediction of Lubricating-Oil Viscosities at High Pressures," Trans. of the ASME, 78, p. 905-8, July (1956).

20. Lockhart, F. J. and Lonior, J. M., "Liquid Viscosities at High Pressure," Petroleum Refiner, 40(3), p. 209-10, March (1961).

21. Chu, P. S. Y. and Cameron, A., "Pressure Viscosity Characteristic of Lubricating Oils," J. of the Inst. of Petrol. 48 (461), p. 147-55, May (1962).

22. Dixon, J. A. and Webb, W., "Viscosity-Pressure Relationships for High-Molecular-Weight Fluids," Proc. of the Am. Petrol. Inst., Section III, 42, p. 146-51, (1962).

23. Roelands, C. J. A., Vlugter, J. C., and Waterman, H. I., "The Viscosity-Temperature-Pressure Relationship of Lubricating Oils and Its Correlation with Chemical Constitution," Trans. of the ASME, J. of Basic Engineering, p. 601-10, December (1963).

24. Van Nes, K. and Van Westem, H. A., "Aspects of the Constitution of Mineral Oils," Elsevier Publishing Company, New York (1951).

25. Appeldoorn, J. K., "A Simplified Viscosity-Pressure-Temperature Equation," SAE J., 71, p. 108, (1963).

26. Kouzel, B., "How Pressure Affects Liquid Viscosity," Hydrocarbon Processing and Pet. Refiner, 44(3), p. 120, March (1965).

27. Fresco, G. P., Klaus, E. E., and Tewksbury, "Measurement and Prediction of Viscosity-Pressure Characteristics of Liquids," Trans. of ASME, J. of Lubrication Technology, p. 451-8, July (1969).

28. Roelands, C. J. A., "Correlation Aspects of the Viscosity-Temperature-Pressure Relationship of Lubricating Oils," Druk. V. R. B., Kleine der A3-4 Groningen, (1966).

29. Klaus, E. E., Johnson, R. H., and Fresco, G. P., "Development of a Precision Capillary-Type Pressure Viscometer," Trans. of ASLE, 9, p. 113, (1966).

30. Sage, B. H. and Lasy, W. N., Monograph for Am. Pet. Inst. Research, Project 37, API (1950).

31. Wright, W. A., "Prediction of Bulk Moduli and Pressure-Volume-Temperature Data for Petroleum Oils," ASLE Trans. 10, p. 349-56, (1967).

32. Technical Data Book Petroleum Refining, p. 6A3.8, American Petroleum Institute.

33. Novak, J. D. and Winer, W. O., "Some Measurements of High Pressure Lubrication Rheology," J. of Lub. Tech., 90C30, p. 580-91, (July 1968).

34. Glasstone, S., Laidler, K. J., and Eyring, H., "The Theory of Rate Processes," McGraw-Hill Book Company, Inc., New York, N.Y. (1941).

35. Turnbull, D., "Free Volume Model of the Liquid State," in "Liquids: Structure, Properties, Solid Interactions," edited by T. J. Hughel, Elsavier Publishing Company, Amsterdam/London/New York (1965).

36. MacCoull, N., "Viscosity-Temperature Chart," Lubrication, June, 1921.

37. "Standard Viscosity-Temperature Charts for Liquid Petroleum Products," ASTM Designation: D 341-43.

38. Eby, L. T., "Tables for Determination of ASTM Slope and Prediction of Viscosity," Chemical Division, Standard Oil Development Co., July (1946).

39. Barus, C., "Isothermals, Isopiestics and Isometrics Relative to Viscosity," American Journal of Science, 45, p. 87-96, (1893).

40. Draper, N. R. and Smith, H., "Applied Regression Analysis," John Wiley and Sons, Inc., New York/London/Sydney (1966).

41. Fox, T. G., Gratch, S., and Loshack, S., "Viscosity Relationships for Polymers in Bulk and in Concentrated Solution," in "Rheology; Theory and Applications," edited by F. R. Eirich; Vol. 1, Academic Press, Inc., New York, N.Y., 1956.

42. Klaus, E. E. and Fenske, M. R., "The Use of ASTM Slope for Predicting Viscosities," ASTM Bulletin, p. 87-94, July 1956.

43. Klaus, E. E., Hersh, R. E., and Pohorilla, M. J., "Slope Index - An Expression for Viscosity-Temperature Characteristics," J. of ASLE, p. 439-47, October 1958.

44. Technical Data Book Petroleum Refining, Chapter 11-Viscosity, American Petroleum Institute.

45. Hardy, W. B. and Doubleday, I., "Boundary Lubrication - The Paraffin Series," Proc. Royal Society, A, Vol. 102, pp. 550-74, 1922.

46. Dowson, D., "The Transition to Boundary Lubrication from Elastohydrodynamic Lubrication." Research Report, The University of Leeds, Dept. of Mechanical Engineering, Nov. 1965.

47. Campbell, W. E., "Discussion on 'Boundary Lubrication' by Douglas Godfrey." Interdisciplinary Approach to Friction and Wear, NASA Symposium, San Antonio, Texas, Nov. 1967.

48. Stribeck, R., "Characteristics of Plain and Roller Bearings." Zeit. Ver. Deut. Ing., Vol. 46, pp. 1341-48, 1902.

49. Hersey, M. D., "Laws of Lubrication of Horizontal Journal Bearings." Trans. ASME, Vol. 37, pp. 167-202, 1915.

50. Archard, J. F. and Kirk, M. T., "Lubrication at Point Contacts." Pro. Royal Society, Series A, 261, 532, 1961.

51. Shaw, M. C. and Macks, F., "Analysis and Lubrication of Bearings." McGraw-Hill Book Co., New York, 1949.

52. Moore, D. F., "A History of Research on Surface Texture Effects." Wear, 13, 381-412, 1969.

53. Green, E., "A Review of Surface Texture Measurement and the Associated Metrological Problems." Inst. Mech. Eng., 30, Oxford, England, April 1968.

54. Brown, E. D., Owens, R. S., and Booser, E. R., "Friction of Dry Surfaces." Boundary Lubrication: An Appraisal of World Literature, A.S.M.E., New York, 1969.

55. Furey, M. J., "Surface Roughness Effects on Metallic Contact and Friction." A.S.L.E. Trans., 6, 49-59, 1963.

56. Greenwood, J. A., Res. Report No. 25, Burndy Research Division, U.S.A., 1965.

57. Adamson, A. W., "Physical Chemistry of Surfaces." Second Ed., Interscience Publishers, John Wiley & Sons, New York, pp. 265, 1967.

58. Beilby, G., "Aggregation and Flow of Solids." Macmillan, New York, 1921.

59. Raether, H., Z. Physik, 124, 286, 1948.

60. Dunning, W. J., "Adhesion." Eley D.D. ed., Oxford Univ. Press, 1961.

61. Adamson, A. W., ASTM Special Technical Publication No. 340, p. 32, 1962.

62. Bailey, J. E. and Hirsch, P. B., Phil. Mag. 5, 485, 1960.

63. Herring, C., J. Appl. Phys. 21, 437, 1951.

64. Bowden, E. P. and Tabor, D., "The Friction and Lubrication of Solids." Osford Univ. Press, New York, 1950.

65. Bowden, E. P. and Thomas, P. H., Proc. Roy. Soc., London, A223, 29, 1954.

66. Bowden, E. P. and Tabor, D., "The Friction and Lubrication of Solids." Part II, The Clarendon Press, Oxford, 1964.

67. Moore, M. A., "A Preliminary Investigation of Frictional Heating During Abrasive Wear." Wear, 17, pp. 51-58, 1971.

68. Blok, H., "Theoretical Study of Temperature Rise at Surfaces of Actual Contact Under Oiliness Lubrication Conditions." Inst. Mech. Engr. Proc., Lubrication Discussion, Group IV, Vol. 2, pp. 26-39, Oct. 1937.

69. Jaeger, J. C., "Moving Sources of Heat and the Temperature at Sliding Contacts." Proc. Roy. Soc., N.S.W., 56, pp. 203-224, 1942.

70. Archard, J. F., "The Temperature of Rubbing Surfaces." Wear, 2, pp. 455, 1959.

71. Quinn, T. F. J., "Oxidational Wear." Wear, 18, pp. 413-419, 1971.

72. Quinn, T. F. J., "The Effect of 'Hot Spot' Temperature on the Unlubricated Wear of Steel." ASLE Trans., 10, pp. 158-168, 1967.

73. Quinn, T. F. J., "An Experimental Study of the Thermal Aspects of Sliding Contacts and Their Relation to the Unlubricated Sliding of Steel." Proc. Inst. Mech. Engrs., London, 183 (3p), pp. 129-137, 1968-69.

74. Quinn, T. F. J., "The Dry Wear of Steel as Revealed by Electron Microscopy and X-ray Diffraction." Proc. Inst. Mech. Engrs., London, 182 (3N), pp. 201-213, 1967-68.

75. Kubaschewski, O. and Hopkins, B. E., "Oxidation of Metals and Alloys." Butterworths, London, 1962.

76. Beerbower, A., "Boundary Lubrication: Scientific and Technical Applications Forecast." Final Report, Office of the Chief of Research and Development, Dept. of the Army, Washington, D.C., 1972.

77. Furey, M. J., "Surface Temperatures in Sliding Contacts." ASLE Trans., 7, pp. 133, 1964.

78. Earles, S. W. E. and Powell, D. G., "Surface Temperature and Its Relation to Periodic Changes in Sliding Conditions Between Unlubricated Steel Surfaces." ASLE Trans., 11, pp. 109-120, 1968.

79. Earles, S. W. E., Hayler, M. G., and Powell, D. G., "A Comparison of Surface Temperature Theories and Experimental Results for High Speed Dry Sliding." ASLE Trans., 14, pp. 135-143, 1971.

80. Tenwick, N. and Earles, S. W. E., "A Simplified Theory for the Oxidative Wear of Steels." Wear, 18, pp. 381-391, 1971.

81. Earles, S. W. E. and Hayler, M. G., "Wear Characteristics of Some Metals in Relation to Surface Temperature." Wear, 20, pp. 51-57, 1972.

82. Berry, G. A., "Comments on 'A Simplified Theory for the Oxidative Wear of Steels'." Wear, 18, pp. 497-498, 1971.

83. Berry, G. A., "Comments on 'Oxidational Wear'." Wear, 18, pp. 499-500, 1971.

84. Amsallem, C., Gaucher, A., and Guilhot, G., "The Unlubricated Frictional Behavior of Sintered Iron." Wear, 23, pp. 97-112, 1973.

85. Furby, N. W., "Mineral Oils" in "Interdisciplinary Approach to Liquid Lubricant Technology," NASA Symposium, Cleveland, Ohio, 1972.

86. Rossini, F. D., Proc. A.P.I., 15, 63, 1935; 19, III, 1, 1938.

87. Mair, B. J., Rubber World, 153, pp. 98, 1966.

88. Bondi, A., "Physical Chemistry of Lubricating Oils." Reinhold Publishing Corp., New York, pp. 232, 1951.

89. Hood, A. and O'Neal, M. J., Jr., "Advances in Mass Spectrometry." London, Institute of Petroleum, pp. 175, 1959.

90. Melpolder, F. W., Brown, R. A., Washall, T. A., Doherty, W., and Headington, C. E., Anal. Chem., 28, pp. 1936, 1956.

91. Lumpkin, H. E. and Johnson, B. H., Anal. Chem., 26, pp. 1719, 1954.

92. Lumpkin, H. E., Anal. Chem., 36, pp. 2399, 1964.

93. Van Nes, K. and Van Westin, H. A., "Aspects of the Constitution of Mineral Oils." Elsevier, New York, N.Y., 1951.

94. Waterman, H. I., Boelhouwer, C., and Cornelissen, "Correlation Between Physical Constants and Chemical Structures." Elsevier, New York, N.Y., 1958.

95. King, R. W., Kust, M. A., and Kurtz, S. S., Jr., Anal. Chem., 32, pp. 738, 1960.

96. Lochte, H. L. and Littmann, E. R., "Petroleum Acids and Bases." Chemical Publishing Co., Inc., New York, N.Y., 1955.

97. Latham, D. R., Okuno, I., and Haines, W. E., "Non-basic Nitrogen Compounds in Petroleum." Hydrocarbon Analysis, ASTM Special Technical Publication 389, pp. 363, 1965.

98. Tanaka, Y. and Kuwata, T., Faculty Eng., Tokyo Imp. Univ., 17, 293-303, 1928.

99. Mair, B. J., "Composition of Viscous Petroleum Oils." Rubber World, 153, 98, 1966.

100. Gulbransen, E. A. and Ruka, R., J. of Metals, 188, pp. 1500, 1950.

101. Paidassi, J., Trans. Amer. Inst. Min. (Metall) Engrs., 197, pp. 1570, 1953.

102. Tao, F. F., "A Study of Oxidation Phenomena in Corrosive Wear." ASLE Trans., Vol. 12, pp. 97, 1969.

103. Tao, F. F., "The Role of Diffusion in Corrosive Wear." ASLE Trans., Vol. 11, p. 121, 1968.

104. Zuidema, H. H., "The Performance of Lubricating Oils." Second Ed., Reinhold Publishing Corp., New York, 1959.

105. Chavanne, *G. and Bode*, E., J. Amer. Chem. Soc., 52, 1609-22, 1930.

106. Chavanne, G. and Tock, G., Bull. Soc. Chim. Belg., 41, 630-47, 1932.

107. Dupont, P. and Chavanne, G., Bull. Soc. Chim. Belg., 42, 537-43, 1933.

108. Fenske, M. R., et al., Ind. Engr. Chem., 33, 516-24, 1941.

109. Larson, R. G., and Co-workers, Shell Development Co., Unpublished Work.

110. Larson, R. G., Thorpe, R. E., and Armfield, F. A., Ind. Engr. Chem., 34, 183-93, 1942.

111. Engler, C. and Wild, W., "Veber die Sogenannte>>Acti-Virung<<des Saverstoffs and U ber Superoxydbildung." Ber., 30, 1669, 1897.

112. Bakh, A., "Du Rôle des Peroxydes Clans les Phenomenes d'oxydation Lenté." Compt. Rend., 124, 951, 1897.

113. Stevens, H. N. and Roduta, F. L., J. Am. Chem. Soc., 57, 2380-1, 1935.

114. Emmanuel, N. M., "Proc. Inter. Oxid. Symp." Am. Chem. Soc. Publ., Part I, 1968.

115. Emmanuel, N. M., Denisov, E. T., and Maizus, Z. K., "Liquid Phase Oxidation of Hydrocarbons." Plenum Press, New York, 1967.

116. Emmanuel, N. M., "The Oxidation of Hydrocarbons in the Liquid Phase." Pergamon Press, MacMillan Co., New York, 1965.

117. Boss, B. D. and Hazlett, R. N., "Oxidation of Hydrocarbons in the Liquid Phase: n-Dodecane in a Borosilicate Glass Chamber at 200°C." Canadian J. Chem. Soc., 47, 22, 4175, 1969.

118. Agabekov, V. E., Denisov, E. T., and Mitskevich, N. I., "Mechanism of Decarboxylation on Aliphatic Dibasic Acids in Liquid-Phase Oxidation." Izv. Akad. Nauk SSSR, Ser. Khim., 10, 2254, 1968.

119. Boudart, M., "Kinetics of Chemical Process." Prentice-Hall, Englewood Cliffs, N.J., 1968.

120. Blake, E. S., Hammann, W. C., Edwards, J. W., Reichard, T. E., and Ort, M. R., "Thermal Stability as a Function of Chemical Structure." ACS Preprints, Pet. Div., Vol. 5, No. 2, pp. B-5, April 1960.

121. Johns, S. B., McEthil, E. A., and Smith, J. O., "The Thermal Stability of Organic Compounds." I. and E.C., 1, 2, 1962.

122. Egloff, G., "The Reactions of Pure Hydrocarbons." Reinhold Publishing Corp., New York, pp. 230, 1937.

123. Morton, J. A. and Pease, R. N., "Kinetics of the Dissociation of Typical Hydrocarbon Vapors." J. Am. Chem. Soc., 55, 3190, 1933.

124. Dobrianski, A. F., Kanep, E. K., and Katsman, S. V., "Pyrogenetic Decomposition of Aliphatic-Aromatic Hydrocarbons." Chem. Zentr., 31, 3251, 1937.

125. Rice, F. P and Herzfeld, K. F., J. Am. Chem. Soc., 56, 284, 1934.

126. Steacie, E. W. R., "Aromatic and Free Radical Reactions." Second Ed., Reinhold Publishing Corp., New York, 1954.

127. Campbell, R. B., "Study of Hypoid-Gear Lubrication Using Radioactive Tracers." Proc. Convention Lub. and Wear, Inst. Mech. Engr., May 1963, Published, pp. 286-90, 1964.

128. Goldfrey, D., "Chemical Changes in Steel Surfaces During Extreme Pressure Lubrication." ASLE Trans., 5, 57, 1962.

129. Klaus, E. E. and Bieber, H. E., "Effect of P^{32} Impurities on the Behavior of Tricresyl Phosphate -32 as an Antiwear Additive." ASLE Trans., 8, 12, 1965

130. Anonymous, "Lubrication and Wear." Lubrication, Vol. 51, No. 6, Texaco Publication, pp. 61, 1965.

131. Tabor, D. and Willis, R. F., "The Formation of Silicone Polymer Films on Metal Surfaces at High Temperatures and Their Boundary Lubricating Properties." Wear, 13, 413-442, 1969.

132. Summers-Smith, D., "Chemical Reactions on Bearings in Lubricated Industrial Machines." Wear, 18, 291-300, 1971.

133. Hermance, H. W. and Egan, T. F., "Organic Deposits on Precious Metal Contacts." Bell System Tech. J., 37, 739-776, 1958.

134. Fein, R. S. and Kreuz, K. L., "Chemistry of Boundary Lubrication of Steel by Hydrocarbons." ASLE Trans., 8, 29-38, 1965.

135. Brown, R. D. and Burton, R. A., "An Experimental Study of the Relationship Between Oxygen Partial Pressure and Friction for 52100 Steel." ASLE Winter Annual Meeting, Pittsburgh, Pa., 1967.

136. Appeldoorn, J. K., Goldman, I. B., and Tao, F. F., "Corrosive Wear by Atmospheric Oxygen and Moisture." ASLE Trans., 12, 140-150, 1969.

137. Goldman, I. B., Appeldoorn, J. K., and Tao, F. F., "Scuffing as Influenced by Oxygen and Moisture." ASLE Trans., 13, 29, 1970.

138. Tingle, E. D., "The Importance of Surface Oxide Films in the Friction and Lubrication of Metals." Trans. Faraday Soc., 46, 93, 1950.

139. Godfrey, D., "The Lubrication Mechanism of Tricresyl Phosphate on Steel." ASLE Trans., 8, 1, 1965.

140. Godfrey, D., "The Effect of High Temperature on Friction and Wear." Proc. of the 5th World Petroleum Congress, Section 6, Paper 23, New York, 1959.

141. Barcroft, F. T. and Daniel, S. G., "The Action of Neutral Organic Phosphates as EP Additives." J. of Basic Engr., ASME Series D, 87, 761, 1965.

142. Benson, S. W., "Thermochemical Kinetics." Wiley, New York, 1968.

143. Kubaschewski, O., Evans, E. L., and Alcock, C. B., "Metallurgical Thermochemistry." Fourth Ed., Pergamon Press, London, 1967.

144. Mortimer, C. T., "Reaction Heats and Bond Strengths." Pergamon Press, New York, 1962.

145. Rosenblum, M., "Chemistry of the Iron Group Metallocenes." John Wiley & Sons, New York, 1965.

146. Marshall, E. F. and Wirth, R. A., "Uses for Organometallics in Fuels and Lubricants." Annals of the New York Academy of Sciences, Vol. 125, Art. 1, p. 198, 1965.

147. Brown, E. D., "Friction and Wear Testing with the Modern Four-Ball Apparatus." Wear, 17, pp. 381-388, 1971.

148. Slavin, W., "Atomic Absorption Spectroscopy." Interscience, New York, 1968.

149. Holman, J. L., "Experimental Methods for Engineers." Second Ed., McGraw-Hill Book Co., New York, pp. 56, 1971.

150. Morecroft, D. W., "Reactions of Octadecane and Decoic Acid with Clean Iron Surfaces." Wear, 18, 333-339, 1971.

151. Chaiken, S. W., "On Friction Polymer." Wear, 10, 49-60, 1967.

152. Fein, R. S. and Kreuz, K. L., "Chemistry of Boundary Lubrication of Steel by Hydrocarbons." ASLE Trans., 8, pp. 29-38, 1965.

153. Vinogradov, G. V., Arkharova, V. V., and Petrov, A. A., "Anti-Wear and Anti-Friction Properties of Hydrocarbons Under Heavy Loads." Wear, 4, pp. 274-291, 1961.

154. Zaslavsky, Y. S., Zaslavsky, R. N., Cherkaskin, M. I., et al., "Some Aspects of Friction Polymer Formation Chemistry." Wear, 30, 267-273, 1974.

155. Sanin. P. I., Vipper, A. B., Shepeleva, E. S., et al., "Interaction of Anti-Wear Additives with Friction Surfaces." Wear, 30, 249-265, 1974.

156. Powell, D. G. and Earles, S. W. E., "An Assessment of Surface Temperature Predictions in the High Speed Sliding of Unlubricated SAE 1113 Steel Surfaces." ASLE Trans., 15, 2, 103-112, 1972.

157. O'Donoghue, J. P., Manton, S. M., and Cameron, A., "The Heat Transfer Coefficient and Lubricated Contact Temperature." ASLE Trans., 10, 175-182, 1967.

158. Holm, R., "Calculation of the Temperature Development in a Contact Heated in the Contact Surface, and the Application to the Problem of the Temperature Rise in a Sliding Contact." J. Appl. Phys., 19, 361-366, 1948.

159. Barber, J. R., "Distribution of Heat Between Sliding Surfaces." J. Inst. Mech. Eng. Sci., Vol. 9, No. 5, 1967.

160. Francis, H. A., "Interfacial Temperature Distribution Within a Sliding Hertzian Contact." ASLE Trans., 14, 41-54, 1970.

161. Fein, R. S., "Transition Temperatures with Four-Ball Machine." ASLE Trans., 3, 34-39, 1960.

162. Bos, A., "The Temperature at the Wear Scars of the Four-Ball Apparatus." Wear, 31, pp. 17-27, 1975.

163. Buckley, D. H., "Oxygen and Sulfur Interaction with a Clean Iron Surface and the Effect of Rubbing Contact on These Interactions." ASLE Trans., Vol. 17, No. 3, pp. 206-212, 1974.

164. Buckley, D. H., "Friction Induced Surface Activity of Some Simple Organic Chlorides and Hydrocarbons with Iron." ASLE Trans., Vol. 17, No. 1, pp. 36-43, 1974.

☆ U. S. GOVERNMENT PRINTING OFFICE: 1976 — 657-630/1015